Surface Functionalization of Electrode Materials with Aryl-Diazonium Salts: Influence on Electronic Structure and Electrochemical Reactivity

Ian A. Murphy

A dissertation

submitted in partial fulfillment of the

requirements for the degree of

Doctor of Philosophy

University of Washington

2021

Reading Committee:

Brandi M. Cossairt, Chair

Bo Zhang

Cody Schlenker

Program Authorized to Offer Degree:

Chemistry

University of Washington

Abstract

Surface Functionalization of Electrode Materials with Aryl-Diazonium Salts:
Influence on Electronic Structure and Electrochemical Reactivity

Ian A. Murphy

Chair of the Supervisory Committee:
Associate Professor Brandi M. Cossairt
Department of Chemistry

The development of efficient and abundant materials for the conversion and storage of renewably generated electricity is the lynchpin for enabling the global transition to a sustainable and cyclical economic model. In this work I explore two promising systems to meet this need; nickel phosphide as a hydrogen evolution electrocatalyst and sulfur cathodes for next-generation rechargeable lithium-ion batteries. Both earth abundant alternative chemistries promise to challenge current state-of-the-art materials, which rely on scarce and expensive metals. However, much work is still needed to tune the electrochemical properties of these materials before their true potential can be realized. Electrochemical activity is dictated by a delicate balance of a material's internal electronic structure and the way in which its surface atoms interact with the external environment, namely the electrolyte and active material substrates. Herein, I show how functional

surface chemistry can address both aspects through the installation of substituted aryl functional groups on the electrode surface *via* reduction of aryl diazonium salts. The functionalization of nickel phosphide nanocrystals with an array of substituted aryl groups of varying electron donating and withdrawing character showcases how the internal electronic structure of a material can be tuned to improve its catalytic activity. Then, the way in which rationally designed surface functional groups can offer new reaction pathways for dynamic conversion electrode reactions is showcased through the installation of thiophenol groups in a sulfur/carbon composite electrode. Though there is still much work to be done in the development of novel material systems for these critical electrochemical applications, I hope that this work can serve as a case study in the utility that surface chemistry can have in altering the intrinsic properties and reactivity of earth abundant materials.

TABLE OF CONTENTS

LIST OF FIGURES

ACKNOWLEDGEMENTS

I would like to firstly acknowledge the giant shoulders on which I stood while conducting this work. This includes the recognizable names of the past, their theorems and their frameworks, but also the countless scientists and research assistants who never received the proper accolades for their contributions. To all those who made this work possible, named, or unnamed, thank you.

Of those scientists that directly and indirectly supported me during my graduate research, I would specifically like to express my heartfelt appreciation to Brandi M. Cossairt and her masterfully cultivated research group. Before we are scientists, we are humans – and Brandi has shown time and again her exceptional talents for recognizing the humanity of her colleagues and protégé alike. This subtle, yet critical differentiating factor between her and many in our community allows for the freedom and safety to truly cultivate our potential as individuals and as scientists. Thank you, Brandi.

It is often said that graduate research is a marathon and not a sprint. Personally, I find it more akin to a vaguely guided trip around the world. One in which you must wake up every day and figure out for yourself how to make it to the next point. Though you may get clues, context, or suggestions from those who have traversed this path before – it remains your personal responsibility to see the expedition through to the end. Through my travels, literal and metaphorical, I have found the most rewarding aspects to be the truly wonderful people I encounter along the way. In a very real sense, the Cossairt Lab is the only reason I was able to complete my voyage. Be it scientific, personal, or void of explicit purpose at all – the conversations and support I received from my dear friends and colleagues in the Cossairt Lab gave me the strength to wake

up each day and feel confident in taking my next step. Thank you, David, Cecilia, Florence, Michael, Tyler, Emily, Ding-Yuan, Ricardo, Micaela, Nayon, Madison, Forrest, Beth, Max, Helen, Hao, Andrew, Shenwei, and Aditi – from the bottom of my heart.

None of this work would be possible without the support of my many amazing collaborators and the staff of the University of Washington Department of Chemistry. For providing assistance, instruction, endless support, and a safe and supportive working environment – thank you.

For ensuring that I was able to make it to a position to conduct such work, I would like to express my unending gratitude to my family – specifically my father David Murphy Jr. Dad, thank you for your endless support and encouragement. Thank you for always being on my team. Thank you for always making sure I felt loved. Thank you for giving me the space to grow. Thank you for teaching me to be flexible and that the grade you receive isn't nearly as important as understanding the core concepts. I love you.

To my chosen family, my constant support system, and my best friends – thank you. Kandi and Jose, this wouldn't have been possible without you.

Finally, to my wonderful wife Raven, thank you darling. Thank you for keeping me grounded when I would begin to lose focus on what is most important. Thank you for listening to me despite not always understanding what I was saying. Thank you for the much-needed distractions. Thank you for being a constant, rather than variable, in my life. Thank you for letting me know I can always count on you. Thank you for your unconditional love. And most importantly, thank you for bearing with me. I know this time has been challenging for us both, but now we can proudly move onto our next chapter where, for a change, you can lean on me. Thank you Raven, I love you.

DEDICATION

This work is dedicated to my mother, Stephanie Speir Murphy.

To the brightest guiding light I've ever known, I hope this can make you proud.

Chapter 1. INTRODUCTION

This chapter is meant to introduce key concepts and provide context for the work discussed in chapters 2-4. As such, many of the ideas here are briefly introduced and then further fleshed out in their respective chapters.

1.1 THE TRANSITION TO A SUSTAINABLE ECONOMY

The prevention of catastrophic climate change is truly the challenge of our time and a key motivating force for innovation throughout all aspects of science, technology, and policy making. To keep the average temperature rise of the atmosphere below 1.5 °C relative to pre-industrial levels we must make drastic cuts to the amount of 'green-house gases' (GHG) released into the atmosphere.[1] Generally, the major contributing species are carbon dioxide (CO_2), methane (CH_4), nitrous oxides (NO_X), and fluorinated species like sulfur hexafluoride (SF_6) – with CO_2 accounting for the vast majority (76%) of GHGs emitted globally.[2] Many different activities contribute to these emissions and have recently been summarized by the US Environmental Protection Agency (Figure 1.1).

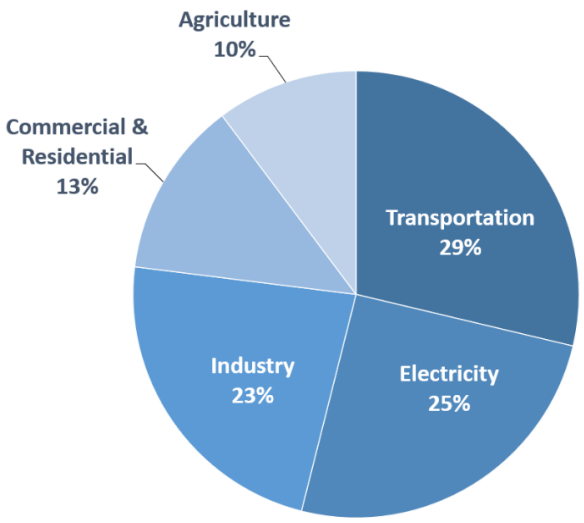

Figure 1.1. Breakdown of GHG emissions by economic sector in the US for 2019.[2]

As it currently stands, the largest percentages of GHG emissions come from transportation and the generation of electricity, which rely on coal and natural gas, and refined liquid hydrocarbons (gasoline), respectively. As these sectors make up the largest fraction of US emissions, they held the largest share of initial focus for developing and deploying carbon independent alternatives. Remarkable global efforts over the past few decades have led to the development of renewable alternatives for electricity generation that are cost competitive with traditional carbon dependent processes, in the form of solar photovoltaic modules and wind turbines.[3] We are now seeing a similar trend in the cost of energy storage systems, namely lithium-ion batteries (LIB), which is a key component to making renewable powered electric grids resilient to the intrinsic limitations of intermittent generation.[4] This renaissance for LIBs is also positioned to drastically reduce the emissions from light-duty transportation as electric vehicles (EVs) become more affordable and reliable.[5]

Despite this amazing progress, there are many sectors of the global economy that cannot be electrified either due to intrinsic limitations of energy storage chemistries or the fundamental

chemical processes required to make a given product. For example, the energy density of a LIB is directly proportional to the amount of material used to make the cell. Thus, higher energy batteries are necessarily heavier, which make current chemistries ill-suited to power heavy-duty transport vessels such as commercial aircraft or transcontinental shipping. Other examples of these limitations include the production of critical materials like steel, plastics, and fertilizers – all of which currently release CO_2 as a byproduct of the chemical reactions used for fabrication. Addressing these embedded sources of global GHG emissions is an effort known as "deep decarbonization" and calls upon us to fundamentally reimagine the way we use energy and abundant elements like H, C, N, and O to produce fundamental materials without emitting more GHG. An example of this "whole system approach" was illustrated by the National Renewable Energy Laboratory (Figure 1.2).[6]

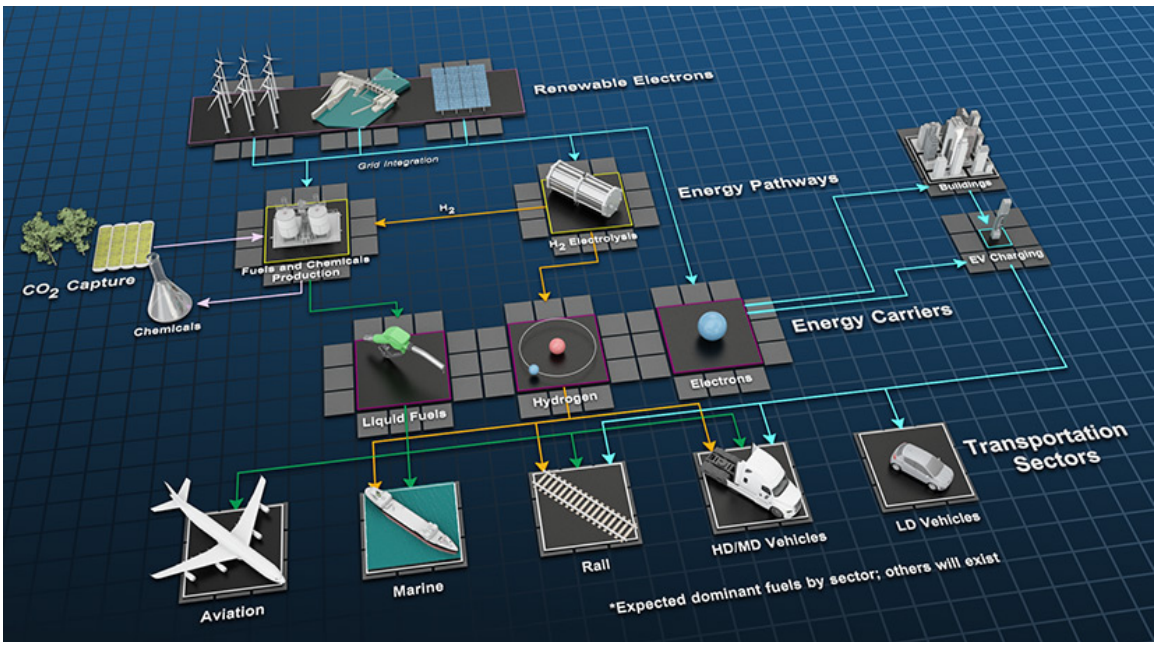

Figure 1.2. Schematic depiction of the integrated use of renewably generated electrons, H_2 made from water, and CO_2 captured from the air to address various aspects of the transportation sector.[6]

Though the immediate importance of this work is to find viable methods to meet the current global standard of living without emitting new equivalents of GHGs, we must be mindful in this moment not to repeat the mistakes of the past and develop unsustainable and unidirectional systems. The demand for energy, materials, food, clean water, etc. is only growing as the standard of living is rapidly increasing for much of the world.[7] As this demand increases, we must thoughtfully embed the practice of recycling and reuse into our technological innovations while always striving to maximize the use and impact of environmentally abundant resources.

1.2 Overview of Electrocatalysis

The foundation of a circular and sustainable economic model is the efficient interchange of atomic building blocks to make necessary materials. In many cases, nature has provided blueprints for how to accomplish such tasks in biological systems that make use of complex enzymatic catalysts.[8] In the same way that these biocatalytic systems uses sunlight to convert CO_2 and H_2O into energy carriers, researchers around the world are working to develop catalysts that utilize sustainably generated energy to facilitate industrially useful chemical transformations (Figure 1.3). Developing abundant and efficient electrocatalysts for key chemical transformations can have wide reaching impact on many different sectors. From the sustainable generation of H_2 as an energy carrier, to the synthesis of sustainable aviation fuel *via* the reduction of CO_2, there are a myriad of valuable reactions to study.[9,10]

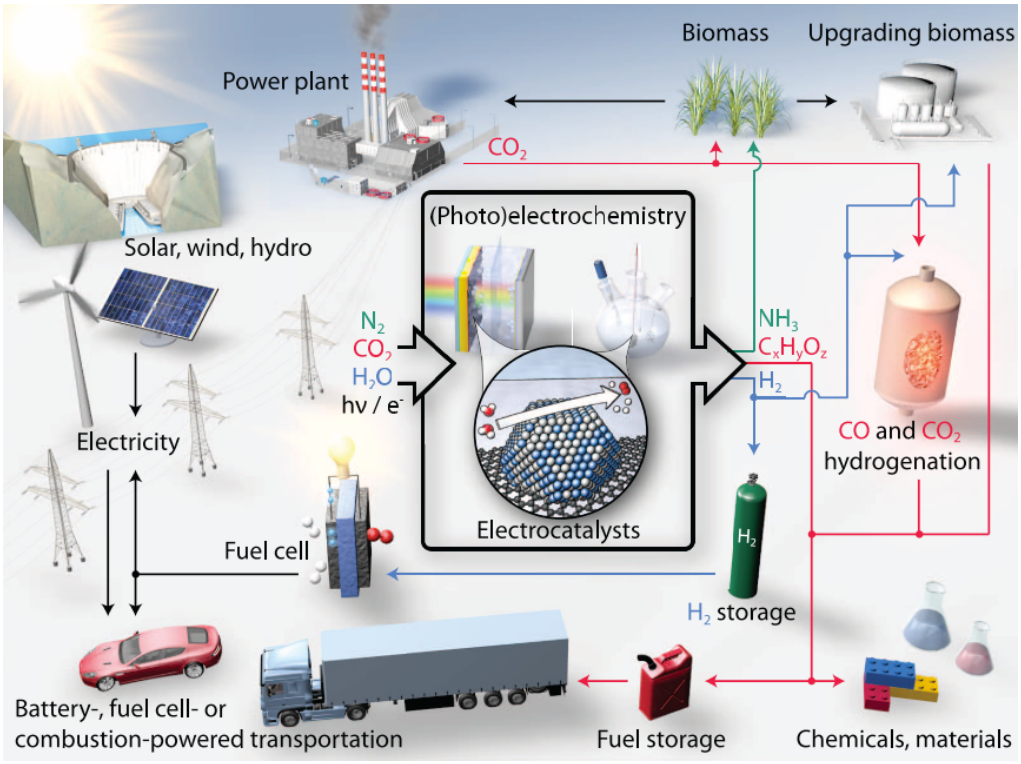

Figure 1.3. Schematic depiction of the core influence (photo)electrocatalysts can have on a sustainable economic model.[10]

1.2.1 *What is a Catalyst?*

Catalysts are species that facilitate chemical reactions by lowering the additional kinetic energy barrier between reactants and products (Figure 1.4). Importantly, catalysts are not consumed but instead are regenerated during the reaction.

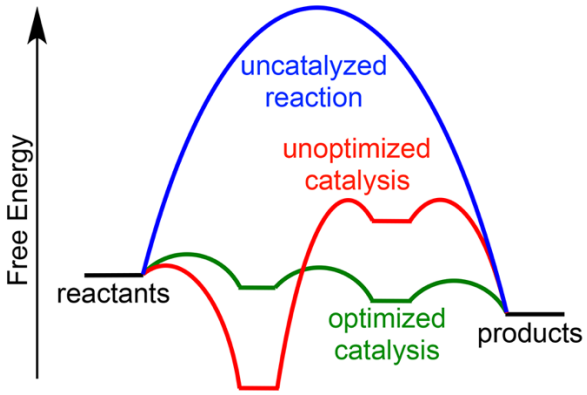

Figure 1.4. Schematic depiction of energy associated with and uncatalyzed, poorly catalyzed, and optimally catalyzed thermodynamically favorable reaction.

An ideal catalyst will result in the smallest activation barriers between products and reactants, is highly stable in the reaction environment, and is selective for a given reaction. Minimizing the additional energy needed to overcome activation barriers is critical for making most efficient use of renewably generated electricity. The energy required to run a reaction can be translated into the electrochemical potential by equation 1.1:

$$P = IE \tag{1.1}$$

Where P represents power in watts, I represents current in amps, and E represents cell voltage in volts. The current in this case directly represents the number of electrons, or charge equivalents (q), that must be delivered to, or taken from, the reactant in order to generate a given product. The cell voltage, or electrochemical potential, is a measure of the energy barrier between the reactant and product states, which can be further broken down to:

$$E = E^0 + \eta \tag{1.2}$$

Where E^0 is the thermodynamic potential difference between the two states and η represents the additional "overpotential" required to address the kinetic limitations of the transformation. Using the example in Figure 1.4, the blue trace would have the largest overpotential, and the green trace would have the lowest overpotential – due to the influence of an optimal catalyst. Thus, there is a direct correlation between the activity of a catalyst and energy savings at the device level.

1.2.2 *Relevant Redox Reactions for Sustainable Fuels*

As discussed above, there is a wide range of chemical transformations that hold industrial relevance. However, the common electrocatalytic reactions that are studied for sustainable fuel applications are summarized below in Figure 1.5.

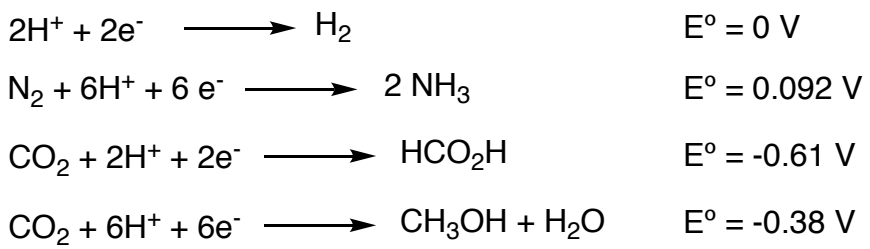

Figure 1.5. Balanced chemical reactions for the formation of sustainable fuels like H_2, NH_3 (ammonia), and CH_3OH (methanol). Thermodynamic potentials for each reaction are reported versus the Natural Hydrogen Electrode (NHE).[11]

These reactions comprise the reductive, or cathodic, half reactions for the full transformation in an acidic medium. For these processes to be sustainable, the proton (H^+) equivalents must be generated from the anodic oxidation of water at the counter electrode (anode), written as:

$$2H_2O \rightarrow 4H^+ + 4e^- + O_2 \quad (1.3)$$

In acid, the thermodynamic potential to drive this reaction is 1.23 V vs NHE. In a full electrochemical cell, both the anodic and cathodic reactions must be completed in tandem to drive

the reaction to completion. In the case of the hydrogen evolution reaction (HER) from water, the simplest electrocatalytic reaction, the balanced equation can be written as:

$$2\mathrm{H}_2O \rightarrow 2H_2 + O_2 \qquad (1.4)$$

1.2.3 *What makes a catalyst active?*

For the production of H_2 and O_2 *via* water electrolysis (equation 1.4), the state-of-the-art catalysts are platinum for the cathodic reaction (HER) and iridium oxide for the anodic reaction (oxygen evolution reaction, or OER). Understanding what makes these materials so effective at facilitating these reactions has been the object of fascination for electrochemists for over a century. In the 1970's, Italian electrochemist Sergio Trasatti published a seminal compilation of various descriptors for a wide range of metals and compared them to the activity they exhibit for HER.[12] The result of this effort was the formulation of a "volcano plot" that related a metal's affinity for making metal-H (metal hydride) bonds to the exchange current density for HER on a given metal (Figure 1.6). The exchange current is a valuable electrochemical term that estimates the reaction kinetics between reactants and products at the thermodynamic potential.[13]

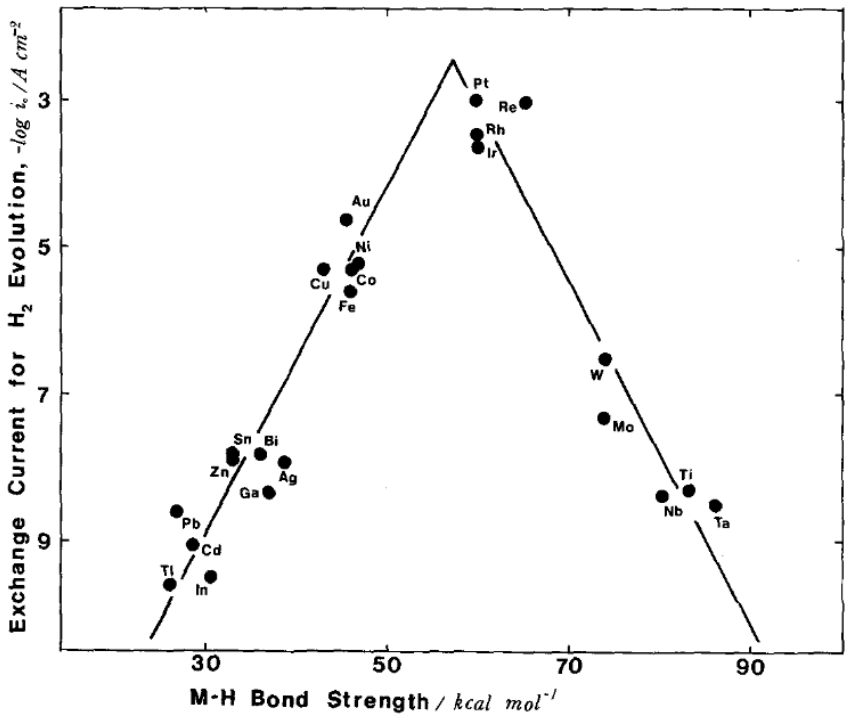

Figure 1.6. Original "volcano plot" by Trasatti showing the relationship of M-H bond strength to the exchange current density for HER on various metal electrodes.[12]

Unfortunately, due to the scarcity of these precious metals, we cannot rely on them to be the basis of a sustainable economy, despite being the most active naturally occurring catalysts.[14] Platinum and iridium account for roughly 0.005 and 0.001 ppm of the earth's crust, respectively, and cost $35 and $193 per gram, respectively, in 2021.[82] As a result, the identification of earth abundant alternatives to these materials has been an intense area of research for the past few decades. Much of this work has been beautifully summarized in a review article written by Jaramillo and Nørskov.[10] Using the principles described in Trasatti's compilation, researchers from around the world aimed at mimicking the activity of platinum by engineering materials to have similar properties, namely that of a thermoneutral metal-hydride energy. This line of inquiry delivered incredible results and led to consistent improvements in electrode overpotential, as illustrated in Figure 1.7.

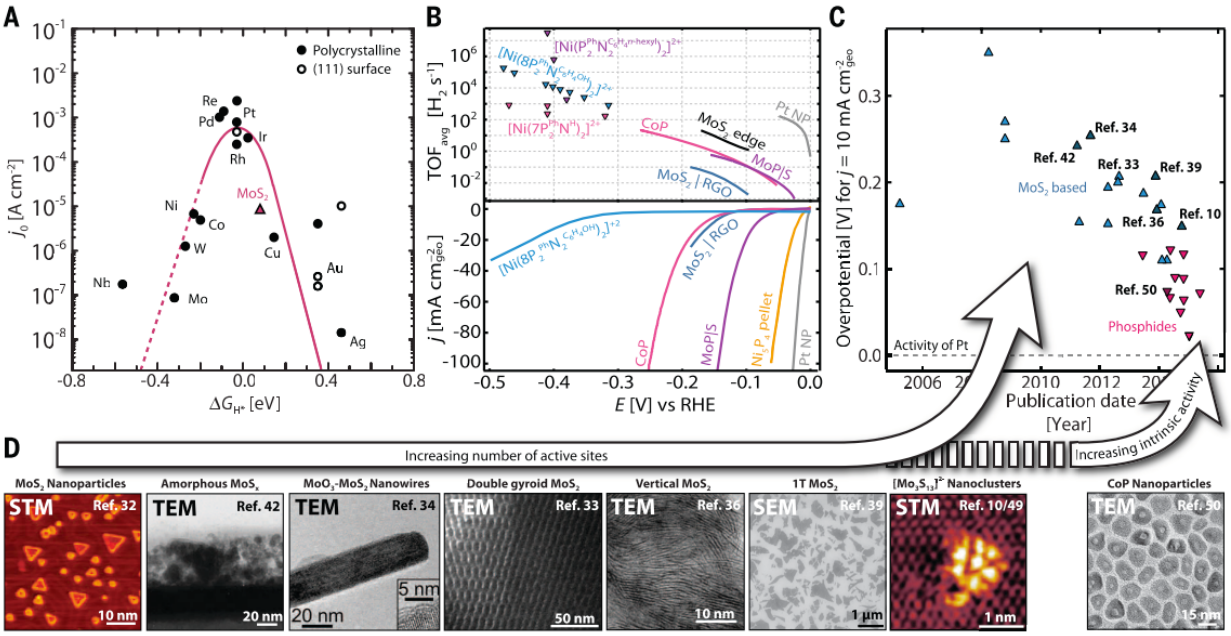

Figure 1.7. Figure summarizing the utilization of descriptor based models in finding alternative HER catalysts. (a) Volcano plot comparing the adsorption energy of H on various transitions metals and MoS_2 to their exchange current density for HER. (b) Comparative linear sweep voltammograms and turn-over-frequencies of various metal-phosphide and sulfide catalysts versus platinum. (c) Plot of catalyst overpotential for HER versus year of report for various metal-sulfide and phosphide materials. (d) Illustrative trend in the investigation of nano structuring to "intrinsic activity" discussed in the report.[10]

Among the material classes discovered to have high activity for HER in acidic media are metal-phosphides, namely the earth abundant CoP, FeP, and Ni_2P.[15,16] However, despite the relatively low overpotential enabled by these catalysts due to their near thermoneutral M-H adsorption energies, their activity falls orders of magnitude short of platinum (Figure 1.8).

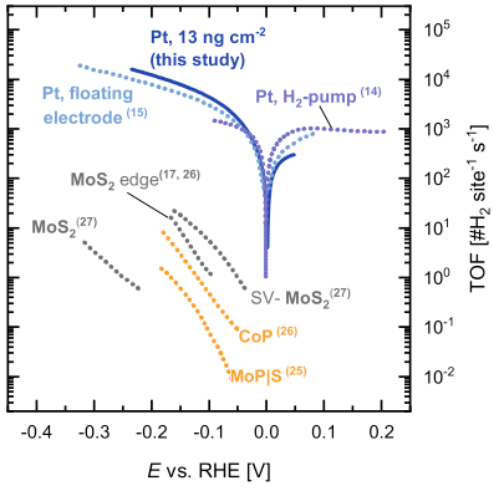

Figure 1.8. Plot of turn-over-frequency for various HER catalysts as a function of applied potential. Authors compare platinum to multiple compelling earth abundant alternatives such as CoP and MoS_2, illustrating the huge difference in true intrinsic activity between these materials and platinum.[17]

Though the root of this discrepancy is still an active field of inquiry, it has been proposed that the optimal reactivity may be, in part, due to the distance *into* the electrolyte that the diffuse frontier orbitals of platinum are able to penetrate.[18] This theory, known as d-band theory, describes the aspects of platinum's electronic structure that cannot be mimicked by lighter atoms in the periodic table.[19] Thus, if there are aspects of a material that cannot be mimicked, we must develop new avenues of inquiry that could lead to further improvement of catalytic activity.

1.2.4 *Future Directions for Catalyst Development*

For centuries synthetic inorganic chemists have recognized the power that ligands, the organic components surrounding a metal center, have on altering their catalytic behavior.[20–23] Many of these lessons were inspired by the field of biomimetic catalysis, which explicitly try to recreate the

environments found within catalytic enzymes.[8,24,25] These rich fields of study provide strong evidence that the environment surround a catalytic site, often shaped by organic ligands, play a critical role in leveling the kinetic barriers associated with complex chemical transformations.[26–28] The idea that this same kind of control can be observed in nanoparticle chemistry is a key driving force for much of my research.

1.3 Overview of Battery Chemistries

For the aspects of a sustainable economy that can operate purely on electricity, batteries play an indispensable enabling role. Whether it be the storage of intermittent electricity generated on the power gird or improving the driving range of electric vehicles (EVs), the cost, capacity, and stability of these devices is imperative.[29–32] It is specifically because of the breakthroughs in LIB manufacturing, resulting is drastic price reductions and improvements in safety and reliability, that many sectors are able to begin shifts to all electric products and services.[4]

Today's LIBs are comprised of two electrodes (Figure 1.9), where the negative electrode (anode) holds the high-potential lithium deposits, and the positive electrode (cathode) is comprised of material that collects lithium as the battery discharges.

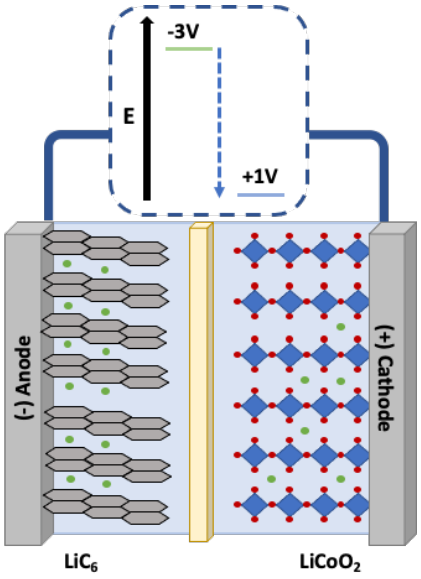

Figure 1.9. Schematic depiction of traditional LIB cells comprised of graphite anodes and $LiCoO_2$ cathodes. Green dots represent lithium ions. The energy landscape at the top represent the cell voltage achieved as lithium is allowed to intercalate into the $LiCoO_2$ host.

As a result of constant consumer pressure for higher capacity cells, researchers and manufactures alike have made valiant efforts towards increasing the number of reactive lithium ions in a cell. Most of this work has focused on the anode, namely replacing the current anode host material, graphite, with higher capacity silicon or removing a host all together and using pure lithium metal.[33,34] Innovations in anode chemistry are poised to roughly double the capacity of current LIBs, however, it seems that the true physical and economic limitations may reside in the structure of the cathode.[35–37]

1.3.1 *Intercalation Cathodes*

Current state-of-the-art cathode materials are mixed metal oxides, typically composed of nickel, cobalt, aluminum, and manganese in various stoichiometries.[38] This class of materials is based on

the principles that Whittingham and Goodenough first explored in the 1970's and 80's, where under applied potential small cations could intercalate in-between the metal oxide's layered structure.[39,40] Through decades of research and refinement, it seems as though this material class may be reaching its thermodynamic limit, which is dictated by the reduction potential of the mixed metal oxide and intrinsic number of lithium ions that be held between its layers.[36] This point of technological advancement comes at a time of unprecedented growth in the manufacturing volume of LIBs.[41] As a result, early warning signs are being set off over the projected scarcity of critical metals needed to fabricate high capacity intercalation cathodes, specifically cobalt.[35] Although cell recycling methods are currently being developed, alternative battery chemistries must be quickly developed in order to maintain a viable supply chain for application where high power LIBs are necessary.

1.3.1 *Conversion Cathodes*

A promising alternative at the cutting edge of current research efforts is a class of materials called conversion cathodes.[42,43] In these systems, lithium explicitly reacts with the host material, rather than simply intercalating between the layers of a larger crystal. This means that more charges are passed in the redox reactions leading to higher overall capacity for a given amount of active material. Further, many of these systems use earth abundant elements like O, F, S, and Fe, which would drastically reduce the cost per kWh of capacity and have a more benign impact on the environment. Of the promising conversion cathode candidates, lithium-sulfur cells have garnered specific attention because of their potential to break the $100/kWh threshold set by the U.S. Department of Energy.[44,45]

1.3.1 *Overview of Lithium-Sulfur Batteries*

Lithium sulfur batteries theoretically offer an order of magnitude increase in specific capacity versus current state-of-the-art intercalation compounds at a fraction of the cost.[45–47]

Table1 | Data for several electrochemical reactions that form the basis of energy-storage devices.

Battery	Cell voltage (V)	Theoretical specific energy (Wh kg^{-1})	Theoretical energy density (Wh l^{-1})
Today's Li-ion $\frac{1}{2}C_6Li + Li_{0.5}CoO_2 \leftrightarrow 3C + LiCoO_2$	3.8	387	1,015
Zn–air $Zn + \frac{1}{2}O_2 \leftrightarrow ZnO$	1.65	1,086	6,091* (ZnO)
Li–S $2Li + S \leftrightarrow Li_2S$	2.2	2,567	2,199† (Li + Li_2S)
Li–O_2 (non-aqueous) $2Li + O_2 \leftrightarrow Li_2O_2$	3.0	3,505	3,436‡ (Li + Li_2O_2)
Li–O_2 (aqueous) $2Li + \frac{1}{2}O_2 + H_2O \leftrightarrow 2LiOH$§	3.2	3,582	2,234‖ (Li + H_2O + LiOH)

*Based on volume of ZnO at the end of discharge; †based on the sum of the volumes of Li at the beginning and Li_2S at the end of discharge; ‡based on the sum of the volumes of Li at the beginning and Li_2O_2 at the end of discharge; §assuming the product is anhydrous LiOH and alkaline conditions; and ‖based on the sum of the volumes of Li + H_2O consumed and the LiOH at the end of discharge.

Figure 1.10. Table comparing multiple battery chemistries. For each system, the chemical reaction is reported along with the voltage, theoretical specific energy, and theoretical energy density.[48]

The difficulty with realizing this promise comes at a fundamental difference in material properties. Sulfur, unlike the metal-oxide materials, is a very poor electrical conductor. This requires the sulfur to be embedded in a highly conductive host material in order to undergo redox reactions with lithium ions. Typically, this is achieved using microstructured graphitic carbons, which are light weight and still relatively inexpensive.[49] The carbon then must additionally be mechanically held together by binding polymers because the volume expansion during lithiation can cause cracks to form in the electrode which can electronically isolate portions of the electrode.[50,51] These necessary composite additives reduce the theoretical specific capacity, but still offer significant advances over current chemistries.

However, the difficulties of commercializing lithium sulfur cells do not end at the poor conductivity of the active material. The conversion of S into its fully lithiated state, Li_2S, goes through a complex set of intermediate species called lithium polysulfides (LiPS) (Figure 1.10).[48] LiPS are highly soluble in most organic electrolyte solvents used in LiS batteries and will dissolve into the electrolyte during cycling which can lead to displacement and eventual capacity fading. Severe cases can result in a phenomenon known as redox shuttling, which effectively shorts the battery as LiPS constantly cycle back and forth between cathode and anode.[52,53]

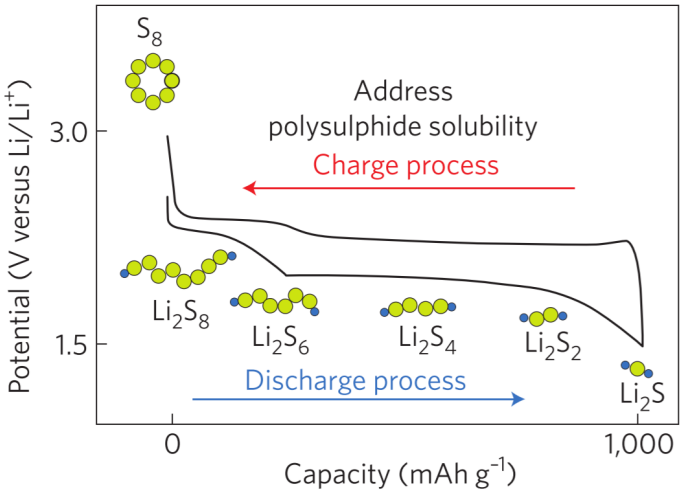

Figure 1.11. Schematic depiction of the conversion reaction of S_8 to Li_2S during the discharge of lithium-sulfur batteries. Speciation is tied to the different regions of charge and discharge as illustration by the voltage profile.[48]

Although it may seem intuitive to simply use solvents that cannot solvate the LiPS, this dynamic is actually required for the cell to have good cycling rate capabilities due to the sluggish kinetics of solid-state sulfur lithiation.[54–56] Thus, to address the issues of sluggish LiPS redox and dissolution and diffusion from the cathode, researchers have been investing the use of polar host materials and embedded catalysts.[57–60] Though this line of inquiry has provided promising results

it adds more inactive mass and more costly materials into the cathode composition. As such, it seems like trying to influence the way graphitic host materials can directly interact with LiPS and the electrolyte environment through functional surface chemistry may be a promising route to improving cell performance.

1.4 General Survey of Surface Chemistry

The concept of installing organic functional groups on the surface of a material or making covalent linkages between molecules and materials has been investigated for many decades.[61] Inspired by the fidelity with which small changes to the chemical structure of organic and organometallic molecules can afford drastic physiochemical and electronic changes, the field of functional surface chemistry has aimed to afford the same degree of control to bulk materials which offer their own distinct benefits such as high conductivity and stability. Exploring this parameter space has shown that surface ligands, or surface functional groups, are able to modulate the electronic properties of a material[62–64], alter its solubility and the way it interacts with the broader environment[65,66], and address degredation conerns.[67–69] Though this work will focus on the influence of functional surface chemistry in catalysis and energy storage chemistries, the impact of field reaches every intersection of materials chemistry and application including biomedical, sensing, and novel semi-conductor systems.[69–72]

1.4.1 *Surface Chemistry in Electrocatalysis*

In the field of electrocatalysis there are generally two ways to approach the challenge of melding molecular (homogeneous) and material (heterogeneous) properties. The first is a "top-down" approach, where researchers have explored methods to covalently tether already developed molecular catalysts to the surface of a conductive substrate, generally graphitic carbon. Two

examples of this are shown below in Figure 1.11. The top panel (Figure 1.11a) shows the covalent tethering of a cobalt porphyrin complex to surface of *p*-doped diamond *via* "click" chemistry with a surface bound azide group.[73] These aliphatic groups were installed by photolysis of the terminal alkene in 10-undecen-1-ol and the hydrogen terminated diamond surface.[74] The resultant hybrid material showed improved activity over the diamond alone and increased stability relative to the molecular catalyst alone. This concept of covalently tethering molecular catalysts is still under active investigation by the Surendranath group who has developed a method to not only immobilize the catalyst onto the electrode surface, but actually embed the catalyst into the band structure of the glassy carbon electrode through highly conjugated phenazine linkages.[75,76] This builds on previous work by decoupling electron transfer between the support, the catalyst, and the substrate.

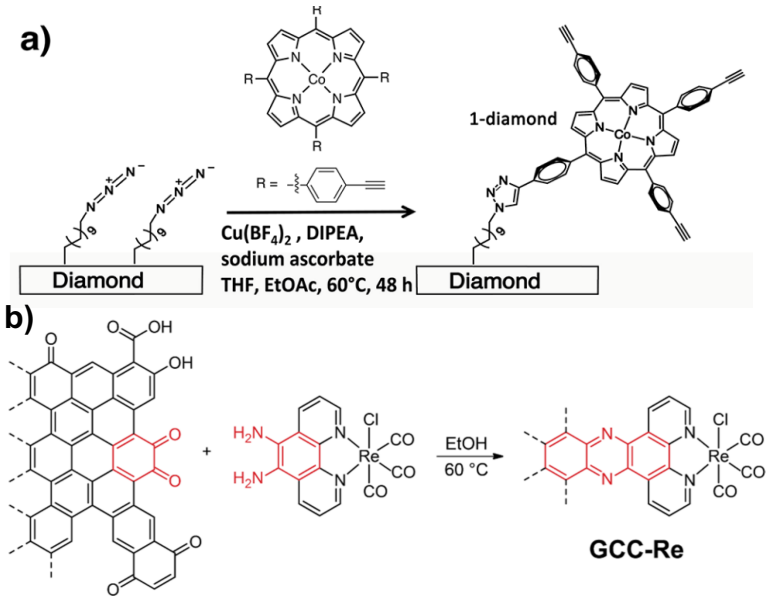

Figure 1.12. Synthetic schemes for the covalent tethering (a)[73] and conjugated integration (b)[70] of molecular catalysts to the surfaces of conductive carbon substrates.

The second, or "bottom-up", approach aims at utilizing the catalytically active surfaces on nanoparticulate heterogeneous catalysts by augmenting their reactivity with surface ligands. This

class of materials is addressed in detail in Chapter 2 and is the foundation of the work presented in Chapter 3. Briefly, a powerful example of this approach was recently shown by Buonsanti and co-workers through their work on improving the selectivity of Ag nanoparticles for the reduction of CO_2.[77] By installing a series of imidazolium-based ligands onto the surface of their catalyst (Figure 1.12) they were able to tease out multiple spheres of influence that the ligand had in directing the electrocatalytic reaction. Ultimately, the authors reported the importance of the interaction of the ligand anchoring group with the particle surface, having stabilizing agents in the inner-coordination sphere (a few bond lengths from the surface), and how the tail group can promote or deter substrate access to control concentration gradients.

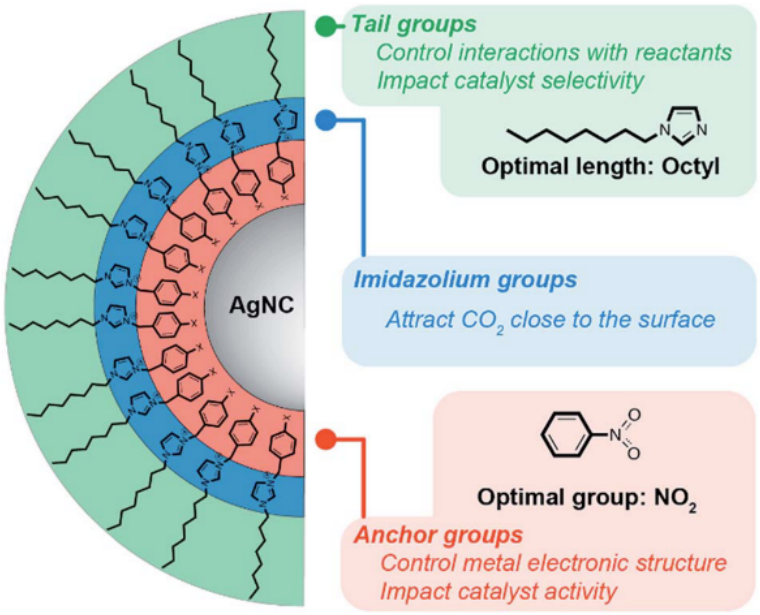

Figure 1.13. Schematic depiction of Ag nanocrystals functionalized with 3-part tailored ligands. Each section reflects the different spheres of influence that organic ligands can have on the reactivity of nanocrystalline electrocatalysts.[77]

1.4.1 *Surface Chemistry in Batteries*

Examples of surface functionalization in battery electrodes are more scarce, but the prospect of its utility are becoming more obvious for the next generation of more dynamic electrode chemistries. Current examples typically focus on better integrating polymer binders,[78,79] formation of "artificial solid-electrolyte-interphases",[80] or inducing surface dipoles to interact with highly charged reaction intermediates.[81] This last example served as the inspiration for the work discussed in Chapter 4, though all effects are relevant and merit further investigation.

1.5 OUTLOOK

I hope this summary has brought some context to the work that will be discussed in the following chapters. We currently face many near impossible challenges to overcome. We must fundamentally change the foundations of our global economy while also devising a system that will not encounter the same scarcity-based limitations. At the center of this effort will be the intelligent and sustainable management of renewable energy and abundant matter. A major piece of this puzzle seems to be solved – that is the means to affordably and efficiently capture natural sources of energy. Now, we must develop methods and materials to store this energy and efficiently direct it to the sectors of our economy that still rely on GHG emitting processes. Though great progress has already been made in this regard, significant innovation is still required to alleviate our reliance on scarce and expensive metals. Over the course of my studies, I have explored the application of functional surface chemistry to address various limitations encountered when using earth abundant materials in the fields of electrochemical energy conversion and storage. Through these studies I provide separate examples of how surface functional groups installed *via* covalent electrode-aryl bonds can influence the electronic properties of nanocrystalline electrocatalysts and the reaction pathways of LiPS in next-generation lithium-

sulfur batteries. Each study provides valuable lessons about the promise and limitations of such approaches and lays the groundwork for integrating both influence on the electrode and electrolyte in one system. Ultimately, I hope that this work can be a critical building block towards the development of elegant, perfectly optimized, electrode-ligand interactions which enable the adoption of novel sustainable technologies.

REFERENCES

(1) IPCC. *SPECIAL REPORT: GLOBAL WARMING OF 1.5 ºC*; 2018; Vol. 1.

(2) USEPA. Sources of Greenhouse Gas Emissions https://www.epa.gov/ghgemissions/sources-greenhouse-gas-emissions.

(3) Roser, M. Why Did Renewables Become so Cheap so Fast? And What Can We Do to Use This Global Opportunity for Green Growth? *Our World in Data*. 2020.

(4) Ziegler, M. S.; Trancik, J. E. Re-Examining Rates of Lithium-Ion Battery Technology Improvement and Cost Decline. *Energy Environ. Sci.* **2021**, *14* (4), 1635–1651. https://doi.org/10.1039/d0ee02681f.

(5) Global EV Outlook 2020. *Glob. EV Outlook 2020* **2020**. https://doi.org/10.1787/d394399e-en.

(6) Lighting the Path to Net Zero: NREL's Strategy Drives Deep Transportation Decarbonization https://www.nrel.gov/news/program/2021/lighting-the-path-to-net-zero-nrels-research-strategy-drives-deep-transportation-decarbonization.html.

(7) Roser, M. The short history of global living conditions and why it matters that we know it - Our World in Data https://ourworldindata.org/a-history-of-global-living-conditions-in-5-charts?linkId=62571595%0Ahttps://ourworldindata.org/a-history-of-global-living-conditions-in-5-charts.

(8) Bullock, R. M.; Che, J. G.; Gagliardi, L.; Chiri, P. J.; Farh, O. K.; Hendo, C. H.; Jone, C. W.; Keit, J. A.; Klosin, J.; Mintee, S. D.; Morri, R. H.; Radosevic, A. T.; Rauchfus, T. B.; Strotma, N. A.; Vojvodic, A.; War, T. R.; Yan, J. Y.; Surendranath, Y. Using Nature's Blueprint to Expand Catalysis with Earth-Abundant Metals. In *Science*; American Association for the Advancement of Science, 2020; Vol. 369, p eabc3183. https://doi.org/10.1126/science.abc3183.

(9) De Luna, P.; Hahn, C.; Higgins, D.; Jaffer, S. A.; Jaramillo, T. F.; Sargent, E. H. What Would It Take for Renewably Powered Electrosynthesis to Displace Petrochemical Processes? *Science (80-.).* **2019**, *364* (6438), eaav3506. https://doi.org/10.1126/science.aav3506.

(10) Seh, Z. W.; Kibsgaard, J.; Dickens, C. F.; Chorkendorff, I.; Nørskov, J. K.; Jaramillo, T. F. Combining Theory and Experiment in Electrocatalysis: Insights into Materials Design. *Science (80-.).* **2017**, *355* (6321), 1–12. https://doi.org/10.1126/science.aad4998.

(11) Kumar, B.; Llorente, M.; Froehlich, J.; Dang, T.; Sathrum, A.; Kubiak, C. P. Photochemical and Photoelectrochemical Reduction of CO2. *Annu. Rev. Phys. Chem.* **2012**, *63*, 541–569. https://doi.org/10.1146/annurev-physchem-032511-143759.

(12) Trasatti, S. Work Function, Electronegativity, and Electrochemical Behaviour of Metals. III. Electrolytic Hydrogen Evolution in Acid Solutions. *J. Electroanal. Chem.* **1972**, *39* (1), 163–184. https://doi.org/10.1016/S0022-0728(72)80485-6.

(13) Bard, A. J.; Faulkner, L. R. *Electrochemical Methods: Fundamentals and Applications*, 2nd ed.; Harris, D., Swain, E., Eds.; John Wiley & Sons, Ltd, 2001; Vol. 677.

(14) Kibsgaard, J.; Chorkendorff, I. Considerations for the Scaling-up of Water Splitting Catalysts. *Nat. Energy* **2019**, *4* (6), 430–433. https://doi.org/10.1038/s41560-019-0407-1.

(15) Kibsgaard, J.; Tsai, C.; Chan, K.; Benck, J. D.; Nørskov, J. K.; Jaramillo, T. F.; Abild-Pedersen, F.; Jaramillo, T. F. Designing an Improved Transition Metal Phosphide Catalyst

for Hydrogen Evolution Using Experimental and Theoretical Trends. *Energy Environ. Sci.* **2015**, *8* (10), 3022–3029. https://doi.org/10.1039/c5ee02179k.
(16) Ledendecker, MarcKasian, O.; Schaak, R. E.; Schalenbach, M.; Zeradjanin, A.; Geiger, S.; Cherevko, S.; Göhl, D.; Mondschein, J. S.; Mayrhofer, K. Stability and Activity of Non-Noble-Metal-Based Catalysts Toward the Hydrogen Evolution Reaction. *Angew. Chemie Int. Ed.* **2017**, *56* (33), 9767–9771. https://doi.org/10.1002/anie.201704021.
(17) Hansen, J. N.; Prats, H.; Toudahl, K. K.; Mørch Secher, N.; Chan, K.; Kibsgaard, J.; Chorkendorff, I. Is There Anything Better than Pt for HER? *ACS Energy Lett.* **2021**, *6* (4), 1175–1180. https://doi.org/10.1021/acsenergylett.1c00246.
(18) Quaino, P.; Juarez, F.; Santos, E.; Schmickler, W. Volcano Plots in Hydrogen Electrocatalysis-Uses and Abuses. *Beilstein J. Nanotechnol.* **2014**, *5* (1), 846–854. https://doi.org/10.3762/bjnano.5.96.
(19) Robinson, P. J.; Holbrook, K. A. Why Gold Is the Noblest of All the Metals. *Nature* **1995**, *376* (July), 238–240.
(20) Dubois, D. L. Development of Molecular Electrocatalysts for Energy Storage. *Inorg. Chem.* **2014**, *53* (8), 3935–3960. https://doi.org/10.1021/ic4026969.
(21) Helm, M. L.; Stewart, M. P.; Bullock, R. M.; DuBois, M. R.; DuBois, D. L. A Synthetic Nickel Electrocatalyst with a Turnover Frequency Above 100,000s-1 for H2 Production. *Science (80-.).* **2007**, *317* (August), 490–494. https://doi.org/10.5061/dryad.5t110.Supplementary.
(22) Chen, S.; DuBois, D. L.; O'Hagan, M.; Yang, J. Y.; Shaw, W. J.; Kilgore, U. J.; Bullock, R. M.; Raugei, S. Moving Protons with Pendant Amines: Proton Mobility in a Nickel Catalyst for Oxidation of Hydrogen. *J. Am. Chem. Soc.* **2011**, *133* (36), 14301–14312. https://doi.org/10.1021/ja201838x.
(23) Wiedner, E. S.; Chambers, M. B.; Pitman, C. L.; Bullock, R. M.; Miller, A. J. M.; Appel, A. M. Thermodynamic Hydricity of Transition Metal Hydrides. *Chem. Rev.* **2016**, *116* (15), 8655–8692. https://doi.org/10.1021/acs.chemrev.6b00168.
(24) Marchetti, L.; Levine, M. Biomimetic Catalysis. *ACS Catalysis*. 2011. https://doi.org/10.1021/cs200171u.
(25) Yuhas, B. D.; Smeigh, A. L.; Douvalis, A. P.; Wasielewski, M. R.; Kanatzidis, M. G. Photocatalytic Hydrogen Evolution from FeMoS-Based Biomimetic Chalcogels. *J. Am. Chem. Soc.* **2012**, *134* (25). https://doi.org/10.1021/ja303640s.
(26) Larsen, R. W.; Wojtas, L.; Perman, J.; Musselman, R. L.; Zaworotko, M. J.; Vetromile, C. M. Mimicking Heme Enzymes in the Solid State: Metal-Organic Materials with Selectively Encapsulated Heme. *J. Am. Chem. Soc.* **2011**, *133* (27). https://doi.org/10.1021/ja203068u.
(27) Nagel, Z. D.; Klinman, J. P. Tunneling and Dynamics in Enzymatic Hydride Transfer. *Chemical Reviews*. 2006. https://doi.org/10.1021/cr050301x.
(28) Bruice, T. C. Computational Approaches: Reaction Trajectories, Structures, and Atomic Motions. Enzyme Reactions and Proficiency. *Chemical Reviews*. 2006. https://doi.org/10.1021/cr050283j.
(29) Cano, Z. P.; Banham, D.; Ye, S.; Hintennach, A.; Lu, J.; Fowler, M.; Chen, Z. Batteries and Fuel Cells for Emerging Electric Vehicle Markets. *Nature Energy*. 2018, pp 279–289. https://doi.org/10.1038/s41560-018-0108-1.
(30) Davies, D. M.; Meng, Y. S.; Rajeev, R.; Verde, M. G.; Elliott, G.; Mnyshenko, O.; Chen, Y. R. Combined Economic and Technological Evaluation of Battery Energy Storage for

Grid Applications. *Nat. Energy* **2018**, *4* (1), 42–50. https://doi.org/10.1038/s41560-018-0290-1.
(31) Kwade, A.; Haselrieder, W.; Leithoff, R.; Modlinger, A.; Dietrich, F.; Droeder, K. Current Status and Challenges for Automotive Battery Production Technologies. *Nat. Energy* **2018**, *3* (April). https://doi.org/10.1038/s41560-018-0130-3.
(32) Schmuch, R.; Wagner, R.; Hörpel, G.; Placke, T.; Winter, M. Materials for Automotive Batteries : Perspective on Performance and Cost of Lithium-Based Rechargeable Batteries. *Nat. Energy* **2017**, *3* (April). https://doi.org/10.1038/s41560-018-0107-2.
(33) Chan, C. K.; Peng, H.; Liu, G.; McIlwrath, K.; Zhang, X. F.; Huggins, R. A.; Cui, Y. High-Performance Lithium Battery Anodes Using Silicon Nanowires. *Nat. Nanotechnol.* **2008**, *3* (1), 31–35. https://doi.org/10.1038/nnano.2007.411.
(34) Lin, D.; Liu, Y.; Cui, Y. Reviving the Lithium Metal Anode for High-Energy Batteries. *Nature Nanotechnology*. 2017. https://doi.org/10.1038/nnano.2017.16.
(35) Turcheniuk, K.; Bondarev, D.; Singhal, V.; Yushin, G. Ten Years Left to Redesign Lithium-Ion Batteries. *Nature* **2018**, *559* (7715), 467–470. https://doi.org/10.1038/d41586-018-05752-3.
(36) Goodenough, J. B.; Kim, Y. Challenges for Rechargeable Li Batteries. *Chem. Mater.* **2010**, *22* (3), 587–603. https://doi.org/10.1021/cm901452z.
(37) Choi, N. S.; Chen, Z.; Freunberger, S. A.; Ji, X.; Sun, Y. K.; Amine, K.; Yushin, G.; Nazar, L. F.; Cho, J.; Bruce, P. G. Challenges Facing Lithium Batteries and Electrical Double-Layer Capacitors. *Angewandte Chemie - International Edition*. 2012, pp 9994–10024. https://doi.org/10.1002/anie.201201429.
(38) Manthiram, A. A Reflection on Lithium-Ion Battery Cathode Chemistry. *Nat. Commun.* **2020**, *11* (1), 1–9. https://doi.org/10.1038/s41467-020-15355-0.
(39) Whittingham, M. S. *Chemistry of Intercalation Compounds: Metal Guests in Chalcogenide Hosts*; 1978; Vol. 12. https://doi.org/10.1016/0079-6786(78)90003-1.
(40) April, R.; Goodenough, C. J. B. A New Cathode Material for Batteries of High Energy Density. **1980**, *15* (c), 783–789.
(41) Lithium-ion batteries - statistics & facts https://www.statista.com/topics/2049/lithium-ion-battery-industry/.
(42) Wu, F.; Yushin, G. Conversion Cathodes for Rechargeable Lithium and Lithium-Ion Batteries. *Energy Environ. Sci.* **2017**, *10* (2), 435–459. https://doi.org/10.1039/c6ee02326f.
(43) Yu, S. H.; Feng, X.; Zhang, N.; Seok, J.; Abruña, H. D. Understanding Conversion-Type Electrodes for Lithium Rechargeable Batteries. *Acc. Chem. Res.* **2018**, *51* (2), 273–281. https://doi.org/10.1021/acs.accounts.7b00487.
(44) Francfort, J.; Walkowicz, K. Electrochemical Energy Storage Technical Team Roadmap. *U.S. Drive* **2017**, No. June, 1–17.
(45) Manthiram, A.; Fu, Y.; Chung, S.-H.; Zu, C.; Su, Y.-S. Rechargeable Lithium–Sulfur Batteries. *Chem. Rev.* **2014**, *114* (23), 11751–11787. https://doi.org/10.1021/cr500062v.
(46) Seh, Z. W.; Sun, Y.; Zhang, Q.; Cui, Y. Designing High-Energy Lithium-Sulfur Batteries. *Chemical Society Reviews*. Royal Society of Chemistry October 2016, pp 5605–5634. https://doi.org/10.1039/c5cs00410a.
(47) Hagen, M.; Hanselmann, D.; Ahlbrecht, K.; Maça, R.; Gerber, D.; Tübke, J. Lithium-Sulfur Cells: The Gap between the State-of-the-Art and the Requirements for High Energy Battery Cells. *Adv. Energy Mater.* **2015**, *5* (16). https://doi.org/10.1002/aenm.201401986.

(48) Bruce, P. G.; Freunberger, S. A.; Hardwick, L. J.; Tarascon, J.-M. Li–O2 and Li–S Batteries with High Energy Storage. *Nat. Mater.* **2011**, *11* (02), 172–172. https://doi.org/10.1038/nmat3237.
(49) Ji, X.; Lee, K. T.; Nazar, L. F. A Highly Ordered Nanostructured Carbon–Sulphur Cathode for Lithium–Sulphur Batteries. *Nat. Mater.* **2009**, *8* (6), 500–506. https://doi.org/10.1038/nmat2460.
(50) Qin, J.; Lin, F.; Hubble, D.; Wang, Y.; Li, Y.; Murphy, I. A.; Jang, S.-H.; Yang, J.; Jen, A. K.-Y. Tuning Self-Healing Properties of Stiff, Ion-Conductive Polymers. *J. Mater. Chem. A* **2019**, *7* (12). https://doi.org/10.1039/c8ta11353j.
(51) Li, L.; Pascal, T. A.; Connell, J. G.; Fan, F. Y.; Meckler, S. M.; Ma, L.; Chiang, Y. M.; Prendergast, D.; Helms, B. A. Molecular Understanding of Polyelectrolyte Binders That Actively Regulate Ion Transport in Sulfur Cathodes. *Nat. Commun.* **2017**, *8* (1). https://doi.org/10.1038/s41467-017-02410-6.
(52) Safari, M.; Kwok, C. Y.; Nazar, L. F. Transport Properties of Polysulfide Species in Lithium-Sulfur Battery Electrolytes: Coupling of Experiment and Theory. *ACS Cent. Sci.* **2016**, *2* (8), 560–568. https://doi.org/10.1021/acscentsci.6b00169.
(53) Zhang, S. S. A New Finding on the Role of LiNO3 in Lithium-Sulfur Battery. *J. Power Sources* **2016**, *322*, 99–105. https://doi.org/10.1016/j.jpowsour.2016.05.009.
(54) Zhang, S.; Ikoma, A.; Li, Z.; Ueno, K.; Ma, X.; Dokko, K.; Watanabe, M. Optimization of Pore Structure of Cathodic Carbon Supports for Solvate Ionic Liquid Electrolytes Based Lithium-Sulfur Batteries. *ACS Appl. Mater. Interfaces* **2016**, *8* (41), 27803–27813. https://doi.org/10.1021/acsami.6b09989.
(55) Choi, J. W.; Cheruvally, G.; Kim, D. S.; Ahn, J. H.; Kim, K. W.; Ahn, H. J. Rechargeable Lithium/Sulfur Battery with Liquid Electrolytes Containing Toluene as Additive. *J. Power Sources* **2008**, *183* (1), 441–445. https://doi.org/10.1016/j.jpowsour.2008.05.038.
(56) Fan, F. Y.; Pan, M. S.; Lau, K. C.; Assary, R. S.; Woodford, W. H.; Curtiss, L. A.; Carter, W. C.; Chiang, Y.-M. Solvent Effects on Polysulfide Redox Kinetics and Ionic Conductivity in Lithium-Sulfur Batteries. *J. Electrochem. Soc.* **2016**, *163* (14), A3111–A3116. https://doi.org/10.1149/2.1181614jes.
(57) Pang, Q.; Liang, X.; Kwok, C. Y.; Nazar, L. F. Advances in Lithium-Sulfur Batteries Based on Multifunctional Cathodes and Electrolytes. *Nat. Energy* **2016**, *1* (9), 1–11. https://doi.org/10.1038/nenergy.2016.132.
(58) Yang, Y.; Zhong, Y.; Shi, Q.; Wang, Z.; Sun, K.; Wang, H. Electrocatalysis in Lithium Sulfur Batteries under Lean Electrolyte Conditions. *Angew. Chemie Int. Ed.* **2018**, *57* (47), 15549–15552. https://doi.org/10.1002/anie.201808311.
(59) Pang, Q.; Kwok, C. Y.; Kundu, D.; Liang, X.; Nazar, L. F. Lightweight Metallic MgB 2 Mediates Polysulfide Redox and Promises High-Energy-Density Lithium-Sulfur Batteries. *Joule* **2019**, *3* (1), 136–148. https://doi.org/10.1016/j.joule.2018.09.024.
(60) Liang, X.; Kwok, C. Y.; Lodi-Marzano, F.; Pang, Q.; Cuisinier, M.; Huang, H.; Hart, C. J.; Houtarde, D.; Kaup, K.; Sommer, H.; Brezesinski, T.; Janek, J.; Nazar, L. F. Tuning Transition Metal Oxide-Sulfur Interactions for Long Life Lithium Sulfur Batteries: The "Goldilocks" Principle. *Adv. Energy Mater.* **2016**, *6* (6), 1–9. https://doi.org/10.1002/aenm.201501636.
(61) Mohamed, A. A.; Salmi, Z.; Dahoumane, S. A.; Mekki, A.; Carbonnier, B.; Chehimi, M. M. Functionalization of Nanomaterials with Aryldiazonium Salts. *Adv. Colloid Interface Sci.* **2015**, *225*, 16–36. https://doi.org/10.1016/j.cis.2015.07.011.

(62) Kroupa, D. M.; Vörös, M.; Brawand, N. P.; McNichols, B. W.; Miller, E. M.; Gu, J.; Nozik, A. J.; Sellinger, A.; Galli, G.; Beard, M. C. Tuning Colloidal Quantum Dot Band Edge Positions through Solution-Phase Surface Chemistry Modification. *Nat. Commun.* **2017**, *8* (May), 2–9. https://doi.org/10.1038/ncomms15257.

(63) Brown, P. R.; Kim, D.; Lunt, R. R.; Zhao, N.; Bawendi, M. G.; Grossman, J. C.; Bulović, V. Energy Level Modification in Lead Sulfide Quantum Dot Thin Films through Ligand Exchange. *ACS Nano* **2014**, *8* (6). https://doi.org/10.1021/nn500897c.

(64) Benson, E. E.; Zhang, H.; Schuman, S. A.; Nanayakkara, S. U.; Bronstein, N. D.; Ferrere, S.; Blackburn, J. L.; Miller, E. M. Balancing the Hydrogen Evolution Reaction, Surface Energetics, and Stability of Metallic MoS 2 Nanosheets via Covalent Functionalization. *J. Am. Chem. Soc.* **2018**, *140* (1), 441–450. https://doi.org/10.1021/jacs.7b11242.

(65) Zobel, M.; Neder, R. B.; Kimber, S. A. J. Universal Solvent Restructuring Induced by Colloidal Nanoparticles. *Science (80-.).* **2015**, *347* (6219), 292–294. https://doi.org/10.1126/science.1261412.

(66) Strano, M. S.; Dyke, C. A.; Usrey, M. L.; Barone, P. W.; Allen, M. J.; Shan, H.; Kittrell, C.; Hauge, R. H.; Tour, J. M.; Smalley. Electronic Structure Control of Single-Walled Carbon Nanotube Functionalization. *Science (80-.).* **2003**, *301* (5639), 1519–1522. https://doi.org/10.1126/science.1087691.

(67) Liu, Y.; Gao, P.; Zhang, T.; Zhu, X.; Zhang, M.; Chen, M.; Du, P.; Wang, G. W.; Ji, H.; Yang, J.; Yang, S. Azide Passivation of Black Phosphorus Nanosheets: Covalent Functionalization Affords Ambient Stability Enhancement. *Angew. Chemie - Int. Ed.* **2019**, *58* (5), 1479–1483. https://doi.org/10.1002/anie.201813218.

(68) Sofer, Z.; Luxa, J.; Bouša, D.; Sedmidubský, D.; Lazar, P.; Hartman, T.; Hardtdegen, H.; Pumera, M. The Covalent Functionalization of Layered Black Phosphorus by Nucleophilic Reagents. *Angew. Chemie - Int. Ed.* **2017**, *56* (33), 9891–9896. https://doi.org/10.1002/anie.201705722.

(69) Ryder, C. R.; Wood, J. D.; Wells, S. A.; Yang, Y.; Jariwala, D.; Marks, T. J.; Schatz, G. C.; Hersam, M. C. Covalent Functionalization and Passivation of Exfoliated Black Phosphorus via Aryl Diazonium Chemistry. *Nat. Chem.* **2016**, *8* (6), 597–602. https://doi.org/10.1038/nchem.2505.

(70) Hirsch, A.; Hauke, F. Post-Graphene 2D Chemistry: The Emerging Field of Molybdenum Disulfide and Black Phosphorus Functionalization. *Angew. Chemie - Int. Ed.* **2018**, *57* (16), 4338–4354. https://doi.org/10.1002/anie.201708211.

(71) Oliverio, M.; Perotto, S.; Messina, G. C.; Lovato, L.; De Angelis, F. Chemical Functionalization of Plasmonic Surface Biosensors: A Tutorial Review on Issues, Strategies, and Costs. *ACS Appl. Mater. Interfaces* **2017**, *9* (35). https://doi.org/10.1021/acsami.7b01583.

(72) Ban, I.; Stergar, J.; Maver, U. NiCu Magnetic Nanoparticles: Review of Synthesis Methods, Surface Functionalization Approaches, and Biomedical Applications. *Nanotechnol. Rev.* **2018**, *7* (2). https://doi.org/10.1515/ntrev-2017-0193.

(73) Yao, S. A.; Ruther, R. E.; Zhang, L.; Franking, R. A.; Hamers, R. J.; Berry, J. F. Covalent Attachment of Catalyst Molecules to Conductive Diamond: CO 2 Reduction Using "Smart" Electrodes. *J. Am. Chem. Soc.* **2012**, *134* (38), 15632–15635. https://doi.org/10.1021/ja304783j.

(74) Ruther, R. E.; Rigsby, M. L.; Gerken, J. B.; Hogendoorn, S. R.; Landis, E. C.; Stahl, S. S.; Hamers, R. J. Highly Stable Redox-Active Molecular Layers by Covalent Grafting to

Conductive Diamond. *J. Am. Chem. Soc.* **2011**, *133* (15). https://doi.org/10.1021/ja200210t.
(75) Jackson, M. N.; Oh, S.; Kaminsky, C. J.; Chu, S. B.; Zhang, G.; Miller, J. T.; Surendranath, Y. Strong Electronic Coupling of Molecular Sites to Graphitic Electrodes via Pyrazine Conjugation. *J. Am. Chem. Soc.* **2018**, *140* (3), 1004–1010. https://doi.org/10.1021/jacs.7b10723.
(76) Oh, S.; Gallagher, J. R.; Miller, J. T.; Surendranath, Y. Graphite-Conjugated Rhenium Catalysts for Carbon Dioxide Reduction. *J. Am. Chem. Soc.* **2016**, *138* (6), 1820–1823. https://doi.org/10.1021/jacs.5b13080.
(77) Pankhurst, J. R.; Guntern, Y. T.; Mensi, M.; Buonsanti, R. Molecular Tunability of Surface-Functionalized Metal Nanocrystals for Selective Electrochemical CO2 Reduction. *Chem. Sci.* **2019**, *10* (44), 10356–10365. https://doi.org/10.1039/c9sc04439f.
(78) Yuan, F. W.; Yang, H. J.; Tuan, H. Y. Alkanethiol-Passivated Ge Nanowires as High-Performance Anode Materials for Lithium-Ion Batteries: The Role of Chemical Surface Functionalization. *ACS Nano* **2012**, *6* (11). https://doi.org/10.1021/nn303519g.
(79) Pandres, E. P.; Olson, J. Z.; Schlenker, C. W.; Holmberg, V. C. Germanium Nanowire Battery Electrodes with Engineered Surface-Binder Interactions Exhibit Improved Cycle Life and High Energy Density without Fluorinated Additives. *ACS Appl. Energy Mater.* **2019**, *2* (9). https://doi.org/10.1021/acsaem.9b00667.
(80) Moock, D. S.; Steinmüller, S. O.; Wessely, I. D.; Llevot, A.; Bitterer, B.; Meier, M. A. R.; Bräse, S.; Ehrenberg, H.; Scheiba, F. Surface Functionalization of Silicon, HOPG, and Graphite Electrodes: Toward an Artificial Solid Electrolyte Interface. *ACS Appl. Mater. Interfaces* **2018**, *10* (28). https://doi.org/10.1021/acsami.8b04877.
(81) Kim, J. H.; Kim, T.; Jeong, Y. C.; Lee, K.; Park, K. T.; Yang, S. J.; Park, C. R. Stabilization of Insoluble Discharge Products by Facile Aniline Modification for High Performance Li-S Batteries. *Adv. Energy Mater.* **2015**, *5* (14), 1–10. https://doi.org/10.1002/aenm.201500268.
(82) Wilson, A., Kleen, G. & Papageorgopoulos, D. *Fuel Cell System Cost – 2017* (US Department of Energy, 2017); www.hydrogen.energy.gov/pdfs/17007_fuel_cell_system_cost_2017.pdf

Chapter 2. DESIGNING NANOPARTICLE INTERFACES FOR INNER-SPHERE CATALYSIS

Significant portions of the following chapter have previously been published by:

David Ung‡, Ian A. Murphy‡, and Brandi M. Cossairt *Dalton Trans.,* 2020, **49**, 4995-5005.

2.1 ABSTRACT

Interfaces are an intrinsic component of nanoparticle catalysts and play a critical role in directing their function. Our understanding of the complexity of the nanoparticle interface and how to manipulate it at the molecular level has advanced significantly in recent years. Given this, attention is shifting towards the creation of designer nanoparticle interfaces that impact the activity and direct the mechanisms of inner-sphere catalytic reactions. In this perspective, we seek to highlight and contextualize these efforts. First, methods to alter nanoparticle surfaces are presented, including annealing and plasma treating, as well as more mild chemical treatments, including ligand exchange, etching, and addition (via covalent functionalization). Then interfacial chemistry developed to alter catalytic activity, selectivity, and reaction environment will be highlighted. Finally, we look forward to the challenges that remain to be overcome for realizing the true potential of colloidal nanoparticle catalysis.

2.2 INTRODUCTION

In the field of molecular catalysis, tuning chemical reactivity is not simply a matter of altering the concentration or availability of catalytic active sites. Careful design of the coordination environment surrounding the active site allows for tuning both the kinetics and mechanism of inner-sphere reactions (defined here as bond making and breaking chemistry at the active site).

This is achieved through steric and electronic control of the catalytic active site as well as by introducing new reaction pathways that rely on metal-ligand cooperativity.[1] In the field of heterogeneous catalysis, on the other hand, tuning chemical reactivity and selectivity is typically achieved by altering the active sites of a pristine surface (composition control) or increasing their relative number through nanostructuring.[2] Most heterogeneous reactions of commercial relevance, however, are not carried out on pristine surfaces, but rather on small nanoparticles of a catalytic material.[2] In such cases the role of interfacial chemistry cannot be ignored given the surface area to volume scaling as these materials approach the small size limit. With the expansion of the field of colloidal nanoscience, researchers have realized the enormous potential of bottom-up colloidal synthesis of catalytically active nanomaterials. On a fundamental level, these materials can be viewed as a bridge between conventional molecular catalysts and heterogeneous surfaces (Figure 1). Because colloidal nanoparticles can be manipulated in solution like small molecules, and because their surfaces are necessarily passivated by organic or inorganic ligands that render them kinetically and colloidally stable,[3] it is clear that interfacial chemistry has a strong role to play in tuning material properties. The field of colloidal nanoparticle catalysis can take inspiration from the growing literature on the surface chemistry of colloidal quantum dots and plasmonic metal nanoparticles.[3,4] For these nanoscale materials, ligands have a direct and significant impact on their function by altering their electronic structure.[5,6] As an illustrative example, and in analogy with the use of ligands to tune metal redox potentials in molecular catalysis, ligands have been shown to dramatically alter the band edge positions of quantum dots by as much as 2 eV.[7–10] Intriguingly, and of great relevance to the topic of catalysis, colloidal quantum dots and plasmonic nanoparticles are widely studied for application in photocatalytic processes that rely on energy or charge transfer mechanisms.[11] Here, ligand permeability, hydrophobicity, and charge density impact the ability

for donor and acceptor species to interact through outer-sphere energy or charge transfer mechanisms. As we make the transition to the realm of colloidal nanoparticles for *inner-sphere* catalysis, the motivation for ligand-based activity control becomes even more apparent. Ligands can be used to directly tune active site availability and the inherent activity and selectivity of a given catalytic transformation. Ligands therefore offer a new dimension of parameter space with which to design catalytic interfaces. Despite this, the most frequent scheme for nanoparticle catalysis is for the nanoparticles to first be supported (or used as a powder) with ligands removed by thermal annealing or a related process.[12]

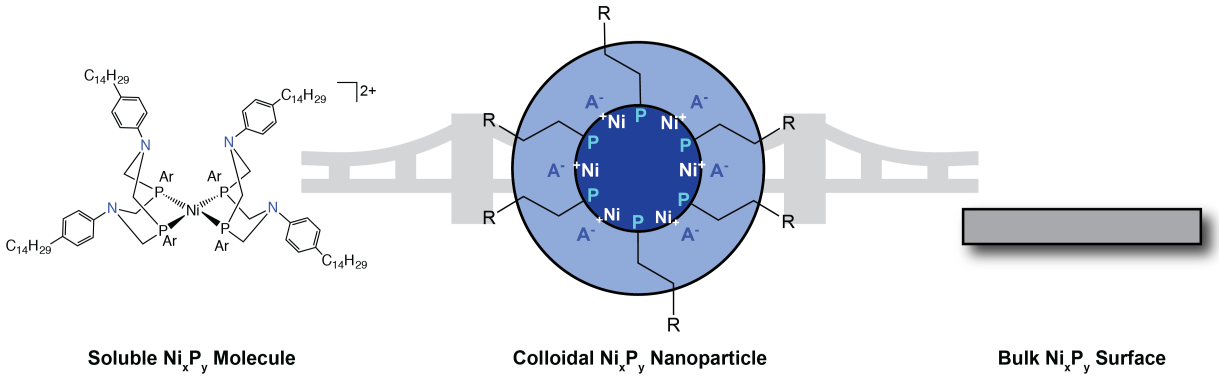

Figure 2.1. Colloidal nanoparticles as a bridge between soluble catalytic molecules and bulk heterogeneous surfaces.

In this perspective, we will first review methods to alter nanoparticle surfaces, including annealing and plasma treating, as well as more mild chemical treatments with a focus on materials with complex, alloyed or multicomponent lattices. We will then focus specifically on interfacial chemistry that has been developed to alter catalytic (i) activity, (ii) selectivity, and (iii) reaction environment through bulk-like interfacial effects such as surface hydrophobicity. Finally, we look forward to the challenges that remain to be overcome for realizing the true potential of colloidal nanoparticle catalysis.

2.3 Primer on Methods to Alter Nanoparticle Surfaces

Traditional schemes for altering the surface chemistry of heterogeneous catalysts are comprised almost entirely of ligand/surfactant removal. These methods are well known throughout the inorganic nanoscience community and can be loosely grouped into two classes: high-energy treatments and chemical treatments. These two approaches have drastically different influence on the chemistry of the underlying nanomaterial, which is manifested in their catalytic and/or optoelectronic applications. In this section, we will not just describe general methodology, but try to put into perspective the chemical transformations occurring at the nanocrystalline surface.

2.3.1 *High Energy Cleaning Methods*

Our description of thermal annealing and plasma treatments will be brief as there are already exhaustive reviews of their impact.[12–15] The fundamental concept for both approaches is to introduce sufficient energy for the cleavage of the surface-surfactant bonds and subsequent vaporization of the liberated molecular species. In the case of thermal annealing, this is accomplished by applying heat. The simplicity of this approach has made it the standard for preparing "clean" crystalline surfaces. However, the mixture of elevated temperatures and unpassivated surfaces provides the driving force for aggregation of neighboring nanocrystals, leading to the growth of larger polydisperse species.[16,17] There has been recent progress on addressing this issue by the use of low-temperature or flash annealing strategies, which can avoid the problem of agglomeration for oxidatively resistant materials.[18,19] While thermal treatments are known to be effective in removing surface ligands and are often associated with improvements in catalytic activity of nanomaterials, it has been shown that calcination does not remove all of the carbon from colloidal nanocrystal assemblies.[20] Further, the choice of annealing atmosphere

(reducing or oxidizing) plays an important role in both the removal of surfactants and the alteration/passivation of the bare nanoparticle's surface.[12,21,22]

The concept of atmospheric non-innocence towards the pristine surface becomes very important when cleaning particles via plasma exposure. For this approach, the energy to liberate surfactants is supplied by high energy ions, radicals, and photon emission which decompose the ligands into smaller molecular fragments. The majority of these fragments can be liberated, but it has been shown that decomposition products can remain strongly bound to the particle surface.[23] Further, the most common and economical plasma source is oxygen, thus requiring the underlying particle to be resistant to oxidation. Recent studies have shown that plasma treatments utilizing "inert" gases like He or Ar can remove a majority of surface ligands while avoiding oxidation of the underlying particle.[24] However, bombardment by high energy ions of any species can induce random defects to form on the exposed surface facets.[25]

Although thermal and plasma annealing strategies have undoubtedly been shown to be effective in removing surface ligands, their influence on surface chemistry is known to vary largely between samples and treatment protocols. Thus, the lack of systematic understanding of the impact that these treatments have on the surface chemistry of nanoparticles should be heavily considered during experimental design and data analysis.

2.3.2 *Chemical Ligand Exchange, Stripping, and Addition*

The unique space that nanoparticles occupy between bulk solids and discrete molecules has spurred decades of research focused on deconvoluting the complex interplay between their stable inorganic cores and dynamic organic/inorganic surfaces. In the colloidal quantum dot community specifically, these efforts have culminated in a surface ligand classification system adapted from

organometallic bonding concepts. These classifications, summarized in Figure 2, were popularized by Owen and co-workers and will serve as the basis for our discussion on post-synthetic ligand exchange methods.[3]

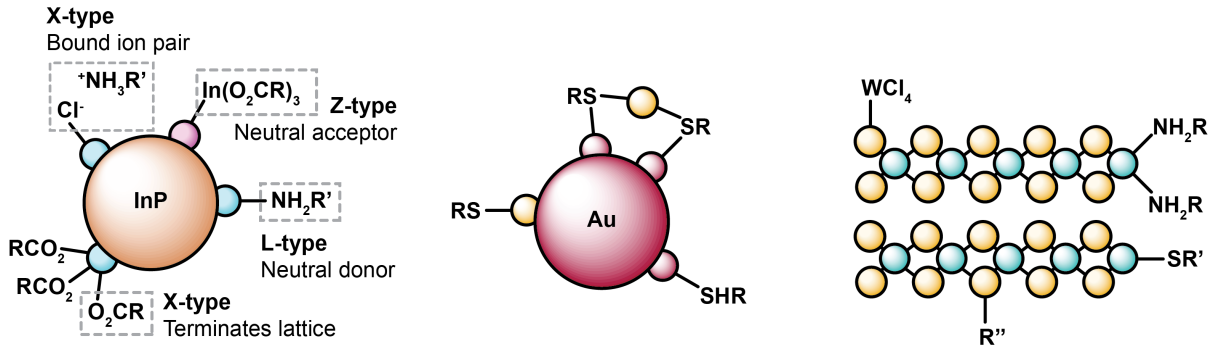

Figure 2.2. The coordination of different types of ligands (L-, X-, and Z-type) to a variety of inorganic nanostructures.

Just like their molecular analogues, charges must be conserved and balanced in nanocrystalline systems. Thus, the reaction mechanism for removing or altering a ligand will depend on their molecular reactivity and relationship to the surface of the particle. These initial ligand environments and the underlying particle's surface chemistry is determined by the synthetic method used to derive the particles. In a conceptual sense, the particles have a "memory" of the way in which they are formed that in-turn influences their morphology, stoichiometry, surface chemistry, and ultimately functionality. For example, most colloidally synthesized nanoparticles are capped with an X-type ligand, typically oleate or other long-chain fatty acid anion, though the specific speciation will vary by synthetic procedure. These X-type ligands are typically coordinated to excess metal cation on the surface of the particle, which is an artifact of the halted growth of nanoparticles that prevents agglomeration into larger crystals. Thus, in order to alter the native ligand environment of such a nanoparticle, one would need to employ strategies to exchange X- or Z-type ligands.

Hens and co-workers have shown that such native oleate ligands could be exchanged for protic alcohols when present in large excess.[26] The authors noted that the protic nature of the reagent was a crucial component of the exchange reaction, as protonation of the formally negative carboxylate species was required to preserve charge balance. This X-type ligand exchange has since been generalized as:

$$[\mathrm{NP}]\text{—}\mathrm{X} + \mathrm{HY} \rightleftarrows [\mathrm{NP}]\text{—}\mathrm{Y} + \mathrm{HX} \tag{2.5}$$

However, it is important to note that ligand exchange is actually an equilibrium process. The same study found that over time the desorbed oleate ligands would rebind. This equilibrium can be shifted by factors like concentration, denticity, and pKa. This concept has been shown by our group and others through monitoring the exchange of native oleate ligands for other organic acids.[27–30] Through these studies it was found that phosphonic acids readily displace carboxylic acids and effectively bind irreversibly due to both their low pKa and multidentate binding modes. This straightforward method to replace native X-type ligands is not limited to acids, but also applies to halides, pseuodhalides, and strong bases.[31–34] Though, when planning ligand exchange reaction conditions, be mindful that some colloidal nanocrystals are not stable in strongly acidic or basic conditions and will either etch or completely dissolve.

As mentioned above, X-type ligands with a formal negative charge neutralize the formally positive charge of excess cations that passivate the particle surface. In fact, it is generally understood that, especially for smaller particles, the surface is often terminated by a layer of excess metal cation coordinated by anionic ligand.[35,36] This is commonly studied by inductively coupled plasma mass spectroscopy (ICP-MS) that show a super-stoichiometric concentration of metal species in as-synthesized materials. These effectively neutral Lewis-acidic ligand complexes are referred to as Z-type ligand. Because these complexes are effectively neutral, ligand exchange

reactions must employ other Z-type complexes or formally neutral Lewis-basic species known as L-type ligands (Figure 3).[36,37] These ligand exchange reactions can also be generalized according the following equations:

$$[\mathrm{NP}]\text{—}\,\mathrm{M_1X} + \mathrm{M_2Y} \rightleftarrows [\mathrm{NP}]\text{—}\,\mathrm{M_2Y} + \mathrm{M_1X} \tag{2.6}$$

$$[\mathrm{NP}]\text{—}\,\mathrm{MX} + 2\mathrm{L} \rightleftarrows [\mathrm{NP}]\text{—}\,\mathrm{L} + \mathrm{LMX} \tag{2.7}$$

In their study, Owen and co-workers thoroughly investigated the complex equilibrium of these exchange reactions and found that the efficacy of ligand exchange was roughly a function of the relative Lewis-basicity of L.[36] They showed that although alcohols, phosphines, and amines were all able to displace some amount of MX_n, short-chain primary amines were the most effective. Further, the efficacy of primary amines was improved by the simultaneous addition of a chelating diamine species. They propose this is due to an increased stabilization of the desorbed L_yMX_n species, coupled with stabilization of the particle surface. Though amines are generally effective species for surface passivation, the real affinity for ligand binding is dictated by individual atomic preferences that can be described by hard soft acid base theory. As such, binding strength will vary with the specific speciation of a system. Because of this, exchange between L-type ligands can also be driven by this difference in intrinsic binding affinity, according the general equation:

$$[\mathrm{NP}]\text{—}\,\mathrm{L_1} + \mathrm{L_2} \rightleftarrows [\mathrm{NP}]\text{—}\,\mathrm{L_2} + \mathrm{L_1} \tag{2.8}$$

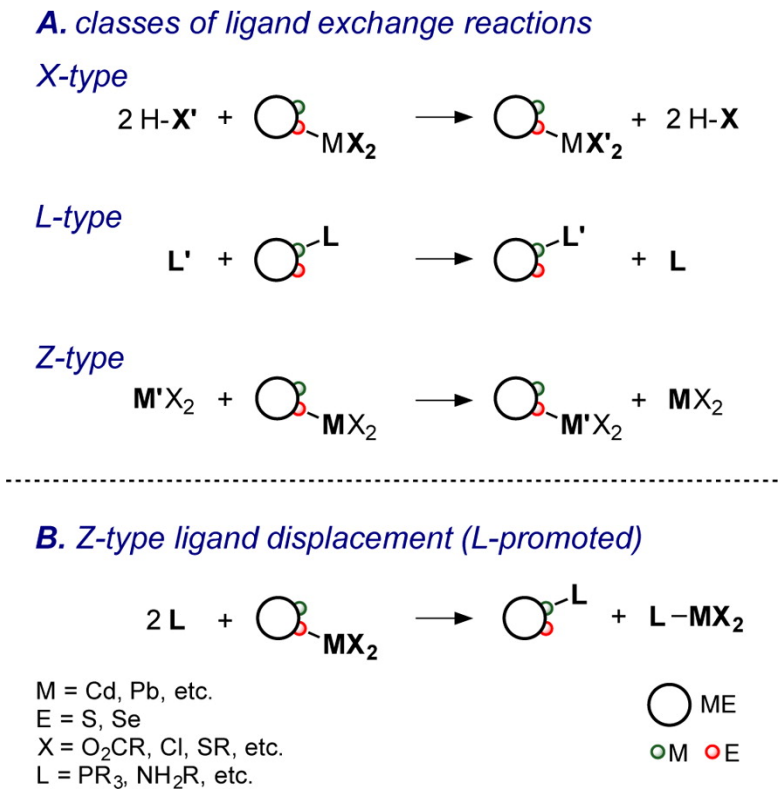

Figure 2.3. Schematic depiction of X-, L-, and Z-type ligand exchange reactions for Cd and Pb chalcogenide model systems. Reprinted with permission from N. C. Anderson, M. P. Hendricks, J. J. Choi, J. S. Owen. *Journal of the American Chemical Society*, 2013, 135, 18536 – 18548. Copyright 2013 American Chemical Society.

In addition to the conventional ligand exchange methods presented above, chemical ligand stripping to terminate the lattice with weakly or non-coordinating anions is being increasingly pursued. Alkylating agents (i.e., $R_3O^+X^-$, Eq. 4) and nitrosonium salts ($NO^+BF_4^-$) can displace the native ligand while reacting to form a neutral species with little binding affinity for the particle surface. The positive charge remaining on the surface of the particle is then neutralized by the counter anion, such as BF_4^-.[38–40] The resulting particles can be soluble in polar solvents, remain monodisperse, retain crystallographic integrity, and can act as blank templates to be re-ligated by other species.[39–41]

$$[\mathrm{NP}]\text{—}\mathrm{X} + \mathrm{R_3O^+Y^-} \rightleftarrows [\mathrm{NP}]^+\mathrm{Y^-} + \mathrm{R\text{—}X} + \mathrm{R_2O} \qquad (2.9)$$

Irreversible ligand stripping by the methods mentioned above can also cause some confusion without a rational understanding of the system. For example, if both ligands and excess cations are desorbed from the surface, the particles become more stoichiometric and develop a balanced charge, thus losing colloidal stability. This can generally be avoided by carrying out reactions in polar, coordinating solvents like DMF that can act as L-type ligands that colloidally stabilize the neutral particles.[42] Still, the complex nature of ligand environment and colloidal stability have pushed researchers to develop other, softer and more reversible, ligand stripping procedures. To this end, Helms and co-workers explored the viability of Lewis-acid-base adducts for X-type ligand removal, but not deactivation.[43] In this study, they showed that oleate ligands could be displaced by BF_3:DMF, according to the following general equation:

$$[\mathrm{NP}]\text{—}\,\mathrm{X} + \mathrm{LA{:}\,LB} \rightleftarrows [\mathrm{NP}]^{+}[\mathrm{LA{:}\,X}]^{-} + \mathrm{LB} \qquad (2.10)$$

This weak electrostatic attraction between the $[\mathrm{LA{:}X}]^{-}$ adduct and the charged particle surface allowed the particles to retain colloidal stability while still providing a malleable template to further alter surface functionality (Figure 2.4).

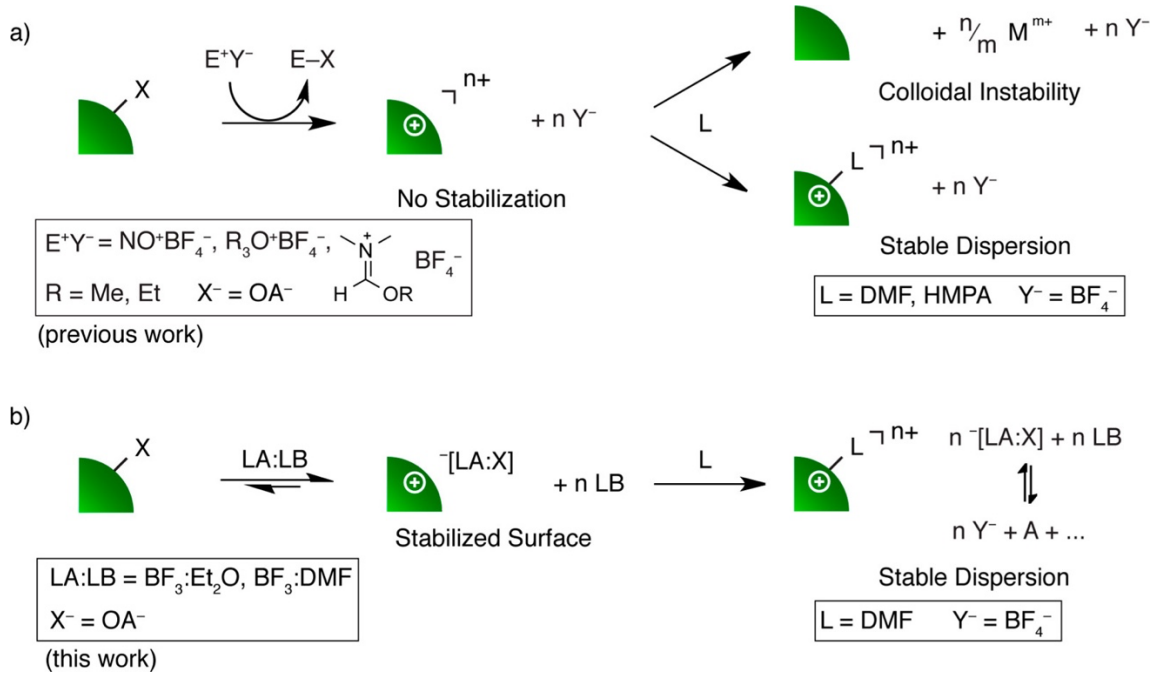

Figure 2.4. Schematic depiction of a) irreversible ligand stripping with strong electrophiles and b) reversible ligand stripping with Lewis acid-base adducts. Abbreviations: X^- = anionic ligand, E^+ = electrophile, Y^- = non-coordinating anion, M^{n+} = metal ion, LA:LB = Lewis acid–base adduct, L = charge-neutral coordinating solvent (e.g., DMF). For sensitive NC compositions, loss of M^{n+} from the surface leads to colloidal instability, particularly when repassivation of surface M^{n+} by L is not competitive with M^{n+} desorption. The dynamic exchange of $[LA:X]^-$ on and off the NC differentiates stripping under equilibrium control from earlier approaches. In the approach described herein, Y^- is generated through disproportionation of $[LA:X]^-$ as described in the main text. Reprinted with permission from S. E. Doris, J. J. Lynch, C. Li, J. J. Urban, B. A. Helms. *Journal of the American Chemical Society*, 2014, 136, 15702 – 15710. Copyright 2014 American Chemical Society.

Depending on the nanomaterials' desired application, full ligand removal for a bare surface may not be necessary. For example, native long chain surface ligands are often a detriment to nanomaterials in electronic applications because of the highly insulating aliphatic tails. Completely removing these surfactants through chemical or thermal treatments may improve electronic communication but can also lead to aggregation of the particles. Rather than full ligand removal,

these insulating ligands can be exchanged with compact halide (Eq. 2.7),[41,44,45] psuedohalide (N_3^-, CN^-, SCN^-, etc.),[33,46] or molecular metal chalcogenides.[32,34,46,47] These compact surfactants behave as X or Z-type surface ligands, but can greatly increase the electronic communication between nanoparticles and with the local environment when compared to the native aliphatic ligands. Below, TMS abbreviates trimethylsilane.

$$[\mathrm{NP}]\text{—}\mathrm{X} + \mathrm{TMS}\text{—}\mathrm{Y} \rightleftarrows [\mathrm{NP}]\text{—}\mathrm{Y} + \mathrm{TMS}\text{—}\mathrm{X} \qquad (2.11)$$

Depending on the type of nanomaterial employed for catalysis, sites for modifying ligand chemistry using coordinate-covalent bonding may not be readily accessible. In these cases, covalent surface modification by forging new main group-main group bonds is a desirable approach. Here we can take the transition metal dichalcogenide MoS_2 as an illustrative example. There are many methods to functionalization this layered material depending on the starting crystal phase.[48] When in the semiconducting 2H phase, the basal planes are considered chemically inert, meaning reactions can only occur at edge and defect sites. When defects are the only accessible reactive site, functionalization is limited to an approach known as "ligand conjugation".[49,50] Ligand conjugation requires a terminal thiol moiety on the functional ligand to react at S-vacant defect sites. It is proposed that the S from the thiol group bonds with the under coordinated Mo atoms, thus embedding the ligand into the edges of the 2D sheet - however the exact mechanism of S-R integration is still under investigation. Although the basal planes are inert in the semiconducting 2H phase, once converted to the metallic 1T phase by exfoliation with alkali metals (usually n-butyllithium) they become quite reactive. It has been shown that in this more reactive polymorph the basal plane S atoms are susceptible to electrophilic addition by diazonium salts[51,52] and organoiodine precursors (Figure 5a).[53,54] This concept of having reactive electrons with a suitably reducing potential accessible to the reaction site is becoming known as a critical factor in driving

covalent functionalization. Recently, Lewis and co-workers explored this idea by adding extra metallocene reductants to a reaction mixture of iodoalkyl species and alkylated MoS_2-R sheets (Figure 5b).[55] They found that the extent of functionalization could be pushed past that accessible by exfoliation with n-butyllithium alone, validating previous studies which postulated that the covalent functionalization was self-limited by the negative charges localized on the sheets after exfoliation. Further, their study showed that the potential of the reductant also played a role in increasing functionalization, where a stronger reductant like cobaltocene induced more functionalization than a weaker reductant like ferrocene.

While we have highlighted the covalent functionalization of MoS_2 here, this type of surface modification can be applied to a wide variety of nanomaterials including carbons and black phosphorus,[56–58] as well as non-layered materials like transition metal phosphides and main-group metal sulfides to alter their physical and electronic structure, and in turn their catalytic activity. It is notable, however, that there is a significant difference in total content and the level of detail found in the literature on the topic of covalent functionalization in comparison to dative ligand interactions. Covalent surface modification is an emerging and rapidly developing field, requiring further exploration into both synthetic methods and the effects that covalent functionalization has on the electronic/structural properties of the underlying material.

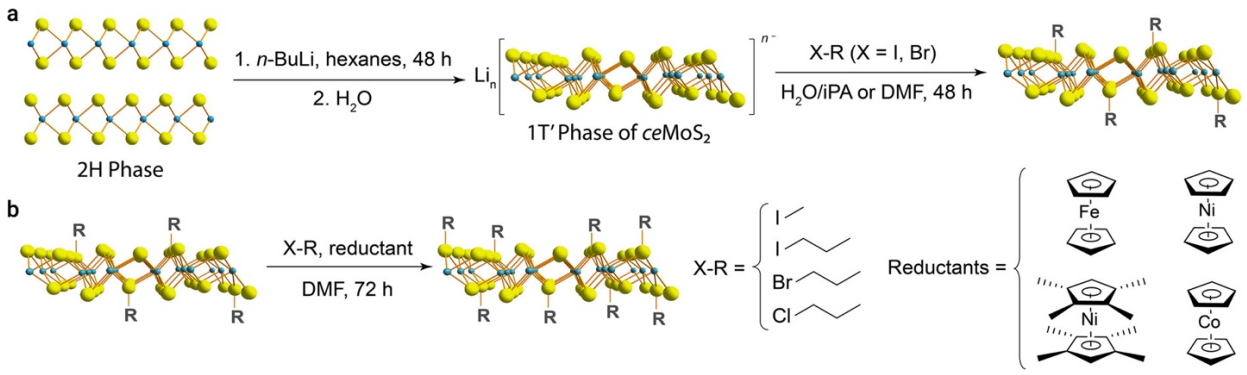

Figure 2.5. a) Conversion of 2H phase to 1T by exfoliation with n-butyllithium followed by conditions for self-limited alkylation with alkylhalide reagents. b) Procedure for further reductant activated alkylation of functionalized MoS_2 sheets. Reprinted with permission from E. X. Yan, M. Cabán-Acevedo, K. M. Papadantonakis, B. S. Brunschwig, N. S. Lewis. *ACS Materials Letter*s, 2020, 2, 133 – 139. Copyright 2020 American Chemical Society.

2.4 Tuning Nanoparticle Catalyst Activity Using Surface Chemistry

As discussed in the previous section, typical surface ligands for colloidally synthesized nanomaterials are comprised of long hydrocarbon chains with polar head groups that bind to the material via dative/coordinate-covalent bonds. For example, long chain carboxylates, amines and related ammonium salts, phosphines, and thiolates have all been used as common surfactants for nanomaterials. The long hydrocarbon chains prevent aggregation of the nanoparticles through steric stabilization and provide solubility in common nonpolar solvents, while the polar head groups bind and stabilize the highly energetic surface of the nanomaterials or provide a site for electrostatic stabilization through charge localization. These surface ligands are typically considered a detriment to catalysis due to the blocking of active sites and are commonly removed via thermal or chemical treatments as described above. However, recent work has shown that these coordinate-covalent bonding surface ligands, in addition to the emerging classes of covalent

functional groups, can be used as a synthetic lever to tune the reactivity of catalysts by modifying the electronic structure of a nanocrystal or by adjusting its interaction with substrates.

2.4.1 *Activity*

Nanoparticles occupy a unique regime between molecules and bulk materials. Similar to how ligands play a large role in the electronic structure of molecular coordination complexes, surface ligands can alter the electronic structure of nanoparticles and influence their behavior even though they can be hundreds to thousands of atoms in size. These changes in electronic structure can have large impacts on the binding strength of reaction intermediates, which in turn can impact the activity of a catalyst due to many of these transformations following a volcano plot behavior, via the Sabatier principle.[59,60] In many cases these ligand effects on electronic structure follow typical chemical design principles, such as inductive effects. For example, increasing the chain length of an alkylthiolate surface ligand on Au nanoparticles increases the charge density in the core, which thereby increases the Fermi level of the nanomaterial (Figure 6).[61] The extent in which the surface ligands influence the electronic structure can be affected by the size of the nanomaterial. Smaller nanomaterials have intrinsically higher ratios of surface atoms, and therefore the ligand-induced electronic effects on catalytic activity may be more prominent than for larger systems. This size-dependent ligand effect has been shown in Au nanomaterials where porphyrin-protected Au clusters (<2 nm) have a much larger enhancement in electrocatalytic HER activity compared to the larger 2.2 and 3.8 nm Au nanoparticles.

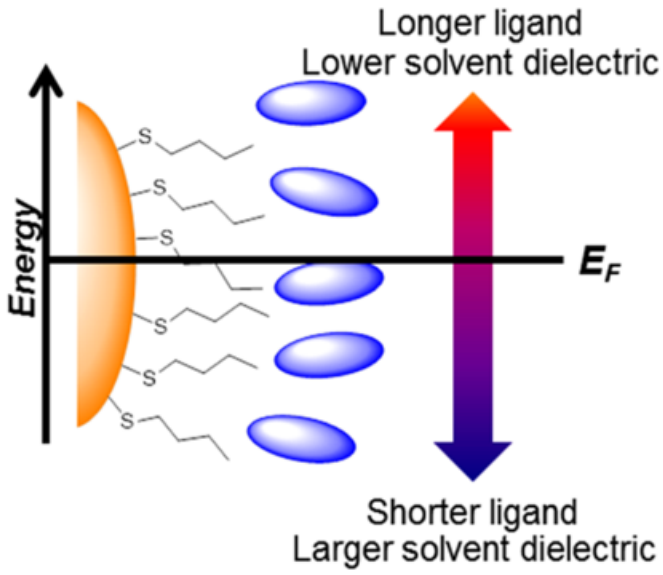

Figure 2.6. Increasing tail length of alkanethiolate surface ligands increases fermi level of Au nanoparticles. Reprinted with permission from A. Cirri, A. Silakov, L. Jensen, B. J. Lear. *Journal of the American Chemical Society,* 2016, 138, 15987 – 15993. Copyright 2016 American Chemical Society.

Traditionally, surface ligands tend to be bound to the nanomaterial via dative or electrostatic interactions as a consequence of the colloidal methods used to make them. However, there has been increasing interest in the covalent functionalization of nanomaterials, with 2D nanomaterials laying the foundation as described in the previous section. Focusing on a study examining catalytic activity, Miller and co-workers have shown that MoS_2 nanosheets can be covalently functionalized with a range of diazonium reagents (Figure 7).[52] By tuning the Hammett parameter of the substituent on the phenyl ring, the authors were able to adjust the electron density on the nanomaterial and vary its reactivity, which influences its electrocatalytic activity for HER. This method of introducing covalently bound surface ligands allows for strong ligand-nanomaterial interactions and can be used to tune the reactivity and stability of nanomaterial catalysts.

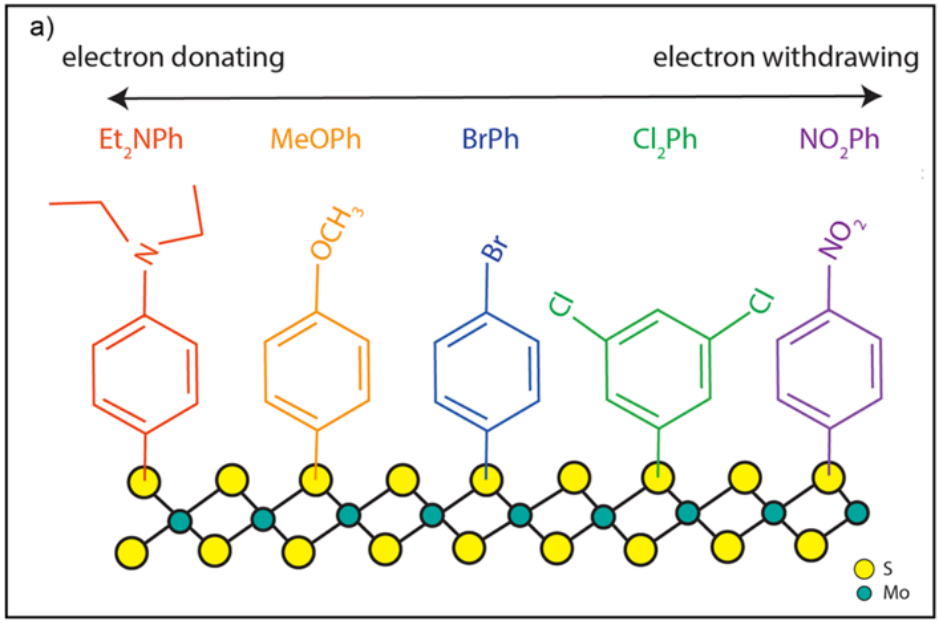

Figure 2.7. Covalently functionalizing nanomaterial surfaces allows for strong ligand interactions and can be used to tune the reactivity and stability of the material. Reprinted with permission from E. E. Benson, H. Zhang, S. A. Schuman, S. U. Nanayakkara, N. D. Bronstein, S. Ferrere, J. L. Blackburn, E. M. Miller. *Journal of the American Chemical Society,* 2018, 140, 441 – 450.

A unique approach to tuning the electronic structure of nanoparticles for heterogeneous catalysis is using surface-anchored organic ligands on a support that has a terminal binding group. These dative interactions with deposited nanoparticles can modify the electronic structure, as shown in the case of Pd nanocrystals on a TiO_2 photocatalyst support for photocatalytic hydrogen peroxide production.[62] In this example, the dative interaction between a TiO_2-anchored amine on the Pd nanocrystal improves the overall photocatalytic activity of the whole system (Figure 8). The amines donate electron density into the Pd nanoparticle, modifying the electronic structure such that the charge separation onto the TiO_2 support is improved, as well as enhancing the intrinsic activity and selectivity of the Pd nanocrystals for ORR to form the H_2O_2 product.[62]

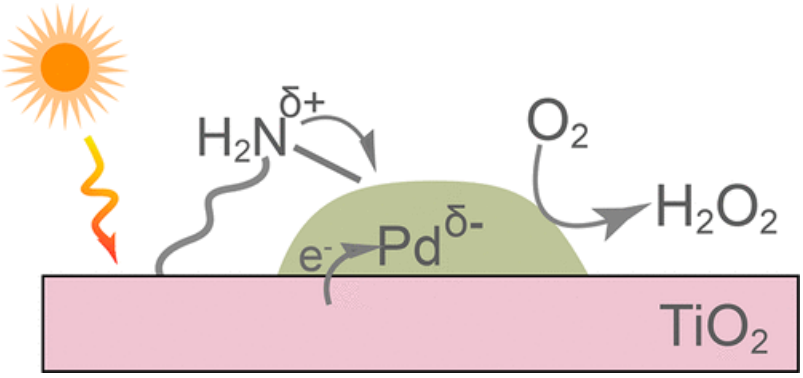

Figure 2.8. Surface anchored organic ligands on the support can be used to adjust the electronic structure of the nanomaterial catalyst. Reprinted with permission from C. Chu, D. Huang, Q. Zhu, E. Stavitski, J. A. Spies, Z. Pan, J. Mao, H. L. Xin, C. A. Schmuttenmaer, S. Hu, J.-H. Kim. *ACS Catalysis,* 2019, 9, 626 – 631. Copyright 2019 American Chemical Society.

Electronic structure effects can be used to rationally design nanoparticle interfaces to tackle common problems in catalysis, such as the poisoning of active sites. One of the major barriers to effective catalysis is strongly binding intermediates preventing the active site from turning over (Figure 9). For example, even though Pt is among the most active single metal catalysts for the oxygen reduction reaction (ORR), its remaining overpotential is linked to the strong adsorption of oxygen and hydroxyl intermediates on the surface.[63] Strongly adsorbing surface ligands on Pt nanoparticles have generally thought to have been detriments to ORR catalysis, but small amounts of amines coordinated to the surface of carbon-supported Pt nanoparticles have been shown to improve electrochemical reactivity even with decreased electrochemically active surface area (ECSA).[63] This is a key discovery because the typical explanation for improved activity through surface ligand removal is increased surface area and therefore the number of active sites. The presence of amine surface ligands on Pt has been shown to shift the frontier d-band structure, which in turn alters the free energy of adsorption (ΔG_{ad}) and the surface coverage of intermediates

on the surface of Pt. Sung and co-workers have shown that this change in ΔG_{ad} weakens the adsorption of oxygen and hydroxyl groups on the surface of Pt, preventing the strong binding of reaction intermediates and improving the overall reactivity of the catalyst.[63]

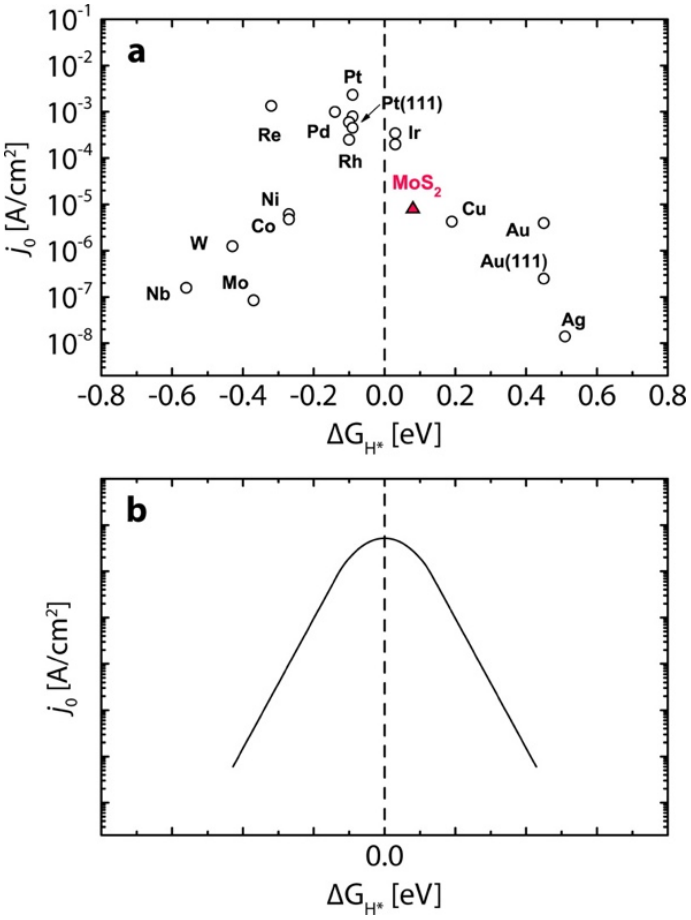

Figure 2.9. Volcano plots (experimental, a and theoretical, b) are a manifestation of the Sabatier principle and are commonly invoked to describe catalytic activity. Materials on either end of the volcano plot either bind the intermediate too strongly or too weakly and this limits turnover. Surface ligands may be utilized to adjust the strength of the binding of required reaction intermediates. Reprinted with permission from J. D. Benck, T. R. Hellstern, J. Kibsgaard, P. Chakthranont, T. F. Jaramillo. *ACS Cataysis,* 2014, 4, 3957 – 3971. Copyright 2014 American Chemical Society.

Adsorption of poisonous spectator species onto the surface can prevent the formation of required surface intermediates and hinder active site turnover, such as PO_4^{3-} on Pt for the ORR.[63,64] H_3PO_4-doped polybenzimidazole (PBI) membranes have been highly studied for proton exchange membrane fuel cells (PEMFCs) because they show improved reactivity and stability at elevated temperatures. However, one major concern for these systems is the competitive adsorption and poisoning of the surface of Pt by PO_4^{3-} anions. Jang and co-workers have illustrated that the native oleylamine surface ligands on Pt nanoparticles enable the "third-body effect," in which the oleylamine surfactants block the poisonous spectator PO_4^{3-} anions from binding to the surface (Figure 10).[64]

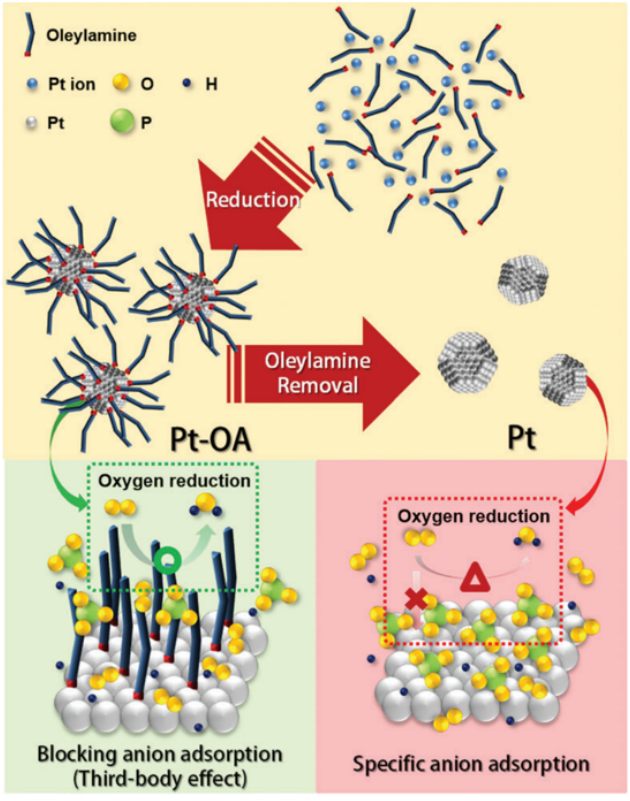

Figure 2.10. Oleylamine on the surface of Pt blocks poisonous PO_4^{3-} adsorption on the catalytically active surface via the "third-body effect". Reproduced from Ref. 64 with permission from The Royal Society of Chemistry.

2.4.2 *Selectivity*

Another major barrier to efficient catalysis is the presence of competing side reactions. This is particularly relevant for the CO_2 reduction reaction (CO_2RR), where selectivity is a central challenge both in targeting a single carbon-containing product and minimizing competition from the hydrogen evolution reaction (HER) due to the necessary presence of protons in the reaction solution. Recent work done by Hwang and co-workers have shown that the tendency of a Ag nanocrystal catalyst to participate in CO_2RR or HER can be modulated with the use of surface ligands.[65] Amine-capped Ag nanocrystals have almost 100% faradaic efficiency for the reduction of CO_2 to CO. However, using a thiol surface ligand actually increases the HER activity and reduces the CO_2RR faradaic efficiency. DFT calculations were used to show that the presence of amine surface ligands improves the binding energy of COOH intermediates while destabilizing adsorbed H intermediates. Conversely, thiol surface ligands improve ΔG_{ad} for both COOH and H intermediates and therefore participates in competitive CO_2RR and HER, reducing the faradaic efficiency for the CO_2RR.[65]

Similar selectivity has been promoted on cysteamine-capped Au nanoparticles for CO_2RR. The sulfur end of the cysteamine ligand binds to the surface of Au nanoparticles and alters the electronic structure of the surface while the terminal amine group on cysteamine is able to participate in a cooperative ligand mechanism by chemisorbing CO_2 and stabilizing its relevant adsorbed intermediates.[66] This lowers the overpotential and improves the faradaic efficiency of Au nanocrystals for electrocatalytic CO_2 reduction to CO.[66]

There has also been work done with "designer" surface ligands on Au nanoparticles with n-heterocyclic carbenes (NHCs). Using the strongly sigma-donating NHCs as surface ligands for Au

nanoparticles has been shown to improve the faradaic efficiency of CO_2 reduction as well as changing the mechanistic pathway by changing the rate-determining step (Figure 11).[67]

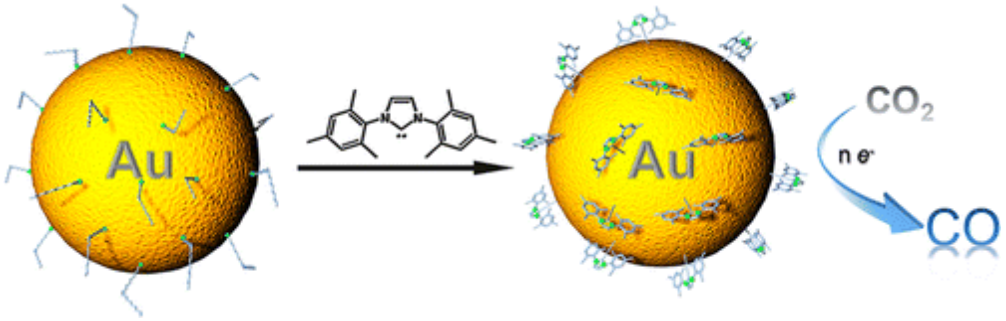

Figure 2.11. Utilizing "designer" NHCs to improve the faradaic efficiency of CO_2 reduction to CO. Reprinted with permission from Z. Cao, D. Kim, D. Hong, Y. Yu, J. Xu, S. Lin, X. Wen, E. M. Nichols, K. Jeong, J. A. Reimer, P. Yang, C. J. Chang. *Journal of the American Chemical Society,* 2016, 138, 8120 – 8125. Copyright 2016 American Chemical Society.

Selectivity also becomes an issue when considering the extent of a reaction. For example, using Pt or Co/Pt nanoparticle catalysts for selective hydrogenation of an alkyne to an alkene can often fully hydrogenate to produce the saturated alkane product. Shevchenko and co-workers have shown that primary amines can be used to tune the selectivity of 4-octyne hydrogenation to 4-octene from 0% to greater than 90% depending on the amine coverage on the surface of the nanoparticle (Figure 12).[68] At high amine coverage, the binding energy of the amine is higher than that of the alkene intermediate, preventing the alkene from reacting with the catalytically active surface to form the undesired alkane product.[68]

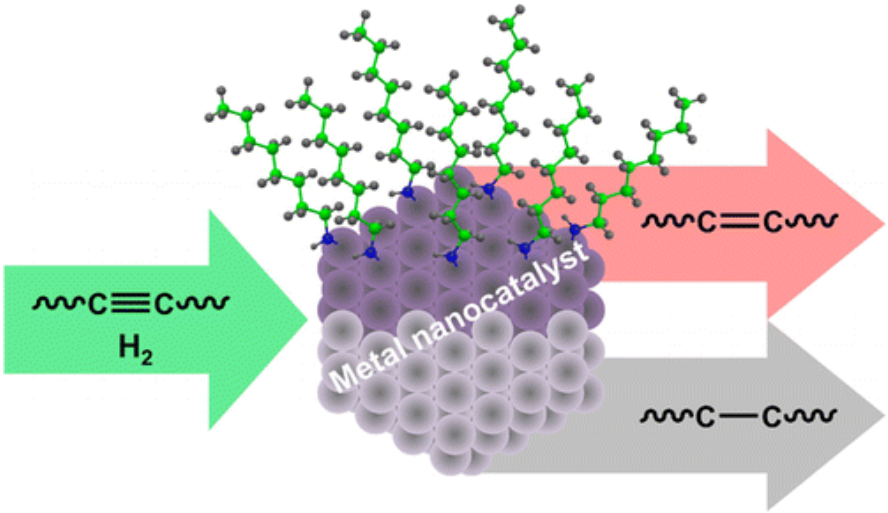

Figure 2.12. Surface ligands can be utilized to adjust the extent of hydrogenation with metal nanocrystal catalysts. Reprinted with permission from S. G. Kwon, G. Krylova, A. Sumer, M. M. Schwartz, E. E. Bunel, C. L. Marshall, S. Chattopadhyay, B. Lee, J. Jellinkek, E. V. Shevchenko. *Nano Letters,* 2012, 12, 5382 – 5388. Copyright 2012 American Chemical Society.

Altering the outer-coordination sphere interactions of the nanoparticle surface with the solvent can also assist in tuning the selectivity of an electrocatalyst. Buonsanti and co-workers have shown that imidazolium ligands can be used to tune selectivity of Ag nanoparticles for CO_2RR when competing with HER.[69] They illustrate that the changes to the electronic structure of the Ag nanocrystal plays a small role in the catalyst performance, and that the length of the hydrocarbon tail plays an important role in balancing the steric properties of the surface with the hydrophobicity, which allows CO_2 to interact with the substrate but limits the amount of H_2O to prevent competitive HER.[69]

2.4.3 *Extra Particle Effects*

Modifying the surface of a nanocrystal catalyst and its synergy with substrate is an obvious component in overall catalytic activity, but a less intuitive factor to catalytic performance is the interface of the catalyst with bulk solvent (and the electrolyte in the case of electrocatalysis). Whether the nanocrystals are colloidally suspended in solution or if they are immobilized onto a heterogeneous support, the surface ligands define the interface between the nanocrystal and solvent. Kimber and co-workers have shown via x-ray pair distribution function analysis that both polar and nonpolar solvents restructure around nanoparticles. This result shows that nanoparticles in solution have a solvation shell that can impact its reactivity. The characteristics of the nanoparticle-solvent interface may greatly alter the catalytic activity of nanocrystals by altering the interactions with the bulk solvent.[70]

Recent work from our lab has shown that the removal of long chain carboxylate and amine surface ligands on CoP greatly improves overpotential for HER due to the improved hydrophilicty of the film (Figure 13). The improved wettability of the electrode film increases electrochemically active surface area (ECSA) because there is no longer a hydrophobic interface preventing the electrolyte solution from interaction with the electrode surface.[40] The hydrophobicity of an interface has also been shown to play a role in the oxygen evolution reaction (OER), where phosphorylation of a NiFe hydroxide film greatly improves the electrocatalytic activity. The phosphorylation increases the ECSA due to improved wettability of the electrolyte solution with the surface of the catalyst.[71]

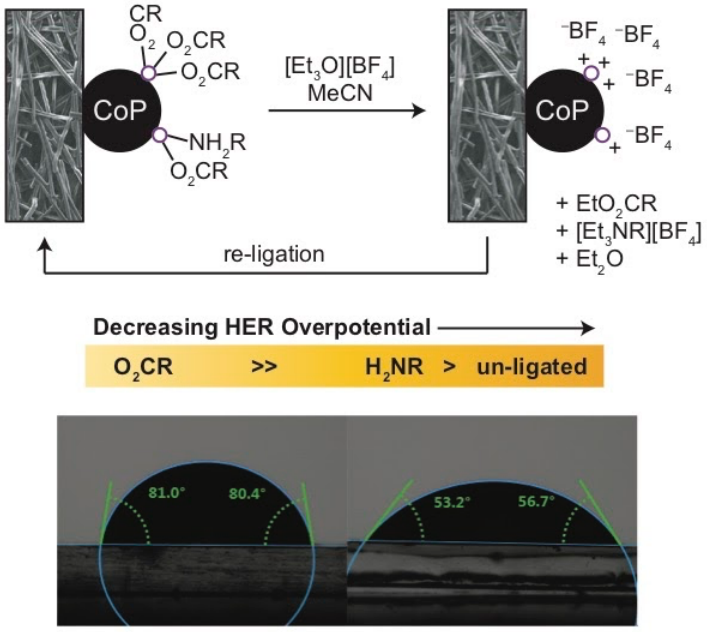

Figure 2.13. Long chain surface ligands on CoP impede electrocatalytic HER by generating a hydrophobic interface. Removing the surface ligands improves the interface with the electrolyte solution in aqueous conditions. Adapted with permission from D. Ung, B. M. Cossairt. *ACS Applied Energy Materials,* 2019, 2, 1642 – 1645. Copyright 2019 American Chemical Society.

Surface ligands can also imbue cooperative ligand effects by interacting with the substrate. For example, certain bifunctional surface ligands have been shown to participate as proton relays and increase the local concentration of protons at the surface of a nanocrystal catalyst. Ethylenediamine functionalized NiMo electrocatalysts have improved HER activity in aqueous alkaline conditions when compared to primary amines. The presence of the terminal amine at the interface of the catalyst and the electrolyte solution improves the adsorption of water molecules and their transportation to the catalyst surface.[72] This improvement in catalytic activity with improved local concentration of substrate can also be seen with polymer-based surface ligands, such as polyethylenimine or polyallylamine. In the case of polyallylamine, Chen and co-workers have

shown that Pt tripods have an onset overpotential that is more positive than the theoretical value of HER in aqueous acidic conditions (0 V vs RHE) because the local proton concentration is increased by orders of magnitude compared to the bulk electrolyte solution.[73,74] Functionalization with cooperative ligands for catalysis acts as a local modification to surface atoms that are able to interact with the substrate. Because of this local effect, these ligands can play a critical role in enhancing catalytic activity for inner-sphere electron transfer transformations, regardless of the size of the nanomaterial.

2.5 CONCLUSIONS

The full potential of nanoscale catalysts will only be realized once we have mastered the manipulation of their interfacial chemistry. To date, only scattered reports of utilizing nanoparticle surface chemistry to alter catalyst activity, selectivity, and extra-particle interactions have been documented. We need to be more systematic in our approach to deduce generalizable design principles for interfacial design. As a community we must study how surface modification impacts inner-sphere reactions and overall reaction landscapes. This will require thinking about heterogeneous active sites as truly molecular entities characterized by bonds being made and broken in an atomically defined manner. Only then will we be able to harness the power of interfacial design in heterogeneous catalysis that has so well served the natural evolved world of biological enzymes and the man-made world of organometallic chemistry. Theoretical studies have been used extensively to probe inner-sphere chemistry,[75–77] but complementary experimental data are lacking. A recent example from the Center for Molecular Electrocatalysis demonstrates the insight that can come from such measurements.[78] On the basis of the reactivity of CoP with various molecular hydrogen donating and accepting reagents, the distribution of binding free energies for H atoms on CoP (both mesoscale particles and colloidal nanoparticles) was estimated

to be roughly 51–66 kcal mol^{-1} ($\Delta G°_H \cong 0$ to −0.7 eV vs H_2). These results highlight the complexity of these surfaces and illustrate that the numbers extracted from calculations on pristine surfaces are an oversimplification.

In order to truly utilize interfacial design for improved catalytic activity, the nanomaterial surface needs to be stable in the desired catalytic conditions. But due to the dynamic nature of coordinate-covalent bonds typified by traditional surface ligands (e.g. carboxylates, amines, etc.), highly engineered interfaces designed to modify activity will evolve over time. For example, HER catalysts typically have the greatest activity in highly acidic electrolyte conditions. However, datively bound carboxylate and amine surface ligands commonly found on colloidally prepared nanomaterials can be easily protonated and removed from the nanomaterial surface. Similarly, ORR catalysts typically have the best performance in highly alkaline electrolyte conditions. But the high concentration of OH^- can displace the surface ligands on the engineered interface by altering the equilibrium or by etching the Z-type ligands on the surface. Of course, this is a problem in the molecular catalysis field as well – ligand displacement under catalytic conditions leads to the formation of uncontrolled nanoparticles or worse, complete catalyst deactivation. We posit that the best method towards designing stable interfaces that can be utilized for improved catalysis in a variety of systems is through covalent modification. Formally covalent bonds between the nanoparticle surface and new surface ligands should be much more stable and less dynamic in the catalytic environment. However, these covalent bonding interactions alter material structure and properties in ways that are largely as yet unknown. Exciting recent examples of this approach can be found in the carbon literature where the covalent modification of graphite has led to novel insight into reaction mechanisms and improved catalyst activity (Figure 14).[79–81] We believe this covalent approach to heterogeneous surface modification, including at complex nanoparticle

interfaces, will have broad implications for the molecular-level design of next-generation catalytic systems.

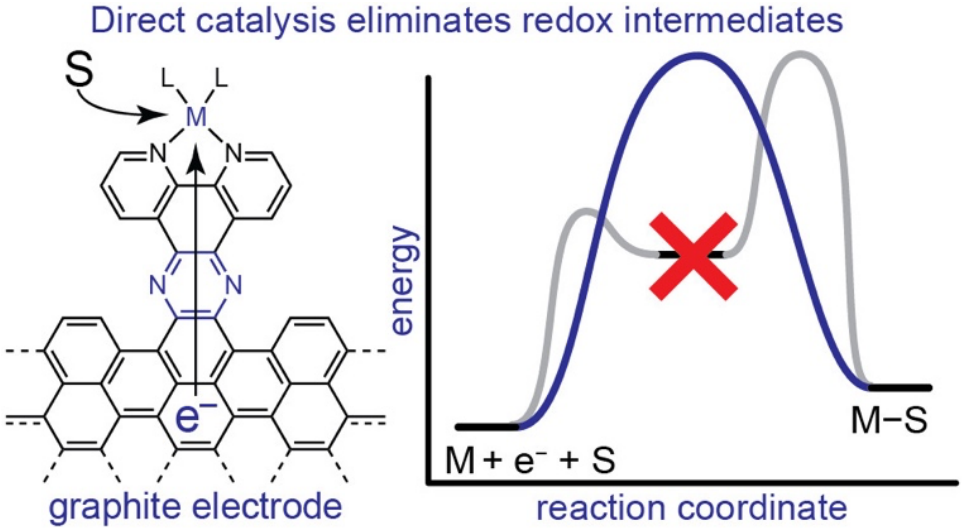

Figure 2.14. The covalent coupling of a molecular hydrogen evolution catalyst to a graphitic electrode eliminates stepwise pathways and forces concerted electron transfer and proton binding. Reprinted with permission from M. N. Jackson, C. J. Kaminsky, S. O. Oh, J. F. Melville, Y. Surendranath. *Journal of the American Chemical Society, 2019, **141**, 14160 – 14167. Copyright 2019 American Chemical Society.*

REFERENCES

(1) Fundamentals of Organometallic Catalysis | Wiley https://www.wiley.com/en-us/Fundamentals+of+Organometallic+Catalysis-p-9783527327171 (accessed 2020 -02 -12).
(2) Modern Heterogeneous Catalysis: An Introduction | Wiley https://www.wiley.com/en-us/Modern+Heterogeneous+Catalysis%3A+An+Introduction-p-9783527339617 (accessed 2020 -02 -13).
(3) Owen, J. S. The Coordination Chemistry of Nanocrystal Surfaces. *Science* **2015**, *347* (6222), 615–616.
(4) Pensa, E.; Cortés, E.; Corthey, G.; Carro, P.; Vericat, C.; Fonticelli, M. H.; Benítez, G.; Rubert, A. A.; Salvarezza, R. C. The Chemistry of the Sulfur–Gold Interface: In Search of a Unified Model. *Acc. Chem. Res.* **2012**, *45* (8), 1183–1192. https://doi.org/10.1021/ar200260p.
(5) Boles, M. A.; Ling, D.; Hyeon, T.; Talapin, D. V. The Surface Science of Nanocrystals. *Nat. Mater.* **2016**, *15* (2), 141–153. https://doi.org/10.1038/nmat4526.
(6) Liu, P.; Qin, R.; Fu, G.; Zheng, N. Surface Coordination Chemistry of Metal Nanomaterials. *J. Am. Chem. Soc.* **2017**, *139* (6), 2122–2131. https://doi.org/10.1021/jacs.6b10978.
(7) Brown, P. R.; Kim, D.; Lunt, R. R.; Zhao, N.; Bawendi, M. G.; Grossman, J. C.; Bulović, V. Energy Level Modification in Lead Sulfide Quantum Dot Thin Films through Ligand Exchange. *ACS Nano* **2014**, *8* (6), 5863–5872. https://doi.org/10.1021/nn500897c.
(8) Chuang, C.-H. M.; Brown, P. R.; Bulović, V.; Bawendi, M. G. Improved Performance and Stability in Quantum Dot Solar Cells through Band Alignment Engineering. *Nat. Mater.* **2014**, *13* (8), 796–801. https://doi.org/10.1038/nmat3984.
(9) Kroupa, D. M.; Vörös, M.; Brawand, N. P.; McNichols, B. W.; Miller, E. M.; Gu, J.; Nozik, A. J.; Sellinger, A.; Galli, G.; Beard, M. C. Tuning Colloidal Quantum Dot Band Edge Positions through Solution-Phase Surface Chemistry Modification. *Nat. Commun.* **2017**, *8*, 15257. https://doi.org/10.1038/ncomms15257.
(10) Bloom, B. P.; Zhao, L.-B.; Wang, Y.; Waldeck, D. H.; Liu, R.; Zhang, P.; Beratan, D. N. Ligand-Induced Changes in the Characteristic Size-Dependent Electronic Energies of CdSe Nanocrystals. *J. Phys. Chem. C* **2013**, *117* (43), 22401–22411. https://doi.org/10.1021/jp403164w.
(11) Weiss, E. A. Designing the Surfaces of Semiconductor Quantum Dots for Colloidal Photocatalysis. *ACS Energy Lett.* **2017**, 1005–1013. https://doi.org/10.1021/acsenergylett.7b00061.
(12) Niu, Z.; Li, Y. Removal and Utilization of Capping Agents in Nanocatalysis. *Chem. Mater.* **2014**, *26* (1), 72–83. https://doi.org/10.1021/cm4022479.
(13) M. Rossi, L.; L. Fiorio, J.; S. Garcia, M. A.; P. Ferraz, C. The Role and Fate of Capping Ligands in Colloidally Prepared Metal Nanoparticle Catalysts. *Dalton Trans.* **2018**, *47* (17), 5889–5915. https://doi.org/10.1039/C7DT04728B.
(14) Nitschke, M. Plasma Modification of Polymer Surfaces and Plasma Polymerization. In *Polymer Surfaces and Interfaces: Characterization, Modification and Applications*; Stamm, M., Ed.; Springer: Berlin, Heidelberg, 2008; pp 203–214. https://doi.org/10.1007/978-3-540-73865-7_10.
(15) Thermal Annealing - an overview | ScienceDirect Topics https://www.sciencedirect.com/topics/engineering/thermal-annealing (accessed 2020 -02 -28).

(16) Baik, S. J.; Kim, K.; Lim, K. S.; Jung, S.; Park, Y.-C.; Han, D. G.; Lim, S.; Yoo, S.; Jeong, S. Low-Temperature Annealing for Highly Conductive Lead Chalcogenide Quantum Dot Solids. *J. Phys. Chem. C* **2011**, *115* (3), 607–612. https://doi.org/10.1021/jp1084668.
(17) Wills, A. W.; Kang, M. S.; Khare, A.; Gladfelter, W. L.; Norris, D. J. Thermally Degradable Ligands for Nanocrystals. *ACS Nano* **2010**, *4* (8), 4523–4530. https://doi.org/10.1021/nn100637u.
(18) Cargnello, M.; Chen, C.; Diroll, B. T.; Doan-Nguyen, V. V. T.; Gorte, R. J.; Murray, C. B. Efficient Removal of Organic Ligands from Supported Nanocrystals by Fast Thermal Annealing Enables Catalytic Studies on Well-Defined Active Phases. *J. Am. Chem. Soc.* **2015**, *137* (21), 6906–6911. https://doi.org/10.1021/jacs.5b03333.
(19) Li, D.; Wang, C.; Tripkovic, D.; Sun, S.; Markovic, N. M.; Stamenkovic, V. R. Surfactant Removal for Colloidal Nanoparticles from Solution Synthesis: The Effect on Catalytic Performance. *ACS Catal.* **2012**, *2* (7), 1358–1362. https://doi.org/10.1021/cs300219j.
(20) Mohapatra, P.; Shaw, S.; Mendivelso-Perez, D.; Bobbitt, J. M.; Silva, T. F.; Naab, F.; Yuan, B.; Tian, X.; Smith, E. A.; Cademartiri, L. Calcination Does Not Remove All Carbon from Colloidal Nanocrystal Assemblies. *Nat. Commun.* **2017**, *8* (1), 1–7. https://doi.org/10.1038/s41467-017-02267-9.
(21) Altowairqi, Y.; Alsubaie, A.; Stroh, K. P.; Perez-Marin, I. G.; Bowen, L.; Szablewski, M.; Halliday, D. P. The Effect of Annealing Conditions: Temperature, Time, Ramping Rate and Atmosphere on Nanocrystal Cu2ZnSnS4 (CZTS) Thin Film Solar Cell Properties. *Mater. Today Proc.* **2019**, *18*, 473–486. https://doi.org/10.1016/j.matpr.2019.06.234.
(22) Chang, J. F.; Lin, W. C.; Hon, M. H. Effects of Post-Annealing on the Structure and Properties of Al-Doped Zinc Oxide Films. *Appl. Surf. Sci.* **2001**, *183* (1), 18–25. https://doi.org/10.1016/S0169-4332(01)00541-4.
(23) Shaw, S.; Colaux, J. L.; Hay, J. L.; Peiris, F. C.; Cademartiri, L. Building Materials from Colloidal Nanocrystal Arrays: Evolution of Structure, Composition, and Mechanical Properties upon the Removal of Ligands by O2 Plasma. *Adv. Mater.* **2016**, *28* (40), 8900–8905. https://doi.org/10.1002/adma.201601873.
(24) Shaw, S.; Tian, X.; Silva, T. F.; Bobbitt, J. M.; Naab, F.; Rodrigues, C. L.; Smith, E. A.; Cademartiri, L. Selective Removal of Ligands from Colloidal Nanocrystal Assemblies with Non-Oxidizing He Plasmas. *Chem. Mater.* **2018**, *30* (17), 5961–5967. https://doi.org/10.1021/acs.chemmater.8b02095.
(25) Wang, L.; Zhang, B.; Rui, Q. Plasma-Induced Vacancy Defects in Oxygen Evolution Cocatalysts on Ta3N5 Photoanodes Promoting Solar Water Splitting. *ACS Catal.* **2018**, *8* (11), 10564–10572. https://doi.org/10.1021/acscatal.8b03111.
(26) Hassinen, A.; Moreels, I.; De Nolf, K.; Smet, P. F.; Martins, J. C.; Hens, Z. Short-Chain Alcohols Strip X-Type Ligands and Quench the Luminescence of PbSe and CdSe Quantum Dots, Acetonitrile Does Not. *J. Am. Chem. Soc.* **2012**, *134* (51), 20705–20712. https://doi.org/10.1021/ja308861d.
(27) Knauf, R. R.; Lennox, J. C.; Dempsey, J. L. Quantifying Ligand Exchange Reactions at CdSe Nanocrystal Surfaces. *Chem. Mater.* **2016**, *28* (13), 4762–4770. https://doi.org/10.1021/acs.chemmater.6b01827.
(28) Kessler, M. L.; Starr, H. E.; Knauf, R. R.; Rountree, K. J.; Dempsey, J. L. Exchange Equilibria of Carboxylate-Terminated Ligands at PbS Nanocrystal Surfaces. *Phys. Chem. Chem. Phys.* **2018**, *20* (36), 23649–23655. https://doi.org/10.1039/C8CP04275F.

(29) Ritchhart, A.; Cossairt, B. M. Quantifying Ligand Exchange on InP Using an Atomically Precise Cluster Platform. *Inorg. Chem.* **2019**. https://doi.org/10.1021/acs.inorgchem.8b03524.
(30) Sluydts, M.; De Nolf, K.; Van Speybroeck, V.; Cottenier, S.; Hens, Z. Ligand Addition Energies and the Stoichiometry of Colloidal Nanocrystals. *ACS Nano* **2016**, *10* (1), 1462–1474. https://doi.org/10.1021/acsnano.5b06965.
(31) Nag, A.; Kovalenko, M. V.; Lee, J. S.; Liu, W. Y.; Spokoyny, B.; Talapin, D. V. Metal-Free Inorganic Ligands for Colloidal Nanocrystals: S(2-), HS(-), Se(2-), HSe(-), Te(2-), HTe(-), TeS(3)(2-), OH(-), and NH(2)(-) as Surface Ligands. *J Am Chem Soc* **2011**, *133* (27), 10612–10620.
(32) Kovalenko, M.; Scheele, M.; Talapin, D. Colloidal Nanocrystals with Molecular Metal Chalcogenide Surface Ligands. *Science* **2009**, *324* (5933), 1417–1420. https://doi.org/10.1126/science.1170524.
(33) Fafarman, A.; Koh, W.; Diroll, B.; Kim, D.; Ko, D.-K.; Oh, S.; Ye, X.; Doan-Nguyen, V.; Crump, M.; Reifsnyder, D.; Murray, C.; Kagan, C. Thiocyanate-Capped Nanocrystal Colloids: Vibrational Reporter of Surface Chemistry and Solution-Based Route to Enhanced Coupling in Nanocrystal Solids. *J. Am. Chem. Soc.* **2011**, *133* (39), 15753–15761. https://doi.org/10.1021/ja206303g.
(34) Fan, J. Z.; Andersen, N. T.; Biondi, M.; Todorović, P.; Sun, B.; Ouellette, O.; Abed, J.; Sagar, L. K.; Choi, M.-J.; Hoogland, S.; Arquer, F. P. G. de; Sargent, E. H. Mixed Lead Halide Passivation of Quantum Dots. *Adv. Mater.* **2019**, *31* (48), 1904304. https://doi.org/10.1002/adma.201904304.
(35) Hughes, B.; Ruddy, D.; Blackburn, J.; Smith, D.; Bergren, M.; Nozik, A.; Johnson, J.; Beard, M. Control of PbSe Quantum Dot Surface Chemistry and Photophysics Using an Alkylselenide Ligand. *ACS Nano* **2012**, 120509235448008. https://doi.org/10.1021/nn301405j.
(36) Anderson, N. C.; Hendricks, M. P.; Choi, J. J.; Owen, J. S. Ligand Exchange and the Stoichiometry of Metal Chalcogenide Nanocrystals: Spectroscopic Observation of Facile Metal-Carboxylate Displacement and Binding. *J. Am. Chem. Soc.* **2013**, *135* (49), 18536–18548.
(37) Gary, D. C.; Petrone, A.; Li, X.; Cossairt, B. M. Investigating the Role of Amine in InP Nanocrystal Synthesis: Destabilizing Cluster Intermediates by Z-Type Ligand Displacement. *Chem. Commun.* **2016**, *53* (1), 161–164. https://doi.org/10.1039/C6CC07952K.
(38) Henckel, D. A.; Lenz, O.; Cossairt, B. M. Effect of Ligand Coverage on Hydrogen Evolution Catalyzed by Colloidal WSe2. *ACS Catal.* **2017**, *7* (4), 2815–2820. https://doi.org/10.1021/acscatal.7b00074.
(39) Nelson, A.; Zong, Y.; Fritz, K. E.; Suntivich, J.; Robinson, R. D. Assessment of Soft Ligand Removal Strategies: Alkylation as a Promising Alternative to High-Temperature Treatments for Colloidal Nanoparticle Surfaces. *ACS Mater. Lett.* **2019**, *1* (1), 177–184. https://doi.org/10.1021/acsmaterialslett.9b00089.
(40) Ung, D.; Cossairt, B. M. Effect of Surface Ligands on CoP for the Hydrogen Evolution Reaction. *ACS Appl. Energy Mater.* **2019**, *2* (3), 1642–1645. https://doi.org/10.1021/acsaem.9b00240.
(41) Anderson, N. C.; Owen, J. S. Soluble, Chloride-Termiated CdSe Nanocrystals: Ligand Exchange Monitored by 1H and 31P NMR Spectroscopy. *Chem Mater* **2013**, *25* (1), 69–76.
(42) Dong, A.; Ye, X.; Chen, J.; Kang, Y.; Gordon, T.; Kikkawa, J. M.; Murray, C. B. A Generalized Ligand-Exchange Strategy Enabling Sequential Surface Functionalization of Colloidal Nanocrystals. *J. Am. Chem. Soc.* **2011**, *133* (4), 998–1006. https://doi.org/10.1021/ja108948z.

(43) Doris, S. E.; Lynch, J. J.; Li, C.; Wills, A. W.; Urban, J. J.; Helms, B. A. Mechanistic Insight into the Formation of Cationic Naked Nanocrystals Generated under Equilibrium Control. *J. Am. Chem. Soc.* **2014**, *136* (44), 15702–15710. https://doi.org/10.1021/ja508675t.
(44) Owen, J. S.; Park, J.; Trudeau, P.; Alivisatos, A. P. Reaction Chemistry and Ligand Exchange at Cadmium-Selenide Nanocrystal Surfaces. *J Am Chem Soc* **2008**, *130*, 12279–12281.
(45) Ning, Z.; Ren, Y.; Hoogland, S.; Voznyy, O.; Levina, L.; Stadler, P.; Lan, X.; Zhitomirsky, D.; Sargent, E. H. All-Inorganic Colloidal Quantum Dot Photovoltaics Employing Solution-Phase Halide Passivation. *Adv. Mater.* **2012**, *24* (47), 6295–6299. https://doi.org/10.1002/adma.201202942.
(46) Zhang, H.; Jang, J.; Liu, W.; Talapin, D. V. Colloidal Nanocrystals with Inorganic Halide, Pseudohalide, and Halometallate Ligands. *ACS Nano* **2014**, *8* (7), 7359–7369. https://doi.org/10.1021/nn502470v.
(47) Kovalenko, M. V.; Bodnarchuk, M. I.; Zaumseil, J.; Lee, J.-S.; Talapin, D. V. Expanding the Chemical Versatility of Colloidal Nanocrystals Capped with Molecular Metal Chalcogenide Ligands. *J. Am. Chem. Soc.* **2010**, *132* (29), 10085–10092. https://doi.org/10.1021/ja1024832.
(48) Chen, X.; McDonald, A. R. Functionalization of Two-Dimensional Transition-Metal Dichalcogenides. *Adv. Mater.* **2016**, *28* (27), 5738–5746. https://doi.org/10.1002/adma.201505345.
(49) Chou, S. S.; De, M.; Kim, J.; Byun, S.; Dykstra, C.; Yu, J.; Huang, J.; Dravid, V. P. Ligand Conjugation of Chemically Exfoliated MoS2. *J. Am. Chem. Soc.* **2013**, *135* (12), 4584–4587. https://doi.org/10.1021/ja310929s.
(50) Zhou, L.; He, B.; Yang, Y.; He, Y. Facile Approach to Surface Functionalized MoS2 Nanosheets. *RSC Adv.* **2014**, *4* (61), 32570–32578. https://doi.org/10.1039/C4RA04682J.
(51) Knirsch, K. C.; Berner, N. C.; Nerl, H. C.; Cucinotta, C. S.; Gholamvand, Z.; McEvoy, N.; Wang, Z.; Abramovic, I.; Vecera, P.; Halik, M.; Sanvito, S.; Duesberg, G. S.; Nicolosi, V.; Hauke, F.; Hirsch, A.; Coleman, J. N.; Backes, C. Basal-Plane Functionalization of Chemically Exfoliated Molybdenum Disulfide by Diazonium Salts. *ACS Nano* **2015**, *9* (6), 6018–6030. https://doi.org/10.1021/acsnano.5b00965.
(52) Benson, E. E.; Zhang, H.; Schuman, S. A.; Nanayakkara, S. U.; Bronstein, N. D.; Ferrere, S.; Blackburn, J. L.; Miller, E. M. Balancing the Hydrogen Evolution Reaction, Surface Energetics, and Stability of Metallic MoS2 Nanosheets via Covalent Functionalization. *J. Am. Chem. Soc.* **2018**, *140* (1), 441–450. https://doi.org/10.1021/jacs.7b11242.
(53) Voiry, D.; Goswami, A.; Kappera, R.; Silva, C. de C. C. e; Kaplan, D.; Fujita, T.; Chen, M.; Asefa, T.; Chhowalla, M. Covalent Functionalization of Monolayered Transition Metal Dichalcogenides by Phase Engineering. *Nat. Chem.* **2015**, *7* (1), 45–49. https://doi.org/10.1038/nchem.2108.
(54) Paredes, J. I.; Munuera, J. M.; Villar-Rodil, S.; Guardia, L.; Ayán-Varela, M.; Pagán, A.; Aznar-Cervantes, S. D.; Cenis, J. L.; Martínez-Alonso, A.; Tascón, J. M. D. Impact of Covalent Functionalization on the Aqueous Processability, Catalytic Activity, and Biocompatibility of Chemically Exfoliated MoS2 Nanosheets. *ACS Appl. Mater. Interfaces* **2016**, *8* (41), 27974–27986. https://doi.org/10.1021/acsami.6b08444.
(55) Yan, E. X.; Cabán-Acevedo, M.; Papadantonakis, K. M.; Brunschwig, B. S.; Lewis, N. S. Reductant-Activated, High-Coverage, Covalent Functionalization of 1T′-MoS2. *ACS Mater. Lett.* **2020**, *2* (2), 133–139. https://doi.org/10.1021/acsmaterialslett.9b00241.

(56) Hirsch, A.; Hauke, F. Post-Graphene 2D Chemistry: The Emerging Field of Molybdenum Disulfide and Black Phosphorus Functionalization. *Angew. Chem. Int. Ed.* **2018**. https://doi.org/10.1002/anie.201708211.
(57) Strano, M. S.; Dyke, C. A.; Usrey, M. L.; Barone, P. W.; Allen, M. J.; Shan, H.; Kittrell, C.; Hauge, R. H.; Tour, J. M.; Smalley, R. E. Electronic Structure Control of Single-Walled Carbon Nanotube Functionalization. *Science* **2003**, *301* (5639), 1519–1522. https://doi.org/10.1126/science.1087691.
(58) Sofer, Z.; Luxa, J.; Bouša, D.; Sedmidubský, D.; Lazar, P.; Hartman, T.; Hardtdegen, H.; Pumera, M. The Covalent Functionalization of Layered Black Phosphorus by Nucleophilic Reagents. *Angew. Chem. Int. Ed.* **2017**, *56* (33), 9891–9896. https://doi.org/10.1002/anie.201705722.
(59) Greeley, J.; Jaramillo, T. F.; Bonde, J.; Chorkendorff, I.; Nørskov, J. K. Computational High-Throughput Screening of Electrocatalytic Materials for Hydrogen Evolution. *Nat. Mater.* **2006**, *5* (11), 909–913. https://doi.org/10.1038/nmat1752.
(60) Seh, Z. W.; Kibsgaard, J.; Dickens, C. F.; Chorkendorff, I.; Nørskov, J. K.; Jaramillo, T. F. Combining Theory and Experiment in Electrocatalysis: Insights into Materials Design. *Science* **2017**, *355* (6321), eaad4998. https://doi.org/10.1126/science.aad4998.
(61) Cirri, A.; Silakov, A.; Jensen, L.; Lear, B. J. Chain Length and Solvent Control over the Electronic Properties of Alkanethiolate-Protected Gold Nanoparticles at the Molecule-to-Metal Transition. *J. Am. Chem. Soc.* **2016**, *138* (49), 15987–15993. https://doi.org/10.1021/jacs.6b09586.
(62) Chu, C.; Huang, D.; Zhu, Q.; Stavitski, E.; Spies, J. A.; Pan, Z.; Mao, J.; Xin, H. L.; Schmuttenmaer, C. A.; Hu, S.; Kim, J.-H. Electronic Tuning of Metal Nanoparticles for Highly Efficient Photocatalytic Hydrogen Peroxide Production. *ACS Catal.* **2019**, *9* (1), 626–631. https://doi.org/10.1021/acscatal.8b03738.
(63) Chung, Y.-H.; Chung, D. Y.; Jung, N.; Sung, Y.-E. Tailoring the Electronic Structure of Nanoelectrocatalysts Induced by a Surface-Capping Organic Molecule for the Oxygen Reduction Reaction. *J. Phys. Chem. Lett.* **2013**, *4* (8), 1304–1309. https://doi.org/10.1021/jz400574f.
(64) Chung, Y.-H.; Kim, S. J.; Chung, D. Y.; Park, H. Y.; Sung, Y.-E.; Yoo, S. J.; Jang, J. H. Third-Body Effects of Native Surfactants on Pt Nanoparticle Electrocatalysts in Proton Exchange Fuel Cells. *Chem. Commun.* **2015**, *51* (14), 2968–2971. https://doi.org/10.1039/C4CC09019E.
(65) Kim, C.; Eom, T.; Jee, M. S.; Jung, H.; Kim, H.; Min, B. K.; Hwang, Y. J. Insight into Electrochemical CO2 Reduction on Surface-Molecule-Mediated Ag Nanoparticles. *ACS Catal.* **2017**, *7* (1), 779–785. https://doi.org/10.1021/acscatal.6b01862.
(66) Wang, Z.; Sun, K.; Liang, C.; Wu, L.; Niu, Z.; Gao, J. Synergistic Chemisorbing and Electronic Effects for Efficient CO2 Reduction Using Cysteamine-Functionalized Gold Nanoparticles. *ACS Appl. Energy Mater.* **2019**, *2* (1), 192–195. https://doi.org/10.1021/acsaem.8b01699.
(67) Cao, Z.; Kim, D.; Hong, D.; Yu, Y.; Xu, J.; Lin, S.; Wen, X.; Nichols, E. M.; Jeong, K.; Reimer, J. A.; Yang, P.; Chang, C. J. A Molecular Surface Functionalization Approach to Tuning Nanoparticle Electrocatalysts for Carbon Dioxide Reduction. *J. Am. Chem. Soc.* **2016**, *138* (26), 8120–8125. https://doi.org/10.1021/jacs.6b02878.
(68) Kwon, S. G.; Krylova, G.; Sumer, A.; Schwartz, M. M.; Bunel, E. E.; Marshall, C. L.; Chattopadhyay, S.; Lee, B.; Jellinek, J.; Shevchenko, E. V. Capping Ligands as Selectivity

Switchers in Hydrogenation Reactions. *Nano Lett.* **2012**, *12* (10), 5382–5388. https://doi.org/10.1021/nl3027636.
(69) Pankhurst, J. R.; Guntern, Y. T.; Mensi, M.; Buonsanti, R. Molecular Tunability of Surface-Functionalized Metal Nanocrystals for Selective Electrochemical CO2 Reduction. *Chem. Sci.* **2019**, *10* (44), 10356–10365. https://doi.org/10.1039/C9SC04439F.
(70) Zobel, M.; Neder, R. B.; Kimber, S. A. J. Universal Solvent Restructuring Induced by Colloidal Nanoparticles. *Science* **2015**, *347* (6219), 292–294. https://doi.org/10.1126/science.1261412.
(71) Li, Y.; Zhao, C. Enhancing Water Oxidation Catalysis on a Synergistic Phosphorylated NiFe Hydroxide by Adjusting Catalyst Wettability. *ACS Catal.* **2017**, *7* (4), 2535–2541. https://doi.org/10.1021/acscatal.6b03497.
(72) Gao, W.; Gou, W.; Zhou, X.; Ho, J. C.; Ma, Y.; Qu, Y. Amine-Modulated/Engineered Interfaces of NiMo Electrocatalysts for Improved Hydrogen Evolution Reaction in Alkaline Solutions. *ACS Appl. Mater. Interfaces* **2018**, *10* (2), 1728–1733. https://doi.org/10.1021/acsami.7b16125.
(73) Xu, G.-R.; Bai, J.; Yao, L.; Xue, Q.; Jiang, J.-X.; Zeng, J.-H.; Chen, Y.; Lee, J.-M. Polyallylamine-Functionalized Platinum Tripods: Enhancement of Hydrogen Evolution Reaction by Proton Carriers. *ACS Catal.* **2017**, *7* (1), 452–458. https://doi.org/10.1021/acscatal.6b03049.
(74) Ding, Y.; Miao, B.-Q.; Jiang, Y.-C.; Yao, H.-C.; Li, X.-F.; Chen, Y. Polyethylenimine-Modified Nickel Phosphide Nanosheets: Interfacial Protons Boost the Hydrogen Evolution Reaction. *J. Mater. Chem. A* **2019**, *7* (22), 13770–13776. https://doi.org/10.1039/C9TA04283K.
(75) Liu, P.; Rodriguez, J. A. Catalysts for Hydrogen Evolution from the [NiFe] Hydrogenase to the Ni2P(001) Surface: The Importance of Ensemble Effect. *J. Am. Chem. Soc.* **2005**, *127* (42), 14871–14878. https://doi.org/10.1021/ja0540019.
(76) Byskov, L. S.; Bollinger, M.; Nørskov, J. K.; Clausen, B. S.; Topsøe, H. Molecular Aspects of the H2 Activation on MoS2 Based Catalysts — the Role of Dynamic Surface Arrangements. *J. Mol. Catal. Chem.* **2000**, *163* (1), 117–122. https://doi.org/10.1016/S1381-1169(00)00404-0.
(77) Lauritsen, J. V.; Bollinger, M. V.; Lægsgaard, E.; Jacobsen, K. W.; Nørskov, J. K.; Clausen, B. S.; Topsøe, H.; Besenbacher, F. Atomic-Scale Insight into Structure and Morphology Changes of MoS2 Nanoclusters in Hydrotreating Catalysts. *J. Catal.* **2004**, *221* (2), 510–522. https://doi.org/10.1016/j.jcat.2003.09.015.
(78) Delley, M. F.; Wu, Z.; Mundy, M. E.; Ung, D.; Cossairt, B. M.; Wang, H.; Mayer, J. M. Hydrogen on Cobalt Phosphide. *J. Am. Chem. Soc.* **2019**, *141* (38), 15390–15402. https://doi.org/10.1021/jacs.9b07986.
(79) Jackson, M. N.; Kaminsky, C. J.; Oh, S.; Melville, J. F.; Surendranath, Y. Graphite Conjugation Eliminates Redox Intermediates in Molecular Electrocatalysis. *J. Am. Chem. Soc.* **2019**, *141* (36), 14160–14167. https://doi.org/10.1021/jacs.9b04981.
(80) Jackson, M. N.; Pegis, M. L.; Surendranath, Y. Graphite-Conjugated Acids Reveal a Molecular Framework for Proton-Coupled Electron Transfer at Electrode Surfaces. *ACS Cent. Sci.* **2019**, *5* (5), 831–841. https://doi.org/10.1021/acscentsci.9b00114.
(81) Jackson, M. N.; Surendranath, Y. Molecular Control of Heterogeneous Electrocatalysis through Graphite Conjugation. *Acc. Chem. Res.* **2019**, *52* (12), 3432–3441. https://doi.org/10.1021/acs.accounts.9b00439.

Chapter 3. COVALENT FUNCTIONALIZATION OF NICKEL PHOSPHIDE NANOCRYSTALS WITH ARYL-DIAZONIUM SALTS

Significant portions of the following chapter have previously been published by:

Ian A. Murphy, Peter Rice, Madison Monahan, Leo B. Zasada, Elisa M. Miller, Simone Raugei, and Brandi M. Cossairt at 10.33774/chemrxiv-2021-3p4pp

3.1 ABSTRACT

Covalent functionalization of Ni2P nanocrystals was demonstrated using aryl-diazonium salts. Spontaneous adsorption of aryl functional groups was observed, with surface coverages ranging from 20-96% depending on the native reactivity of the salt as determined by the aryl substitution pattern. Increased coverage was possible for low reactivity species using a sacrificial reductant. Functionalization was confirmed using thermogravimetric analysis, FTIR and X-ray photoelectron spectroscopy. The structure and energetics of this nanocrystal electrocatalyst system, as a function of ligand coverage, was explored with density functional theory calculations. The Hammett parameter of the surface functional group was found to linearly correlate with the change in Ni and P core-electron binding energies and the nanocrystal's work-function. The electrocatalytic activity and stability of the functionalized nanocrystals for hydrogen evolution were also improved when compared to the unfunctionalized material, but a simple trend based on electrostatics was not evident.

3.2 INTRODUCTION

Great progress has been made over the past few decades in the development and deployment of renewable energy technologies. This global effort has positioned sustainably generated electricity to, in some cases, be cheaper than carbon-based competitors.1 While renewably-sourced electricity will be a key factor in decarbonizing the power and light passenger transportation sectors, there is still significant work to be done in decarbonizing other carbon intensive sectors such as industrial transportation and chemical commodities.[2–4] To achieve the same emissions reductions in these sectors, we must fundamentally alter the way we produce and recycle small molecule chemical feedstocks such as H_2, O_2, N_2, and CO_2. The key component to enabling this kind of sustainable circular economy is the development of efficient, selective, and economically viable (photo)electrocatalysts.[5]

Today, the most active catalytic materials are scarce noble metals such as platinum, palladium, and iridium. Specifically in the case of the hydrogen evolution reaction (HER), the high activity of these materials has been ascribed to their ideal metal-hydride (M-H) bond dissociation free energies (BDFEs), their diffuse frontier orbitals that span the Fermi level, and their stability in highly acidic and basic media.[6–8] The relationship between these types of "descriptors" and the intrinsic activity of a catalyst is still being investigated and qualified by many computational and electroanalytical groups.[5,9–15] Descriptor-based models for understanding catalytic activity have led to the discovery of earth-abundant catalytic materials with relatively high intrinsic activity.[5] Initial efforts in this space were focused, in some instances, on the investigation of molybdenum disulfide due to its solution processability, low toxicity, and long history of use as a hydrodesulfurization catalyst.[16–19] This same line of theory driven inquiry led to the investigation of transition metal phosphides as a new class of materials with excellent catalytic activity for HER

and high stability in acidic media. Research efforts over the past decade have explored many aspects of these materials including synthetic methodology and mechanisms[20,21,30,22–29], the effects of varying atomic composition[31–34], nano-structuring[35–37], and computational modeling of their catalytically active surface sites.[31,38–44]

Despite great progress in developing this class of materials, earth abundant alternatives still present orders of magnitude lower activity than their precious metal counterparts. This begs the question many researchers are now investigating, "what are we missing in the current descriptor- based models?" If we can already achieve thermoneutral surface binding sites, maybe the answer lies just beyond the surface in the secondary and outer substrate coordination spheres?

More than a century of metal-based molecular (homogeneous) catalyst development highlighted the pivotal role of ligands in determining the chemical properties of a metal center, such as redox potential and metal-substrate BDFE.[9,45–48] It is also clear that the way ligands interact with substrate and solvent, through secondary and outer-coordination sphere effects, have a dramatic influence on the rate of catalytic turnover and product selectivity.[49–52] We propose hybrid inorganic nanomaterials with tailor-made organic surface ligands could offer a strategy to translate the lessons learned in molecular systems to nanoparticles and represent a vast and underexplored parameter space in heterogeneous electrocatalysis.[53–55]

Previous studies from our laboratory have demonstrated the importance of the interface between heterogeneous nanoparticle surfaces and the bulk solvent.[56,57] Through this work, for instance, we found that the predominant reason long chain aliphatic ligands hinder catalytic activity in aqueous media is because of the poor interface formed between the non-polar surface and the polar electrolyte. Just as aliphatic ligands make a poor interface with polar solvents, it has been shown that polar ligands that are able to hydrogen bond with a polar solvent can induce some degree of

local order near the surface of a nanoparticle.[58] We also know that surface ligands are able to shift the Fermi level of a nanomaterial based on their electron withdrawing/donating ability by inducing or enhancing the surface dipole.[59–61] These isolated studies provide, in concert, a road map to tune a variety of catalytically relevant parameters in heterogenous nanoparticle catalysts.

In colloidal nanoparticle systems, ligand chemistry is most commonly explored using dative Lewis acid/base interactions between surface metal cation sites and electron rich binding groups such as amines, carboxylates, and phosphonates.[62,63] Well understood mechanisms for ligand exchange have been developed based on concentration gradients, salt metathesis, and displacement by higher binding affinity head groups.[64–70] Unfortunately, the same chemical principles that make these ligand exchange reactions viable also make them unstable in catalytically relevant conditions. Especially the strong acid conditions, typically 0.5 M sulfuric acid, required for HER lead to the protonation and desorption of such ligands.

Thus, to explore the influence that ligand surface chemistry can have in altering the catalytic activity and stability of colloidal nanoparticles, we must first establish synthetic methods to create more robust nanoparticle-ligand bonds. One such method that has been explored in the literature is the covalent functionalization of surfaces by substituted aryldiazonium salts. Diazonium salts are a diverse class of organic reagents that have been shown to form covalent bonds with electron-rich surfaces.[71–76] Specifically, Saveant showed decades ago that these reagents could functionalize the surface of glassy carbon electrodes and that these functional groups were stable to physical abrasion and electrochemical cycling.[77] More recently, diazonium reactivity has been explored with two-dimensional materials, namely MoS_2 nanosheets.[78,79] Miller and co-workers explored the effects of covalent surface functionalization on the catalytic activity of MoS_2 for HER and found strong correlations between the functional group Hammett parameter, MoS_2 electronic structure,

and overpotential for HER.[61] Though this chemistry has never been explored on colloidal heteroatomic nanoparticles, specifically transition metal phosphides, there is precedent for the approach being viable for P-functionalization based on studies on phosphorene.[78,80]

Herein, we explore the synthetic conditions required to make a well-defined covalent ligand shell on the surface of colloidally synthesized Ni2P nanocrystals. The effects of substituted aryl ligands on electronic structure, catalytic activity, and stability are presented using a combination of spectroscopic, electrochemical measurements, and density functional theory (DFT) calculations. Finally, synthetic challenges and design principles for future development of colloidal nanocrystal electrocatalysts are presented.

3.3 Experimental Details

2-propanol (anhydrous, 99.5%), triethyloxonium tetrafluoroborate (≥97.0%, Meerwein's reagent), acetonitrile (anhydrous, 99.8%,), chloroform (anhydrous, ≥99), 4-nitrobenzenediazonium tetra fluoroborate (97%), 4-methoxybenezenediazonium tetrafluoroborate (98%), 3,5-dichlorobenzenediazonium tetrafluoroborate, and bi(cyclopentyldienyl)cobalt(II) were all purchase from Millipore-Sigma, stored in a nitrogen atmosphere glovebox, and used without further purification. Diazonium salts and Meerwein's reagent were stored at -20 °C in a glovebox freezer. *Tris*-diethylaminophosphine (97%, Millipore-Sigma) was stored in ambient conditions and used as received. Nickel (II) chloride (98%, Millipore-Sigma) was dried at 100 °C under vacuum overnight before being stored in a nitrogen glovebox until use. Oleylamine (technical grade, 90%), was dried over CaH_2, distilled, and stored over 4 Å sieves in a nitrogen glovebox.

3.3.1 *Synthetic Details*

Ni_2P nanocrystals were synthesized using air-free Schlenk techniques under an N_2 atmosphere. Glassware, including a 100 mL three neck round bottom flask (RBF), two condensing columns (used without flowing water), a hose adapter, glass thermal well, Teflon magnetic stir bar, 100 mL Schlenk flash, canula needle, and 14/20 ground glass stopper were all dried in the oven at 160 °C overnight prior to use. The next day, the reaction vessel was assembled on top of a heating mantle and connected to the Schlenk line, evacuated, and refilled with dry N_2. In an N_2 glovebox, 944 mg (7.2 mmol) of $NiCl_2$ was measured. $NiCl_2$ was quickly transferred out of the glovebox and added to the reaction vessel. The vessel was purged with high vacuum/N_2 flushes three times. 48 mL (146 mmol or 20 mol eq. relative to Ni) of oleylamine was added to the reaction vessel under an N_2 atmosphere through a rubber stopper. The mixture of $NiCl_2$ and oleylamine was heated to 120 °C and vigorously stirred under vacuum for 60 min to remove trace O_2/H_2O and volatile organic contaminants. The vessel was wrapped in glass wool to promote uniform heating. The reaction temperature was measured by an internal probe, submerged in the reaction vessel through contact with a glass thermal well. After 60 min, the reaction mixture was cooled to ~50 °C. 8 mL (28.8 mmol or 4 mol eq. relative to Ni) *tris*-diethylaminophosphine was injected through the rubber stopper. The reaction vessel was then heated to 250 °C at a ramp rate of roughly 10 °C min-1 and held for 60 min. After about 12 min, at 178 °C, a red hue was observed. The solution quickly became black as the temperature climbed above 200 °C. At this point vapors were observed in the vessel. After 1 hour at 250 °C the vessel was lifted from the heating mantle and the glass wool was removed, allowing the solution to cool.

As the solution cooled, an oven dried Schlenk flask was attached to the Schlenk line and purged with three flushes of vacuum/N_2 and finally held under N_2 flow. Once the reaction mixture reached

~80 °C it was transferred to the Schlenk flash *via* canula. The Schlenk flask was then sealed with a greased ground glass stopper which was fastened with electrical tape and brought into the glovebox. The reaction mixture was separated into 6 individual 45 mL Falcon tubes, diluted with 2x volume of 2-propanol, and centrifuged at 7.83 kRPM for 15 min. This was repeated until the supernatant for all tubes was clear. The nanocrystals were redispersed in minimal pentane and diluted with 10x volume of 2-propanol before centrifugation at 7.83 kRPM for 15min. This process was repeated three times, and then another three times using a toluene solvent/acetonitrile antisolvent (1:10) mixture. Finally, the cleaned product was dissolved in minimal chloroform and transferred to a tared 20 mL scintillation vial. Once the solvent was removed by vacuum the product appeared as a free-flowing black powder. 842 mg of Ni_2P was recovered.

3.3.2 *Ligand Stripping Details*

The treatment of Ni_2P with Meerwein's salt was carried out in a 250 mL round bottom flask that was dried a 160 °C overnight before use. 100 mg of Ni_2P was dissolved in 40 mL of toluene and 1.425 g of Meerwein's salt was dissolved in 50 mL of acetonitrile (0.1 M and 50 mol eq. relative to oleylamine, assuming it accounts for 20% of the Ni_2P sample mass). These solutions were mixed and stirred vigorously for a few minutes to make a homogeneous dark black solution, then left still overnight. The next day a black precipitate was observed at the bottom of the flask. The clear solution was poured off, and the black powder was collected by addition of minimal fresh acetonitrile. Stripped particles, Ni_2Ps, were then moved to a 45 mL Falcon tube where another 10 mL of acetonitrile was added. The sample was centrifuged at 7.83 kRPM for 15 min, resulting in a clear supernatant that was decanted. This process was repeated twice more. Washed Ni_2Ps was then transferred to a tared 20 mL scintillation vial as a solution in toluene, and then dried by vacuum.

3.3.3 *Estimation of Ni and P Atoms in Sample*

To estimate the concentration of Ni and P atoms in a single particle we model our system from the information made available by the materials project with the following assumptions that the Ni_2P unit cell is 100 $Å^3$, the particles are perfect spheres, and all particles are 5 nm in diameter. Number of atoms per unit cell are 6 Ni and 3 P (Figure 3.1).

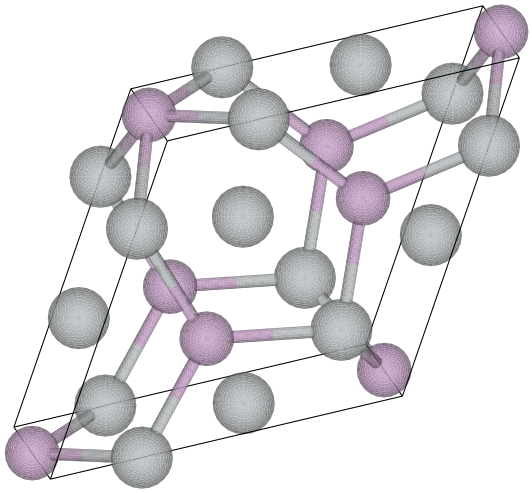

Figure 3.1. Hexagonal Ni_2P unit cell.

The volume of each nanocrystal can be calculated according to equation 3.1:

$$V = \frac{4}{3}\pi r^3 = \frac{4}{3}\pi 25Å^3 = 6.54 \times 10^4 Å^3 \tag{3.12}$$

Thus, the number of unit cells per nanocrystal can be calculated according to equation 3.2:

$$\frac{6.54\times10^4 Å^3}{\left(\frac{100Å^3}{UC}\right)} = 654\ UC \tag{3.13}$$

And then the number of atoms per nanocrystal can be estimated according to equation 3.3 an 3.4:

$$\left(\frac{654\ UC}{NC}\right)\left(\frac{6\ Ni\ atom}{UC}\right)\left(\frac{1\ mol}{6.022\times10^{23}\ atom}\right)\left(\frac{1000\ mmol}{1\ mol}\right) = \frac{6.516\times10^{-22}\ mmol\ Ni}{NC} \tag{3.14}$$

$$\left(\frac{654\ UC}{NC}\right)\left(\frac{3\ P\ atom}{UC}\right)\left(\frac{1\ mol}{6.022\times10^{23}\ atom}\right)\left(\frac{1000\ mmol}{1\ mol}\right) = \frac{3.258\times10^{-18}\ mmol\ P}{NC} \tag{3.15}$$

To find the mass of each particle, we find the mass of Ni and P first (equations 3.5 and 3.6) and then find the sum in equation 3.7:

$$\left(\frac{6\ Ni\ atom}{UC}\right)\left(\frac{1\ mol}{6.022\times10^{23}\ atom}\right)\left(\frac{58.693\ g}{mol}\right) = \frac{5.847\times10^{-22} g\ Ni}{UC} \tag{3.16}$$

$$\left(\frac{3\ P\ atom}{UC}\right)\left(\frac{1\ mol}{6.022\times10^{23}\ atom}\right)\left(\frac{30.974\ g}{mol}\right) = \frac{1.543\times10^{-22} g\ P}{UC} \tag{3.17}$$

$$\left(\frac{(5.847\ g+1.543\ g)10^{-22}}{UC}\right)\left(\frac{654\ UC}{NC}\right) = \frac{4.833\times10^{-19} g}{NC} \tag{3.18}$$

And finally we can find the molar concentration of Ni and P per mass of nanocrystalline sample though equations 3.8 and 3.9:

$$\left(\frac{6.516\times10^{-18} mmol\ Ni}{4.833\times10^{-19} g}\right) = 13.48\ {}^{mmol\ Ni}/_{g} \tag{3.19}$$

$$\left(\frac{3.258\times10^{-18} mmol\ P}{4.833\times10^{-19} g}\right) = 6.74\ {}^{mmol\ P}/_{g} \tag{3.20}$$

3.3.4 *Covalent Functionalization Details*

Surface functionalization reactions were carried out in an N_2 glovebox in 20 mL scintillation vials that were oven dried overnight at 160 °C before use. 40 mg of Ni_2Ps (when corrected for 15 mass% oleylamine, this translates to 34 mg Ni_2P or 0.229 mmol P) was dissolved in 10 mL of chloroform and added to a 20 mL scintillation vial with a Teflon stir bar and set to stir at 700 RPM. While stirring, in the cases that a chemical reductant was added, 0.115 mmol (2 mol eq. to surface P) of the reducing agent (bi(cyclopentyldienyl)cobalt(II) or cobaltocene) was measured and added to the chloroform solution. Then, 0.115 mmol (2 mol eq. to surface P) of the respective diazonium salt was weighed out and dissolved in 10 mL of acetonitrile. The diazonium solution was added to the vial of stirring Ni_2Ps in a slow, dropwise manner. The effervescence of N_2 in the form of small bubbles was observed after addition of the diazonium, signaling the initiation of radical formation. Solutions were allowed to stir while lightly capped for 48 hours. For purifying the functionalized

nanocrystals, the solvent was first removed under vacuum. Once dried, 5 mL of clean acetonitrile was added to the residue and shaken to disperse. This solution was transferred to a 45 mL Falcon tube and centrifuged at 5 kRPM for 10 min. The supernatant, which had a faint yellow color, was either discarded or collected for analysis. Washing and centrifugation using fresh acetonitrile was repeated 3 more times. Samples were then dissolved in minimal chloroform, transferred to tared 20 mL scintillation vials, and pumped down to a fine, free flowing, black powder.

3.3.5 *Characterization Details*

Powder X-ray diffraction (XRD) data was collected on a Bruker Microfocus instrument. Powder XRD samples were prepared by drop-casting a solution of Ni_2P onto silicon single crystal wafers. Diffuse reflectance infrared Fourier transform spectroscopy (DRIFTS) was collected on a Bruker Alpha IR instrument. Samples were prepared by grinding the Ni_2P together with FT-IR grade potassium bromide (KBr, >99%; Alfa Aesar) using an agate mortar and pestle. Background measurements were taken with a golden puck. ^{1}H and ^{31}P spectra were recorded on Bruker AV300 and Bruker AV500 spectrometers, respectively. Deuterated chloroform ($CDCl_3$) and acetonitrile (CD_3CN) were purchased from Cambridge isotope labs and dried over calcium hydride, vacuum-transferred, and stored over 4 Å sieves in a N_2 glovebox. $CDCl_3$ contained a 1% internal standard of tetramethyl silane. ^{31}P spectra were corrected to an 85% phosphoric acid standard in water. X-ray photoelectron spectroscopy (XPS) was conducted on a Kratos AXIS Ultra DLD. Pass energy for survey spectra (to calculate composition) was 150 eV. Data point spacing was 1.0 eV per step for survey spectra, and 0.4 eV per step for detailed spectra. Pass energy for high-resolution spectra was 50 eV, with a data point spacing of 0.065 eV. All spectra were calibrated to align carbon peak intensities at 284.8 eV. Ultraviolet photoelectron spectroscopy (UPS) was also conducted on a Kratos AXIS Ultra DLD. The UV source was a He(I) lamp with photon energy of 21.2 eV. Pass

energy was 5 eV with a step size of 0.01 eV. Aperture (spot) size was 100 mm. Take off angle was 0 degrees, and the stage was biased by a 9V battery while collecting data. All spectra were corrected to a sputter cleaned gold sample's fermi edge at 0 eV. Transmission electron microscopy (TEM) images were collected on an FEI Tecnai G2 F20 microscope. Samples were drop cast from toluene onto lacey carbon grids and vacuum dried overnight. Scanning electron microscopy (SEM) images were collected on a ThermoFisher Scientific Apreo Variable Pressure SEM with integrated energy dispersive x-ray spectrometer (EDS) from Oxford. Elemental quantification was carried out using a Perkin Elmer Optima 8300 Inductively Coupled Plasma-Optical Emission Spectrophotometer (ICP-OES). Thermogravimetric Analysis (TGA) measurements experiments were carried out using a TA Instruments TGA Q5000. ~10 mg of material was loaded onto an aluminum pan at ambient conditions, then raised to 500 °C at a ramp rate of 10 °C/min under N_2 with a flow rate of 25 mL/min. All electrochemical measurements were performed with a Gamry Interface 1000. Measurements were conducted under Ar flow in 0.5M H_2SO_4 with 18 MΩ Millipore water in a custom four-neck cell fitted with a graphite rod counter electrode separated in a fritted compartment, a Ag/Ag_2SO_4 reference electrode separated by a Vycor frit, and a glassy carbon working electrode. A desired volume of a known mass% solution was drop cast onto the glassy carbon electrode to disperse the catalyst. Glassy carbon electrodes were consecutively polished with 5, 1, and 0.05 mm alumina paste and sonicated/washed with 18 MΩ Millipore water prior to use.

3.3.6 *DFT Calculations*

Spin-polarized DFT calculations were carried out using the Quantum ESPRESSO[81] package (v6.5). Exchange-correlation effects are described using the Perdew−Burke−Ernzerhof (PBE) functional[82] along with the semi-empirical Grimme's D2 van der Waals (vdW) corrections.[83] The

bonding environment of each system is described under the projector augmented wave method (PAW)[84]. The expansion of valence wave functions has been accounted for with a plane wave cut-off energy of 680 eV. All simulations used a 3x3x1 Γ-centered Monkhorst-Pack[85] k-point integration of the Brillouin zone. Surface reactions are modelled using an 8-layer periodically repeated hexagonal supercell (11.8 Å x 11.8 Å x 41.6 Å) belonging to the $P\bar{6}2m$ space group to model the coverage effect of surface adsorbates. A 25 Å vacuum space was employed to prevent spurious interactions between the periodically repeated images. Atomic coordinates were relaxed using the Broyden–Fletcher–Goldfarb–Shanno[86] (BFGS) algorithm until the Hellmann-Feynman forces on all relaxed atoms fell below 0.05 eV/Å. For geometry optimization the electron occupancies were determined by the Gaussian smearing method with a smearing value of 0.07 eV, while for accurate total energy and partial density of states analysis we adopt the optimized tetrahedron method.[87] Due to the relatively large system sizes in this study (144-204 atoms), only the top two layers are relaxed, with the bottom 6 layers remaining fixed to that of the bulk values. Preliminary analysis indicated that $C_6H_4NO_2$ preferentially binds to the P top site with high coordination Ni and P sites being disfavored in terms of total energy (See SI for more details). The $Ni_2P(0001)$ slab with the Ni_3P_2 surface termination was chosen for three main reasons: (i) it closely resembles the experimental synthesis which has an observed stoichiometry of ($Ni_{1.78}P$), (ii) it is known to be stable under the electrochemical conditions relevant in this study[41] and (iii) it provides a point of reference with the current published literature.

3.4 Results and Discussion

3.4.1 *Nickel Phosphide Synthesis and Characterization*

Nickel phosphide nanocrystals were prepared using a modified literature procedure.[20] Briefly, nickel(II) chloride was mixed with tris(diethylamino)phosphine in neat oleylamine. After heating to 250 °C for 60 min, phase pure Ni_2P nanocrystals with an average diameter of 5 nm (Figure 3.2C) were recovered from a viscous black reaction mixture after successive rounds of precipitation, centrifugation at 7830 RPM, and redissolution with isopropanol/pentane followed by toluene/acetonitrile. TEM images reveal an approximately spherical morphology with an average diameter of 5 nm ± 0.9 nm (Figure 3.2A). The powder XRD pattern is in agreement with the reported reference powder pattern (PDF 01-074-1385). (Figure 3.2B).

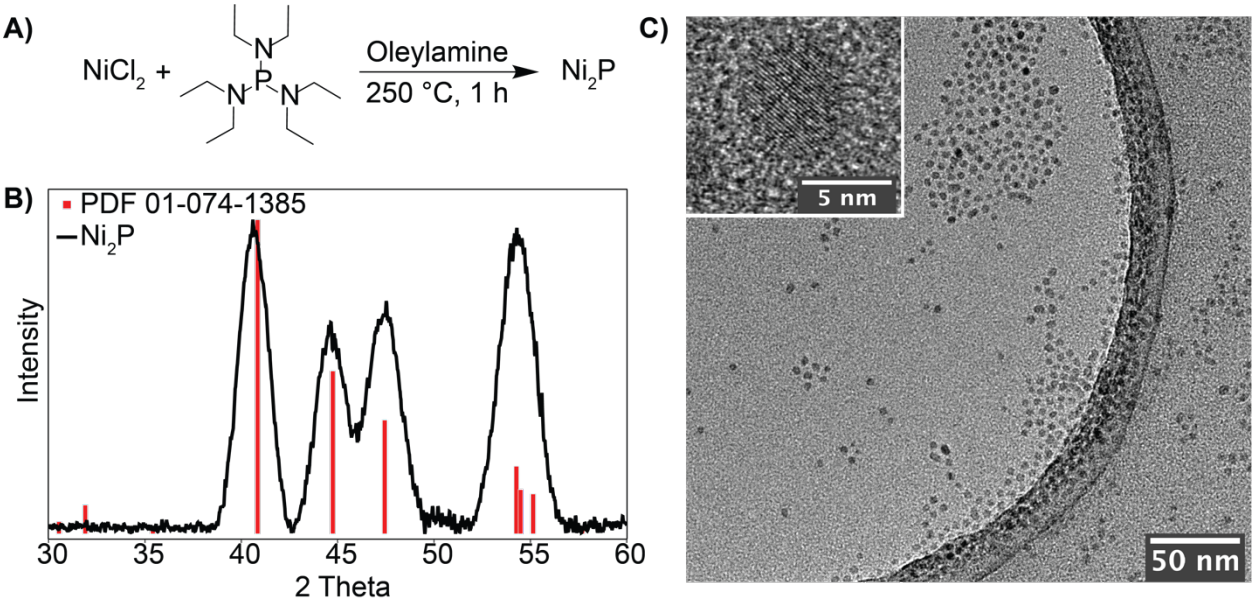

Figure 3.2. A) General reaction scheme for the synthesis of Ni2P nanocrystals with aminophosphines. B) XRD of Ni2P nanocrystals references against powder pattern (PDF 01-074-1385). C) TEM of Ni2P product, showing 5 ± 0.9 nm spherical nanocrystals. Inset shows a single nanocrystal with a 5 nm scale bar for reference. Full image reflects a larger sample set of nanocrystals all reflecting similar sizes and morphologies with a 50 nm scale bar for reference.

Scherrer analysis reflects an average crystalline domain size of 5.18 nm, consistent with the TEM analysis. ICP-OES reveals a composition that is phosphorous rich, with an average stoichiometry of $Ni_{1.78}P$. This is a notable departure from the cation rich nature of more ionic nanomaterials synthesized with aminophosphine precursors, namely InP.[88,89] We believe this composition is reflective of the inorganic nanocrystal core composition since there was no trace of excess molecular precursor or phosphonium salt byproduct found by NMR or FTIR spectroscopy of the purified end material (Figure 3.3 and 3.6).

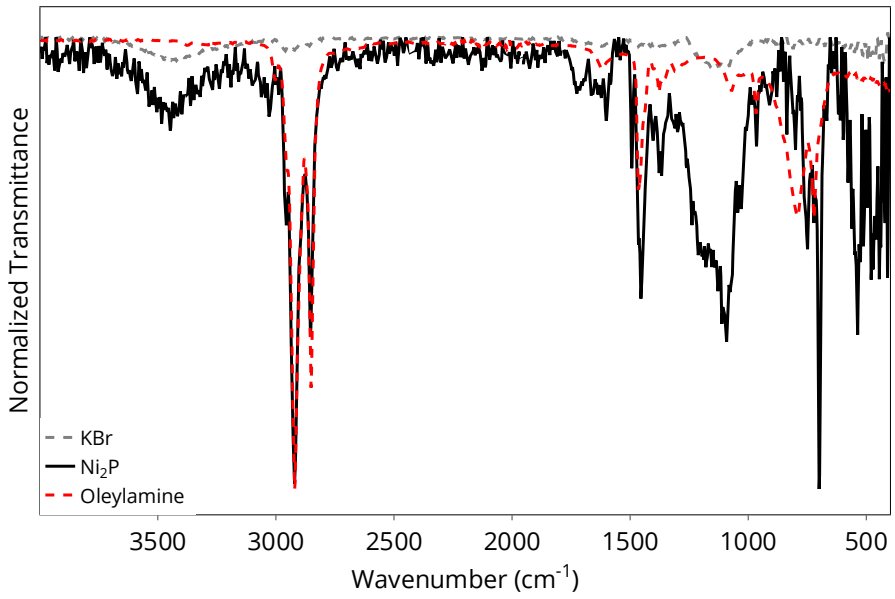

Figure 3.3. DRIFTS spectrum of Ni_2P (black) powder against the KBr matrix (grey) control and neat oleylamine (red).

Analysis by diffuse reflectance infrared Fourier transform spectroscopy (DRIFTS) and ^1H NMR spectroscopy supports a ligand shell composed of oleylamine (Figure 3.3). The IR spectra showed signatures of long-chain aliphatic hydrocarbons at 1,450, 2,850, and 2,920 cm^{-1}, as well as the expected alkene resonances at 1,600 and 3,000 cm^{-1}.[90,91] ^1H NMR spectra show resonances associated with aliphatic protons in the range of 1-2 ppm and the alkene protons at 5.3 ppm.[92] Further, the broadness of these peaks is indicative of the long relaxation times expected for

molecules bound to a nanoparticle surface.[65,93] Though previous reports of nanocrystals prepared using combinations of metal halide salts and aminophosphine precursors show evidence of a mixed ligand shell comprised of both amine and chloride ions, no evidence of Cl atoms are observed in the XPS survey spectrum (Figure 3.4).[89]

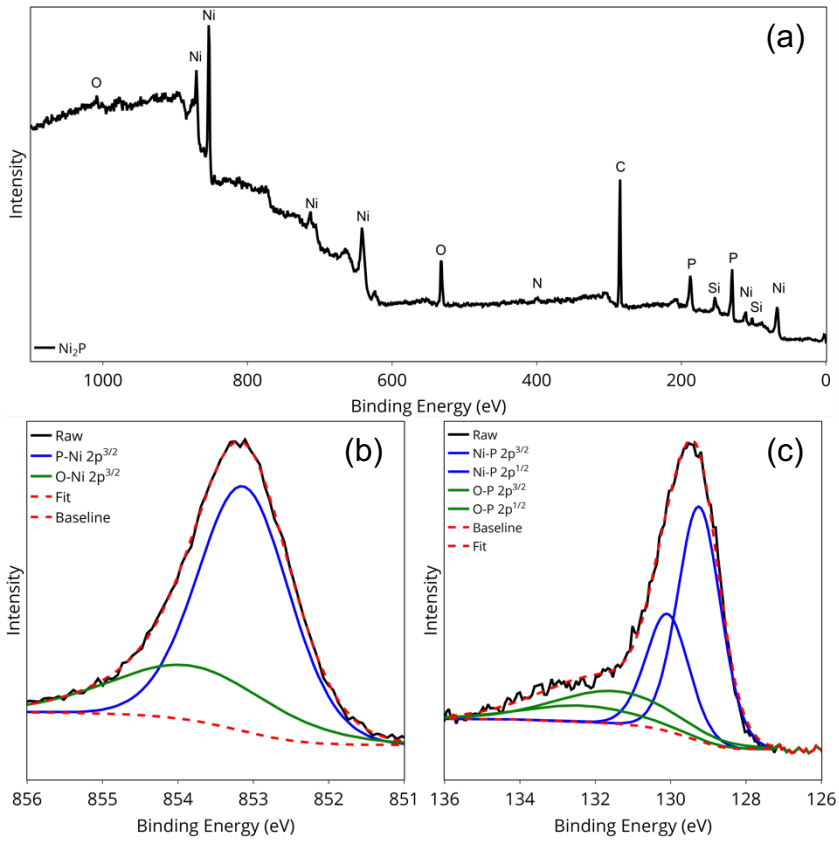

Figure 3.4. (a) Survey XPS spectrum of Ni2P film deposited on Si substrate. (b) Ni 2p3/2 spectrum showing a major Ni environment centered at 853.3 eV (72%), reflective of the metal phosphide environment. The higher energy species (853.5 eV, 28%) is like surface oxide. (c) P 2p high resolution XPS spectrum showing majority composition belonging to the metal phosphide environment (129.2 eV, 72%). The higher oxidation state species encompassed by the broad peak centered at 131.5 eV (28%) are likely surface phosphate species.

Further, thermogravimetric analysis suggests that the surface ligands compose 19% of the sample by mass (Figure 3.5). The first derivative of mass loss for this sample shows a peak at ~350 °C, matching closely with the boiling point of neat oleylamine (365 °C).

High resolution XPS analysis of the Ni and P 2p electron binding energies are consistent with a covalent metal-phosphide material.[38,28] The P 2p spectrum (Figure 3.4C) shows a spin-orbit doublet with the center of the parent peak located at 129 eV consistent with P in the 0 oxidation state and representing 72% of the total P in the sample. A higher energy shoulder centered at 131.5 eV was fit to a broad doublet peak, representing what is likely multiple ill-defined higher oxidation state P components within the material. This species comes at a slightly lower binding energy than is expected of phosphate salts (132.5 eV), which leads us to believe it is likely a partially oxidized surface site.[94] Similarly, the Ni 2p spectrum (Figure 3.4B) shows an unusual Ni binding energy of 853 eV, which lies in-between that of Ni^0 and Ni^{2+} (852 eV and 854 eV, respectively).[95] This result is indicative of the relatively high amount of electron density that remains on the Ni sites within the phosphide lattice. The $2p_{3/2}$ environment can be deconvoluted into two contributions. The first being the metal-phosphide species centered at 853 eV which represents 72% of the sample. The second, centered at 853.5 eV, accounts for 28% of the sample and is likely the slightly reduced surface oxide, similar to that observed in the P 2p spectrum.

3.4.2 *Ligand Stripping*

Prior to covalent functionalization of Ni_2P, the concentration of native oleylamine ligands was reduced *via* alkylation using Meerwein's salt. Alkylation is a widely used method for the removal of common ligands including oleylamine, oleate, and phosphate species.[96,97] Typically, ligand stripping procedures for colloidally dispersed nanoparticles consist of preparing a biphasic solution where the non-polar phase contains the native nanocrystals dissolved in hexanes and the polar phase is a solution of Meerwein's salt in acetonitrile or DMF. Vortex mixing leads to rapid precipitation of the nanocrystals from solution. The recovered nanocrystals can be washed to remove residual aliphatic ligands before the particles are able to be resuspended by solvents with

weak binding affinities such as DMF. In the most successful examples, complete loss of aliphatic C-H vibrations in FTIR spectra coupled with elemental analysis showing a lower concentration of C atoms are observed.[96,98] Interestingly, this method of ligand stripping was not as efficient in the case of the oleylamine-ligated Ni_2P nanocrystals studied here. Following synthesis and purification, the Ni_2P nanocrystals showed only sparing solubility in hexanes, limiting our ability to directly use the procedure as previously reported. Additionally, vortex mixing the biphasic solution resulted in formation of a highly viscous gel. Ultimately, the ligand exchange was accomplished using a homogenous solution of the nanocrystals (5 mg/mL) in toluene with a large excess of Meerwein's salt (50 mol equiv. vs oleylamine) in acetonitrile. This solution was mixed vigorously for several minutes in a round bottom flask and left to sit overnight, resulting in the formation of a black precipitate. The supernatant was decanted, and the resulting nanocrystal powder was dissolved in toluene and subjected to repeated rounds of precipitation and redissolution from acetonitrile.

The Meerwein's salt-treated nanocrystals were characterized by TGA, IR, and NMR spectroscopy (Figure 3.5, 3.6). These data suggest that roughly 30% of the initial oleylamine surface ligands were removed. However, oleylamine still accounted for 15% of the sample by mass, and signature spectroscopic features were still observed in the DRIFTS and ^{1}H NMR spectra. We do note that changes in the ^{31}P NMR spectra suggest that alkylation is an effective method to remove the surface phosphate species that formed from ambient oxidation. Successive alkylation treatments had limited added effect and we have not managed to realize complete ligand removal in this system (Figure 3.5), suggesting that the starting nanocrystals have a range of amine binding energies and that only the weakest bound subset can be removed using this method.

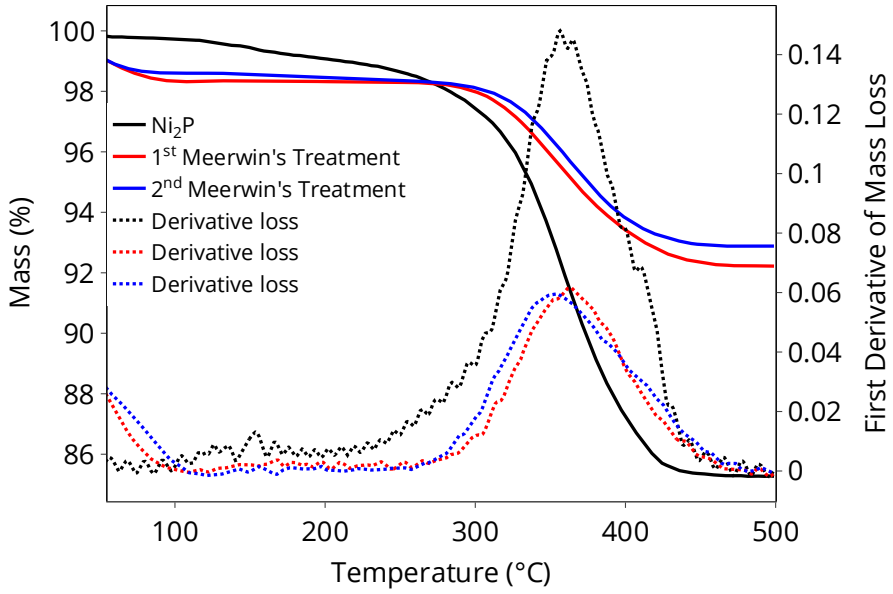

Figure 3.5. TGA trace of as-synthesized Ni_2P (black), Ni_2P treated with once with Meerwein's salt (blue), and Ni_2P treated twice with Meerwein's salt (red). Black trace corresponds to 15% mass loss. Red trace corresponds to 8.2% mass loss. Blue trace corresponds to 8.8% mass loss.

This result stands in contrast to earlier examples of Meerwein's salt treatment of nanocrystals for ligand stripping, a fact that may be attributable to differences in the covalent bonding character of the Ni_2P. Early examples from Helms and co-workers showcased the method's efficacy on highly ionic materials such as CdSe, TiO_2, and ITO.[96] Later studies, however, have shown less consistent results. In a study from Suntivich *et al.* TGA suggested that alkylation did not remove all oleate ligands from the surface of Mn_3O_4 particles, despite the ionic nature of that lattice.[97] In contrast, a recent paper from Buonsanti *et al.* showed complete removal of native phosphate and tri-alkylamine ligands from the surface of Cu^0 nanospheres.[98]

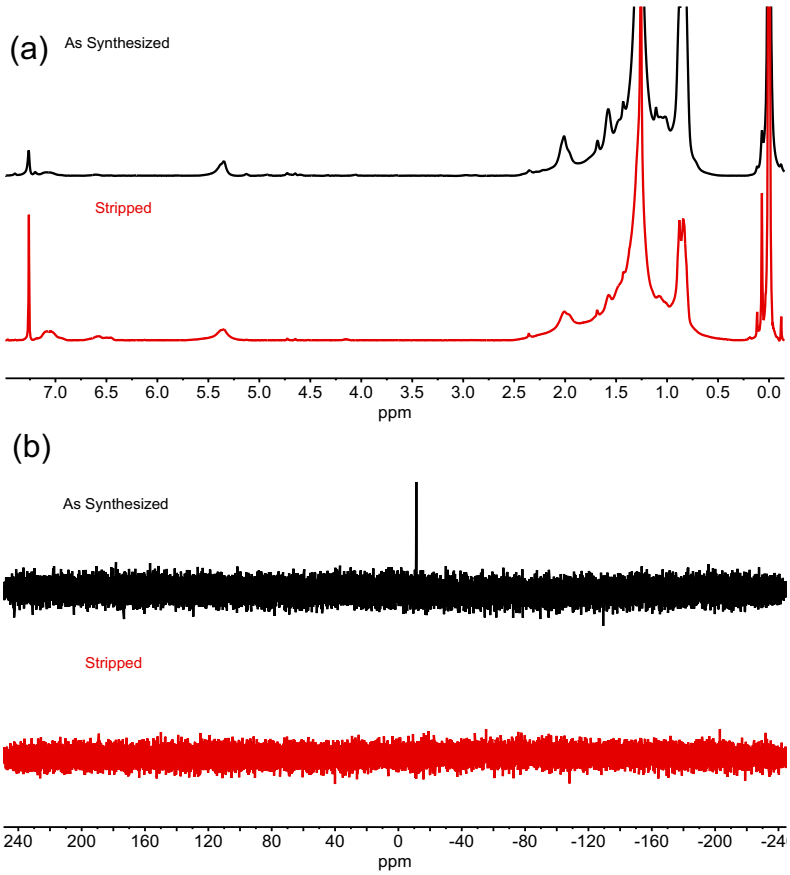

Figure 3.6. ^{1}H (a) and ^{31}P (b) NMR of as synthesized and Meerwein's treated ("stripped") Ni_2P samples in $CDCl_3$ with tetramethylsilane internal standard (0 ppm). ^{1}H spectra show the retention of aliphatic protons in the 0.5-2.5 ppm range and the alkene protons at 5.3 ppm. These signals are much weaker after Meerwein's treatment, relative to the $CHCl_3$ (residual solvent) resonance at 7.2 ppm. ^{31}P spectra show the loss of surface phosphate species at -11 ppm.

3.4.3 *Covalent Functionalization*

To a chloroform solution of Meerwein's salt-treated Ni_2P nanocrystals (Ni_2Ps) a solution of diazonium salt in acetonitrile was added dropwise. A spontaneous reaction was indicated by effervescence as N_2 gas was released. In some instances, a toluene solution of cobaltocene was added dropwise prior to addition of diazonium. In either case, the solution was capped loosely and left to stir for 48 hours. The functionalized nanocrystals were purified by first removing the solvent

from the crude mixture under vacuum. Once the sample was dry, the powder was dispersed in acetonitrile by vigorous shaking or sonication, followed by multiple rounds of precipitation via centrifugation, removal of supernatant, and redissolution in acetonitrile to remove excess diazonium salt. Subsequent washes with isopropanol and/or pentane were performed to remove any aliphatic reaction co-products. After multiple washes, the particles remained highly soluble in chloroform and/or toluene. Solvent removal under vacuum resulted in a free-flowing black powder. We note that during initial washing steps the supernatant was observed to have a slightly yellow hue. Upon further investigation, we determined this side product was likely the result of reactivity between the diazonium ions and oleylamine. In fact, diazonium salts have been previously documented to act as ligand stripping reagents for colloidal quantum dots.[99] Though the authors did not speak much to the mechanism, they showed the loss of prominent aliphatic vibrations after treatment and the growth of a BF_4 signal – suggesting some sort of ion exchange reaction. We propose that the mechanism is likely much more complicated due to the complex reactivity of highly electrophilic diazonium ions and nucleophilic primary amines.[100] ^{1}H NMR spectra of oleylamine, 4-nitrobenezene diazonium tetrafluoroborate, and an equimolar mixture of the two can be found in the supporting information (Figure 3.7). We can observe large signal in the aliphatic region in the reaction supernatant which hints at some surface bound oleylamine reacting with added diazonium salt. The aromatic protons are not those of the parent diazonium salt (doublet at 8.67 and 8.78 ppm), but of some decomposition product that is observed to form over longer time periods. The side reaction seems to be influenced by the catalytically competent nanoparticles based on the variety of relatively intense signals between 3.4 and 4.9 ppm in the supernatant. None of these species are observed in appreciable quantity after purification, as shown below (Figure 3.8).

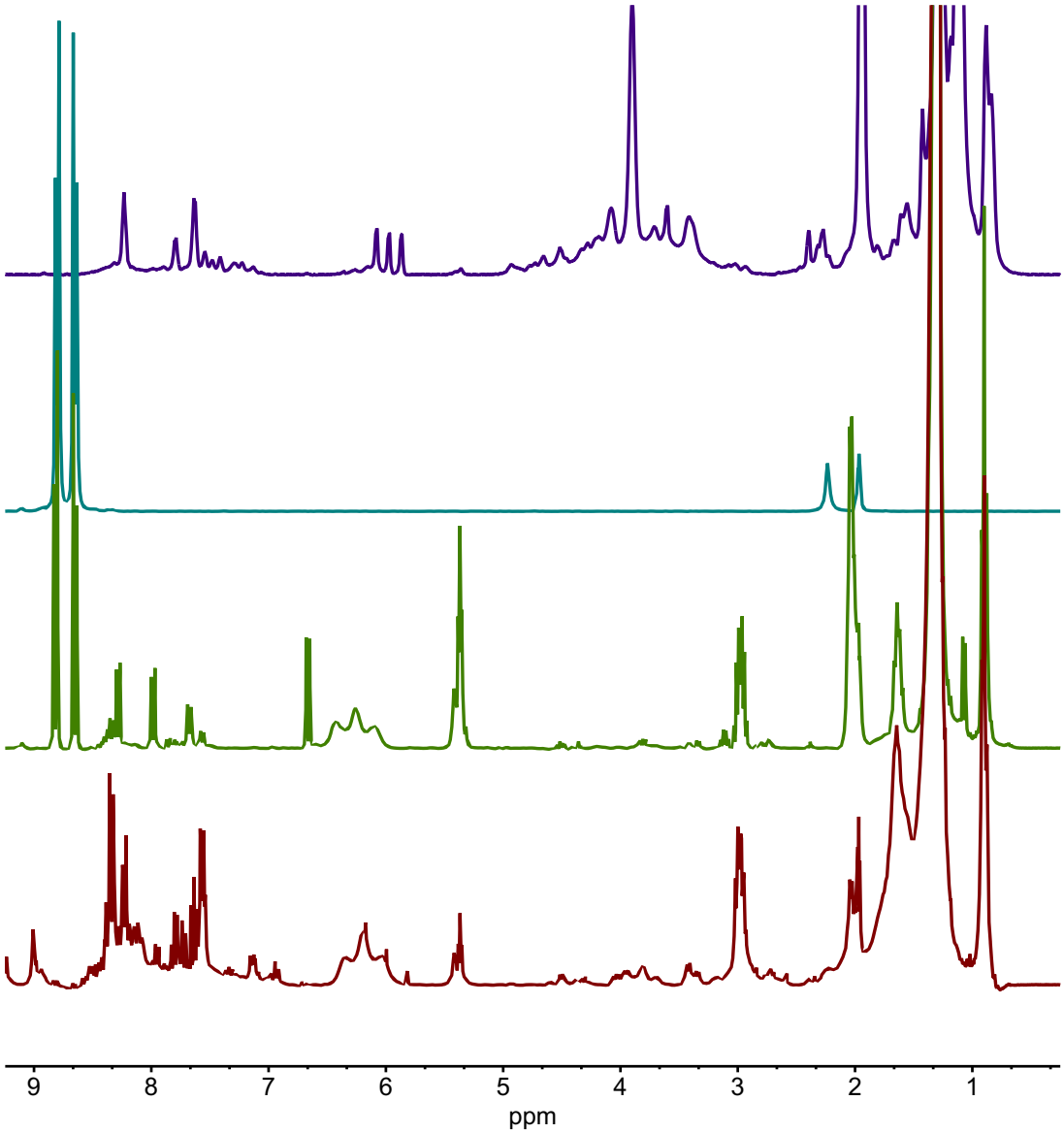

Figure 3.7. ^{1}H NMR spectrum of Ni_2P-$C_6H_4NO_2$ reaction supernatant (purple), 4-nitrobenzenediazonium tetrafluoroborate (teal), equimolar mixture of 4-nitrobenzenediazonium tetrafluoroborate and oleylamine taken shortly after mixing (green), and the same mixture taken after two days (maroon) in CD_3CN with a 300 MHz probe.

Here we can observe the degradation of the clean aryl doublets (8.8 and 8.6 ppm) found in the parent diazonium into a convolution of multiple aryl species that are more electron rich, as suggested by their downfield shift (spanning from 7.6 to 8.3 ppm). We also observe that the reaction continues to evolve over the course of two days, by which point the original aryl

resonances are no longer observed. We compare this control sample to the supernatant from our Ni_2P-$C_6H_4NO_2$ sample and observe many similar features, including the convoluted aryl signals and overwhelming aliphatic protons from the oleylamine.

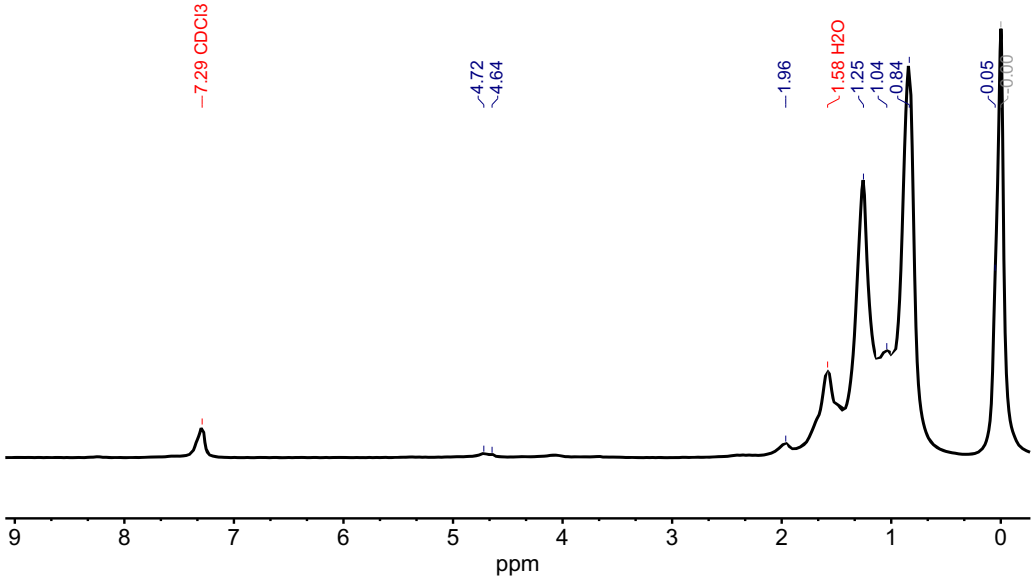

Figure 3.8. ^{1}H NMR spectrum of purified Ni_2P-$C_6H_4NO_2$ in $CDCl_3$ with a tretramathylsilane internal standard (0 ppm). Speciation is reminiscent of Meerwein's treated Ni_2P with a displaced, or possibly shifted, alkene resonance (peaks at 4.72 and 4.53 ppm). Side reaction species are not observed in any relevant concentrations, nor are signal from surface bound nitrobenzene groups.

A survey of early work studying the reactivity of diazonium ions lays out multiple paths of reactivity between these species, including nucleophilic attack at the beta-N, substitution at the C-2 and C-4 positions, heterolytic dediazoniations, and homomolecular coupling.[100] This wide array of possible products is even further muddied by the influence of catalytic nanoparticles that provide competing bonding affinities, reducing equivalents, and catalytically active surfaces that can alter the reaction landscape. Further, the comparison of reaction supernatant and control sample suggest the reaction products *are* different, or at least are formed in very different ratios. However, none of these spectral features are observed in the purified products (Figure 3.8)

suggesting that these species can be completely removed from the system by thorough washing and do not result in persistent contamination.

Evidence of spontaneous functionalization of the Ni_2P nanocrystals was provided by TGA and DRIFTS of the purified and dried nanocrystal powders. The DRIFTS spectra reflected a mixed ligand shell, composed of remnant oleylamine and substituted aryl groups. Importantly, when comparing the spectra of functionalized nanocrystals to the parent diazonium salt (Figures 3.9-3.13) we observed the absence of the N-N triple bond at ~2200 cm^{-1}. This is evidence that the nanocrystals were able to reduce the parent diazonium, cleaving the N_2-Ar bond. Further, this implies that the new spectral features observed in the fingerprint region are from surface bound functional groups rather than remnant/physiosorbed diazonium salt. Closer analysis of the features found in the fingerprint region show key vibrational modes associated with the specific functional groups expected in each sample, despite overlapping signal from oleylamine at ~1450 cm^{-1}.[90] In the Ni_2P-C_6H_4OMe sample, the Ar-O stretch at 1291 cm^{-1} as well as the O-CH_3 rocking mode at 1180 cm^{-1} were observed. An additional peak at 1493 cm^{-1} was attributed to aryl ring deformations induced by electron donating groups, thus only being observed in this sample. The peak observed from 1586-1590 cm^{-1} in each sample is another characteristic aryl ring deformation attributed to C=C-C stretches.[101] Characteristic symmetric and asymmetric N-O stretches were observed in the Ni_2P-$C_6H_4NO_2$ sample at 1513 and 1346 cm^{-1}, respectively. The in and out of plane NO scissor modes were difficult to resolve but could be observed at 856 and 724 cm^{-1}, respectively. Interestingly these values were shifted to slightly lower frequencies than those of the parent diazonium salt, implying that the nanoparticle surface is acting as an electron donor, weakening the N-O bond.[102] We note that all of the observed vibrational frequencies in our sample are in agreement with those previously reported in the functionalization of MoS_2 by aryl diazonium salts,

implying the distortion of bond energies *via* electronic effects from the underlying material is a common theme.[61,103]

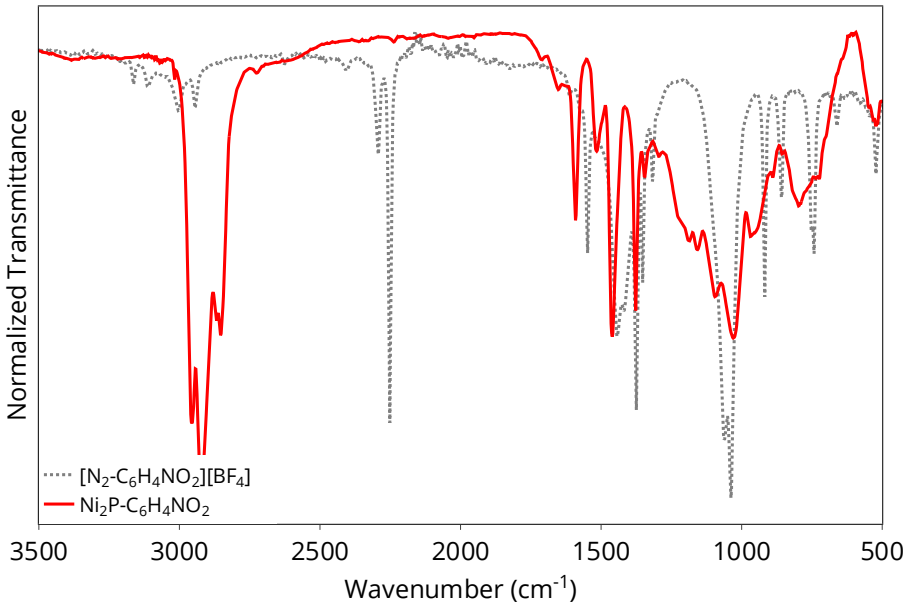

Figure 3.9. DRIFTS spectrum of purified Ni_2P-$C_6H_4NO_2$ (red) and 4-nitrobenzenediazonium tetrafluoroborate (grey) in KBr. Notable differences include aliphatic vibrations still present in Ni_2P-$C_6H_4NO_2$ and the loss of N≡N mode at 2,250 cm^{-1}.

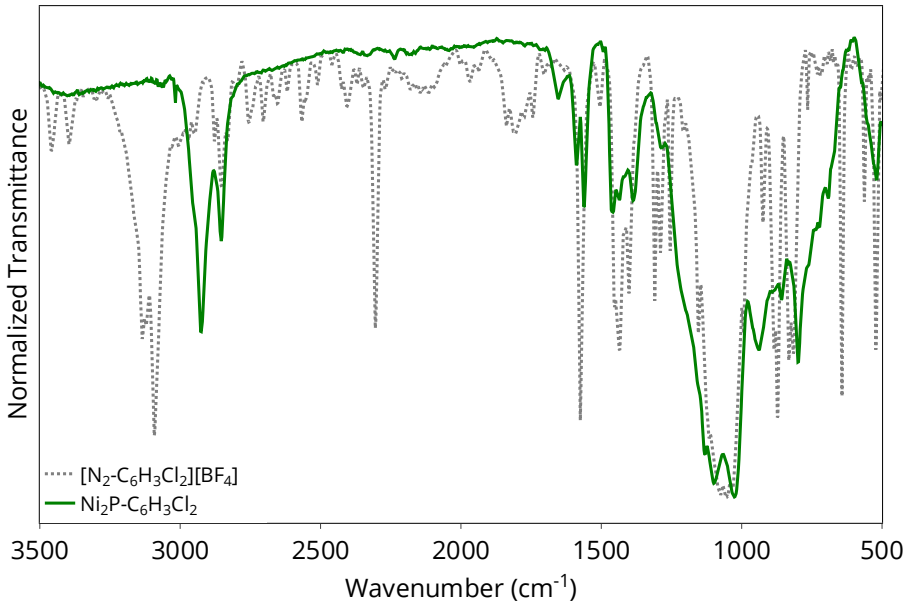

Figure 3.10. DRIFTS spectrum of purified Ni_2P-$C_6H_3Cl_2$ (green) and 3,5-dichlorobenzenediazonium tetrafluoroborate (grey) in KBr. Notable differences include aliphatic vibrations still present in Ni_2P-$C_6H_3Cl_2$ and the loss of N≡N mode at 2,304 cm^{-1}.

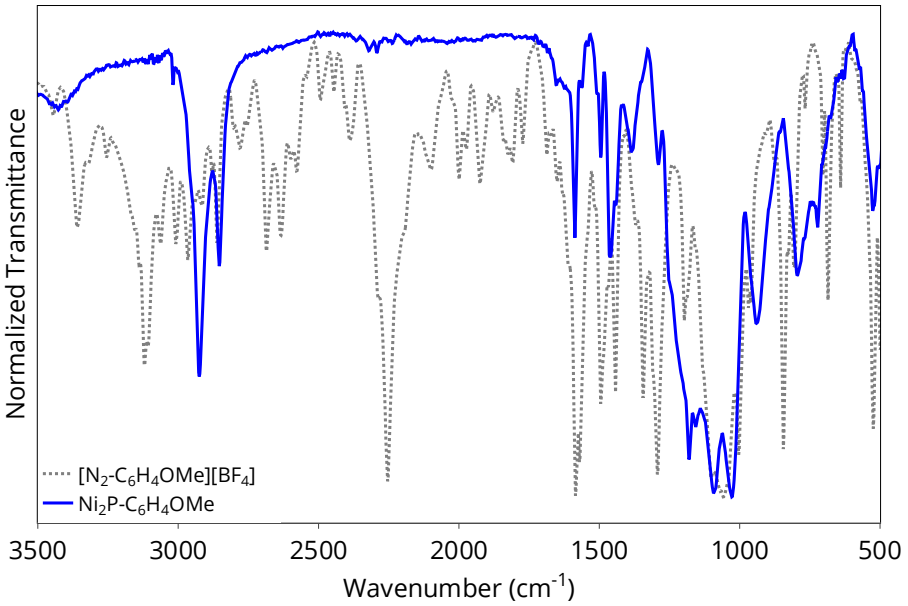

Figure 3.11. DRIFTS spectrum of purified Ni_2P-C_6H_4OMe (blue) and 4-methoxybenzenediazonium tetrafluoroborate (grey) in KBr. Notable differences include aliphatic vibrations still present in Ni_2P-C_6H_4OMe and the loss of N≡N mode at 2,254 cm^{-1}.

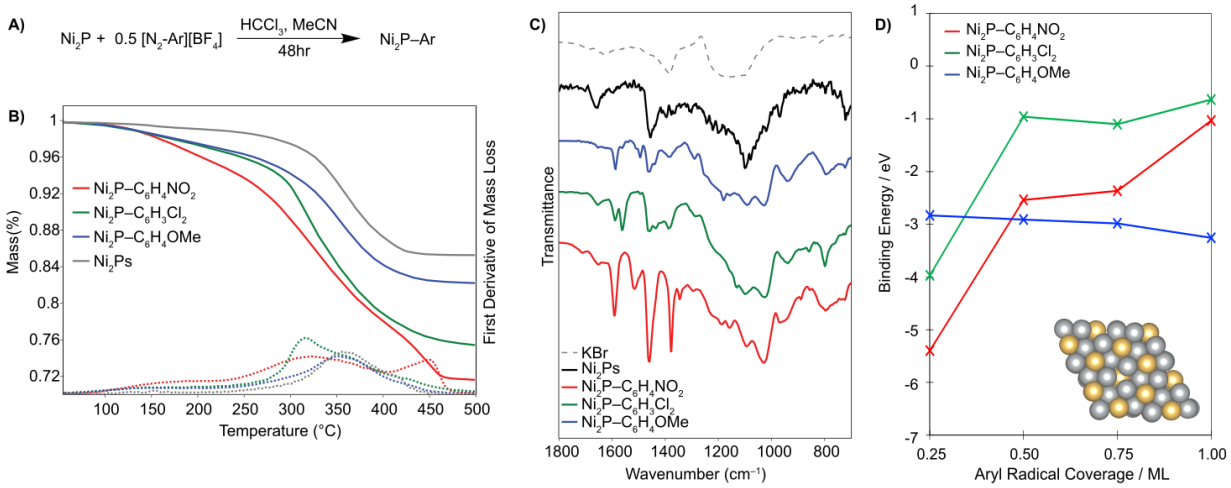

Figure 3.12. A) General reaction scheme for spontaneous functionalization of Meerwein's treated Ni_2P nanocrystals with substituted aryldiazonium salts. B) DRIFTS spectrum of

nanocrystals dispersed in KBr matrix. Diagnostic peaks are discussed in the main text. C) TGA trace of nanocrystals heated to 500 °C at 10 °C/min. Solid lines represent percent mass loss relative to the initial sample mass. Dotted lines show the first derivative of the mass loss curve, describing temperature ranges with sharper mass losses. D) DFT calculated aryl radical binding energy as a function of surface coverage; the insert depicts the bare $Ni_3P_2(0001)$ surface.

TGA data (**Fig. 2B**) confirm a higher degree of functionalization with increasing Hammett parameter of the aryl substituent (NO_2>Cl_2>OMe), and hence increasing reactivity of the diazonium salt. This is consistent with previous observations in the literature, with the note that many papers use different methods of reporting the degree of functionalization depending on the system under investigation. For example, in studies of electrografting diazoniums onto glassy carbon surfaces authors report the magnitude of reductive current as a measure of functionalization yield.[72,77,104,105] Another common method is reporting atomic ratios determined by XPS or S-Mo:S-C ratios in the case of MoS_2 functionalization.[61,79,106] Though many of these studies supplement their findings with TGA and find the same result. We note, however, that the TGA data collected here is convoluted by the persistence of oleylamine in our sample, precluding direct correlation of the absolute mass loss values to covalently bound functional groups. In any case, we estimate the surface coverage of each sample with the assumption that 15% mass loss from oleylamine is constant across all samples, and that any further mass loss is from covalently bound surface functional groups. With these assumptions, we observed an upper bound for functionalization of 14% by mass for the nitrophenyl group. Assuming a 100 mg sample, this translates to 14 mg, or 114 mmol of nitrobenzene equivalents.

$$0.014\ g\ C_6H_4NO_2\left(\frac{1\ mol}{122.11\ g}\right) = 0.114\ mmol\ C_6H_5NO_2 \tag{3.21}$$

In the same sample, 71 mg of Ni_2P would translate to 119 mmol of surface P sites:

$$0.071\ g\ Ni_2P\left(\frac{6.74\ mmol\ P}{1\ g\ Ni_2P}\right) = 0.478\ mmol\ P(25\%\ surf.atom) = 0.119\ mmol\ surface\ P \quad (3.22)$$

translating to 96% surface P sites being functionalized:

$$\frac{0.114\ mmol\ C_6H_5NO_2}{0.119\ mmol\ surface\ P} = 96\%\ surface\ P\ sites \quad (3.23)$$

Following this logic, methoxybenzene and 3,5-dichlorobenzene samples translate to 27 and 68 mmol, or 20% and 54% surface P-Ar sites, respectively. All functionalization densities were below 100% saturation and were less than the molar equivalents of parent diazonium added to the reaction mixture.

DFT calculations support the idea that adsorption of C_6H_4-NO_2, C_6H_3-Cl_2 and C_6H_4-OCH_3 is spontaneous (Figure 3.12D). Here, adsorbate-adsorbate and adsorbate-substrate interactions dictate the binding energy trends, with the electron donating/withdrawing character playing a key role. For instance, the adsorption energy of the electron withdrawing radicals (C_6H_3-Cl_2 and C_6H_4-NO_2) become less favorable as we increase the surface coverage. While the electron donating propensity of C_6H_4-OMe counteracts the effects of adsorbate-adsorbate interaction, highlighted by the near constant binding energy as a function of surface coverage. Similar trends in binding energy have been observed in the literature for black phosphorous[107] and molybdenum disulfide[108]. It should be noted that these calculations do not include thermal effects, which could significantly destabilize the adsorption of diazonium salts under reaction conditions. Other factors, such as, the presence of excess oleylamine capping ligands is shown to further destabilize the adsorption energetics (Figure 3.13) That said, the low coverage trend of these species is consistent with the observed experimental coverages: 96% (C_6H_4-NO_2), 54% (C_6H_3-Cl_2) and 20% (C_6H_4-OMe).

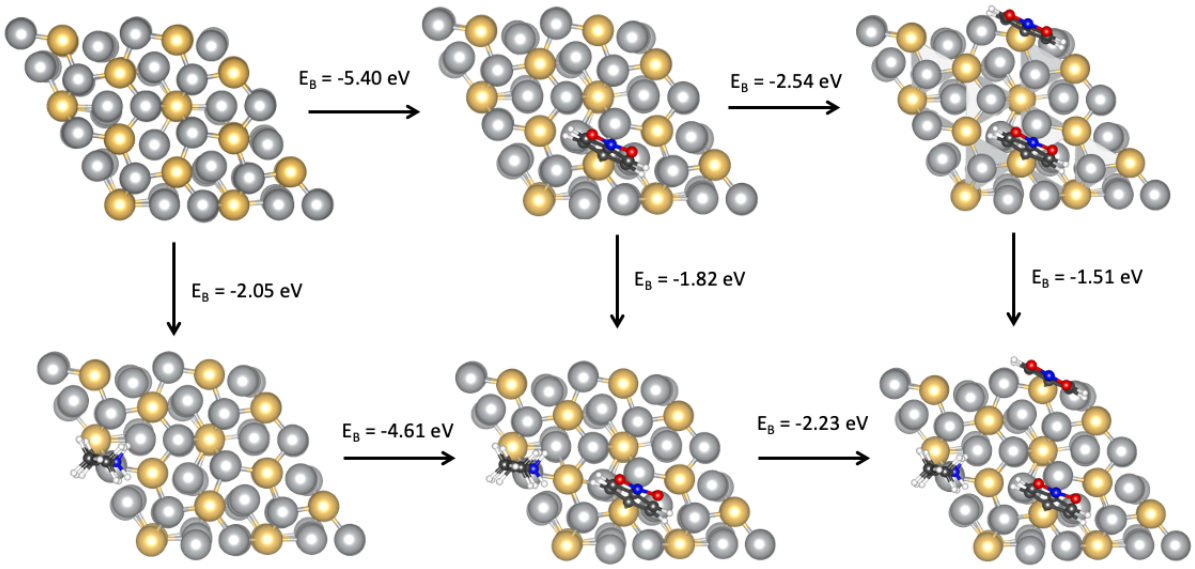

Figure 3.13. Effect of co-adsorbed amine ligands on $C_6H_4NO_2$ adsorption energetics.

To address the issue of unsaturated surface coverage, presumably due to the insufficient reducing potential or equivalents in the reaction mixture, the effect of adding a molecular reductant was investigated. This concept was recently validated by the Lewis group who showed that the functionalization density of MoS_2 by alkyl iodide species could be increased by adding sacrificial reductants to the reaction mixture.[109] This study demonstrated a strong correlation between the strength of the reductant and the coverage of functional groups, supporting our hypothesis that each surface functional group equivalent becomes increasingly difficult to generate and is strongly dependent on the thermodynamic driving force for both generating the radical species and facilitating surface-C bond formation.

We experimentally validated this hypothesis in our own system by adding equimolar concentrations of cobaltocene (relative to diazonium) to our reaction mixtures. The resulting differences between batches of Ni_2P-$C_6H_4NO_2$ is shown in Figure 3.14. The TGA data show a clear increase in mass loss and suggest that the organic content has increased to roughly 40% of the total sample mass. Following our earlier estimate of surface coverage, this would reflect a large

excess (225% of surface P sites) of nitrobenzene groups. This super saturation can be rationalized by the formation of hyperbranched nitrophenyl oligomers on the nanocrystal surface, as shown in Figure 3.14D.

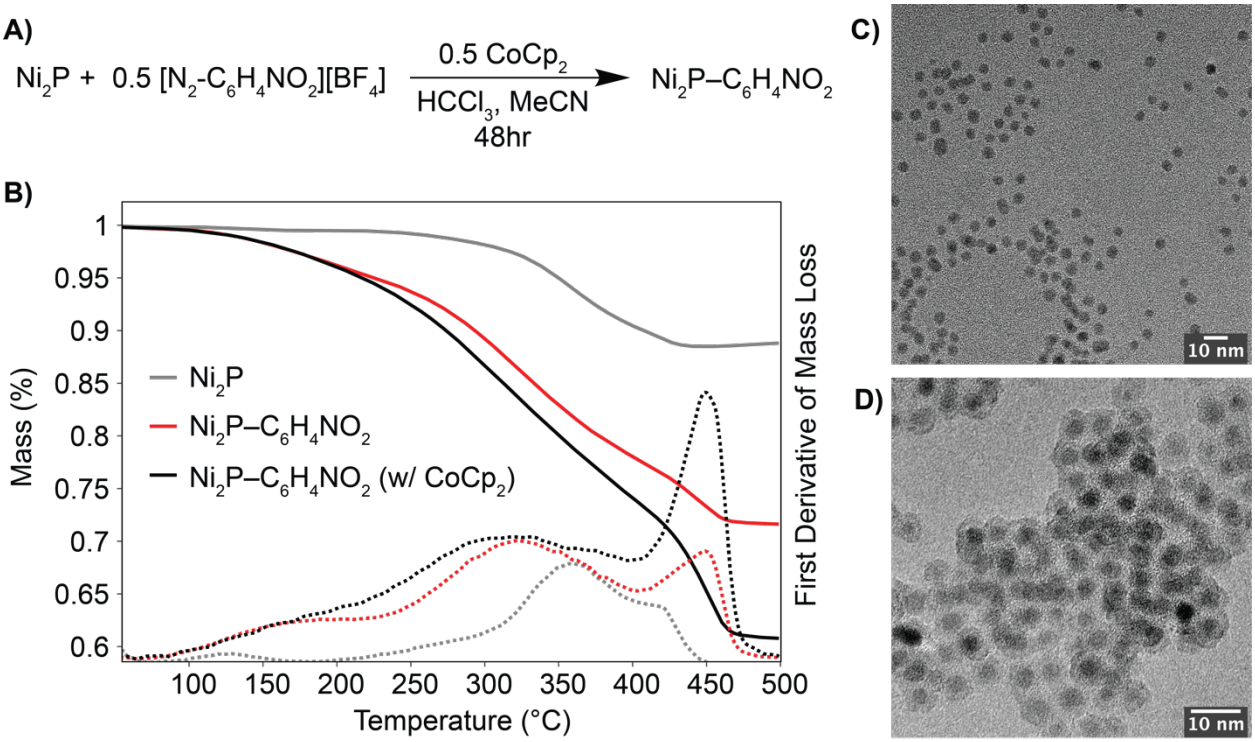

Figure 3.14. A) Reaction scheme showing functionalization of Ni_2P using $[N_2\text{-}C_6H_4NO_2][BF_4]$ with the addition of cobaltocene as a sacrificial reductant. B) TGA of both samples, showing an increase in mass loss percent for samples made with added cobaltocene. Dotted lines show the first derivative of the mass loss percent line. C) TEM of $Ni_2P\text{-}C_6H_4NO_2$ nanocrystals synthesized with no added reductant. Particles are still uniform and maintain their morphological integrity. Scale bar is 10 nm. D) TEM of $Ni_2P\text{-}C_6H_4NO_2$ synthesized with added cobaltocene. Particles show aggregation induced by the extensive aryl-multilayer film formation caused by aryl radical hyperbranching. Scale bar is 10 nm.

Uncontrolled reactivity, or hyperbranching, is a common phenomenon observed in diazonium chemistry. It is well known that aryl radicals react readily with sp^2 carbons, hence their usefulness

in functionalizing graphitic carbons. As such, they are also able to react with the sp^2 carbons present in surface arenes. This can lead to the formation of large polymeric films, sometimes on the order of tens of nanometers thick.[110]

3.4.4 *Effect of Functionalization on Electronic Structure*

The higher concentration of functional groups in the samples, derived from reactions in which a reductant was added, makes observation of functional groups with XPS easier. Spectra showing the presence of Cl and NO_2 functional groups can be observed in the Figure 3.15.

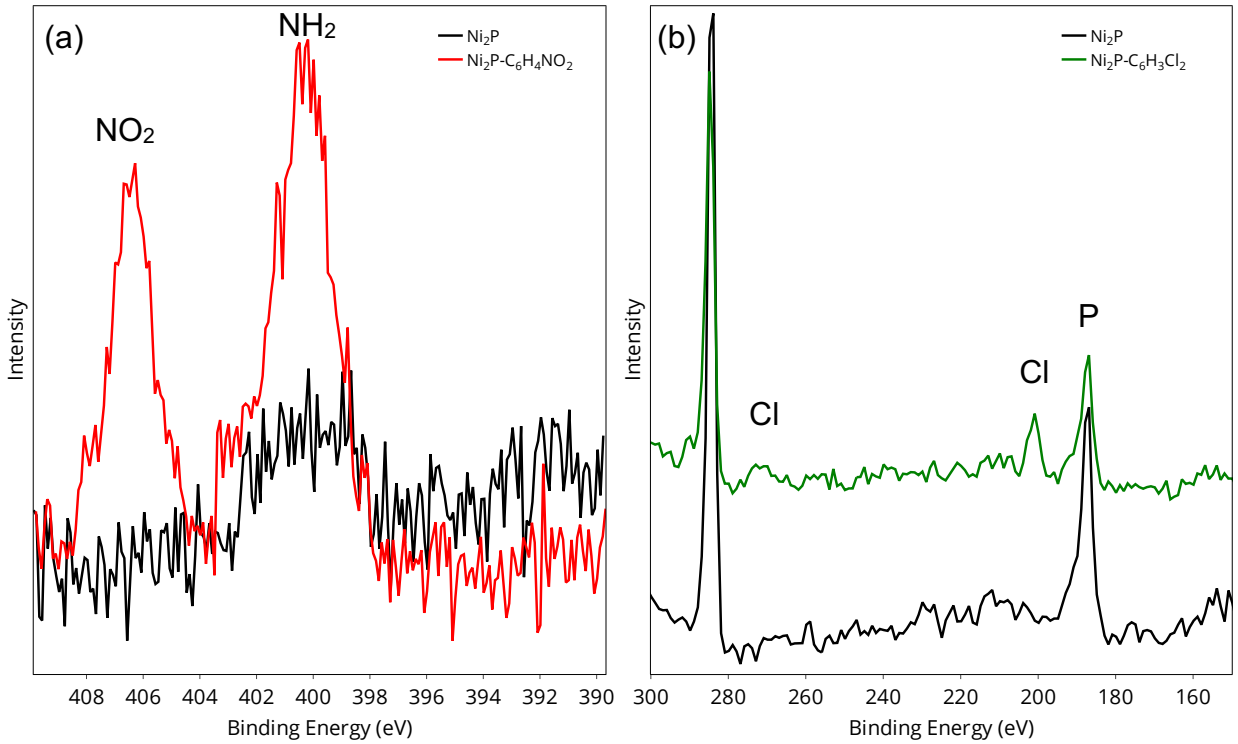

Figure 3.15. XPS N 1s high resolution spectrum (a) and survey spectrum (b) of Ni_2P-$C_6H_4NO_2$ and Ni_2P-$C_6H_3Cl_2$, respectively, plotted against Ni_2P. The N 1s spectrum in figure (a) shows the presence of NO_2 functional group at the characteristic binding energy of 406 eV. The lower binding energy species, attributed to amines, is likely a combination of remnant oleylamine and photo-reduced nitro groups, which is known to occur under X-Ray irradiation. The survey

spectrum in figure (b) shows the presence of Cl atoms with the new peak at 200 eV being evidence of the 2p photoelectrons. The 2s photoelectron signal is less intense and is barely observable through the noise at 270 eV.

What's more interesting, is the comparison of the Ni and P 2p high resolution scans between Ni_2P-$C_6H_4NO_2$ samples made with and without added reductant (Figures 3.16A and 3.16B). Rather than distinct peaks indicating the formation of a P-Ar or Ni-Ar bonds, we observe systematic shifts of the entire 'metal phosphide' signal. Although this result is surprising, it can be interpreted as the functionalization perturbing core-level electron density throughout the entire nanoparticle, which is reflected in the electronic density of states (DOS) inferred from the DFT calculations (**Fig. S25**).

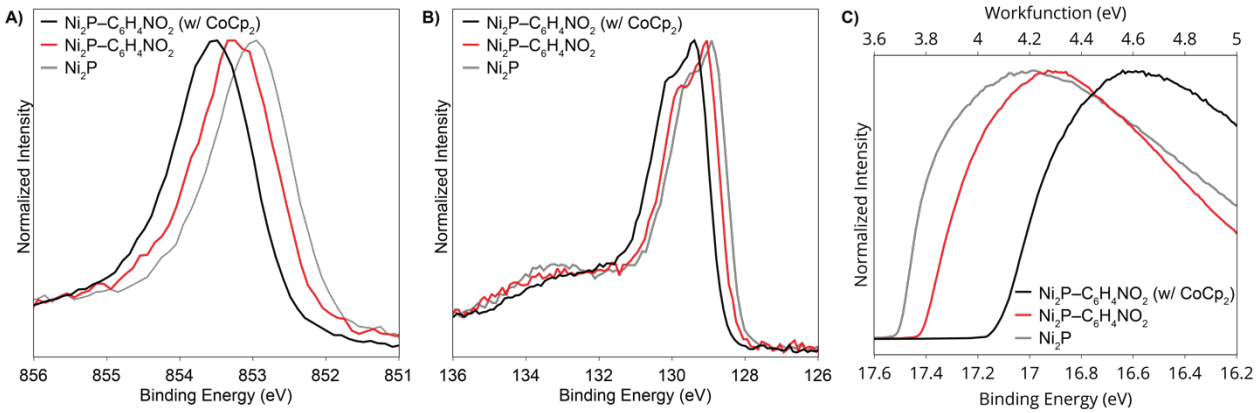

Figure 3.16. A) High resolution XPS spectra showing the gradual progression of the Ni $2p_{3/2}$ signal shifting to higher binding energies as the coverage of nitrobenzene groups increases (black > red). B) P 2p spectra of the same sample set, showing a similar systematic shift. C) UPS spectra of the same samples, showing the increased binding energy of the secondary electron cut off point, or work function. This illustrates increasing difficulty to eject an electron from the surface of the material as the coverage of nitrobenzene groups increases.

For the bare surface, the partial DOS plot shows that Ni_2P exhibits metallic type conductivity with the states around the Fermi level consisting largely of Ni 3d-states with only a minor contribution from the overlapping P 3p-states. On adsorption of nitrobenzene groups, we observe a clear perturbation of these states and redistribution of electrons due to the electron withdrawing properties of the adsorbate. Despite our model only considering diazonium species adsorbed on the P-top sites, the change in total DOS can be attributed to a shift of both the P 3p-states and Ni 3d-states as-well-as a local increase in the P 3p-states.

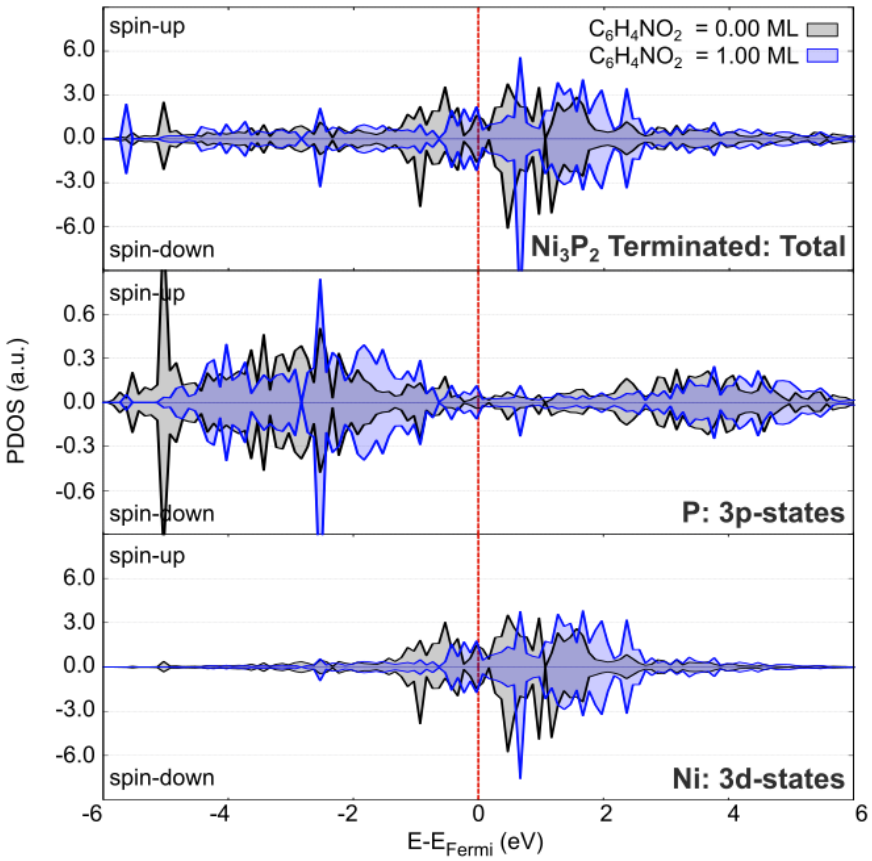

Figure 3.17. Partial density of states (PDOS) per atom comparing 0.00 ML (black) and 1.00 ML (blue) coverages of $C_6H_4NO_2$. The Fermi level is set to 0.00 eV (red dotted line).

While we would typically expect this shift in electron density to be localized and correlated with the functionalized surface sites, we propose the high level of covalency, and the metallic character of these metal phosphide nanocrystals allow localized perturbations to be compensated for by the 'bulk' material. Further, the same trend is reflected in the work function of these materials. The work function is made more positive with higher degrees of functionalization, which can be interpreted as the highly polar nitrophenyl functional groups inducing a stronger surface dipole moment away from the crystal's core, in-turn requiring more energy to remove an electron from valence orbitals to vacuum.

Although this phenomenon is unexpected when compared to studies of exfoliated MoS_2 and black phosphorous nanosheets, it is reminiscent of the effects observed when doping metal phosphides with metals of varying electronegativity.[111] In this study, Mar and coworkers observed a systematic shift in the P and Ni $2p_{3/2}$ binding energy over the range of ~500 meV. The authors find that as more electropositive ions (Co<Fe<Mn<Cr) are doped into the lattice the P $2p_{3/2}$ binding energy systematically decreases. They rationalize this finding by considering a charge potential model to balance the inter and intraatomic effects of dopants on the P atoms in the lattice.[112] Based on this model, intraatomic effects would lead to a decrease in binding energy due to increased nuclear screening and greater negative charge of P core electrons induced by their more electropositive environment. In contrast, interatomic effects would lead to a positive shift in binding energy due to the general increase in Madelung potential felt by each atom in the more electropositive lattice. We believe this rationale supports our interpretation of highly coupled covalent surface functional groups being able to perturb the 'bulk' electronic structure of the nanocrystal by inducing strong interatomic screening effects. The result of which is a systematic perturbation of the core-level

binding energies in both Ni and P based on the degree of electron density that is donated or withdrawn by the surface functional group.

We further validate this hypothesis by showing systematic variation of core-level binding energies and NC work function across our Hammett series (Figure 3.18). There is a clear linear trend observed in both Ni and P 2p high-resolution spectra where a larger Hammett parameter increases the core-level binding energy. This effect is most pronounced in the comparison of work functions across the Hammett series shown in Figure 3.18C. To ensure this wasn't purely an electrostatic screening effect, we validated our hypothesis against a computational model where the same trend is observed (Figure 3.19E).

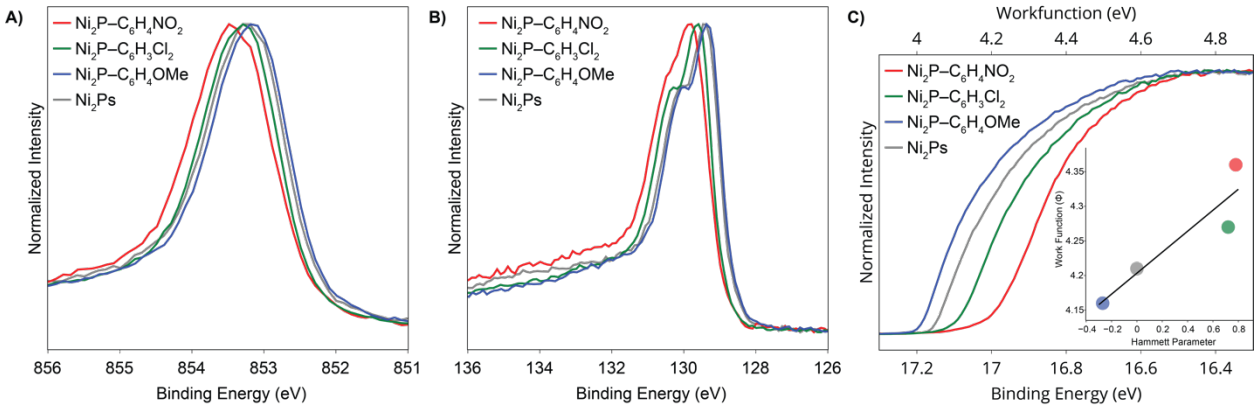

Figure 3.18. A) High resolution XPS spectra showing the shift of Ni $2p_{3/2}$ signal in response to the Hammett parameter of the surface functional group. B) P 2p spectra of the same sample set, showing a similar systematic shift. C) UPS spectra of the same samples, showing the response of material work function to the Hammett parameter of surface functional group. Inlet shows the linear correlation between these descriptors.

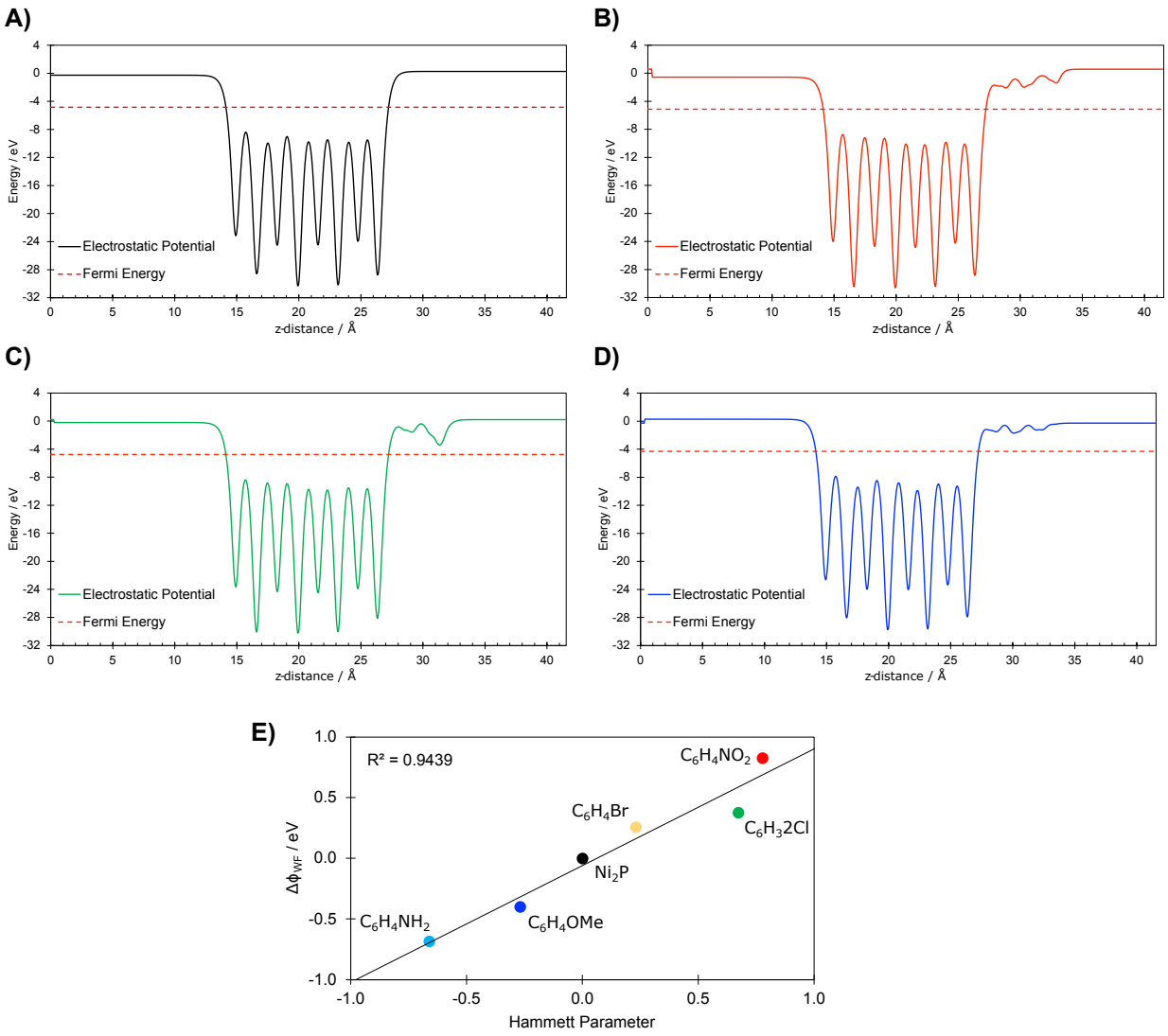

Figure 3.19. Plots showing the planar averaged electrostatic potential along the z-direction for (a) The bare $Ni_2P(0001)$ surface, (b) Ni_2P-$C_6H_4NO_2$, (c) Ni_2P-C_6H_32Cl and (d) Ni_2P-C_6H_4OMe. (e) Plot showing the change in workfunction vs Hammett parameter for each diazonium salt.

The workfunction (Φ_{WF}) is calculated by taking the difference in energy between the fermi energy (E_{Fermi}) and the vacuum potential (Φ_{Vac}):

$$\Phi_{WF} = \Phi_{Vac} - E_{Fermi} \tag{3.24}$$

3.4.5 *Electrocatalytic HER Activity*

To test the effect that surface functionalization has on the electrocatalytic activity for HER of the Ni_2P nanocrystals, 20 µL of a 10 mg/mL solution of Ni_2P nanocrystals in toluene were drop casted onto a 1.5 mm diameter glassy carbon electrode. Samples were prepared in a glovebox and transferred to a vessel of 0.5 M H_2SO_4 that was sparged with argon and held under a constant argon flow. Here we report the current density normalized by the geometric surface area of the glassy carbon electrode due to inconsistencies in estimating the electrochemically active surface area of the nanocrystal films (Figures 3.20-3.24).[113]

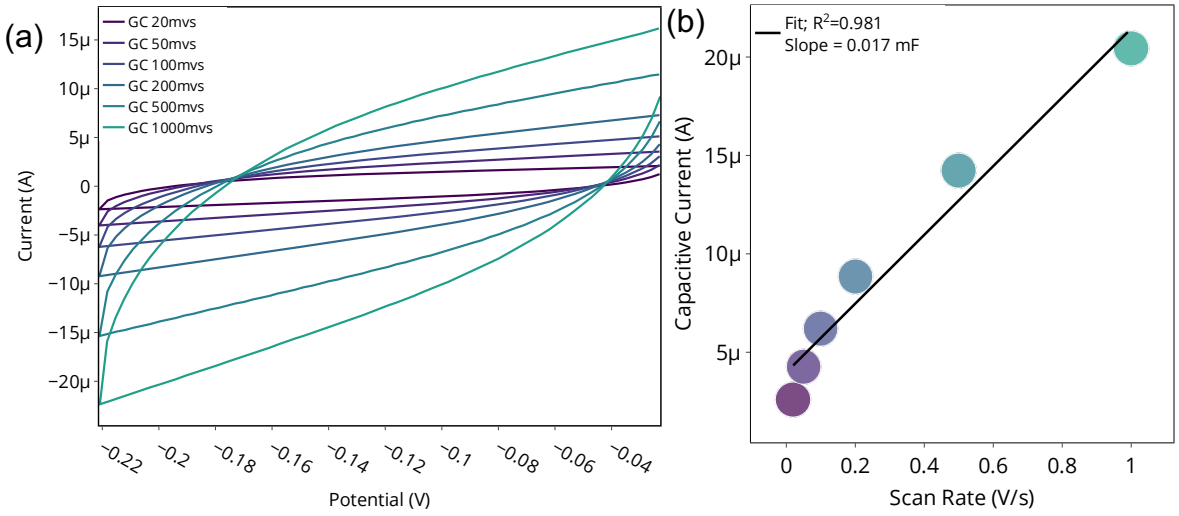

Figure 3.20. (a) Cyclic voltammograms at various scan rates of glassy carbon electrode in 0.5 M H_2SO_4. (b) Magnitude of capacitive current plotted against the scan rate of the cyclic voltammogram. The slope of the fitted line provides the capacitance of the electrode. Magnitude taken as difference between cathodic and anodic current at OCP (mid-point).

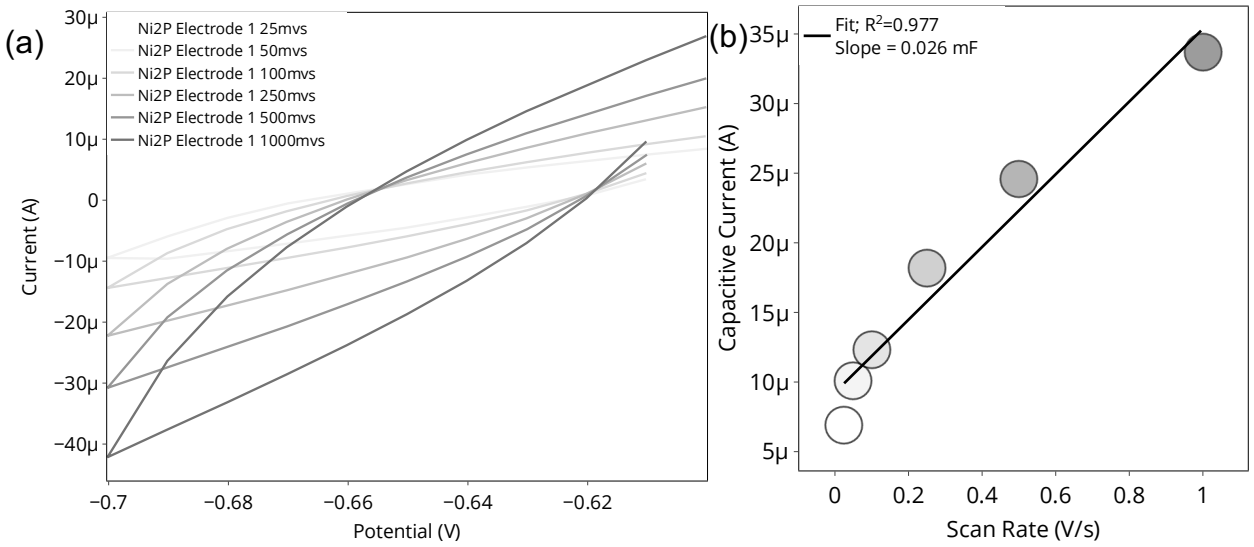

Figure 3.21. (a) Cyclic voltammograms at various scan rates of 200 µg Ni_2P deposited on glassy carbon electrode in 0.5 M H_2SO_4. (b) Magnitude of capacitive current plotted against the scan rate of the cyclic voltammogram. The slope of the fitted line provides the capacitance of the electrode. Magnitude taken as difference between cathodic and anodic current at OCP (mid-point).

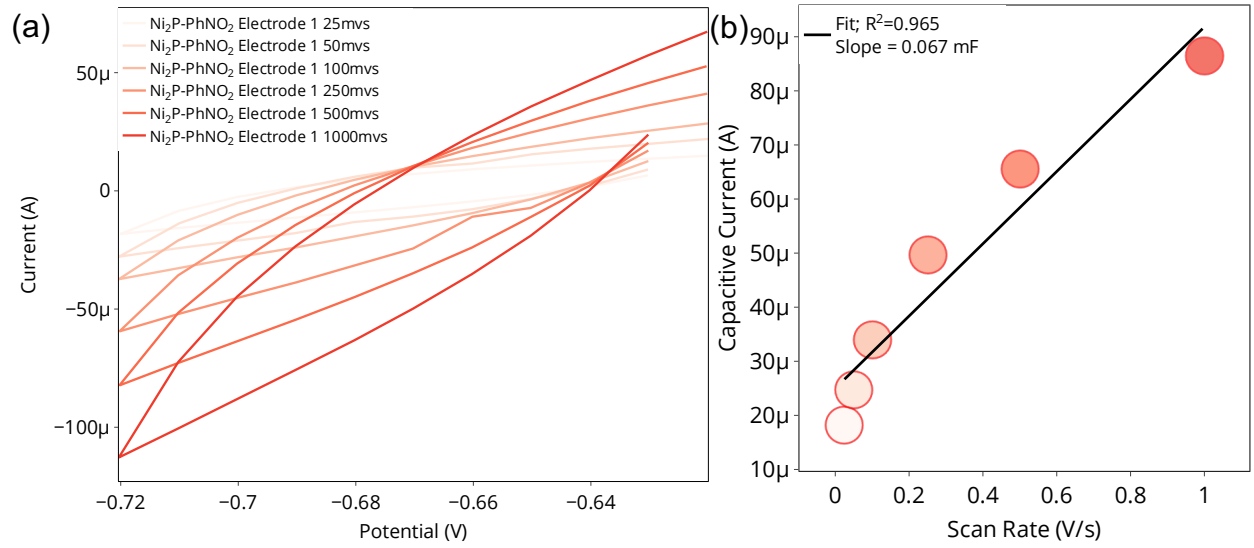

Figure 3.22. (a) Cyclic voltammograms at various scan rates of 200 µg Ni_2P-$C_6H_4NO_2$ deposited on glassy carbon electrode in 0.5 M H_2SO_4. (b) Magnitude of capacitive current plotted against the scan rate of the cyclic voltammogram. The slope of the fitted line provides the capacitance of

the electrode. Magnitude taken as difference between cathodic and anodic current at OCP (mid-point).

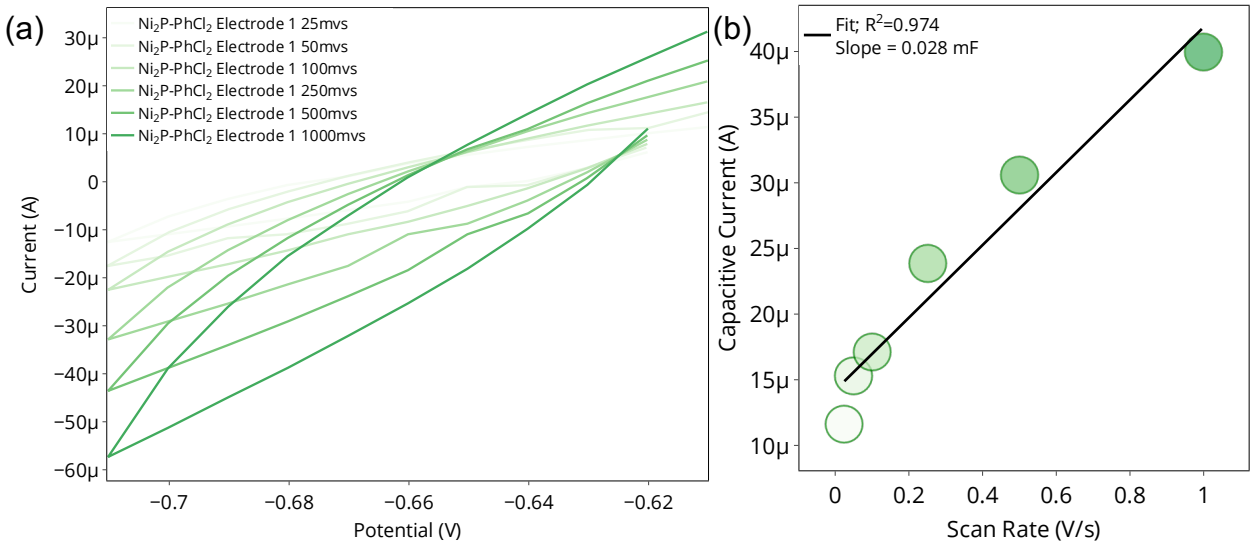

Figure 3.23. (a) Cyclic voltammograms at various scan rates of 200 µg Ni_2P-$C_6H_3Cl_2$ deposited on glassy carbon electrode in 0.5 M H_2SO_4. (b) Magnitude of capacitive current plotted against the scan rate of the cyclic voltammogram. The slope of the fitted line provides the capacitance of the electrode. Magnitude taken as difference between cathodic and anodic current at OCP (mid-point).

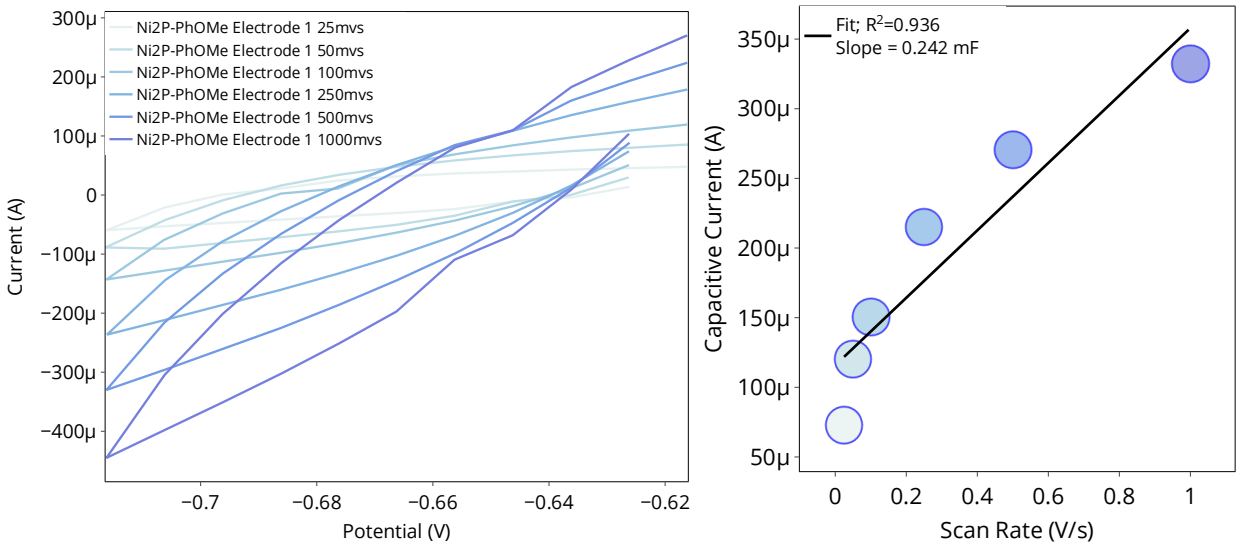

Figure 3.24. (a) Cyclic voltammograms at various scan rates of 200 µg Ni_2P-C_6H_4OMe deposited on glassy carbon electrode in 0.5 M H_2SO_4. (b) Magnitude of capacitive current plotted against the scan rate of the cyclic voltammogram. The slope of the fitted line provides the capacitance of the electrode. Magnitude taken as difference between cathodic and anodic current at OCP (mid-point).

Metal phosphides are known to have exceptionally high specific capacitance values due to pseudocapacitive effects, which typically leads to over estimation of electrochemically active area.[31,114,115] These pseudocapacitive properties would be affected by alteration of surface charge induced by the surface functional groups. This added complication makes it difficult to uniformly attribute "capacitive" current to strictly ion adsorption on a metallic surface, which is the base assumption in the estimation of electrochemically active surface area.[116] This is reflected in our inability to find a potential region that reflects a purely capacitive response characterized by a square-wave with equal anodic and cathodic current. Instead, we observe variable cathodic current around the open-circuit potential with added resistive losses, potentially due to mass-transport limitation though the nanocrystal film. Though this may preclude us from reporting the true intrinsic activity of our catalysts, we can still compare relative activity within the series.

The catalytic activity results are summarized in Figure 2.35 and reflect multiple key results. First, we observe over the course of 24 hours and 75 polarization cycles that the catalytic activity does not track the Hammett parameter, instead Ni_2P-C_6H_4OMe is the most active catalyst followed by Ni_2P-$C_6H_4NO_2$ and then Ni_2P-$C_6H_3Cl_2$ being the least active. This contrasts with previous studies by Miller and co-workers on covalently functionalized MoS_2, where they found that catalytic activity was correlated with the functional group's Hammett parameter, although the nitrobenzene functionalized sample was not measured in that instance.[61] Comparisons between these systems brings us to our second key result, which is improved catalytic activity in all functionalized samples when compared to Ni_2P in the first 20 polarization cycles. We propose these discrepancies reflect that the influence of covalently tethered ligands is more nuanced than simple electronic effects and that their impact may vary depending on the nature of the catalyst's surface chemistry and the density of grafted aryl groups. For example, the documented active site for MoS_2 is the edge atoms of the 2D sheet while the basal plane surface is relatively inert for HER. Thus, it is possible that functional groups that bond at the basal plane surface do not have added steric effects because of spatial separation from the catalytically active site. As we show below, that is not the case in Ni_2P nanocrystals, for which the aryl functional groups bond to atoms directly adjacent to active sites. This could allow for the same functional group to result in different effects based on the intrinsic reactivity and structure of the underlying material.

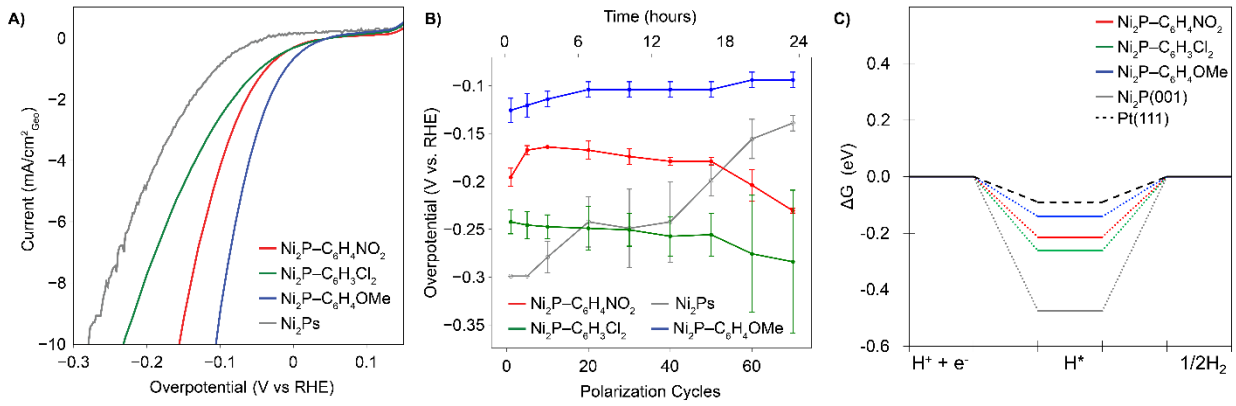

Figure 3.25. (a) LSV of the 10th polarization cycle for Ni_2P and Hammett series electrodes collected at 5 mVs^{-1}. (b) Overpotential at 10 mA/cm^2 averaged across three separate electrodes for each sample over the course of 24 hours and 75 polarization cycles. (c) Calculated free energy profile at 0.00 V, pH = 0 and 300 K for the adsorption of H onto the $Ni_2P(0001)$ Ni_3 hollow site, with and without surface functional groups.

For efficient hydrogen evolution, the hydrogen adsorption free energy should be slightly negative, so that there is a driving force for hydrogen to adsorb onto the catalyst surface, but the adsorption energy is low enough to allow for the subsequent proton coupling steps. As can be seen from Figure 3.25C, DFT calculations predict that the free energy for hydrogen adsorption at the $Ni_2P(0001)$ Ni 3-fold hollow site (possible surface binding sites are shown in Figure 3.26) can be modified substantially with surface functionalization of diazonium salts. The trend follows: Ni_2P(-0.47 eV) > Ni_2P-$C_6H_3Cl_2$(-0.26 eV) > Ni_2P-$C_6H_4NO_2$ (-0.22 eV) > Ni_2P-C_6H_4OMe(-0.14 eV), which is in agreement with our experimental findings. In turn, this suggests that the adsorption energies of H on the nanocrystal surface do not directly follow the electrostatic trend.

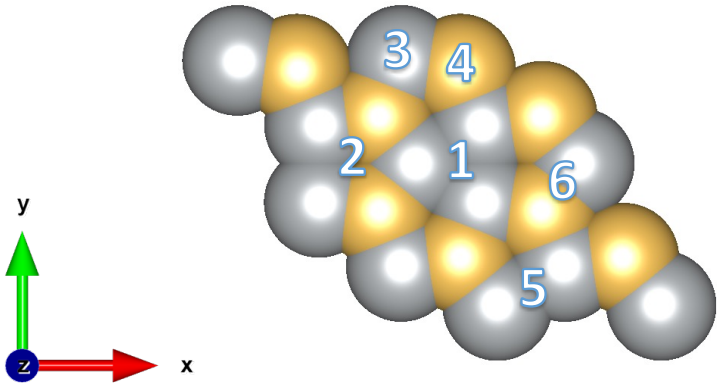

Figure 3.26. Schematic representation of the available surface sites on the Ni_3P_2 termination of the $Ni_2P(0001)$ surface.

The diazonium salt binding energy (E_B) is calculated according to the following equation:

$$E_B = E_{total} - (E_{sub} + E_{ads}) \quad (3.25)$$

Where, E_{total} is the total energy of the entire adsorbate-substrate system, E_{sub} is the total energy of the clean $Ni_2P(0001)$ substrate by itself, and E_{ads} is the total energy of the isolated adsorbate in the gas phase. The results are summarized in Table 3.1 with the available surface sites indicated in Figure 3.25. $C_6H_4NO_2$ prefers to diffuse from the high coordination hollow sites to more stable P top sites or P/Ni bridge sites.

Table 3.1. DFT calculated binding energy of $C_6H_4NO_2$ relative to the P top site. The surface sites are depicted in Figure S22. High coordination sites are disfavored for diazonium salt adsorption.

Site	Site Index	ΔE_B / eV
Hollow – Ni_3	1	-
Hollow – Ni/P	2	-
Top – Ni	3	0.69
Top – P	4	0.00
Bridge – Ni	5	0.57
Bridge – Ni/P	6	0.25

To further probe the origins of the observed trend, we examined the effects of electron transfer between the nanocrystal atoms and surface adsorbates by calculating their charge density difference (CDD) (Figure 3.26**)**. Figure 3.26A shows, that once adsorbed on the surface, hydrogen accumulates electron density from nearby Ni atoms, forming a surface hydride. Interestingly, from Figures 3.26B to 2.36D, adsorption of diazonium salts on P top sites exhibit non-local charge redistribution at the Ni_3 hollow site.

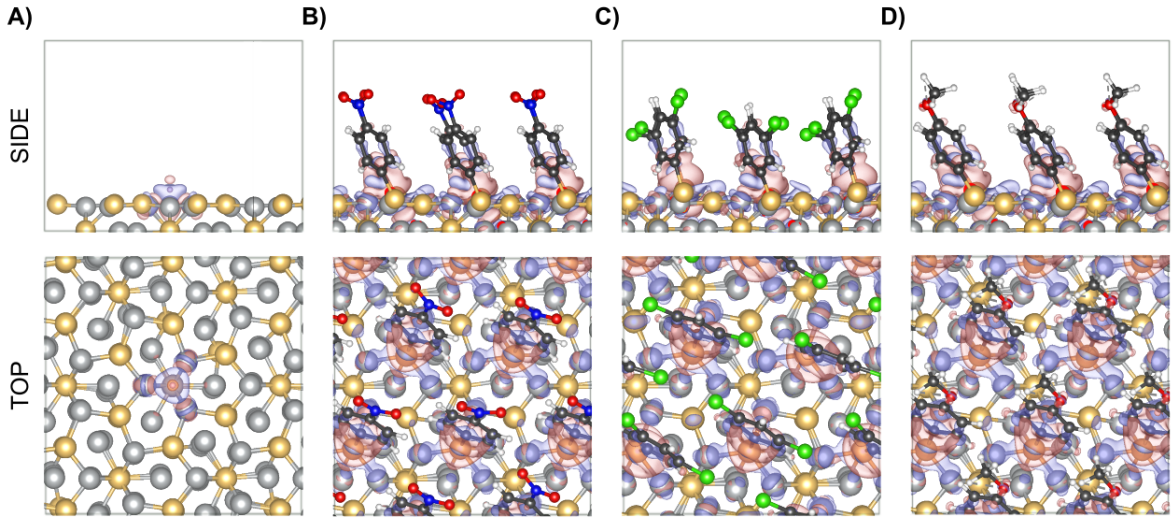

Figure 3.27. Charge density difference plots highlighting the interactions of key species at the $Ni_2P(0001)$ interface. (a) H adsorbed at the Ni_3 hollow site. (b) C_6H_4-NO_2, (c) C_6H_3-Cl_2 and (d) C_6H_4-OMe adsorbed on the P top sites. Red and blue shading represent electron depletion and electron accumulation respectively. The iso-surface level is set to 0.013 e/Å^3.

The net effect of functionalization is the tuning of the hydrogen adsorption free energy at the Ni_3 hollow site via electron redistribution resulting in a weaker adsorption energy for H atoms, thus making the catalytic landscape more thermoneutral relative to the bare surface. These local fluctuations in Ni charge density can facilitate H atom diffusion onto the Ni-Ni bridge site (Figures 3.28 and 3.29).

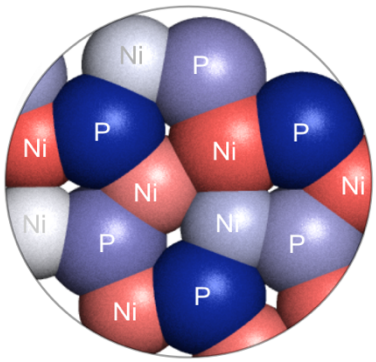

Figure 3.28. Heat map highlighting the difference in the Lowden charge on addition of 1.00 ML diazonium salts to the bare $Ni_2P(0001)$ surface. All three diazonium salts exhibited a similar behavior. Blue and red shading represent electron depletion and electron accumulation respectively.

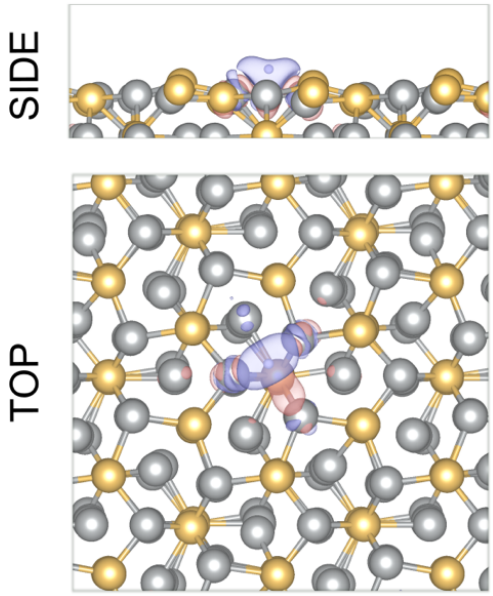

Figure 3.29. Charge density difference plot for hydrogen adsorbed at the bridge site position. Red and blue shading represent electron depletion and electron accumulation respectively. The iso-surface level is set to 0.013 e/Å^3.

The Ni-Ni bridge site is expected to be a catalytically active site in computational studies but is generally only accessed at higher H coverages.[40,117] We further note that the transition from a surface hollow site to lower coordination sites would be hindered by the Pauli repulsion exhibited by the Cl atoms of the C_6H_3-Cl_2 functional groups and the hydride nature of adsorbed H ($H^{\delta-}$-$Cl^{\delta-}$). Additionally, this charge redistribution depends strongly on the alignment of diazonium species above the P top site. Most noticeable is the repulsive interactions exhibited by $C_6H_3Cl_2$ (Figure 3.27), which is reflected in the binding energy discussed previously. The $Cl^{\delta-}$-$Cl^{\delta-}$ repulsion results in a staggered array of $C_6H_3Cl_2$ species and a disfavored alignment of the C p_z-orbitals with P 3p-states. To compensate for this, some P atoms are pulled away from the surface plane, resulting in significant distortion and a weaker interaction with the surface atoms. The trend in P-atom distortions C_6H_3-Cl_2(0.57 Å)> C_6H_4-NO_2(0.31 Å) > C_6H_4-OMe(0.29 Å) suggests that para substitution minimizes adsorbate-adsorbate interactions leading to an optimal surface packing of diazonium salts relative to the meta substituted functional groups. Overall, we find that the local electronic structure and bonding interactions of the diazonium salts influence the charge density across the surface, which we hypothesize being the cause of our observed trend.

For these calculations, The hydrogen adsorption free energies are calculated using the CHE method developed by Norskov.[124] Here, we assume that protons (H^+) and electrons (e^-) are at equilibrium with hydrogen gas ($H_2(g)$) at 1 atm, 298 K, and pH = 0:

$$H^+ + e^- \rightarrow \frac{1}{2} H_2(g) \tag{3.26}$$

In the absence of an applied potential (0.00 V) we assume that:

$$\mu_{H^+} + \mu_{e^-} = \frac{1}{2}\mu_{H_2} \tag{3.27}$$

where μ_{H^+}, μ_{e^-}, and μ_{H_2} are the chemical potentials of a proton, electron, and hydrogen, respectively. For the adsorption of hydrogen on a Ni_2P(0001) surface ($Surf_{Ni_2P}$):

$$Surf_{Ni_2P} + H^+ + e^- \rightarrow Surf_{Ni_2P-H} \quad (3.28)$$

The free energy can be calculated as:

$$\Delta G = \Delta E^{DFT} + \Delta ZPE - T\Delta S + \Delta G^U + \Delta G^{pH} \quad (3.29)$$

Where, ΔE^{DFT}, ΔZPE and ΔS are the changes of the DFT reaction energy, zero-point energy, and entropy, respectively. ΔG^U is the free energy contributions related to the applied electrode potential U. $\Delta G^{pH} = \ln(10) k_B T ln(pH)$ is the concertation correction to the H^+ free energy, where T = 300 K and k_B is the Boltzmann constant. Here, we apply the same approximations for calculating ΔZPE as the work by Wexler *et al.*[125]

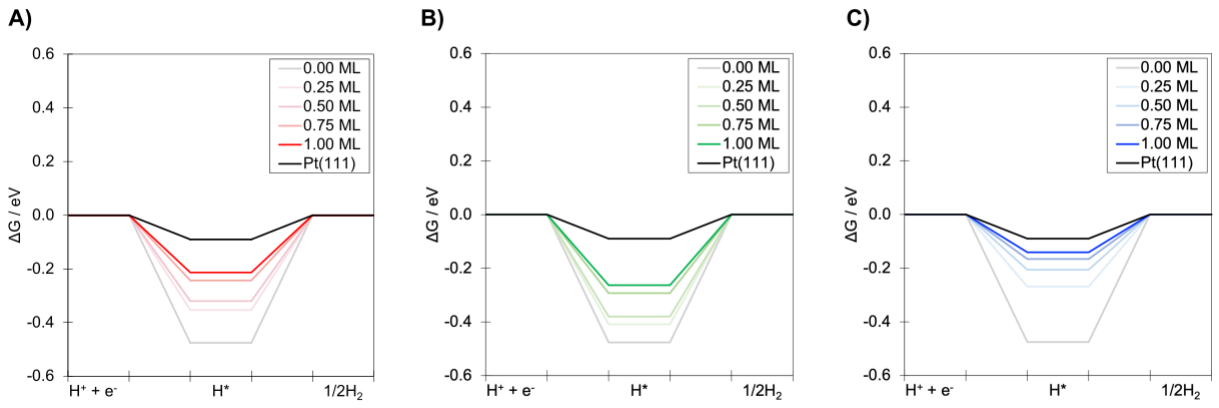

Figure 3.30. Hydrogen adsorption free energy as a function of aryl radical coverage for (a) C_6H_4-NO_2, (b) C_6H_3-Cl_2 and (c) C_6H_4-OMe at 0.00 V, pH = 0 and 300 K.

3.4.6 *Electrocatalytic Stability*

The next key finding is the variation of activity over multiple polarization cycles. The first and most important point is that the trend in activity induced by the functional groups is held over 24 hours of exposure to catalytic conditions. We propose this is strong evidence in favor of covalent functional groups being a viable pathway to stable hybrid nanomaterials. Another interesting point is the variability, or lack thereof, in activity over time. We observed a gradual increase in activity

after successive polarizations for the ligand stripped Ni_2P sample, as shown in Figure 3.25B. This is presumably due to the removal of remnant oleylamine from the surface, allowing for a better wetting of the electrolyte as previously demonstrated in our lab.[56] However, we cannot count out the possibility of surface reconstruction, which has been theoretically predicted and experimentally measured to take place during catalysis.[40,42,118–120] If, after prolonged cycling, the dominant surface facet is no longer the Ni_3P_2 (0001) termination it could account for the gradual disagreement with the predicted thermodynamic landscape that we observe in earlier cycles (Figure 3.25C). Further, this swing in activity is quite large, showing an improvement of 150 mV over the course of our measurements. This contrasts with the functionalized samples which show very little variability under the same conditions, reflecting a maximum average deviation of only 25 mV. We note that although the activity of the Ni_2P electrodes did improve over time, they never achieved higher current densities or lower overpotential than the Ni_2P-C_6H_4OMe sample, even in the few samples we measured out to 100 polarization cycles (Figures 3.31 and 3.32). Another practically relevant observation during our analysis was the I-V response during cycling. Consistently, we observed wild variations in the current response from Ni_2P electrodes, presumably due to the formation of hydrogen bubbles. This is reflected in the noisy LSV reported in Figure 3.25A but becomes even more apparent at high current densities (Figure 3.32).

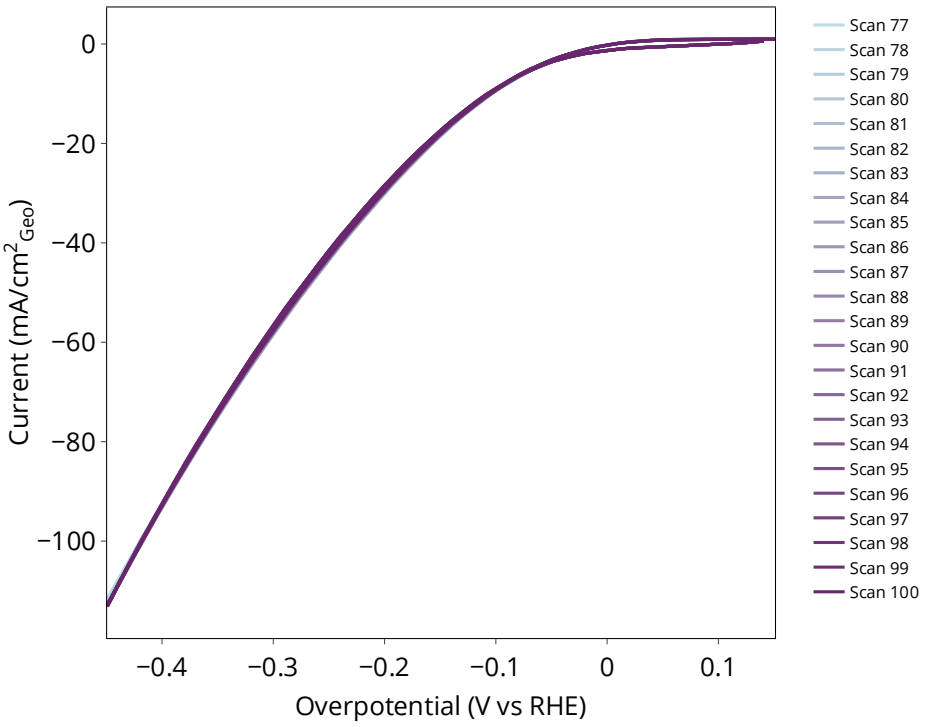

Figure 3.31. Repeated cycling of Ni_2P-C_6H_4OMe electrode in 0.5 M H_2SO_4. Polarization achieved through 23 cyclic voltammetry cycles at 10 mVs^{-1}. The electrode was not touched between cycles.

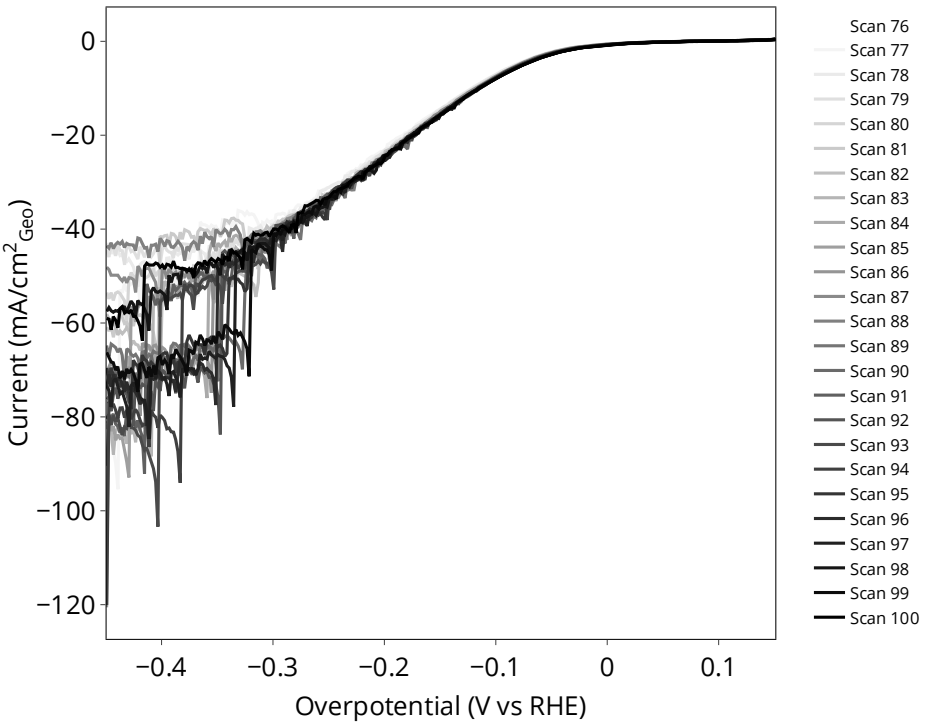

Figure 3.32. Repeated cycling of Ni_2Ps electrode in 0.5 M H_2SO_4. Polarization achieved through 24 consecutive linear sweep voltammograms at 10 mVs^{-1}. The electrode was knocked against the cell wall after each polarization curve to remove excessive H_2 bubble buildup.

Finally, we were able to observe the retention of key atomic handles by SEM-EDS after repeated cycling, presented in Figure 3.33. Critically, this illustrates that the chlorine atoms from the 3,5-dichlorobenzene functional group remain observable and are specifically observed in regions of the image where Ni and P are also detected, rather than randomly scattered across the sample.

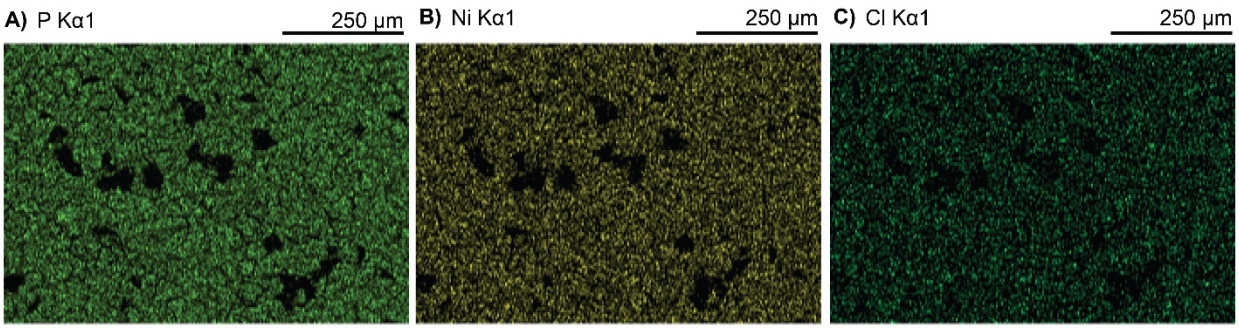

Figure 3.33. SEM-EDS map of Ni_2P-$C_6H_3Cl_2$ electrode after 100 polarization cycles showing the presence and spatial overlap of P (a), Ni (b), and Cl (c) on the electrode after cycling.

3.5 CONCLUSIONS

In conclusion, we have formulated synthetic conditions for generating (sub)monolayer coverages of substituted aryl functional groups covalently bound to the surface of Ni_2P nanocrystals and measured the resultant effects on the nanomaterial's electronic and electrocatalytic properties. Through our study we have highlighted the need for further investigation into soft ligand removal strategies for colloidal metal phosphide nanocrystals. We have shown that native ligands can participate in side reactions with functionalization precursors and convolute characterization. Still, we show that Ni_2P nanocrystals can be spontaneously functionalized by substituted aryldiazonium salts. Though we did not observe explicit experimental evidence, computation modeling suggests this functionalization occurs *via* formation of covalent P-C bonds. The degree of functionalization is dictated by the electron density in the aryl ring, where substituents that withdraw more electron density result in higher functionalization densities. We find that the electron donating/withdrawing nature of the surface functional group systematically alters core-level electron density and the bulk Fermi-level of the materials. Interestingly, we find that the influence on electrocatalytic activity is improved by the addition of substituted aryl groups, but the trend does not clearly track the electrostatic influence of the substituent functional groups. Though unexpected, these findings are

validated by DFT modeling of our system which identifies the same broken trend. Through this model we propose that the functional groups have a nuanced effect on activity, which go beyond simple surface dipole effects, and can alter the binding energetics at active sites through surface deformation and steric repulsion. Further, we find that this trend in altered electrocatalytic activity for the HER is maintained over the course of 24 hours and more than 75 polarization cycles, signaling the promise for covalently bound ligands to be robust to catalytic conditions.

3.6 OUTLOOK

Though sterically rigid aryl functional groups are likely not the key ingredient for making an earth abundant catalyst rival the activity of platinum, the utilization of this well-studied class of surface functionalization agents is a promising starting point. We propose that building models and further refining this relatively simple system will lay the groundwork for the development of synthetic procedures to produce elegant systems of covalently tethered proton relay ligands that fully utilize secondary and outer coordination sphere effects. However, there is still much work to be done as a community before such a system can be conceived. For example, exploring the range of electro/nucleophilicities required to form bonds with surface atoms so we can move away from harsh and difficult-to-control radical chemistry. These ideas lead to a further question: would we install an already synthesized complex ligand on the surface, or build it from the bottom-up using post-synthetic transformations once a suitable reactive fragment is bound to the particle surface? Surendranath and co-workers have covalently tethered organometallic catalysts to the edges and defect sites of carbon materials.[121,122] In those systems, the authors were able to leverage native *o*-quinone moieties that irreversibly condense with diamines to form their covalent linkages. Though such native defects are not as well documented in nanocrystalline phosphide or other more complex materials, a better understanding of the chemical nature of these materials' surface atoms

should allow for the development of more elegant functionalization strategies. In fact, collaborative studies between our group and the Mayer group have taken aim at building a more molecular understanding of colloidal metal phosphide nanocrystals.[123] This concept and line of study will directly bolster our on-going efforts to refine surface functionalization procedures and create better defined hybrid nanomaterials.

REFERENCES

(1) Roser, M. Why Did Renewables Become so Cheap so Fast? And What Can We Do to Use This Global Opportunity for Green Growth? *Our World in Data*. 2020. https://ourworldindata.org/cheap-renewables-growth

(2) Haldorsen, H. H.; Leach, P. Energy 360: Invited Perspective: The Outlook for Energy: A View to 2040. *J. Pet. Technol.* **2015**, *67*, 14–19. https://doi.org/10.2118/0415-0014-jpt.

(3) Geels, F. W.; Sovacool, B.; Schwanen, T.; Sorrell, S. Accelerating Innovation Is as Important as Climate Policy. *Policy Forum* **2017**, *357*, 1242–1244.

(4) De Luna, P.; Hahn, C.; Higgins, D.; Jaffer, S. A.; Jaramillo, T. F.; Sargent, E. H. What Would It Take for Renewably Powered Electrosynthesis to Displace Petrochemical Processes? *Science* **2019**, *364*, eeav3506. https://doi.org/10.1126/science.aav3506.

(5) Seh, Z. W.; Kibsgaard, J.; Dickens, C. F.; Chorkendorff, I.; Nørskov, J. K.; Jaramillo, T. F. Combining Theory and Experiment in Electrocatalysis: Insights into Materials Design. *Science* **2017**, *355*, eaad4998. https://doi.org/10.1126/science.aad4998.

(6) Hammer, B.; Norskov, J. K. Why Gold Is the Noblest of All the Metals. *Nature* **1995**, *376*, 238–240. https://doi.org/10.1038/376238a0.

(7) Trasatti, S. Work Function, Electronegativity, and Electrochemical Behaviour of Metals. III. Electrolytic Hydrogen Evolution in Acid Solutions. *J. Electroanal. Chem.* **1972**, *39*, 163–184. https://doi.org/10.1016/S0022-0728(72)80485-6.

(8) Hammer, B.; Nørskov, J. K. Electronic Factors Determining the Reactivity of Metal Surfaces. *Surf. Sci.* **1995**, *343*, 211–220. https://doi.org/10.1016/0039-6028(96)80007-0.

(9) Raugei, S.; Dubois, D. L.; Rousseau, R.; Chen, S.; Ho, M. H.; Bullock, R. M.; Dupuis, M. Toward Molecular Catalysts by Computer. *Acc. Chem. Res*. **2015**, *48*, 248–255. https://doi.org/10.1021/ar500342g.

(10) Hammes-Schiffer, S. Controlling Electrons and Protons through Theory: Molecular Electrocatalysts to Nanoparticles. *Acc. Chem. Res.* **2018**, *51*, 1975–1983. https://doi.org/10.1021/acs.accounts.8b00240.

(11) and, Z.-P. L.; Hu*, P. General Rules for Predicting Where a Catalytic Reaction Should Occur on Metal Surfaces: A Density Functional Theory Study of C−H and C−O Bond Breaking/Making on Flat, Stepped, and Kinked Metal Surfaces. *J. Am. Chem. Soc.* **2003**, *125*, 1958–1967. https://doi.org/10.1021/JA0207551.

(12) Trasatti, S. Work Function, Electronegativity, and Electrochemical Behaviour of Metals. II. Potentials of Zero Charge and "Electrochemical" Work Functions. *J. Electroanal. Chem.* **1971**, *33*, 351–378. https://doi.org/10.1016/S0022-0728(71)80123-7.

(13) Quaino, P.; Juarez, F.; Santos, E.; Schmickler, W. Volcano Plots in Hydrogen Electrocatalysis-Uses and Abuses. *Beilstein J. Nanotechnol.* **2014**, *5*, 846–854. https://doi.org/10.3762/bjnano.5.96.

(14) Hansen, J. N.; Prats, H.; Toudahl, K. K.; Mørch Secher, N.; Chan, K.; Kibsgaard, J.; Chorkendorff, I. Is There Anything Better than Pt for HER? *ACS Energy Lett.* **2021**, *6*, 1175–1180. https://doi.org/10.1021/acsenergylett.1c00246.

(15) Solis, B. H.; Hammes-Schiffer, S. Proton-Coupled Electron Transfer in Molecular Electrocatalysis: Theoretical Methods and Design Principles. *Inorg. Chem.* **2014**, *53*, 6427–6443. https://doi.org/10.1021/ic5002896.

(16) Tributsch, H.; Bennett, J. C. Electrochemistry and Photochemistry of MoS2 Layer

Crystals. I. *J. Electroanal. Chem.* **1977**, *81*, 97–111. https://doi.org/10.1016/S0022-0728(77)80363-X.
(17) Benck, J. D.; Hellstern, T. R.; Kibsgaard, J.; Chakthranont, P.; Jaramillo, T. F. Catalyzing the Hydrogen Evolution Reaction (HER) with Molybdenum Sulfide Nanomaterials. *ACS Catal*. **2014**, *4*, 3957–3971. https://doi.org/10.1021/cs500923c.
(18) Lukowski, M. A.; Daniel, A. S.; Meng, F.; Forticaux, A.; Li, L.; Jin, S. Enhanced Hydrogen Evolution Catalysis from Chemically Exfoliated Metallic MoS2 Nanosheets. *J. Am. Chem. Soc.* **2013**, *135*, 10274–10277. https://doi.org/10.1021/ja404523s.
(19) Voiry, D.; Salehi, M.; Silva, R.; Fujita, T.; Chen, M.; Asefa, T.; Shenoy, V. B.; Eda, G.; Chhowalla, M. Conducting MoS2 Nanosheets as Catalysts for Hydrogen Evolution Reaction. *Nano Lett.* **2013**, *13*, 6222–6227. https://doi.org/10.1021/nl403661s.
(20) Mundy, M. E.; Ung, D.; Lai, N. L.; Jahrman, E. P.; Seidler, G. T.; Cossairt, B. M. Aminophosphines as Versatile Precursors for the Synthesis of Metal Phosphide Nanocrystals. *Chem. Mater.* **2018**, *30*, 5373–5379. https://doi.org/10.1021/acs.chemmater.8b02206.
(21) Layan Savithra, G. H.; Muthuswamy, E.; Bowker, R. H.; Carrillo, B. A.; Bussell, M. E.; Brock, S. L. Rational Design of Nickel Phosphide Hydrodesulfurization Catalysts: Controlling Particle Size and Preventing Sintering. *Chem. Mater.* **2013**, *25*, 825–833. https://doi.org/10.1021/cm302680j.
(22) Li, D.; Senevirathne, K.; Aquilina, L.; Brock, S. L. Effect of Synthetic Levers on Nickel Phosphide Nanoparticle Formation: Ni_5P_4 and NiP_2. *Inorg. Chem.* **2015**, *54*, 7968–7975. https://doi.org/10.1021/acs.inorgchem.5b01125.
(23) Muthuswamy, E.; Savithra, G. H. L.; Brock, S. L. Synthetic Levers Enabling Independent Control of Phase, Size, and Morphology in Nickel Phosphide Nanoparticles. *ACS Nano* **2011**, *5*, 2402–2411. https://doi.org/10.1021/nn1033357.
(24) Popczun, E. J.; Mckone, J. R.; Read, C. G.; Biacchi, A. J.; Wiltrout, A. M.; Lewis, N. S.; Schaak, R. E. Nanostructured Nickel Phosphide as an Electrocatalyst for the Hydrogen Evolution Reaction. *J. Am. Chem. Soc* **2013**, *135*, 9267–9270.
(25) Popczun, E. J.; McKone, J. R.; Read, C. G.; Biacchi, A. J.; Wiltrout, A. M.; Lewis, N. S.; Schaak, R. E. Nanostructured Nickel Phosphide as an Electrocatalyst for the Hydrogen Evolution Reaction. *J. Am. Chem. Soc.* **2013**, *135*, 9267–9270. https://doi.org/10.1021/ja403440e.
(26) Callejas, J. F.; Read, C. G.; Roske, C. W.; Lewis, N. S.; Schaak, R. E. Synthesis, Characterization, and Properties of Metal Phosphide Catalysts for the Hydrogen-Evolution Reaction. *Chem. Mater.* **2016**, *28*, 6017–6044. https://doi.org/10.1021/acs.chemmater.6b02148.
(27) Popczun, E. J.; Read, C. G.; Roske, C. W.; Lewis, N. S.; Schaak, R. E. Highly Active Electrocatalysis of the Hydrogen Evolution Reaction by Cobalt Phosphide Nanoparticles. *Angew. Chem. Int. Ed.* **2014**, *53*, 5427–5430. https://doi.org/10.1002/anie.201402646.
(28) Carenco, S.; Liu, Z.; Salmeron, M. The Birth of Nickel Phosphide Catalysts: Monitoring Phosphorus Insertion into Nickel. *ChemCatChem* **2017**, *9*, 2318–2323. https://doi.org/10.1002/cctc.201601526.
(29) Henkes, A. E.; Vasquez, Y.; Schaak, R. E. Converting Metals into Phosphides: A General Strategy for the Synthesis of Metal Phosphide Nanocrystals. *J. Am. Chem. Soc.* **2007**, *129*, 1896–1897. https://doi.org/10.1021/ja068502l.
(30) Eagle, F. W.; Rivera-Maldonado, R. A.; Cossairt, B. M. Surface Chemistry of Metal

Phosphide Nanocrystals. *Annu. Rev. Mater. Res.* **2021**, *51*, 1–24. https://doi.org/10.1146/annurev-matsci-080819-011036.
(31) Kibsgaard, J.; Tsai, C.; Chan, K.; Benck, J. D.; Nørskov, J. K.; Jaramillo, T. F.; Abild-Pedersen, F.; Jaramillo, T. F. Designing an Improved Transition Metal Phosphide Catalyst for Hydrogen Evolution Using Experimental and Theoretical Trends. *Energy Environ. Sci.* **2015**, *8*, 3022–3029. https://doi.org/10.1039/c5ee02179k.
(32) Man, H. W.; Tsang, C. S.; Li, M. M. J.; Mo, J.; Huang, B.; Lee, L. Y. S.; Leung, Y. chung; Wong, K. Y.; Tsang, S. C. E. Tailored Transition Metal-Doped Nickel Phosphide Nanoparticles for the Electrochemical Oxygen Evolution Reaction (OER). *Chem. Commun.* **2018**, *54*, 8630–8633. https://doi.org/10.1039/c8cc03870h.
(33) Liu, J.; Wang, Z.; David, J.; Llorca, J.; Li, J.; Yu, X.; Shavel, A.; Arbiol, J.; Meyns, M.; Cabot, A. Colloidal Ni2-xCoxP Nanocrystals for the Hydrogen Evolution Reaction. *J. Mater. Chem. A* **2018**, *6*, 11453–11462. https://doi.org/10.1039/c8ta03485k.
(34) El-Refaei, S. M.; Russo, P. A.; Pinna, N. Recent Advances in Multimetal and Doped Transition-Metal Phosphides for the Hydrogen Evolution Reaction at Different PH Values. *ACS Appl. Mater. Interf.* **2021**, *13*, 22077–22097. https://doi.org/10.1021/acsami.1c02129.
(35) Hitihami-Mudiyanselage, A.; Senevirathne, K.; Brock, S. L. Bottom-Up Assembly of Ni_2P Nanoparticles into Three-Dimensional Architectures: An Alternative Mechanism for Phosphide Gelation. *Chem. Mater.* **2014**, *26*, 6251–6256. https://doi.org/10.1021/cm5030958.
(36) Yu, X.; Yu, Z. Y.; Zhang, X. L.; Zheng, Y. R.; Duan, Y.; Gao, Q.; Wu, R.; Sun, B.; Gao, M. R.; Wang, G.; Yu, S. H. "Superaerophobic" Nickel Phosphide Nanoarray Catalyst for Efficient Hydrogen Evolution at Ultrahigh Current Densities. *J. Am. Chem. Soc.* **2019**, *141*, 7537–7543. https://doi.org/10.1021/jacs.9b02527.
(37) Li, S.-H.; Qi, M.-Y.; Tang, Z.-R.; Xu, Y.-J. Nanostructured Metal Phosphides: From Controllable Synthesis to Sustainable Catalysis. *Chem. Soc. Rev.* **2021**, *50*, 7539–7586. https://doi.org/10.1039/d1cs00323b.
(38) Liu, P.; Rodriguez, J. A. Catalysts for Hydrogen Evolution from the [NiFe] Hydrogenase to the Ni2P(001) Surface: The Importance of Ensemble Effect. *J. Am. Chem. Soc.* **2005**, *127*, 14871–14878. https://doi.org/10.1021/ja0540019.
(39) Hansen, M. H.; Stern, L. A.; Feng, L.; Rossmeisl, J.; Hu, X. Widely Available Active Sites on Ni2P for Electrochemical Hydrogen Evolution - Insights from First Principles Calculations. *Phys. Chem. Chem. Phys.* **2015**, *17*, 10823–10829. https://doi.org/10.1039/c5cp01065a.
(40) Wexler, R. B.; Martirez, J. M. P.; Rappe, A. M. Active Role of Phosphorus in the Hydrogen Evolving Activity of Nickel Phosphide (0001) Surfaces. *ACS Catal.* **2017**, *7*, 7718–7725. https://doi.org/10.1021/acscatal.7b02761.
(41) Wexler, R. B.; Martirez, J. M. P.; Rappe, A. M. Stable Phosphorus-Enriched (0001) Surfaces of Nickel Phosphides. *Chem. Mater.* **2016**, *28*, 5365–5372. https://doi.org/10.1021/acs.chemmater.6b01437.
(42) Wexler, R. B.; Martirez, J. M. P.; Rappe, A. M. Chemical Pressure-Driven Enhancement of the Hydrogen Evolving Activity of Ni2P from Nonmetal Surface Doping Interpreted via Machine Learning. *J. Am. Chem. Soc.* **2018**, *140*, 4678–4683. https://doi.org/10.1021/jacs.8b00947.
(43) Rice, P. S.; Hu, P. Understanding Supported Noble Metal Catalysts Using First-Principles

Calculations. *J. Chem. Phys*. **2019**, 180902. https://doi.org/10.1063/1.5126090.
(44) Guharoy, U.; Ramirez Reina, T.; Olsson, E.; Gu, S.; Cai, Q. Theoretical Insights of Ni2P (0001) Surface toward Its Potential Applicability in CO2 Conversion via Dry Reforming of Methane. *ACS Catal.* **2019**, *9*, 3487–3497. https://doi.org/10.1021/acscatal.8b04423.
(45) Chen, S.; Rousseau, R.; Raugei, S.; Dupuis, M.; DuBois, D. L.; Bullock, R. M. Comprehensive Thermodynamics of Nickel Hydride Bis(Diphosphine) Complexes: A Predictive Model through Computations. *Organometallics* **2011**, *30*, 6108–6118. https://doi.org/10.1021/om200645x.
(46) Wiedner, E. S. Thermodynamic Hydricity of [FeFe]-Hydrogenases. *J. Am. Chem. Soc*. **2019**, *141*, 7212–7222. https://doi.org/10.1021/jacs.8b13084.
(47) Wiedner, E. S.; Chambers, M. B.; Pitman, C. L.; Bullock, R. M.; Miller, A. J. M.; Appel, A. M. Thermodynamic Hydricity of Transition Metal Hydrides. *Chem. Rev.* **2016**, *116*, 8655–8692. https://doi.org/10.1021/acs.chemrev.6b00168.
(48) McCarthy, B. D.; Dempsey, J. L. Decoding Proton-Coupled Electron Transfer with Potential-PKa Diagrams. *Inorg. Chem.* **2017**, *56*, 1225–1231. https://doi.org/10.1021/acs.inorgchem.6b02325.
(49) Helm, M. L.; Stewart, M. P.; Bullock, R. M.; DuBois, M. R.; Dubois, D. L. A Synthetic Nickel Electrocatalyst with a Turnover Frequency Above 100,000 S−1 for H2 Production. *Science* **2011**, *333*, 863–866. https://doi.org/10.1126/science.1205864.
(50) O'Hagan, M.; Shaw, W. J.; Raugei, S.; Chen, S.; Yang, J. Y.; Kilgore, U. J.; Dubois, D. L.; Bullock, R. M. Moving Protons with Pendant Amines: Proton Mobility in a Nickel Catalyst for Oxidation of Hydrogen. *J. Am. Chem. Soc.* **2011**, *133*, 14301–14312. https://doi.org/10.1021/ja201838x.
(51) Liao, Q.; Liu, T.; Johnson, S. I.; Klug, C. M.; Wiedner, E. S.; Morris Bullock, R.; Dubois, D. L. Evaluation of Attractive Interactions in the Second Coordination Sphere of Iron Complexes Containing Pendant Amines. *Dalt. Trans.* **2019**, *48*, 4867–4878. https://doi.org/10.1039/c9dt00708c.
(52) Wang, Y. H.; Schneider, P. E.; Goldsmith, Z. K.; Mondal, B.; Hammes-Schiffer, S.; Stahl, S. S. Brønsted Acid Scaling Relationships Enable Control over Product Selectivity from O2 Reduction with a Mononuclear Cobalt Porphyrin Catalyst. *ACS Cent. Sci.* **2019**, *5*, 1024–1034. https://doi.org/10.1021/acscentsci.9b00194.
(53) Ung, D.; Murphy, I. A.; Cossairt, B. M. Designing Nanoparticle Interfaces for Inner-Sphere Catalysis. *Dalt. Trans.* **2020**, *49*, 4995–5005. https://doi.org/10.1039/d0dt00785d.
(54) Rossi, L. M.; Fiorio, J. L.; Garcia, M. A. S.; Ferraz, C. P. The Role and Fate of Capping Ligands in Colloidally Prepared Metal Nanoparticle Catalysts. *Dalt. Trans.* **2018**, *47*, 5889–5915. https://doi.org/10.1039/c7dt04728b.
(55) Ortunõ, M. A.; López, N. Reaction Mechanisms at the Homogeneous-Heterogeneous Frontier: Insights from First-Principles Studies on Ligand-Decorated Metal Nanoparticles. *Catal. Sci. Technol.* **2019**, *9*, 5173–5185. https://doi.org/10.1039/c9cy01351b.
(56) Ung, D.; Cossairt, B. M. Effect of Surface Ligands on CoP for the Hydrogen Evolution Reaction. *ACS Appl. Energy Mater.* **2019**, *2*, 1642–1645. https://doi.org/10.1021/acsaem.9b00240.
(57) Henckel, D. A.; Lenz, O.; Cossairt, B. M. Effect of Ligand Coverage on Hydrogen Evolution Catalyzed by Colloidal WSe2. *ACS Catal.* **2017**, *7*, 2815–2820. https://doi.org/10.1021/acscatal.7b00074.
(58) Zobel, M.; Neder, R. B.; Kimber, S. A. J. Universal Solvent Restructuring Induced by

Colloidal Nanoparticles. *Science* **2015**, *347*, 292–294. https://doi.org/10.1126/science.1261412.
(59) Kroupa, D. M.; Vörös, M.; Brawand, N. P.; McNichols, B. W.; Miller, E. M.; Gu, J.; Nozik, A. J.; Sellinger, A.; Galli, G.; Beard, M. C. Tuning Colloidal Quantum Dot Band Edge Positions through Solution-Phase Surface Chemistry Modification. *Nat. Commun.* **2017**, *8*, 15257. https://doi.org/10.1038/ncomms15257.
(60) Brown, P. R.; Kim, D.; Lunt, R. R.; Zhao, N.; Bawendi, M. G.; Grossman, J. C.; Bulović, V. Energy Level Modification in Lead Sulfide Quantum Dot Thin Films through Ligand Exchange. *ACS Nano* **2014**, *8*, 5863–5872. https://doi.org/10.1021/nn500897c.
(61) Benson, E. E.; Zhang, H.; Schuman, S. A.; Nanayakkara, S. U.; Bronstein, N. D.; Ferrere, S.; Blackburn, J. L.; Miller, E. M. Balancing the Hydrogen Evolution Reaction, Surface Energetics, and Stability of Metallic MoS2 Nanosheets via Covalent Functionalization. *J. Am. Chem. Soc.* **2018**, *140*, 441–450. https://doi.org/10.1021/jacs.7b11242.
(62) Anderson, N. C.; Hendricks, M. P.; Choi, J. J.; Owen, J. S. Ligand Exchange and the Stoichiometry of Metal Chalcogenide Nanocrystals: Spectroscopic Observation of Facile Metal-Carboxylate Displacement and Binding. *J. Am. Chem. Soc.* **2013**, *135*, 18536–18548. https://doi.org/10.1021/ja4086758.
(63) Heuer-Jungemann, A.; Feliu, N.; Bakaimi, I.; Hamaly, M.; Alkilany, A.; Chakraborty, I.; Masood, A.; Casula, M. F.; Kostopoulou, A.; Oh, E.; Susumu, K.; Stewart, M. H.; Medintz, I. L.; Stratakis, E.; Parak, W. J.; Kanaras, A. G. The Role of Ligands in the Chemical Synthesis and Applications of Inorganic Nanoparticles. *Chem. Rev*. **2019**, 119, 4819–4880. https://doi.org/10.1021/acs.chemrev.8b00733.
(64) Hassinen, A.; Moreels, I.; De Nolf, K.; Smet, P. F.; Martins, J. C.; Hens, Z. Short-Chain Alcohols Strip X-Type Ligands and Quench the Luminescence of PbSe and CdSe Quantum Dots, Acetonitrile Does Not. *J. Am. Chem. Soc.* **2012**, *134*, 20705–20712. https://doi.org/10.1021/ja308861d.
(65) Ritchhart, A.; Cossairt, B. M. Quantifying Ligand Exchange on InP Using an Atomically Precise Cluster Platform. *Inorg. Chem.* **2019**, *58*, 2840–2847. https://doi.org/10.1021/acs.inorgchem.8b03524.
(66) Knauf, R. R.; Lennox, J. C.; Dempsey, J. L. Quantifying Ligand Exchange Reactions at CdSe Nanocrystal Surfaces. *Chem. Mater.* **2016**, *28*, 4762–4770. https://doi.org/10.1021/acs.chemmater.6b01827.
(67) Sluydts, M.; De Nolf, K.; Van Speybroeck, V.; Cottenier, S.; Hens, Z. Ligand Addition Energies and the Stoichiometry of Colloidal Nanocrystals. *ACS Nano* **2016**, *10*, 1462–1474. https://doi.org/10.1021/acsnano.5b06965.
(68) Nag, A.; Kovalenko, M. V.; Lee, J. S.; Liu, W.; Spokoyny, B.; Talapin, D. V. Metal-Free Inorganic Ligands for Colloidal Nanocrystals: S2-, HS-, Se2-, HSe-, Te2-, HTe -, TeS32-, OH-, and NH 2- as Surface Ligands. *J. Am. Chem. Soc.* **2011**, *133*, 10612–10620. https://doi.org/10.1021/ja2029415.
(69) Fan, J. Z.; Andersen, N. T.; Biondi, M.; Todorović, P.; Sun, B.; Ouellette, O.; Abed, J.; Sagar, L. K.; Choi, M. J.; Hoogland, S.; de Arquer, F. P. G.; Sargent, E. H. Mixed Lead Halide Passivation of Quantum Dots. *Adv. Mater.* **2019**, *31*, 1904304. https://doi.org/10.1002/adma.201904304.
(70) Hughes, B. K.; Ruddy, D. A.; Blackburn, J. L.; Smith, D. K.; Bergren, M. R.; Nozik, A. J.; Johnson, J. C.; Beard, M. C. Control of PbSe Quantum Dot Surface Chemistry and Photophysics Using an Alkylselenide Ligand. *ACS Nano* **2012**, *6*, 5498–5506.

https://doi.org/10.1021/nn301405j.
(71) Mohamed, A. A.; Salmi, Z.; Dahoumane, S. A.; Mekki, A.; Carbonnier, B.; Chehimi, M. M. Functionalization of Nanomaterials with Aryldiazonium Salts. *Adv. Colloid Interface Sci.* **2015**, *225*, 16–36. https://doi.org/10.1016/j.cis.2015.07.011.
(72) Bouden, S.; Pinson, J.; Vautrin-Ul, C. Electrografting of Diazonium Salts: A Kinetics Study. *Electrochem. commun.* **2017**, *81*, 120–123. https://doi.org/10.1016/j.elecom.2017.06.007.
(73) Adenier, A.; Cabet-Deliry, E.; Chaussé, A.; Griveau, S.; Mercier, F.; Pinson, J.; Vautrin-Ul, C. Grafting of Nitrophenyl Groups on Carbon and Metallic Surfaces without Electrochemical Induction. *Chem. Mater.* **2005**, *17*, 491–501. https://doi.org/10.1021/cm0490625.
(74) Toupin, M.; Bélanger, D. Spontaneous Functionalization of Carbon Black by Reaction with 4-Nitrophenyldiazonium Cations. *Langmuir* **2008**, *24*, 1910–1917. https://doi.org/10.1021/la702556n.
(75) Paulus, G. L. C.; Wang, Q. H.; Strano, M. S. Covalent Electron Transfer Chemistry of Graphene with Diazonium Salts. *Acc. Chem. Res.* **2013**, *46*, 160–170. https://doi.org/10.1021/ar300119z.
(76) Strano, M. S.; Dyke, C. A.; Usrey, M. L.; Barone, P. W.; Allen, M. J.; Shan, H.; Kittrell, C.; Hauge, R. H.; Tour, J. M.; Smalley. Electronic Structure Control of Single-Walled Carbon Nanotube Functionalization. *Science* **2003**, *301*, 1519–1522. https://doi.org/10.1126/science.1087691.
(77) Allongue, P.; Delamar, M.; Desbat, B.; Fagebaume, O.; Hitmi, R.; Pinson, J.; Savéant, J. M. Covalent Modification of Carbon Surfaces by Aryl Radicals Generated from the Electrochemical Reduction of Diazonium Salts. *J. Am. Chem. Soc.* **1997**, *119*, 201–207. https://doi.org/10.1021/ja963354s.
(78) Hirsch, A.; Hauke, F. Post-Graphene 2D Chemistry: The Emerging Field of Molybdenum Disulfide and Black Phosphorus Functionalization. *Angew. Chem. Int. Ed.* **2018**, *57*, 4338–4354. https://doi.org/10.1002/anie.201708211.
(79) Knirsch, K. C.; Berner, N. C.; Nerl, H. C.; Cucinotta, C. S.; Gholamvand, Z.; McEvoy, N.; Wang, Z.; Abramovic, I.; Vecera, P.; Halik, M.; Sanvito, S.; Duesberg, G. S.; Nicolosi, V.; Hauke, F.; Hirsch, A.; Coleman, J. N.; Backes, C. Basal-Plane Functionalization of Chemically Exfoliated Molybdenum Disulfide by Diazonium Salts. *ACS Nano* **2015**, *9*, 6018–6030. https://doi.org/10.1021/acsnano.5b00965.
(80) Ryder, C. R.; Wood, J. D.; Wells, S. A.; Yang, Y.; Jariwala, D.; Marks, T. J.; Schatz, G. C.; Hersam, M. C. Covalent Functionalization and Passivation of Exfoliated Black Phosphorus via Aryl Diazonium Chemistry. *Nat. Chem.* **2016**, *8*, 597–602. https://doi.org/10.1038/nchem.2505.
(81) Giannozzi, P.; Baroni, S.; Bonini, N.; Calandra, M.; Car, R.; Cavazzoni, C.; Ceresoli, D.; Chiarotti, G. L.; Cococcioni, M.; Dabo, I.; Dal Corso, A.; De Gironcoli, S.; Fabris, S.; Fratesi, G.; Gebauer, R.; Gerstmann, U.; Gougoussis, C.; Kokalj, A.; Lazzeri, M.; Martin-Samos, L.; Marzari, N.; Mauri, F.; Mazzarello, R.; Paolini, S.; Pasquarello, A.; Paulatto, L.; Sbraccia, C.; Scandolo, S.; Sclauzero, G.; Seitsonen, A. P.; Smogunov, A.; Umari, P.; Wentzcovitch, R. M. QUANTUM ESPRESSO: A Modular and Open-Source Software Project for Quantum Simulations of Materials. *J. Phys. Condens. Matter* **2009**, *21*, 395502. https://doi.org/10.1088/0953-8984/21/39/395502.
(82) Perdew, J. P.; Burke, K.; Ernzerhof, M. Generalized Gradient Approximation Made

Simple. *Phys. Rev. Lett.* **1996**, *77*, 3865–3868. https://doi.org/10.1103/PhysRevLett.77.3865.
(83) Grimme, S. Semiempirical GGA-Type Density Functional Constructed with a Long-Range Dispersion Correction. *J. Comput. Chem.* **2006**, *27*, 1787–1799. https://doi.org/10.1002/jcc.20495.
(84) Joubert, D. From Ultrasoft Pseudopotentials to the Projector Augmented-Wave Method. *Phys. Rev. B - Condens. Matter Mater. Phys.* **1999**, *59*, 1758–1775. https://doi.org/10.1103/PhysRevB.59.1758.
(85) Monkhorst, H. J.; Pack, J. D. Special Points for Brillouin-Zone Integrations. *Phys. Rev. B* **1976**, *13*, 5188–5192. https://doi.org/10.1103/PhysRevB.13.5188.
(86) Head, J. D.; Zerner, M. C. A Broyden—Fletcher—Goldfarb—Shanno Optimization Procedure for Molecular Geometries. *Chem. Phys. Lett.* **1985**, *122*, 264–270. https://doi.org/10.1016/0009-2614(85)80574-1.
(87) Kawamura, M.; Gohda, Y.; Tsuneyuki, S. Improved Tetrahedron Method for the Brillouin-Zone Integration Applicable to Response Functions. *Phys. Rev. B - Condens. Matter Mater. Phys.* **2014**, *89*, 94515. https://doi.org/10.1103/PhysRevB.89.094515.
(88) Buffard, A.; Dreyfuss, S.; Nadal, B.; Heuclin, H.; Xu, X.; Patriarche, G.; Mézailles, N.; Dubertret, B. Mechanistic Insight and Optimization of InP Nanocrystals Synthesized with Aminophosphines. *Chem. Mater.* **2016**, *28*, 5925–5934. https://doi.org/10.1021/acs.chemmater.6b02456.
(89) Kim, K.; Yoo, D.; Choi, H.; Tamang, S.; Ko, J. H.; Kim, S.; Kim, Y. H.; Jeong, S. Halide-Amine Co-Passivated Indium Phosphide Colloidal Quantum Dots in Tetrahedral Shape. *Angew. Chem. Int. Ed.* **2016**, *55*, 3714–3718. https://doi.org/10.1002/anie.201600289.
(90) Lin-Vien, D.; Colthup, N. B.; Fateley, W. G.; Grasselli, J. G. Introduction. In *The Handbook of Infrared and Raman Characteristic Frequencies of Organic Molecules*; 1991. https://doi.org/10.1016/b978-0-08-057116-4.50007-9.
(91) Mourdikoudis, S.; Liz-Marzán, L. M. Oleylamine in Nanoparticle Synthesis. *Chem. Mater.* **2013**, *25*, 1465–1476. https://doi.org/10.1021/cm4000476.
(92) Baranov, D.; Lynch, M. J.; Curtis, A. C.; Carollo, A. R.; Douglass, C. R.; Mateo-Tejada, A. M.; Jonas, D. M. Purification of Oleylamine for Materials Synthesis and Spectroscopic Diagnostics for Trans Isomers. *Chem. Mater.* **2019**, *31*, 1223–1230. https://doi.org/10.1021/acs.chemmater.8b04198.
(93) Kessler, M. L.; Starr, H. E.; Knauf, R. R.; Rountree, K. J.; Dempsey, J. L. Exchange Equilibria of Carboxylate-Terminated Ligands at PbS Nanocrystal Surfaces. *Phys. Chem. Chem. Phys.* **2018**, *20*, 23649–23655. https://doi.org/10.1039/c8cp04275f.
(94) Kuntz, K. L.; Wells, R. A.; Hu, J.; Yang, T.; Dong, B.; Guo, H.; Woomer, A. H.; Druffel, D. L.; Alabanza, A.; Tománek, D.; Warren, S. C. Control of Surface and Edge Oxidation on Phosphorene. *ACS Appl. Mater. Interfaces* **2017**, *9*, 9126–9135. https://doi.org/10.1021/acsami.6b16111.
(95) Briggs, D. X-Ray Photoelectron Spectroscopy (XPS). *Handb. Adhes. Second Ed.* **2005**, 621–622. https://doi.org/10.1002/0470014229.ch22.
(96) Rosen, E. L.; Buonsanti, R.; Llordes, A.; Sawvel, A. M.; Milliron, D. J.; Helms, B. A. Exceptionally Mild Reactive Stripping of Native Ligands from Nanocrystal Surfaces by Using Meerwein's Salt. *Angew. Chem. Int. Ed.* **2012**, *51*, 684–689. https://doi.org/10.1002/anie.201105996.
(97) Nelson, A.; Zong, Y.; Fritz, K. E.; Suntivich, J.; Robinson, R. D. Assessment of Soft

Ligand Removal Strategies: Alkylation as a Promising Alternative to High-Temperature Treatments for Colloidal Nanoparticle Surfaces. *ACS Mater. Lett.* **2019**, *1*, 177–184. https://doi.org/10.1021/acsmaterialslett.9b00089.
(98) Pankhurst, J. R.; Iyengar, P.; Loiudice, A.; Mensi, M.; Buonsanti, R. Metal-Ligand Bond Strength Determines the Fate of Organic Ligands on the Catalyst Surface during the Electrochemical CO2reduction Reaction. *Chem. Sci.* **2020**, *11*, 9296–9302. https://doi.org/10.1039/d0sc03061a.
(99) Dong, A.; Ye, X.; Chen, J.; Kang, Y.; Gordon, T.; Kikkawa, J. M.; Murray, C. B. A Generalized Ligand-Exchange Strategy Enabling Sequential Surface Functionalization of Colloidal Nanocrystals. *J. Am. Chem. Soc.* **2011**, *133*, 998–1006. https://doi.org/10.1021/ja108948z.
(100) Zollinger, H. Reactivity and Stability of Arenediazonium Ions. *Acc. Chem. Res.* **1973**, *6*, 335–341. https://doi.org/10.1021/ar50070a002.
(101) Nandiyanto, A. B. D.; Oktiani, R.; Ragadhita, R. How to Read and Interpret Ftir Spectroscope of Organic Material. *Indones. J. Sci. Technol.* **2019**, *4*. https://doi.org/10.17509/ijost.v4i1.15806.
(102) Slovetskii, V. I. IR Spectra of Nitro Compounds. *Bull. Acad. Sci. USSR, Div. Chem. Sci.* **1971**, *19*, 2086–2091.
(103) Chen, X.; Denninger, P.; Stimpel-Lindner, T.; Spiecker, E.; Duesberg, G. S.; Backes, C.; Knirsch, K. C.; Hirsch, A. Defect Engineering of Two-Dimensional Molybdenum Disulfide. *Chem. Eur. J.* **2020**, *26*, 6535–6544. https://doi.org/10.1002/chem.202000286.
(104) Menanteau, T.; Levillain, E.; Breton, T. Electrografting via Diazonium Chemistry: From Multilayer to Monolayer Using Radical Scavenger. *Chem. Mater.* **2013**, *25*, 2905–2909. https://doi.org/10.1021/cm401512c.
(105) Actis, P.; Caulliez, G.; Shul, G.; Opallo, M.; Mermoux, M.; Marcus, B.; Boukherroub, R.; Szunerits, S. Functionalization of Glassy Carbon with Diazonium Salts in Ionic Liquids. *Langmuir* **2008**, *24*, 6327–6333. https://doi.org/10.1021/la703714a.
(106) Saby, C.; Ortiz, B.; Champagne, G. Y.; Bélanger, D. Electrochemical Modification of Glassy Carbon Electrode Using Aromatic Diazonium Salts. 1. Blocking Effect of 4-Nitrophenyl and 4-Carboxyphenyl Groups. *Langmuir* **1997**, *13*, 6805–6813. https://doi.org/10.1021/la961033o.
(107) Zhou, W.; Dong, L.; Tan, L.; Tang, Q. Enhancing the Surface Reactivity of Black Phosphorus on Hydrogen Evolution by Covalent Chemistry. *J. Phys. Chem. C* **2021**, *125*, 7581–7589. https://doi.org/10.1021/acs.jpcc.1c01110.
(108) Chu, X. S.; Yousaf, A.; Li, D. O.; Tang, A. A.; Debnath, A.; Ma, D.; Green, A. A.; Santos, E. J. G.; Wang, Q. H. Direct Covalent Chemical Functionalization of Unmodified Two-Dimensional Molybdenum Disulfide. *Chem. Mater.* **2018**, *30*, 2112–2128. https://doi.org/10.1021/acs.chemmater.8b00173.
(109) Yan, E. X.; Cabán-Acevedo, M.; Papadantonakis, K. M.; Brunschwig, B. S.; Lewis, N. S. Reductant-Activated, High-Coverage, Covalent Functionalization of 1T′-MoS 2. *ACS Mater. Lett.* **2020**, *2*, 133–139. https://doi.org/10.1021/acsmaterialslett.9b00241.
(110) Kariuki, J. K.; McDermott, M. T. Formation of Multilayers on Glassy Carbon Electrodes via the Reduction of Diazonium Salts. *Langmuir* **2001**, *17*, 5947–5951. https://doi.org/10.1021/la010415d.
(111) Blanchard, P. E. R.; Grosvenor, A. P.; Cavell, R. G.; Mar, A. Effects of Metal Substitution in Transition-Metal Phosphides (Ni 1-XM′x)2P (M′ = Cr, Fe, Co) Studied by X-Ray

Photoelectron and Absorption Spectroscopy. *J. Mater. Chem.* **2009**, *19*, 6015–6022. https://doi.org/10.1039/b904250d.
(112) Van Der Heide, P. A. W. Photoelectron Binding Energy Shifts Observed during Oxidation of Group IIA, IIIA and IVA Elemental Surfaces. *J. Electron Spectros. Relat. Phenomena* **2006**, *151*, 79–91. https://doi.org/10.1016/j.elspec.2005.11.001.
(113) Voiry, D.; Chhowalla, M.; Gogotsi, Y.; Kotov, N. A.; Li, Y.; Penner, R. M.; Schaak, R. E.; Weiss, P. S. Best Practices for Reporting Electrocatalytic Performance of Nanomaterials. *ACS Nano* **2018**, *12*, 9635–9638. https://doi.org/10.1021/acsnano.8b07700.
(114) Aziz, S. T.; Kumar, S.; Riyajuddin, S.; Ghosh, K.; Nessim, G. D.; Dubal, D. P. Bimetallic Phosphides for Hybrid Supercapacitors. *J. Phys. Chem. Lett*. **2021**, *12*, 5138–5149. https://doi.org/10.1021/acs.jpclett.1c00562.
(115) Li, L.; Mai, W.; Lu, J.; Zhou, W.; Zhou, K.; Tang, Z.; Yang, L.; Cheng, S.; Chen, S. Ultrahigh-Performance Pseudocapacitor Electrodes Based on Transition Metal Phosphide Nanosheets Array via Phosphorization: A General and Effective Approach. *Adv. Funct. Mater.* **2015**, *25*, 7530–7538. https://doi.org/10.1002/adfm.201503662.
(116) Trasatti, S.; Petrii, O. A. Real Surface Area Measurements in Electrochemistry. *J. Electroanal. Chem.* **1992**, *327*, 353–376. https://doi.org/10.1016/0926-860x(96)80148-7.
(117) Wang, G.; Shi, Y.; Mei, J.; Xiao, C.; Hu, D.; Chi, K.; Gao, S.; Duan, A.; Zheng, P. DFT Insights into Hydrogen Activation on the Doping Ni2P Surfaces under the Hydrodesulfurization Condition. *Appl. Surf. Sci.* **2021**, *538*, 148160. https://doi.org/10.1016/j.apsusc.2020.148160.
(118) Laursen, A. B.; Wexler, R. B.; Whitaker, M. J.; Izett, E. J.; Calvinho, K. U. D.; Hwang, S.; Rucker, R.; Wang, H.; Li, J.; Garfunkel, E.; Greenblatt, M.; Rappe, A. M.; Dismukes, G. C. Climbing the Volcano of Electrocatalytic Activity While Avoiding Catalyst Corrosion: Ni3P, a Hydrogen Evolution Electrocatalyst Stable in Both Acid and Alkali. *ACS Catal.* **2018**, *8*, 4408–4419. https://doi.org/10.1021/acscatal.7b04466.
(119) Saadi, F. H.; Carim, A. I.; Verlage, E.; Hemminger, J. C.; Lewis, N. S.; Soriaga, M. P. CoP as an Acid-Stable Active Electrocatalyst for the Hydrogen-Evolution Reaction: Electrochemical Synthesis, Interfacial Characterization and Performance Evaluation. *J. Phys. Chem. C* **2014**, *118*, 29294–29300. https://doi.org/10.1021/jp5054452.
(120) Saadi, F. H.; Carim, A. I.; Drisdell, W. S.; Gul, S.; Baricuatro, J. H.; Yano, J.; Soriaga, M. P.; Lewis, N. S. Operando Spectroscopic Analysis of CoP Films Electrocatalyzing the Hydrogen-Evolution Reaction. *J. Am. Chem. Soc.* **2017**, *139*, 12927–12930. https://doi.org/10.1021/jacs.7b07606.
(121) Jackson, M. N.; Oh, S.; Kaminsky, C. J.; Chu, S. B.; Zhang, G.; Miller, J. T.; Surendranath, Y. Strong Electronic Coupling of Molecular Sites to Graphitic Electrodes via Pyrazine Conjugation. *J. Am. Chem. Soc.* **2018**, *140*, 1004–1010. https://doi.org/10.1021/jacs.7b10723.
(122) Oh, S.; Gallagher, J. R.; Miller, J. T.; Surendranath, Y. Graphite-Conjugated Rhenium Catalysts for Carbon Dioxide Reduction. *J. Am. Chem. Soc.* **2016**, *138*, 1820–1823. https://doi.org/10.1021/jacs.5b13080.
(123) Delley, M. F.; Wu, Z.; Mundy, M. E.; Ung, D.; Cossairt, B. M.; Wang, H.; Mayer, J. M. Hydrogen on Cobalt Phosphide. *J. Am. Chem. Soc.* **2019**, *141*, 15390–15402. https://doi.org/10.1021/jacs.9b07986.
(124) Nørskov, J. K.; Rossmeisl, J.; Logadottir, A.; Lindqvist, L.; Kitchin, J. R.; Bligaard, T.;

Jónsson, H. Origin of the Overpotential for Oxygen Reduction at a Fuel-Cell Cathode. *J. Phys. Chem. B* **2004**, *108*, 17886–17892. https://doi.org/10.1021/jp047349j.
(125) Wexler, R. B.; Martirez, J. M. P.; Rappe, A. M. Active Role of Phosphorus in the Hydrogen Evolving Activity of Nickel Phosphide (0001) Surfaces. *ACS Catal.* **2017**, *7*, 7718–7725. https://doi.org/10.1021/acscatal.7b02761.

Chapter 4. A MULTI-FUNCTIONAL INTERFACE DERIVED FROM THIOL-MODIFIED MESOPOROUS CARBON IN LITHIUM–SULFUR BATTERIES

Significant portions of the following chapter have previously been published by:

Yun Li‡, Ian A. Murphy‡, Ying Chen, Francis Lin, Xiang Wang, Shanyu Wang, Dion Hubble, Sei-Hum Jang, Karl T. Muller, Chongmin Wang, Alex K.-Y. Jen*, and Jihui Yang*. *J. Mater. Chem. A,* 2019, **7**, 13372-13381.

4.1 ABSTRACT

Lithium-sulfur (Li-S) batteries hold great promise as a next-generation energy-storage technology. Their practical application, however, is hindered by the rapid capacity fade associated with the dissolution of lithium polysulfides (LiPSs) into the organic electrolytes. In this work, we successfully impede these losses by anchoring thiol (-SH) functional groups to the nonpolar surface of a mesoporous carbon host. This new strategy increases the surface polarity of the conductive carbons and traps LiPSs inside the cathodes. By utilizing various spectroscopic methods, we investigate the mechanisms of LiPSs trapping, which originate from the electrostatic and covalent interactions of the thiol functional groups with Li^+ from the electrolytes and with S from the LiPS chains, respectively. Here, we for the first time identify the multiple bonding modes that are induced by a small molecular interface upon cycling and correlate them with the electrochemical behavior. The fundamental insight on the thiol functionality suggests a further rational design of multi-functional interfaces to achieve better Li-S performance.

4.2 INTRODUCTION

Energy storage devices with high energy density are of increasing importance due to the growing demand for smart grid energy storage systems and long-range electric vehicles.[1,2] Lithium-sulfur (Li-S) batteries have attracted broad interest due to their high theoretical specific capacity (1672 mAh g^{-1}, an order of magnitude greater than that of the current commercial $LiCoO_2$ cathode material), low environmental impact, and low cost.[3] However, the commercialization of Li-S batteries has been hindered by multiple failure mechanisms which result in rapid capacity fading upon extended cycling.[4] This capacity fade is mainly caused by the dissolution of soluble lithium polysulfides (LiPSs) redox intermediates generated during the complex multi-step charge/discharge reactions.[5,6] Approaches which aim simply to lower LiPS solubility would introduce new performance deficits such as reduced reaction kinetics and poor active material utilization.[7,8] So as not to sacrifice general performance for the sake of cyclability, the design of cathode host materials which can better retain solvated LiPSs has become an area of intense research.[9]

Initial work on LiPS trapping was focused on designing nanostructured carbon materials such as mesoporous carbon particles, carbon nanotubes (CNTs), graphene/graphene oxide sheets, etc.[10–15] Carbon materials were preferentially investigated as a means to physically confine solvated LiPSs in the host matrix due to their high electrical conductivity, large specific surface area, and ability to modulate the pore volume available for sulfur infiltration. Although these materials greatly improve cell performance, it has been found that physical confinement alone is not sufficient to prevent large capacity losses, as LiPSs will still gradually diffuse out of the porous network due to the polarity difference between non-polar carbon and polar LiPSs.[16] The non-polar carbon also introduces a new challenge, namely a poor electrolyte wetting for the thick electrodes.[16,17] Thus,

research efforts have trended towards implementing chemical functionality to further improve a host material's ability to trap LiPSs. Most approaches implement inherently polar materials such as heteroatom-doped carbon structures,[18,19] polymer coatings,[20,21] metal-organic frameworks,[22,23] metal-chalcogenide blends,[24,25] etc. Although these approaches have realized some success in improving cyclability, they often rely only on limited electrostatic interactions, suffer reduced electrical conductivity, or involve heavy/expensive nanostructures, which sacrifice the potential advantages of Li-S chemistry.[10,26,27]

With all the challenges in mind, a light-weight sulfur host material with a good electrical conductivity and improved wettability to the electrolytes, that not only confines LiPSs physically but also contains a very high accessible fraction of LiPS chemisorption sites, is well-suited to realize long-life and high-loading Li−S batteries. To achieve the goal, we suggest to chemically functionalize the relatively nonpolar surface of nanostructured carbon materials. Functionalizing graphene materials such as graphene oxide sheets decorated with hydroxyl and epoxide functional groups has been reported to possess chemical interactions with polysulfides.[28–30] However, due to the complexity of graphene materials such as the random orientation of graphene sheets and their discrepant defects, these functional groups are often unstable and it is also difficult to control their contents, which impede the mass production of functionalized graphene materials.[31–33] CNT represents another promising nanostructured carbon for use in the Li-S batteries owing to its exceptional electrical, thermal, and mechanical properties.[34–37] However, the surface modification of CNTs suffers from tedious synthetic procedure or limited scalability and the harsh reaction conditions would introduce large amounts of structural damages in carbon framework and compromise the intrinsic properties of CNTs.[34]

In this work, we select to modify a commercially available mesoporous carbon material with a thin layer of phenylthiol small molecules via a one-pot reaction where we *in-situ* generate aryl-diazonium ions.[38] This approach has many benefits including simplicity, scalability, tunability, and general applicability to any surface with the sp^2 hybridized carbon functionality. Due to the widely-studied interconversion between the thiol (S-H) and disulfide (S-S) bonding modes through intermediate thiolates ($-S^-$) and thiyl radicals (-S•),[39–42] thiol groups are chosen to potentially allow for covalent tethering of LiPSs to the surface of mesoporous carbon hosts. Furthermore, the thiol modifier could enhance the electrolyte wettability of electrodes by creating a more polar electrode surface, inducing electrostatic interactions with the solvated Li^+ ions of dissolved LiPSs, as well as lithium bis(trifluoromethanesulfonyl)imide (LiTFSI) salt in the 1,3-dioxolane/1,2-dimethoxythane (DOL/DME) based electrolytes. This effect has important implications for high-sulfur-loading cathodes, which are required for commercially viable cells and is often overlooked when discussing cathode additives/strategies.[16,17] The thiol-functionalized carbon host has not been studied probably because thiol functionality was predominantly consumed as reactive groups to prepare crosslinked organosulfur polymers in Li-S batteries.[43–45] These sulfur-rich polymers usually suffer from inherently low conductivity and require larger amounts of inert conductive additives, in addition to the inert mass added by the organic structures themselves, which detracts from the overall energy density. However, the successful cycling of these systems does provide precedent for the electrochemical formation and cleavage of S-S bonds.

This type of multifunctional interfaces between the mesoporous carbons and solvated active materials not only represents a new strategy for improving cell performance, but also raises additional questions about their roles and challenges associated with the cell performance. In Li-S batteries, it is quite challenging for most materials to identify the specific role of individual species

in cell function owing to the complexity in characterizing amorphous structures and versatile ionic species.[46] In this work, we successfully utilize solid-state Nuclear magnetic resonance (NMR) spectroscopy, X-ray photoelectron spectroscopy (XPS), and electrochemical impedance spectroscopy (EIS) to monitor the molecular motion and surface interactions of the thiol groups with active materials inside cathodes upon cycling. Moreover, we conduct a systematic study of the influence of multi-functional thiol surfaces on high-sulfur-loading (4 mg cm^{-2}) cathodes by controlling the concentration of thiol groups on the surface. Though ultimately successful in improving cyclability, our analysis reveals some inherent limitations of this particular surface modification strategy, including a slight increase in cell overpotential and kinetic limitation during discharge. We thus present future steps that might be taken to mitigate these challenges.

4.3 Experimental Detail

4.3.1 *Preparation of [SH]-Thiol MJ430 Carbon*

As-received MJ430 (Porous Carbon CNovelTM; TOYO TANSO USA, INC.) was purified by acid wash with 2M HCl in ethanol. Purified carbon powders were mixed with 5,10,15, 20, and 50 mol% 4-aminophenylthiol (Sigma Aldrich) and sonicated in anhydrous tetrahydrofuran for 20 min. This mixture was then placed in an ice bath before adding a stoichiometric equivalent of isoamylnitrite (Sigma Aldrich) and double stoichiometric equivalent of HCl to initiate *in-situ* diazotization. Initiation of the reaction should produce N_2 gas, which bubbles out of the solution. Once the gas generation has ceased, reaction mixture was heated to 70 ◦C and stirred vigorously for 12 h. Reaction products were cleaned and filtered with subsequent washes of (2:1) ethanol:ammonium hydroxide, tetrahydrofuran, water, and finally acetone. Cleaned products were then vacuum dried under high-vacuum at 90 ◦C for 12 h.

4.3.2 *Material Characterization*

Thermogravimetric analysis (TGA) was measured under a nitrogen flow of 50 mL/min with a heating rate of 10 ◦C min^{-1} to 800 ◦C by using a Mettler Toledo TFA/DSC 3+. Surface area of the samples was determined from the isotherms collected with a QUANTACHROME NOVA 2200e gas sorption system by using the BET method. The BJH method was used for the porosity and pore size analyses. Surface chemical characteristics of the samples were examined using XPS spectra were taken on a Surface Science Instruments S-Probe photoelectron spectrometer. This instrument has a monochromatized Al Kα X-ray source which was operated at 20 mA and 10 kV, and a low energy electron flood gun for charge neutralization. Pass energy for survey and detail spectra (to calculate composition) was 150 eV. Data point spacing was 1.0 eV/step for survey spectra, and 0.4 eV/step for detail spectra. Pass energy for high-resolution spectra was 50 eV, with a data point spacing of 0.065 eV. The samples were mounted on double-sided tapes that run as insulators. X-ray analysis area for these acquisitions was approximately 800 □m across. Pressure in the analytical chamber during spectral acquisition was less than 5 x 10^{-9} torr. The take-off angle (the angle between the sample normal and the input axis of the energy analyzer) was 0°, (0° take-off angle ≅ 100 Å sampling depth). Service Physics Hawk version 7 data analysis software was used to calculate the elemental compositions from peak areas measured above an inelastic scattering (Shirley) background. Powder samples were transported to instrument in air. Cycled cathode samples were disassembled in an Ar atmosphere glovebox, transferred to instrument in sealed vials, then mounted in ambient conditions. The physiochemical structures were examined using a Renishaw inVia Raman Microscope. Electrical conductivity was measured by the four-point method using a IV SourceMeter (2450, Keithley). The MJ430-S and SH-MJ430-S films were fabricated by slurry casting method on polyethylene naphthalate (PEN). Morphology and structure

of the materials were characterized using SEM (Phillips XL-30 Sirion FE-SEM with EDAX). Microstructures and compositions were analyzed by S/TEM (FEI Titan 80-300kV, USA).

4.3.3 *Preparation of MJ430-S and [SH]-MJ430-S Composites*

To impregnate sulfur into MJ430 or [SH]-MJ430 carbon for preparing MJ430-S or [SH]-MJ430-S, a mixture of 100 mg carbon and 100 mg sulfur was heated at 155 °C for 24 h in a sealed vacuum tube under Ar.

4.3.4 *Electrochemical Measurements*

The MJ430-S or [SH]-MJ430-S composite was mixed with Carbon Nanotubes (CNTs, Sigma-Aldrich) and poly(vinylidene difluoride) (PVDF; MTI Cop.) as the binder in a weight ratio of 80:10:10, in N-methyl-2-pyrrolidone (NMP; Sigma-Aldrich) as a dispersant. The slurry was cast on an Al foil current collector and dried overnight at 60 °C under vacuum. A thick cathode with 4 mg S cm^{-2} loading was prepared similarly. The slurry was casted on a C-coated Al foil current collector (MTI Corp.). 2032 coin-type cells were assembled using lithium metal (250 □m thick, Alfa Aesar) as the anode, polypropylene (PP) Celgard2500 (Celgard, LLC Corp) as the separator, and 1 M LiTFSI (Sigma-Aldrich) and 1 wt% $LiNO_3$ (Alfa Aesar) in DOL/DME (Sigma-Aldrich, v/v =1:1) as the electrolyte for each cell. The electrochemical performances of the cells were evaluated at 30 °C in a voltage window of 1.9-2.8 V vs. Li^+/Li at various C-rates using a battery tester (BT-2043, Arbin).

4.3.5 *Spectroscopic Characterization*

Electrochemical impedance spectroscopy (EIS) of Li-S cells at different discharge stages were examined using an AMETEK VersaSTAT4 Potentiostat/Galvanostat in the frequency range of 10^{-2}-10^6 Hz by applying a 5 mV ac oscillation. ^7Li, ^{19}F, and ^{13}C MAS NMR were performed on a

Varian Inova spectrometer with a 600 MHz (14.1 T) magnet, using 1.6 mm rotors operating at a spinning speed of 36 kHz. The 90˚ pulse width was 3 μs for ^{7}Li, 1.5 μs for ^{13}C, and 5 μs for ^{19}F. The ^{7}Li spectra were obtained with 640 scans, using a flip angle of 9° (a pulse width of 0.3 μs) with a recycling delay of 5 s for quantitative comparison. The ^{19}F spectra were obtained using a spin-echo pulse sequence with 48 scans and a recycling delay of 5 s. Due to the low sensitivity of ^{13}C in the naturally abundant materials, 10240 scans were used with a 30˚ pulse and a recycling delay of 5 s. Temperature was maintained at 25 ˚C for all NMR measurements. For the preparation of the first set of samples, 0.6 ml of 0.1M Li_2S_8 in DME was added to 20 mg MJ430/20% SH-MJ430 carbon material to form a homogenous slurry. Both slurries with MJ430/20% SH-MJ430 carbon material were dried for 12 h in a glove box to form concentrated samples and then packed into the NMR rotors. For the second series of samples, the cycled coin cells were disassembled at different voltage stages in a glovebox, and the composites were scratched off from the cathodes immediately and filled into the NMR router.

4.4 Results and Discussion

4.4.1 *Introduction of SH-MJ430*

As a platform to investigate our multifunctional interface, a commercially available mesoporous carbon host referred to as MJ430 was utilized, with an average surface area of 689 m^2 g^{-1}. A schematic depiction of our approach to confine active materials in the MJ430 pores using a multifunctional thiol surface modifier (SH-MJ430) is shown in Fig. 1. In our proposed strategy, there are three unique interactions occurring at the cathode interface which contribute to an increase in cell performance. The first is an electrostatic “lithium bond” between solvated Li^+ in the LiTFSI electrolyte and lone pairs on the reduced phenylthiolate moiety ($-S^-$). The second is a similar lithium bond involving the solvated Li^+ tails of dissolved LiPS. Finally, the third interaction

is described as covalent disulfide bonding that is formed between -S^- (or phenylthiyl radicals -S•) and LiPSs. Evidence supporting each of these proposed interactions are present in the following sections.

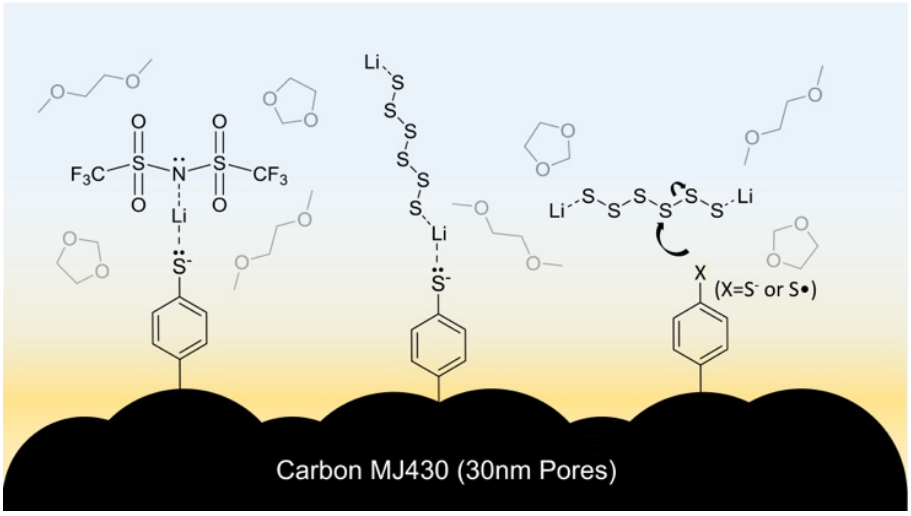

Figure 4.1. Schematic depiction of the multiple interactions of thiol surface modifiers with solvated active materials. Proposed mechanisms include electrostatic interactions with Li^+ (left, middle), covalent disulfide bonding (right), and the subsequent attraction of solvent molecules to these aggregated charges.

4.4.2 *Characterization of Functionalized SH-MJ430 Cabron*

The functionalization of conductive carbon surfaces is made possible by a one-pot synthetic strategy that utilizes *in-situ* generated diazonium ions from common and inexpensive organic precursors.[38] We prepared a series of samples in which the concentration of surface modifiers was varied between 0 and 20 wt%. A mechanistic schematic of this reaction is shown in Figure 4.2.

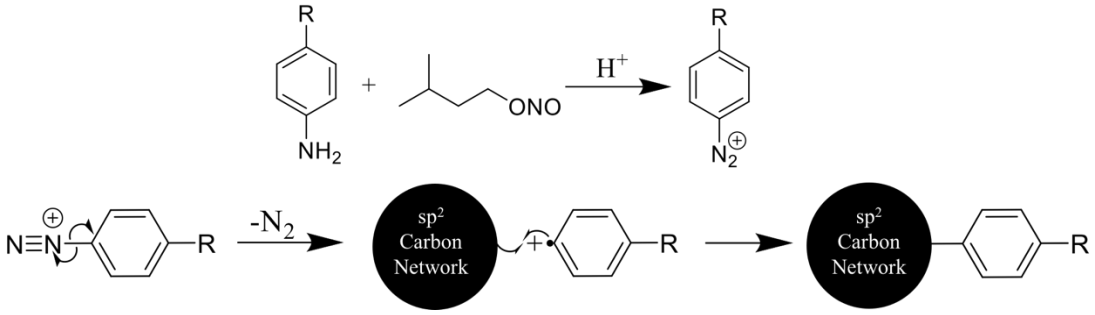

Figure 4.2. Schematic of *in-situ* functionalization of modifiers ("R"=SH) onto the surface of MJ430 carbon *via* diazotization. The diazonium ions dissociate into N_2 gas and a phenylthiol radical, which can react with sp^2-hydridized carbon frameworks to form sp^3 C-C bonds. This approach is advantageous for many applications because of the ability to tune the functionality of grafted small molecules, as well as controlling the degree of functionalization.

We sought to confirm the functionalization by both physical and spectroscopic analyses, all of which are reported in Figures 4.3 and 4.7. For these experiments, all "pristine" control samples were exposed to the same reaction conditions, barring the organic nitrite reagent which is necessary for diazotization. This was done to ensure the presence of functional groups was due to covalent anchoring to the surface, rather than physisorption or trapping of thiol precursors in the carbon pores. The addition of mass to carbon particles after a series of surface modification was tested by TGA (Figure 4.3a). It was found that a maximum of ~ 20 wt% of mass could be added to pristine particles, as attempts to push reaction equilibrium even further towards functionalization (e.g. by adding 50 mol% diazonium precursors) yielded little additional mass increase (Figure 4.4）

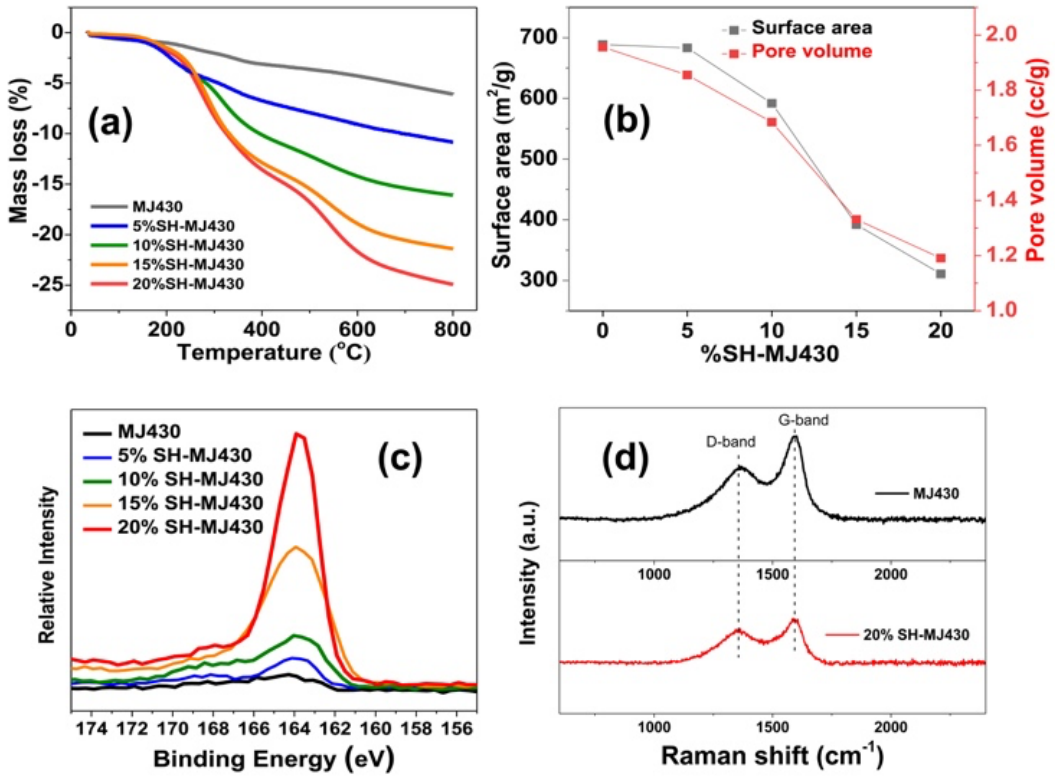

Figure 4.3. Characterization of functionalized [SH]-MJ430 carbons ([SH] = 0, 5, 10, 15, 20 wt% SH), controlled via reaction conditions. (a) TGA analysis, (b) surface area and total pore volume attained from the N_2 isotherms analysis, and (c) XPS S_{2p} spectra of a series of [SH]-MJ430 carbons. (d) Raman spectra of MJ430 and 20% SH-MJ430 carbons.

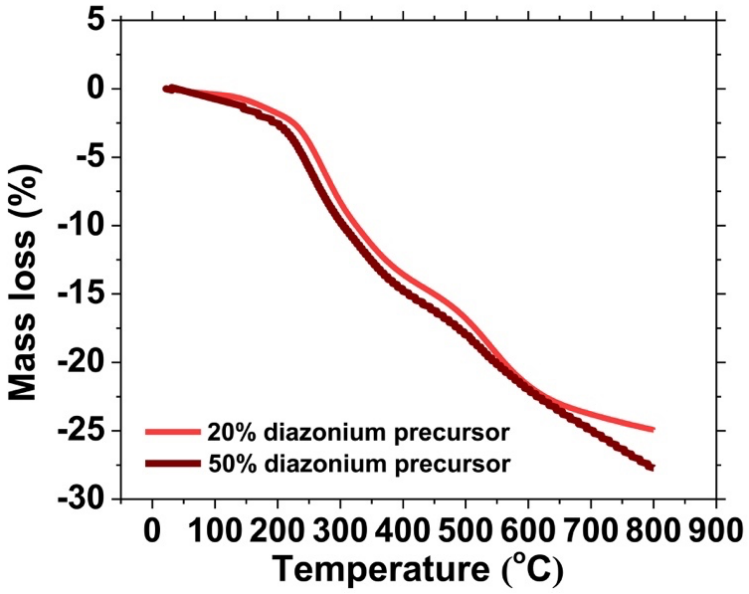

Figure 4.4. TGA of resultant modified MJ430 carbons from mixing purified MJ430 with 20 and 50 mol% diazonium precursors, respectively. The former displays a 25 wt% of overall mass loss (20 wt% among which comes from the modifiers), while the latter only shows a 3% increase of overall mass loss with overwhelmingly addition of diazonium precursors.

This finding may be attributed to a combination of precursor reactivity and the finite surface area readily available for attachment,[47] which would be optimized in the future such as by selecting other promising nanostructured carbons. Next, we confirmed that modifiers lined the pores of the host substrate through analysis of N_2 adsorption/desorption isotherms at 77K (Figure 4.5).

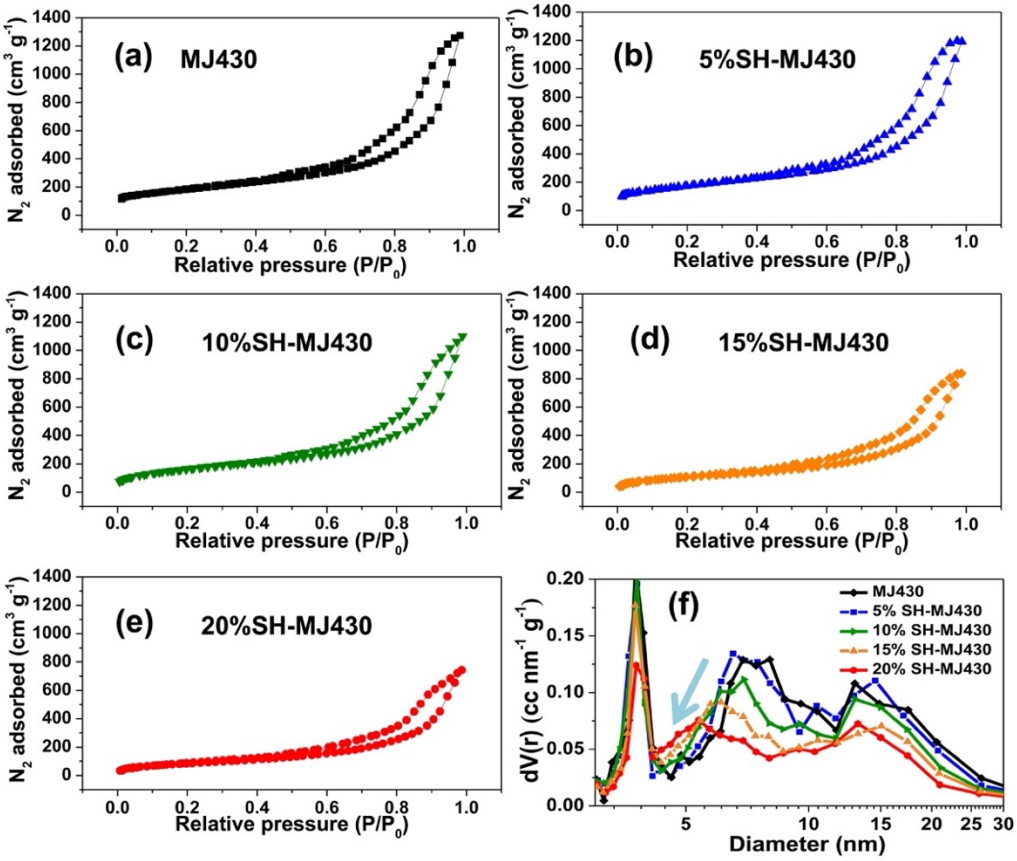

Figure 4.5. The N_2 isotherms at 77 K for the (a) MJ430, (b) 5% SH-MJ430, (c) 10% SH-MJ430, (d) 15% SH-MJ430, (e) 20% SH-MJ430 carbon and (f) their relating pore size distribution. The distribution plot of MJ430 reveals that mesoporous carbon MJ430 has three pore types. These pore types originated from capillary condensation in micropores (from the carbon walls), primary mesopores, and secondary mesopores (from interparticle capillary condensation),[1] with pore diameters of approximately 3.8, 7.4, and 13.5 nm, respectively. After surface modification, the primary mesopores decrease from 7.4 to 5.4 nm, as shown with the arrow.

From these N_2 isotherms with Brunauer-Emmett-Teller (BET) and Barrett-Joyner-Halenda (BJH) analysis, an average surface area decreases from 689 to 310 m^2 g^{-1} and a total pore volume (including all types of pores) decrease from 1.96 to 1.19 cc g^{-1} was observed after maximal

modification (Figure 4.3b). The pore size distribution plots reveal a gradual decrease in the primary mesopore size from 7.4 to 5.4 nm (Figure 4.5f). Moreover, the surface chemical composition of [SH]-MJ430 carbons was determined by XPS. The comparison of S_{2p} XPS spectra (Figure 4.3c) clearly shows an increase in the S signal (observed at 164 eV) as the concentration of precursors is increased. Figure 4.3c is a detailed scan with a relatively low resolution (150 eV pass energy), which is meant to illustrate the intensity of the S signal. The high-resolution S_{2p} spectra (50 eV pass energy) are shown below in Figures 4.6c and 4.6e.

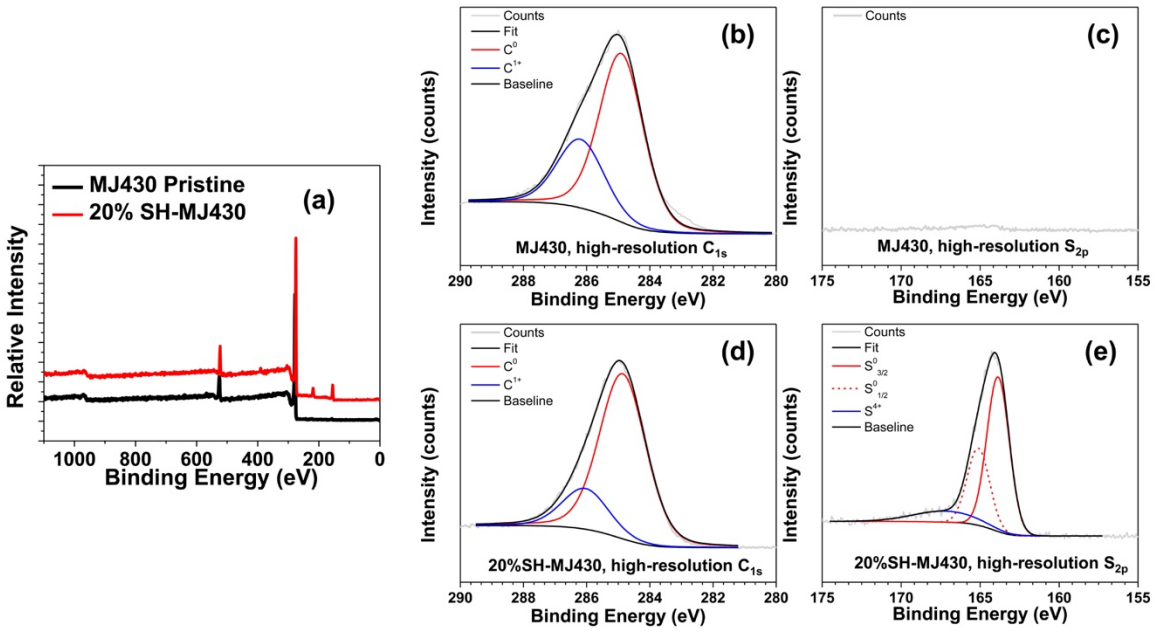

Figure 4.6. (a) XPS wide spectra of MJ430 and 20% SH-MJ430 (O_{1s} 529-535 eV, C_{1s} 284-289 eV, S_{2s} ~ 220 eV, S_{2p} 161-169 eV). High-resolution C_{1s} and S_{2p} spectra of (b,c) MJ430 and (d,e) 20%SH-MJ430 carbon.

They suggest that only after exposure to the diazonium ions, a doublet peak centered at 164 eV can be observed, reflecting the anticipated spin-orbit splitting of an aryl-thiol species after modification.[48] In Figure 4.6a, characteristic peaks of C and O atom clearly appear in both MJ430 and 20% SH-MJ430 spectra, which is to be expected from mesoprorous carbons. Upon further

analysis of high-resolution C_{1s} spectra (Figures 4.6b and 4.6d) a larger contribution of C-C signal in the 20% SH-MJ430 sample presumably results from the addition of C-C from the phenylthiol modifiers to MJ430. Finally, we tested for the degree of defects or disorders in the MJ430 mesoporous carbon before/after thiol modification by Raman spectrum in Figure 4.3d. The intensity ratio of the D (~ 1357 cm^{-1}) and G (~ 1590 cm^{-1}) bands, I_D/I_G, slightly increases from 0.54 to 0.76 after the thiol modification, representing an increased defects/disorders of the mesoporous carbon and a decreased average size of the sp^2 conjugated domains in the carbon.[37,49] The relatively low increase in I_D/I_G value implies that our method results in limited damage to the conjugated structure of the pristine carbon matrix.[34,38] After thiol functionalization, the electrical conductivity of the cathode decreased slightly from 1.51 to 0.50 S cm^{-1}, but this value is still sufficiently high to make an electrochemically active electrode.[50]

Additional insight into how modification affects the physical nature of carbon particles was gained by imaging them using scanning electron microscopy (SEM) and scanning/transmission electron microscopy (S/TEM). No significant difference in carbon morphology was observed by SEM after modification, as is shown in Figures 4.7a and 4.7d. TEM images show that the transparent mesopores in MJ430 (Figures 4.7b, 4.7c, and 4.8a) have turned into slightly turbid mesopores with thicker carbon walls after the thiol modification (Figs. 4.7e, 4.7f, and 4.8b), revealing a thin multi-layer of phenylthiol modifiers. This multi-layer structure likely results from hyper-branching of diazonium intermediates during modification, a known process in this type of reaction.[51] The average thickness of the carbon walls was visibly seen to increase by about 1.4 nm, from 1.82 nm to 3.22 nm, which agrees reasonably well with the reduced pore size presented in Figure 4.5f.

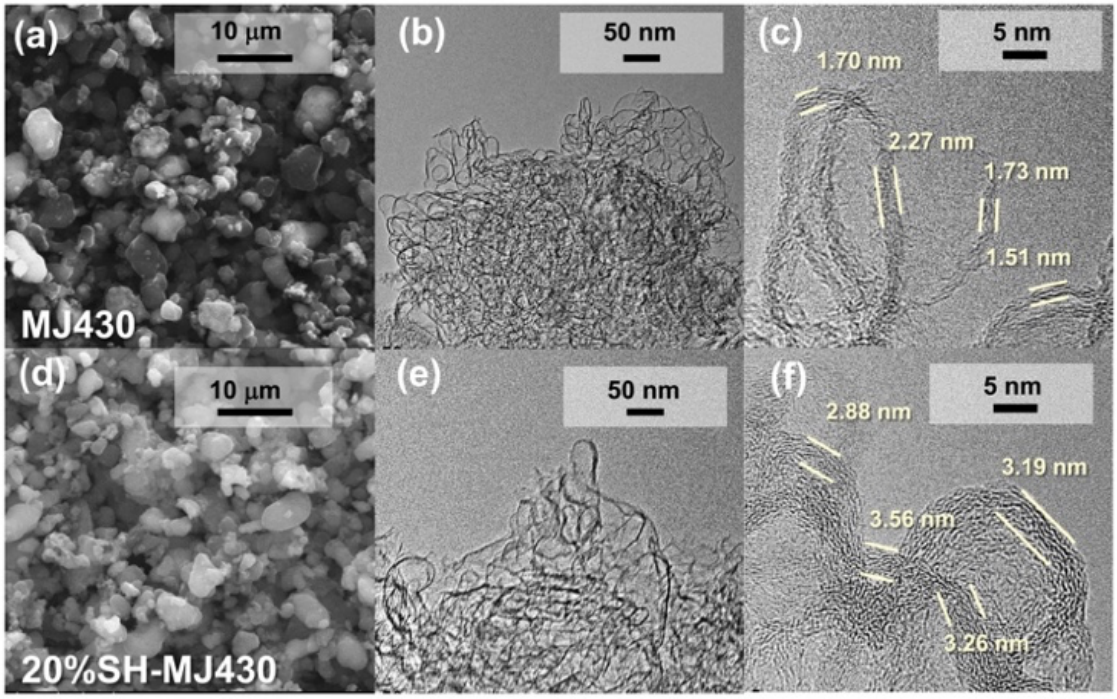

Figure 4.7. SEM and TEM images of (a-c) MJ430 and (d-f) 20% SH-MJ430.

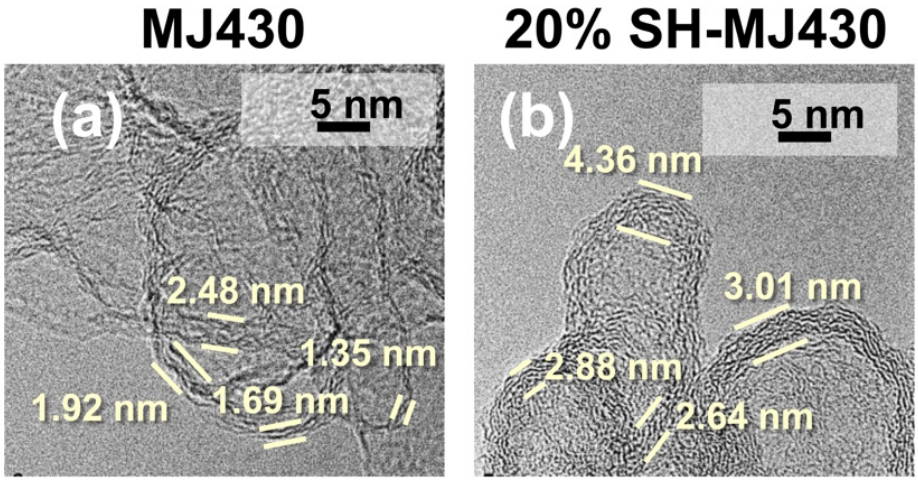

Figure 4.8. More TEM images of (a) MJ430 and (d) 20% SH-MJ430.

4.4.3 *Electrochemical Performance of Li-S Batteries with SH-MJ430-S Cathodes*

After characterization of the functionalized [SH]-MJ430 carbon, sulfur was infused into MJ430 and [SH]-MJ430 carbon to form MJ430-S and [SH]-MJ430-S composites. The exact weight content of sulfur in the composites was determined by TGA as shown in Figure 4.9.

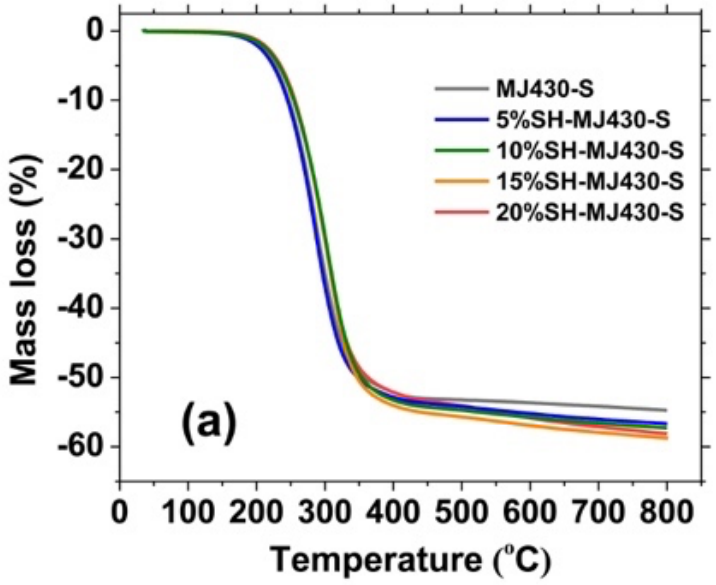

Figure 4.9. TGA of a series of [SH]-MJ430-S composites with an increasing weight percentage of the thiol modifier from 0% to 20%, controlled via reaction conditions.

The discharge/charge voltage profiles of MJ430-S and 20% SH-MJ430 cathodes at 0.05 C for the first 2 activation cycles and at 0.25 C for the following cycles (1C=1672 mA g^{-1}) are shown in Figure 4.10. Initially, a sulfur loading of ~ 1 mg cm^{-2} was utilized to compare with reported work on Li-S batteries, most of which use very thin (< 2 mg cm^{-2}) S electrodes.[10,24,43,44] The voltage profile features of the electrodes reflect those expected of a Li-S system, consisting of two discharge plateaus at 2.4 V and 2.1 V.[52] It is generally accepted that the upper plateau is related to a solid-liquid two phase conversion from elemental S_8 to long-chain $Li_2S_{(8,6)}$, while the lower is

associated with a transition from liquid to solid-phase species as soluble chains are reduced to insoluble discharge products, $Li_2S_{(2,1)}$. In the initial charge process, the MJ430-S cathode shows an obvious overcharging behavior at 2.37 V, which is attributed to the occurrence of redox shuttling of dissolved LiPSs.[53,54] Briefly, the dissolved LiPSs escaping from the cathode, are continuously reduced at the anode and oxidized at the cathode, shuttling back and forth between each event. This behavior is inhibited in the 20% SH-MJ430-S cathode indicating an efficient protection of LiPS diffusion from the cathode to the Li anode, due to the interactions of the SH modifiers with LiPSs. Figure 4.10b compares the corresponding long-term cycling performance of MJ430-S and 20% SH-MJ430-S cathodes. As expected, the modified cathode displays an obvious improvement in capacity retention. The capacity of the unmodified MJ430-S decreased from 812 to 486 mAh g^{-1} at 0.25 C (a capacity retention of 60%) after 300 cycles. Over the same number of cycles, the 20% SH-MJ430-S cathode shows a capacity retention of 89%, with the discharge capacity dropping from 838 to 745 mAh g^{-1}.

The enhanced capability of LiPS trapping in the 20% SH-MJ430-S cathode (1 mg S cm^{-2}) due to our modified surface allows us to address critical concerns in developing high-S-loaded Li-S cells, providing an effective means to increase areal capacity of the resultant batteries. The thiol modifier could also enhance the electrolyte wettability of electrodes by creating a more polar electrode surface, which is equally beneficial for the high-sulfur-loading cathodes. This point is addressed in more detail later on. The electrochemical performance of MJ430-S and 20% SH-MJ430-S cathodes with a high sulfur loading of 4 mg cm^{-2} is evaluated in Figures 4.10c and 4.10d. In Figure 4.10c, the thick MJ430-S and 20% SH-MJ430-S cathodes deliver higher discharge capacities than the thin electrodes in Figure 4.10a, due to the improved electrical conductivity of C-coated Al foil current collectors used in our high loading cells. More interestingly, the decreased coulombic

efficiency of MJ430-S and 20% SH-MJ430-S cathodes (Figure 4.10d) suggests a severe dissolution of LiPSs in the thick cathodes. After 180 cycles, the MJ430-S cells show a poor cycling retention of 56% at 0.25C (556 mAh g^{-1}, Figure 4.10d), whereas the capacity retention in the 20% SH-MJ430-S cells remains at 87% (865 mAh g^{-1}, Figure 4.10d). We attribute the enhanced capacity retention of 20% SH-MJ430-S cells to the improved wettability and the restriction of LiPS dissolution in the modified cathode.

The rate capability of MJ430-S and 20% SH-MJ430-S cells is exhibited in Figures 4.10e and 4.10f. The discharge capacities of 20% SH-MJ430-S at 0.05, 0.25, 0.5, 1, and 2C are 1121, 956, 811, 537, and 270 mAh g^{-1}, respectively. Upon close examination of the discharge curves of MJ430-S and 20% SH-MJ430-S cells, we can find an increased polarization in 20% SH-MJ430-S compared to MJ430-S especially for the second discharge plateau. This difference of the second discharge plateau is consistent with the distinction in the cyclic voltammogram of MJ430-S and 20% SH-MJ430-S cells (Figure 4.11). After modification, a distinction is recognized that the second reduction peak (~ 2.05 V for the MJ430-S) becomes broad and is shifted to ~ 2.02 V, which indicates that the thiol interface plays a significant role on the reduction of soluble LiPSs. The mechanism by which LiPSs dissolve and disproportionate will be further explored in following sections. Furthermore, to investigate the relationship between the thiol modifiers and the resultant electrochemical overpotentials, the electrochemical performance of [SH]-MJ430-S cathodes ([SH]= 0, 5, 10, 15, 20 wt% SH) is investigated in Figures 4.12a and 4.12b. A gradual reduction in overpotential was observed as the concentration of SH modifier decreases (Fig. S6b, ESI†), whereas 20wt% SH-MJ430-S still displays the highest discharge capacity after long-term cycling (Figure 4.12b). Moreover, the SEM images of cycled 20% SH-MJ430-S cathodes (Figure 4.13) show less pulverization of carbon particles upon repeated cycling, suggesting that the amorphous

surface film produced by our modifiers can also enhance the long-term mechanical integrity of the electrode.

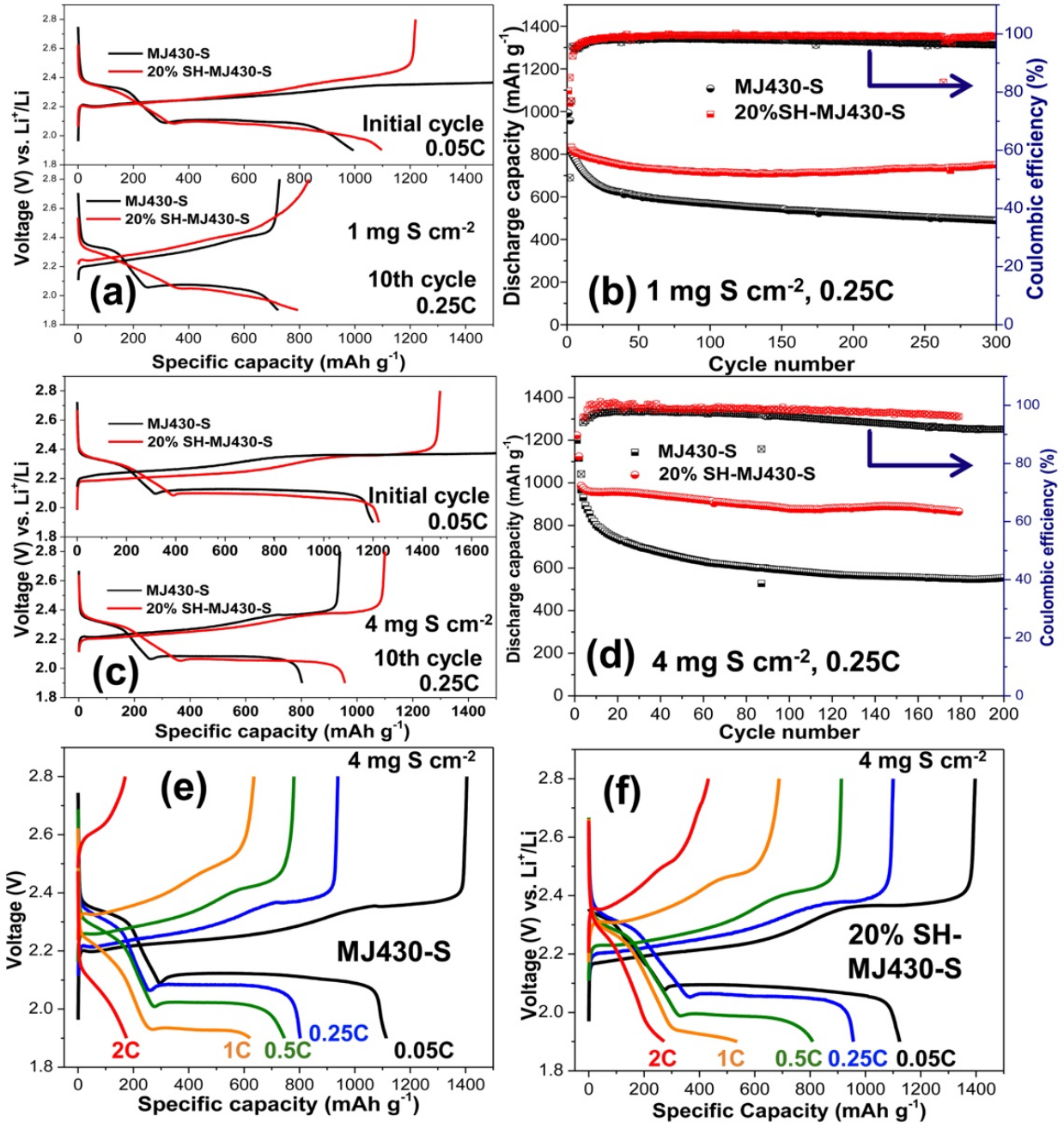

Figure 4.10. a) The discharge/charge voltage profiles of MJ430-S and 20% SH-MJ430-S electrodes based on a S loading of 1 mg cm^{-2} at the initial activation cycle (0.05 C) and the 10th cycle (0.25C) and (b) the corresponding cycling performance within the first 300 cycles. (c) The

discharge/charge voltage profiles and (d) the corresponding cycling performance of MJ430-S and 20% SH-MJ430-S electrodes based on a S loading of 4 mg cm^{-2}. The discharge/charge voltage profiles of (e) MJ430-S and (f) 20% SH-MJ430-S electrodes at various rates

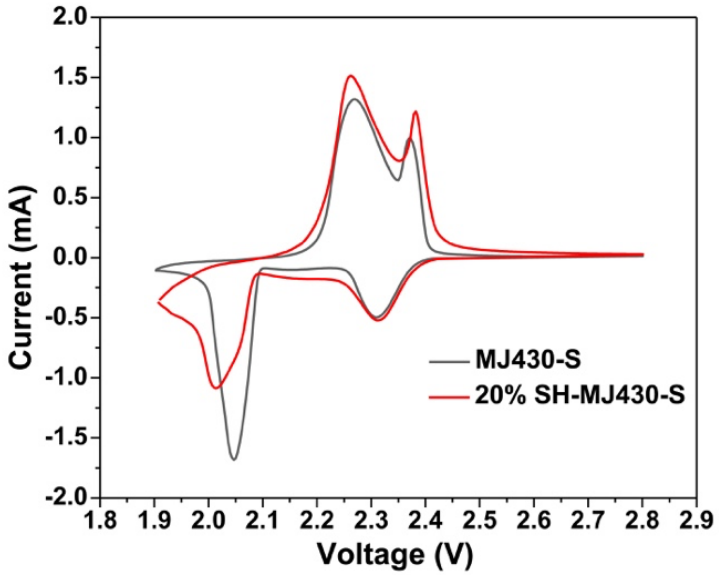

Figure 4.11. CV of the Li-S cells using MJ430-S and 20% SH-MJ430-S cathodes at the seep rate of 0.02 mV s^{-1}.

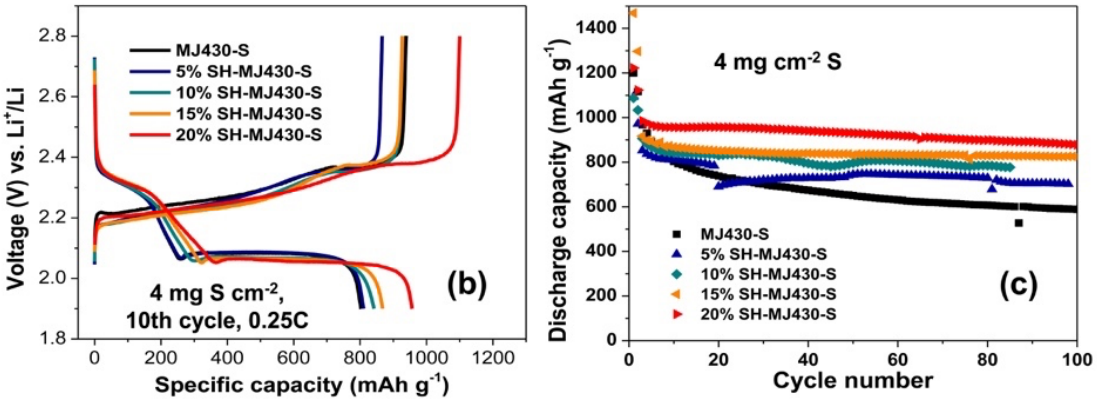

Figure 4.12. (a) Charge/discharge voltage profiles and (b) cycling performance of [SH]-MJ430-S composite electrodes with thiol modifeier loadings of 0-20%.

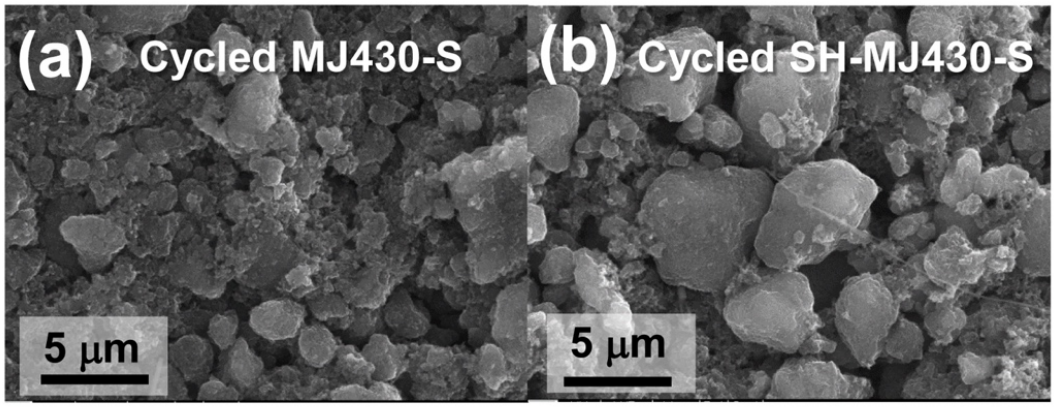

Figure 4.13. SEM images of (a) MJ430-S and (b) 20% SH-MJ430-S cathode discharged to 1.9 V after long-term cycling.

In the future, we will explore the surface modification of other highly sp^2-hybridized carbons (e.g. CNTs) to provide an interconnected conductive scaffold, reduce polarization, and achieve higher energy densities in particular for the long-term cycle performance of Li-S batteries. In this work, however, considering the complexity of surface modification of CNTs and graphene as mentioned in the introduction, we adopt the mesoporous carbon matrix as the platform to isolate the additional effects of CNTs and graphene on the SH-modified cells, even though the mesoporous carbon matrix would compromise the overall cycling performance of Li-S batteries.

4.4.4 *Spectroscopic Analysis of Interactions between Solvated Active Species and Electrode Surface*

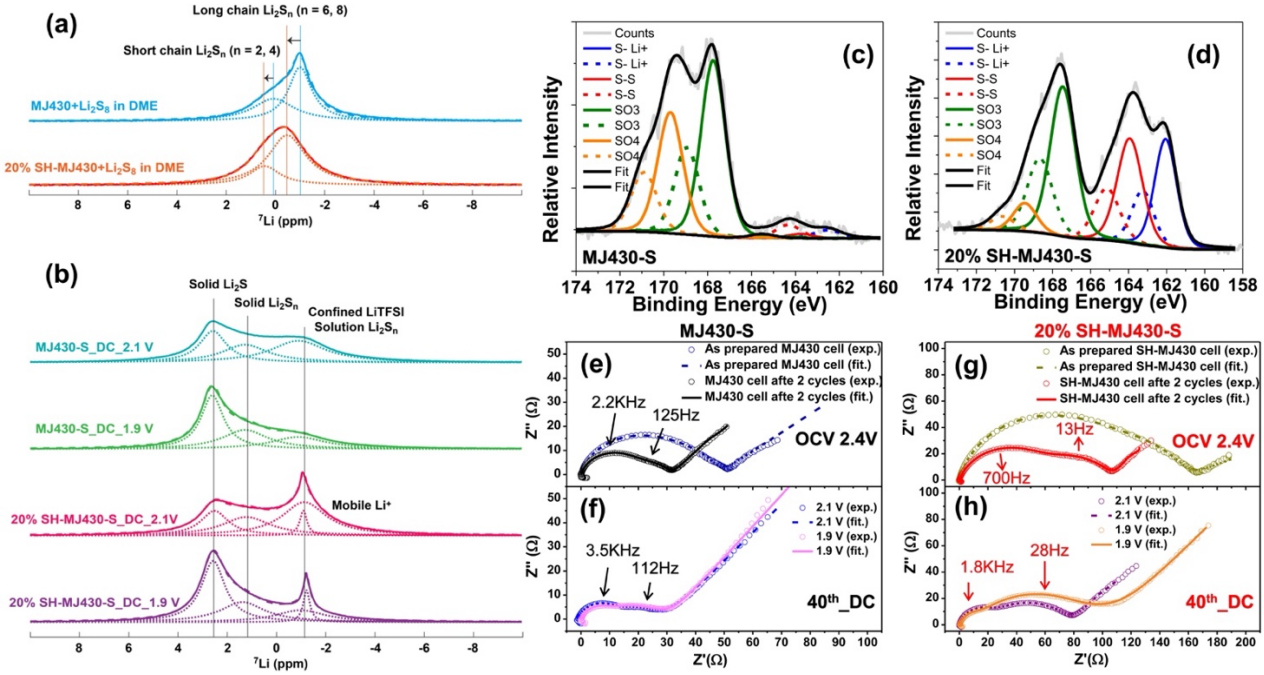

Figure 4.14. a) ^{7}Li MAS NMR spectra of Li_2S_8 solution interacting with the MJ430 and 20% SH-MJ430. (b) ^{7}Li MAS NMR spectra of cathode materials with the MJ430-S and 20% SH-MJ430-S from Li-S cells that are discharged to different voltages, with experimental data in solid lines, deconvolution peaks in dot lines, and the sum of deconvolution peaks in dash lines. High resolution S_{2p} XPS spectra of (c) MJ430-S and (d) 20% SH-MJ430-S cathodes, obtained from Li-S cells discharged to 1.9 V after 100 cycles, where solid and dashed lines represent the high and low spin-orbit doublets, respectively. EIS analysis of (e-f) MJ430-S and (g-h) 20% SH-MJ430-S cells at different stages of discharge within 40 cycles.

4.4.4.1 NMR and Contact Angle Analysis

As discussed above, the improved capacity retention of MJ430-S cathodes with thiol modifiers is presumed to strongly correspond to the multifunctional interactions on the thiol surface, especially during the second discharge stage. To verify our postulated electrostatic interactions of the thiol groups with active materials, solid-state magic angle spinning (MAS) NMR was performed on

various samples to reveal the changes in the atomic environments. Here ^{7}Li, ^{13}C, and ^{19}F NMR were collected on two sets of samples to probe the various possible interactions. In the first set, the ^{7}Li spectra shows the interactions of MJ430/20% SH-MJ430 carbon with a concentrated Li_2S_8 solution in DME. In Figure 4.14a, the spectra of both samples can be fit using two Lorentzian peaks. Here we assign the upfield resonance at -1 ppm to long chain Li_2S_n (n = 6, 8), and the downfield resonance at around 0 ppm to its short chain byproducts Li_2S_n (n = 2, 4) of the dynamic equilibrium in LiPS solutions.[55] It has been both theoretically and experimentally documented that Li^+ coordinated by the Lewis-basic donors results in a downfield shift of around 0.5 ppm.[56] As such, the 0.5ppm shift observed in Figure 4.14a (from MJ430 to 20% SH-MJ430) was attributed to be the formation of electrostatic Li bonds between the terminal Li in LiPSs and the filled p-orbitals of S from the thiol surface. This result suggests that our surface modifiers can interact with LiPSs in organic solvents even without applying an external bias to electrochemically drive disulfide bonding.

To further understand the effect of a thiol surface on battery performance, our second set of samples are cathode materials from cycled cells discharged to different voltages (1.9 V and 2.1 V). All the samples are acquired without them being washed to capture both soluble and insoluble species. Figure 4.14b shows ^{7}Li MAS NMR spectra after normalizing to the weight of active materials packed in rotors. While the resonances at 2.5 ppm and 1.2 ppm are attributed to solid Li_2S and solid Li_2S_n, respectively,[57] the relatively broad peak at -1 ppm includes the signals from solution Li_2S_n and LiTFSI that is confined on the carbon surface or inside the nanoscale pores.[7] ^{19}F signal at around -80 ppm and 13C signal at -121 ppm in Figure 4.15 both confirm the presence of confined LiTFSI solution.

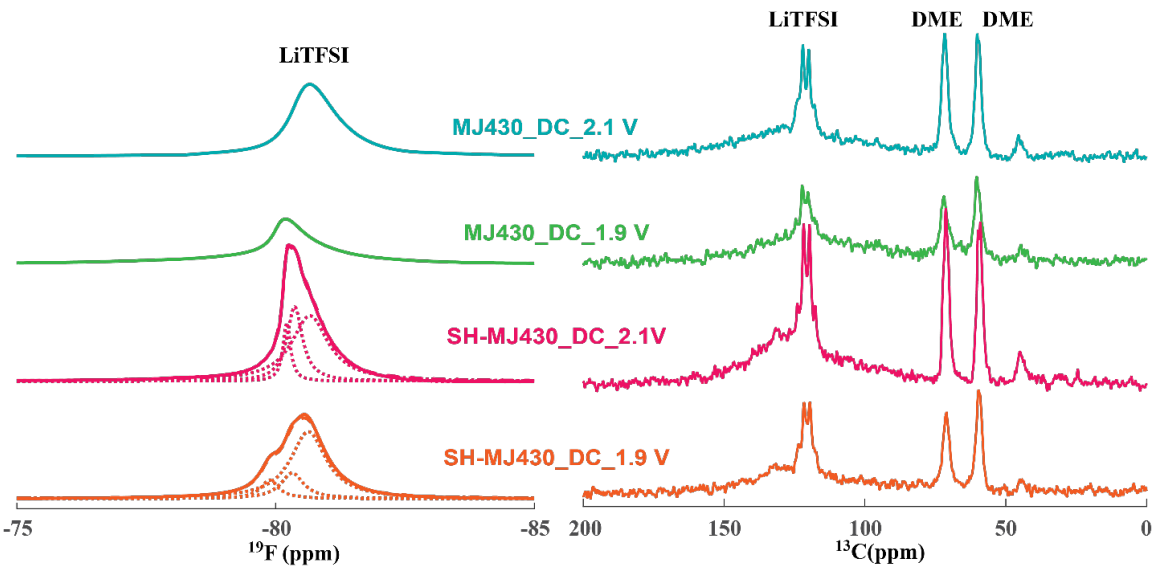

Figure 4.15. ^{19}F (left) and ^{13}C (right) MAS NMR spectra of cathode materials with the MJ430-S (top two) and 20% SH-MJ430-S (bottom two) from Li-S batteries that are discharged to different voltages.

The relatively sharp ^{7}Li signal at around -1 ppm (Figure 4.14b) shown only in 20% SH-MJ430-S suggests the existence of mobile Li^+ species surrounded by solvent molecules in the modified cathodes. As a result, the existence of mobile Li^+ species implies that the surface modification improves integration of electrolyte into the cathode matrix, probably due to the dipole-dipole interaction of thiol groups with solvated Li^+ and with polar molecules or moieties from the electrolyte. The improved wettability was further confirmed by the contact angle analysis in Figure 4.16, which suggests stronger adhesion between the electrolyte and the 20% SH-MJ430-S than that at the electrolyte and the MJ430-S interface.

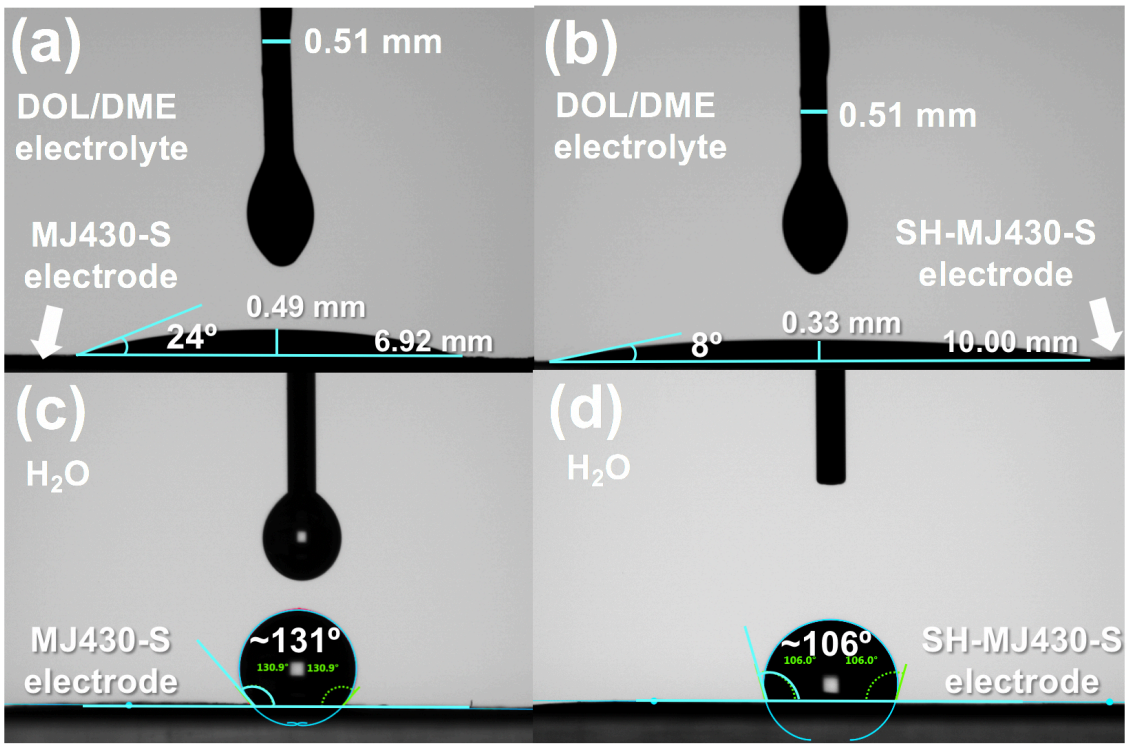

Figure 4.16. contact angle analysis of (a) MJ430-S and (b) 20% SH-MJ430-S cathode with LiTFSI-DOL/DME electrolyte, as well as (c) MJ430-S and (d) 20% SH-MJ430-S cathode with H_2O. The photographs were obtained by dropping the same amount of electrolyte or H_2O onto the MJ430-S/20% SH-MJ430-S electrode. The angle at the electrolyte/MJ430-S electrode interface is 24°, while that at the electrolyte/20% SH-MJ430-S electrode interface is 8°. This suggests stronger adhesion between the electrolyte and the 20% SH-MJ430-S than that at the electrolyte and the MJ430-S interface, which would significantly confine the LiTFSI-DOL/DME electrolyte with dissolved LiPSs inside the cathode. The different contact angle at the H_2O/MJ430-S and H_2O/20% SH-MJ430-S interface also verify the improved wettability of modified SH-MJ430-S cathode.

This effect could lead to improved utilization of active materials during cycling, since better access to the electrolyte within pores would aid in solvation and confinement of solvated LiPSs. It is consistent with the integration area of each deconvolution peak in Figure 4.14b, which shows that the amount of LiPSs and LiTFSI increases by 50% in the modified electrode when discharged to 2.1 V and these LiPSs are further reduced to solid Li_2S at 1.9 V increasing the accumulation of Li_2S. The downfield chemical shift at -1 ppm in the powder materials (Figure 4.14a) is not observed in the cycled cells (Figure 4.14b), perhaps due to the fact that Li^+ is in great excess to the SH-thiol modifiers in the cycled cells (~ 1 Li^+ to 0.1 SH). Therefore, the electrostatic Li bond does not contribute as significantly as in the powder materials where Li^+ is comparable to the SH-thiol modifiers (~ 1 Li^+ to 1.6 SH).

4.4.4.2 XPS

With strong evidence to support the reaction mechanisms through changes in Li^+ environment, we utilized XPS to spectroscopically identify changes of sulfur speciation in cycled cathodes. Although S_{2p} high-resolution analysis can determine the difference between S-S bonds (S^0; 164eV) and S^-Li^+ bonds (S^{-1}; 161eV),[58] it cannot distinguish between physiosorbed and chemically anchored S species. Thus, to minimize convolution from non-surface bound sulfur species, cycled cathodes were thoroughly washed with DOL/DME to remove any soluble sulfur species, which presumably includes all polysulfides not bound to the surface. The comparative photoelectron spectra of modified and pristine cathodes are shown in Figures 4.14c and 4.14d. The successful removal of non-surface-bound sulfur species was confirmed by the unmodified cathode spectrum, Figure 4.14c. Only very minor photoelectron signals at 161 or 164 eV, which correspond to the tail and core sulfur species of LiPS, respectively, are detectable, indicating that virtually all free LiPSs has been removed. This is in contrast with the spectra in Figure 4.14d, which shows a large

signal for both states of sulfur, suggesting that despite thorough washing, LiPS chains remain tethered to the electrode surface with the thiol modifiers via covalent disulfide bonds. Further, the absence of Li_2S (S^{-2}; 160eV)[59] from the washed electrodes lends support to our proposed bonding mechanism in scheme 1, where polysulfide chains are bound between phenylthiol and a Li^+ tail. During repeated discharge/charge processes, the thiol modifiers are primarily regarded as thiolates ($-S^-$) and thiyl radicals (-S•) in the electrochemical system.[41] The oxidized species in both XPS samples were not studied the same extent; however, thiosulfate species have been documented to have binding energies of 167 eV, which agree nicely with the observed peak at 167.5 eV.[58, 59] In these studies, Nazar et al. showed that the introduction of these species is reliant on cathode additives having a sufficiently positive oxidation potential, within the range of 2.4-3.05V vs Li/Li^+. They found that graphene-oxide formed thiosulfate species, which may explain the observation of such species in Figure 4.14c. We speculate that this phenomenon is enhanced, based on the much larger intensity in Figure 4.14d, by the phenylthiol modifiers which also have a sufficient oxidation potential of ~3.1V vs Li/Li^+.[60] Lastly, we expect that the signal at 169.5 eV is from persistent LiTFSI.[61]

4.4.4.3 Electrochemical Impedance Spectroscopy

In our cells, we observe an additional rate-dependent overpotential in modified cathodes (Figures 4.10a and 4.10c), which is indicative of a kinetic-limiting chemical reaction occurring as a result of thiol modification. To further discern this influence, EIS was performed on the cells with/without SH modifiers at different stages of discharge within 40 cycles. The Nyquist plots are shown in Figures 4.14e-h and Figures 4.17a-f. In order to obtain mechanistic insights from these plots, we fitted the impedance data using an electric equivalent circuit (EEC) and the element values derived from the EEC fit are summarized in Figures 4.17g and 4.17h.

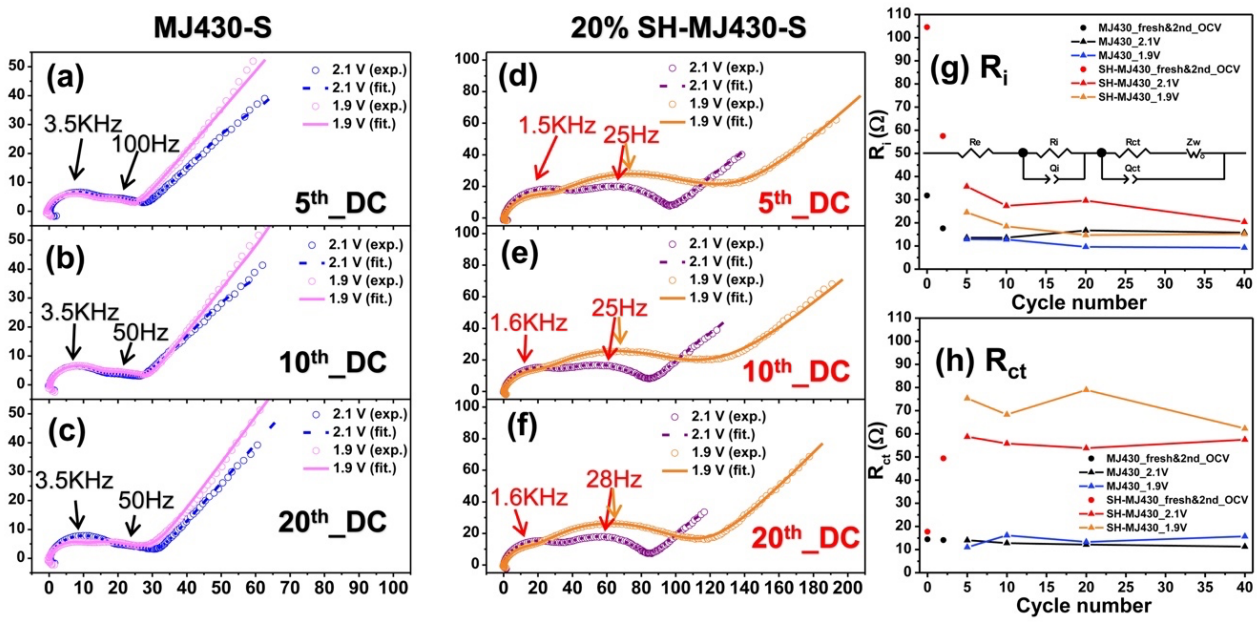

Figure 4.17. EIS analysis of (a-c) MJ430-S and (d-f) 20% SH-MJ430-S cells at different stages of discharge within 40 cycles. Fitted values of (g) the interface resistance R_i and (h) the charge transfer resistance R_{ct} of MJ430-S and 20% SH-MJ430-S cells at different voltage stages. The electric equivalent circuit (EEC) used to fit impedance data is an inset in (g).

By comparing the plots of as prepared cells held at the open circuit (Figures 4.14e and 4.14g), we observed that the high-frequency interphase resistance (R_i) of 20% SH-MJ430-S cathode ($R_{i,fresh,SH}$ =104.5 Ω) is three-fold higher than that of the cells with MJ430-S cathodes ($R_{i,fresh}$ =31.8 Ω). The large increase in $R_{i,fresh}$ after the modification is primarily ascribed to the reduced lithium diffusion in the thicker surface film produced by the modification. After two formation cycles, R_i of both MJ430-S and 20% SH-MJ430-S cells dramatically decreased, likely attributable to the redistribution of sulfur species on the surface of the carbon host, allowing for better interface contacts. In contrast, the mid-frequency charge transfer resistance (R_{ct}) of 20% SH-MJ430-S cathode quickly increases ($R_{ct,fresh,SH}$ =17.7 Ω vs. $R_{ct,2nd,SH}$ = 49.4 Ω) and continues growing to 70-

80 Ω in the following cycles, while R_{ct} of the cell with MJ430-S cathode remains constant (~ 15 Ω) upon cycling. The growth of $R_{ct,SH}$ is likely related to the kinetically limiting formation of covalent disulfide bonds with thiol modifiers. Additionally, we notice a ~ 10 Ω increase in $R_{ct,SH}$ when the 20% SH-MJ430-S cell is discharged from 2.1 to 1.9 V (Figure 4.14h). We hypothesized that the increased resistance at lower potentials may be caused in part by an increasing activation barrier for further reduction of polysulfide chains tethered to the surface. Therefore, we suggest that the kinetic limitation after the modification is partially due to the need to drive additional surface reactions (formation of disulfide bonding), and partially due to a thickening of the dynamic semi-solid layer of active material within cathode pores (a result of more, and stronger, interaction modes with LiPSs), which hinders Li^+ diffusion within the carbon matrix.

4.5 CONCLUSIONS

In summary, the utility of a thiol-based, multifunctional, redox-active interface has been demonstrated for LiPS trapping and improved electrolyte wetting in C/S composite electrodes for Li-S batteries. This was achieved through a highly flexible synthetic method which grafts organic molecules onto the surface of conductive carbon host materials, allowing for variability in both desired functionality and degree of functionalization. In this study, we showed that thiol surfaces can interact with solvated active materials in multiple ways, including covalent interactions and electrostatic lithium bonding. Although the surface interaction increased the $R_{ct,SH}$ and cell overpotential, these side-effects can be balanced by fine-tuning the modifier concentration. We will plan to explore the potential of altering the molecular structure of modifiers to improve reaction kinetics with LiPSs in future studies. For example, since forming additional covalent disulfide bonds has been identified as the rate-limiting step during redox reactions, a dithiol molecular functionalization could be considered to address the issue, as several dithiols have been

reported to catalyst the reduction of polysulfides in chemical or biochemical systems.[35,42] Additionally, the polar, nucleophilic surface introduced by thiol modifiers allowed for a better wetting of the electrode surface by the electrolytes due to the dipole-dipole interaction of thiol groups with Li^+ from the electrolyte. This improved wettability allowed for better sulfur utilization in high loading (4 mg cm^{-2}) cells while maintaining the tethering of solvated LiPSs to the cathode surface. The thick cells were discharged at a relatively low rate to prevent the tremendous problems of Li anode during cycling at elevated discharge/charge current densities, including dendrite formation, pulverization, and solid electrolyte interphase buildup.[16] Future work associated with the Li-metal anode will be pursued to allow high discharge/charge current densities for high-sulfur-loading cells. In this work, the realization of multiple performance enhancements from a single functional group suggests the possibility of further rational molecular design of cathode systems based on small molecule interfaces.

REFERENCES

(1) Dunn, B.; Kamath, H.; Tarascon, J.-M. M. Electrical Energy Storage for the Grid: A Battery of Choices. *Science* **2011**, *334* (6058), 928–935. https://doi.org/10.1126/science.1212741.

(2) Howell, D.; Cunningham, B.; Duong, T.; Faguy, P. VTO Battery R & D Funding. **2016**, 24.

(3) Goodenough, J. B.; Park, K. S. The Li-Ion Rechargeable Battery: A Perspective. *Journal of the American Chemical Society*. 2013, pp 1167–1176. https://doi.org/10.1021/ja3091438.

(4) Hagen, M.; Hanselmann, D.; Ahlbrecht, K.; Maça, R.; Gerber, D.; Tübke, J. Lithium-Sulfur Cells: The Gap between the State-of-the-Art and the Requirements for High Energy Battery Cells. *Adv. Energy Mater.* **2015**, *5* (16), 1401986. https://doi.org/10.1002/aenm.201401986.

(5) Li, G.; Wang, S.; Zhang, Y.; Li, M.; Chen, Z.; Lu, J. Revisiting the Role of Polysulfides in Lithium-Sulfur Batteries. *Adv. Mater.* **2018**, *1705590*, 1–19. https://doi.org/10.1002/adma.201705590.

(6) Xu, R.; Lu, J.; Amine, K. Progress in Mechanistic Understanding and Characterization Techniques of Li-S Batteries. *Advanced Energy Materials*. Wiley-Blackwell August 1, 2015, p 1500408. https://doi.org/10.1002/aenm.201500408.

(7) Chen, J.; Han, K. S.; Henderson, W. A.; Lau, K. C.; Vijayakumar, M.; Dzwiniel, T.; Pan, H.; Curtiss, L. A.; Xiao, J.; Mueller, K. T.; Shao, Y.; Liu, J. Restricting the Solubility of Polysulfides in Li-S Batteries Via Electrolyte Salt Selection. *Adv. Energy Mater.* **2016**, *6* (11), 1600160. https://doi.org/10.1002/aenm.201600160.

(8) Zhang, S.; Ikoma, A.; Li, Z.; Ueno, K.; Ma, X.; Dokko, K.; Watanabe, M. Optimization of Pore Structure of Cathodic Carbon Supports for Solvate Ionic Liquid Electrolytes Based Lithium–Sulfur Batteries. *ACS Appl. Mater. Interfaces* **2016**, *8* (41), 27803–27813. https://doi.org/10.1021/acsami.6b09989.

(9) Eftekhari, A.; Kim, D.-W. Cathode Materials for Lithium–Sulfur Batteries: A Practical Perspective. *J Mater Chem A* **2017**. https://doi.org/10.1039/C7TA00799J.

(10) Pang, Q.; Liang, X.; Kwok, C. Y.; Nazar, L. F. Advances in Lithium-Sulfur Batteries Based on Multifunctional Cathodes and Electrolytes. *Nature Energy*. Macmillan Publishers Limited 2016, p 16132. https://doi.org/10.1038/nenergy.2016.132.

(11) Ji, X.; Lee, K. T.; Nazar, L. F. A Highly Ordered Nanostructured Carbon–Sulphur Cathode for Lithium–Sulphur Batteries. *Nat. Mater.* **2009**, *8* (6), 500–506. https://doi.org/10.1038/nmat2460.

(12) Li, Z.; Wu, H. Bin; Lou, X. W. Rational Designs and Engineering of Hollow Micro-/Nanostructures as Sulfur Hosts for Advanced Lithium-Sulfur Batteries. *Energy and Environmental Science*. Royal Society of Chemistry October 5, 2016, pp 3061–3070. https://doi.org/10.1039/c6ee02364a.

(13) Evers, S.; Nazar, L. F. Graphene-Enveloped Sulfur in a One Pot Reaction: A Cathode with Good Coulombic Efficiency and High Practical Sulfur Content. *Chem Commun* **2012**, *48* (9), 1233–1235. https://doi.org/10.1039/C2CC16726C.

(14) Fujimori, T.; Morelos-Gómez, A.; Zhu, Z.; Muramatsu, H.; Futamura, R.; Urita, K.; Terrones, M.; Hayashi, T.; Endo, M.; Young Hong, S.; Chul Choi, Y.; Tománek, D.; Kaneko, K. Conducting Linear Chains of Sulphur inside Carbon Nanotubes. *Nat. Commun.* **2013**, *4*, 2162. https://doi.org/10.1038/ncomms3162.

(15) Yuan, Z.; Peng, H. J.; Huang, J. Q.; Liu, X. Y.; Wang, D. W.; Cheng, X. B.; Zhang, Q. Hierarchical Free-Standing Carbon-Nanotube Paper Electrodes with Ultrahigh Sulfur-Loading for Lithium-Sulfur Batteries. *Adv. Funct. Mater.* **2014**, *24* (39), 6105–6112. https://doi.org/10.1002/adfm.201401501.
(16) Lochala, J.; Liu, D.; Wu, B.; Robinson, C.; Xiao, J. Research Progress toward the Practical Applications of Lithium–Sulfur Batteries. *ACS Appl. Mater. Interfaces* **2017**, *9* (29), 24407–24421. https://doi.org/10.1021/acsami.7b06208.
(17) Lv, D.; Zheng, J.; Li, Q.; Xie, X.; Ferrara, S.; Nie, Z.; Mehdi, L. B.; Browning, N. D.; Zhang, J. G.; Graff, G. L.; Liu, J.; Xiao, J. High Energy Density Lithium-Sulfur Batteries: Challenges of Thick Sulfur Cathodes. *Adv. Energy Mater.* **2015**, *5* (16), 1402290. https://doi.org/10.1002/aenm.201402290.
(18) Zhang, J.; Shi, Y.; Ding, Y.; Peng, L.; Zhang, W.; Yu, G. A Conductive Molecular Framework Derived Li2S/N,P-Codoped Carbon Cathode for Advanced Lithium–Sulfur Batteries. *Adv. Energy Mater.* **2017**, *7* (14), 1602876. https://doi.org/10.1002/aenm.201602876.
(19) Xiao, Z.; Yang, Z.; Zhang, L.; Pan, H.; Wang, R. Sandwich-Type NbS_2 @S@I-Doped Graphene for High-Sulfur-Loaded, Ultrahigh-Rate, and Long-Life Lithium–Sulfur Batteries. *ACS Nano* **2017**, *11* (8), 8488–8498. https://doi.org/10.1021/acsnano.7b04442.
(20) Zhou, W.; Chen, H.; Yu, Y.; Wang, D.; Cui, Z.; Disalvo, F. J.; Abruña, H. D. Amylopectin Wrapped Graphene Oxide/Sulfur for Improved Cyclability of Lithium-Sulfur Battery. *ACS Nano* **2013**, *7* (10), 8801–8808. https://doi.org/10.1021/nn403237b.
(21) Chen, H.; Dong, W.; Ge, J.; Wang, C.; Wu, X.; Lu, W.; Chen, L. Ultrafine Sulfur Nanoparticles in Conducting Polymer Shell as Cathode Materials for High Performance Lithium/Sulfur Batteries. *Sci. Rep.* **2013**, *3* (1), 1910. https://doi.org/10.1038/srep01910.
(22) Xia, W.; Mahmood, A.; Zou, R.; Xu, Q. Metal–Organic Frameworks and Their Derived Nanostructures for Electrochemical Energy Storage and Conversion. *Energy Environ. Sci.* **2015**, *8* (7), 1837–1866. https://doi.org/10.1039/C5EE00762C.
(23) Zhou, J.; Yu, X.; Fan, X.; Wang, X.; Li, H.; Zhang, Y.; Li, W.; Zheng, J.; Wang, B.; Li, X. The Impact of the Particle Size of a Metal-Organic Framework for Sulfur Storage in Li-S Batteries. *J. Mater. Chem. A* **2015**, *3* (16), 8272–8275. https://doi.org/10.1039/c5ta00524h.
(24) Liu, X.; Huang, J.-Q.; Zhang, Q.; Mai, L. Nanostructured Metal Oxides and Sulfides for Lithium-Sulfur Batteries. *Adv. Mater.* **2017**, *29* (20), 1601759. https://doi.org/10.1002/adma.201601759.
(25) Pei, F.; Lin, L.; Fu, A.; Mo, S.; Ou, D.; Fang, X.; Zheng, N. A Two-Dimensional Porous Carbon-Modified Separator for High-Energy-Density Li-S Batteries. *Joule* **2018**, *2* (2), 323–336. https://doi.org/10.1016/j.joule.2017.12.003.
(26) Seh, Z. W.; Sun, Y.; Zhang, Q.; Cui, Y. Designing High-Energy Lithium-Sulfur Batteries. *Chemical Society Reviews*. Royal Society of Chemistry October 10, 2016, pp 5605–5634. https://doi.org/10.1039/c5cs00410a.
(27) Pang, Q.; Liang, X.; Kwok, C. Y.; Nazar, L. F. Review—The Importance of Chemical Interactions between Sulfur Host Materials and Lithium Polysulfides for Advanced Lithium-Sulfur Batteries. *J. Electrochem. Soc.* **2015**, *162* (14), A2567–A2576. https://doi.org/10.1149/2.0171514jes.
(28) Zhou, G.; Yin, L.-C.; Wang, D.-W.; Li, L.; Pei, S.; Gentle, I. R.; Li, F.; Cheng, H.-M. Fibrous Hybrid of Graphene and Sulfur Nanocrystals for High-Performance Lithium–Sulfur Batteries. *ACS Nano* **2013**, *7* (6), 5367–5375. https://doi.org/10.1021/nn401228t.

(29) Zhou, G.; Paek, E.; Hwang, G. S.; Manthiram, A. Long-Life Li/Polysulphide Batteries with High Sulphur Loading Enabled by Lightweight Three-Dimensional Nitrogen/Sulphur-Codoped Graphene Sponge. *Nat. Commun.* **2015**, *6* (1), 7760. https://doi.org/10.1038/ncomms8760.
(30) Chang, C. H.; Manthiram, A. Covalently Grafted Polysulfur-Graphene Nanocomposites for Ultrahigh Sulfur-Loading Lithium-Polysulfur Batteries. *ACS Energy Lett.* **2018**, *3* (1), 72–77. https://doi.org/10.1021/acsenergylett.7b01031.
(31) Song, M. K.; Zhang, Y.; Cairns, E. J. A Long-Life, High-Rate Lithium/Sulfur Cell: A Multifaceted Approach to Enhancing Cell Performance. *Nano Lett.* **2013**, *13* (12), 5891–5899. https://doi.org/10.1021/nl402793z.
(32) Sun, Z.; Zhang, J.; Yin, L.; Hu, G.; Fang, R.; Cheng, H. M.; Li, F. Conductive Porous Vanadium Nitride/Graphene Composite as Chemical Anchor of Polysulfides for Lithium-Sulfur Batteries. *Nat. Commun.* **2017**, *8*, 14627. https://doi.org/10.1038/ncomms14627.
(33) Shaibani, M.; Akbari, A.; Sheath, P.; Easton, C. D.; Banerjee, P. C.; Konstas, K.; Fakhfouri, A.; Barghamadi, M.; Musameh, M. M.; Best, A. S.; Rüther, T.; Mahon, P. J.; Hill, M. R.; Hollenkamp, A. F.; Majumder, M. Suppressed Polysulfide Crossover in Li-S Batteries through a High-Flux Graphene Oxide Membrane Supported on a Sulfur Cathode. *ACS Nano* **2016**, *10* (8), 7768–7779. https://doi.org/10.1021/acsnano.6b03285.
(34) Mao, J.; Wang, Y.; Zhu, J.; Yu, J.; Hu, Z. Thiol Functionalized Carbon Nanotubes: Synthesis by Sulfur Chemistry and Their Multi-Purpose Applications. *Appl. Surf. Sci.* **2018**, *447*, 235–243. https://doi.org/10.1016/j.apsusc.2018.03.188.
(35) Hua, W.; Yang, Z.; Nie, H.; Li, Z.; Yang, J.; Guo, Z.; Ruan, C.; Chen, X.; Huang, S. Polysulfide-Scission Reagents for the Suppression of the Shuttle Effect in Lithium-Sulfur Batteries. *ACS Nano* **2017**, *11* (2), 2209–2218. https://doi.org/10.1021/acsnano.6b08627.
(36) Ponraj, R.; Kannan, A. G.; Ahn, J. H.; Lee, J. H.; Kang, J.; Han, B.; Kim, D. W. Effective Trapping of Lithium Polysulfides Using a Functionalized Carbon Nanotube-Coated Separator for Lithium-Sulfur Cells with Enhanced Cycling Stability. *ACS Appl. Mater. Interfaces* **2017**, *9* (44), 38445–38454. https://doi.org/10.1021/acsami.7b10641.
(37) Ma, L.; Zhuang, H. L.; Wei, S.; Hendrickson, K. E.; Kim, M. S.; Cohn, G.; Hennig, R. G.; Archer, L. A. Enhanced Li-S Batteries Using Amine-Functionalized Carbon Nanotubes in the Cathode. *ACS Nano* **2016**, *10* (1), 1050–1059. https://doi.org/10.1021/acsnano.5b06373.
(38) Kim, J. H.; Kim, T.; Jeong, Y. C.; Lee, K.; Park, K. T.; Yang, S. J.; Park, C. R. Stabilization of Insoluble Discharge Products by Facile Aniline Modification for High Performance Li-S Batteries. *Adv. Energy Mater.* **2015**, *5* (14), 1500268. https://doi.org/10.1002/aenm.201500268.
(39) Liu, M.; Visco, S. J.; Jonghe, L. C. De. ELECTROCHEMICAL PROPERTIES OF ORGANIC DISULFIDE/THIOLATE REDOX COUPLES. *J. Electrochem. Soc.* **1989**, *136* (9), 2570–2575. https://doi.org/10.1149/1.2097478.
(40) Joseph, A.; George, B. THE CURRENT STATUS OF SULPHUR VULCANIZATION AND DEVULCANIZATION CHEMISTRY: DEVULCANIZATION. *Rubber Sci.* **2016**, *29(1)*, 62–100.
(41) Borsari, M.; Cannio, M.; Gavioli, G. Electrochemical Behavior of Diphenyl Disulfide and Thiophenol on Glassy Carbon and Gold Electrodes in Aprotic Media. *Electroanalysis* **2003**, *15* (14), 1192–1197. https://doi.org/10.1002/elan.200390146.

(42) Lamoureux, G. V.; Whitesides, G. M. Synthesis of Dithiols as Reducing Agents for Disulfides in Neutral Aqueous Solution and Comparison of Reduction Potentials. *J. Org. Chem.* **1993**, *58* (3), 633–641. https://doi.org/10.1021/jo00055a015.
(43) Xu, N.; Qian, T.; Liu, X.; Liu, J.; Chen, Y.; Yan, C. Greatly Suppressed Shuttle Effect for Improved Lithium Sulfur Battery Performance through Short Chain Intermediates. *Nano Lett.* **2017**, *17* (1), 538–543. https://doi.org/10.1021/acs.nanolett.6b04610.
(44) Kim, H.; Lee, J.; Ahn, H.; Kim, O.; Park, M. J. Synthesis of Three-Dimensionally Interconnected Sulfur-Rich Polymers for Cathode Materials of High-Rate Lithium-Sulfur Batteries. *Nat. Commun.* **2015**, *6* (1), 7278. https://doi.org/10.1038/ncomms8278.
(45) Choudhury, S.; Srimuk, P.; Raju, K.; Tolosa, A.; Fleischmann, S.; Zeiger, M.; Ozoemena, K. I.; Borchardt, L.; Presser, V. Carbon Onion/Sulfur Hybrid Cathodes via Inverse Vulcanization for Lithium–Sulfur Batteries. *Sustain. Energy Fuels* **2018**, *2* (1), 133–146. https://doi.org/10.1039/C7SE00452D.
(46) Hoefling, A.; Nguyen, D. T.; Partovi-Azar, P.; Sebastiani, D.; Theato, P.; Song, S.-W.; Lee, Y. J. Mechanism for the Stable Performance of Sulfur-Copolymer Cathode in Lithium–Sulfur Battery Studied by Solid-State NMR Spectroscopy. *Chem. Mater.* **2018**, acs.chemmater.7b05105. https://doi.org/10.1021/acs.chemmater.7b05105.
(47) Toupin, M.; Bélanger, D. Spontaneous Functionalization of Carbon Black by Reaction with 4-Nitrophenyldiazonium Cations. *Langmuir* **2008**, *24* (5), 1910–1917. https://doi.org/10.1021/la702556n.
(48) Castner, D. G.; Hinds, K.; Grainger, D. W. *X-Ray Photoelectron Spectroscopy Sulfur 2p Study of Organic Thiol and Disulfide Binding Interactions with Gold Surfaces*; 1996.
(49) Li, G.; Sun, J.; Hou, W.; Jiang, S.; Huang, Y.; Geng, J. Three-Dimensional Porous Carbon Composites Containing High Sulfur Nanoparticle Content for High-Performance Lithium-Sulfur Batteries. *Nat. Commun.* **2016**, *7*, 10601. https://doi.org/10.1038/ncomms10601.
(50) Kwon, S. J.; Kim, C. W.; Jeong, W. T.; Lee, K. S. Synthesis and Electrochemical Properties of Olivine LiFePO4 as a Cathode Material Prepared by Mechanical Alloying. *J. Power Sources* **2004**, *137* (1), 93–99. https://doi.org/10.1016/J.JPOWSOUR.2004.05.048.
(51) Viel, P.; Le, X. T.; Huc, V.; Bar, J.; Benedetto, A.; Le Goff, A.; Filoramo, A.; Alamarguy, D.; Noël, S.; Baraton, L.; Palacin, S. Covalent Grafting onto Self-Adhesive Surfaces Based on Aryldiazonium Salt Seed Layers. *J. Mater. Chem.* **2008**, *18* (48), 5913. https://doi.org/10.1039/b811299a.
(52) Manthiram, A.; Fu, Y.; Chung, S.-H.; Zu, C.; Su, Y.-S. Rechargeable Lithium–Sulfur Batteries. *Chem. Rev.* **2014**, *114* (23), 11751–11787. https://doi.org/10.1021/cr500062v.
(53) Park, J. W.; Yamauchi, K.; Takashima, E.; Tachikawa, N.; Ueno, K.; Dokko, K.; Watanabe, M. Solvent Effect of Room Temperature Ionic Liquids on Electrochemical Reactions in Lithium-Sulfur Batteries. *J. Phys. Chem. C* **2013**, *117* (9), 4431–4440. https://doi.org/10.1021/jp400153m.
(54) Mikhaylik, Y. V.; Akridge, J. R. Polysulfide Shuttle Study in the Li/S Battery System. *J. Electrochem. Soc.* **2004**, *151* (11), A1969. https://doi.org/10.1149/1.1806394.
(55) Cuisinier, M.; Cabelguen, P.-E.; Evers, S.; He, G.; Kolbeck, M.; Garsuch, A.; Bolin, T.; Balasubramanian, M.; Nazar, L. F. Sulfur Speciation in Li–S Batteries Determined by Operando X-Ray Absorption Spectroscopy. *J. Phys. Chem. Lett.* **2013**, *4* (19), 3227–3232. https://doi.org/10.1021/jz401763d.

(56) Hou, T. Z.; Xu, W. T.; Chen, X.; Peng, H. J.; Huang, J. Q.; Zhang, Q. Lithium Bond Chemistry in Lithium–Sulfur Batteries. *Angew. Chem. - Int. Ed.* **2017**, *56* (28), 8178–8182. https://doi.org/10.1002/anie.201704324.
(57) Patel, M. U. M.; Arčon, I.; Aquilanti, G.; Stievano, L.; Mali, G.; Dominko, R. X-Ray Absorption Near-Edge Structure and Nuclear Magnetic Resonance Study of the Lithium-Sulfur Battery and Its Components. *ChemPhysChem* **2014**, *15* (5), 894–904. https://doi.org/10.1002/cphc.201300972.
(58) Liang, X.; Kwok, C. Y.; Lodi-Marzano, F.; Pang, Q.; Cuisinier, M.; Huang, H.; Hart, C. J.; Houtarde, D.; Kaup, K.; Sommer, H.; Brezesinski, T.; Janek, J.; Nazar, L. F. Tuning Transition Metal Oxide-Sulfur Interactions for Long Life Lithium Sulfur Batteries: The "Goldilocks" Principle. *Adv. Energy Mater.* **2016**, *6* (6), 1501636. https://doi.org/10.1002/aenm.201501636.

VITA

Ian A. Murphy was born in Jacksonville, Florida on September 9th, 1993, to Stephanie and David Murphy. Much to his mother's dismay, Ian's academic performance was average at best until he entered college. Shortly after his mother lost her battle with cancer, Ian began his studies in chemistry at the Tallahassee Community College before transferring to the Florida State University.

After transitioning to FSU, Ian began his research career under the guidance of Professor Kenneth Hanson. During this time, Ian studied the interaction of organometallic chromophore assemblies on metal-oxide surfaces. This work culminated in the publication of "Energy and Electron Transfer Cascade in Self-Assembled Bilayer Dye-Sensitized Solar Cells" with his colleague Dr. Omotola O. Ogunsolu (*ACS Appl. Mater. Interfaces* 2016, 8, 42, 28633-28640). Ian graduated from FSU with a B.S. in chemistry with honors.

In 2016, Ian began his graduate studies at the University of Washington studying lithium-sulfur batteries under the guidance of Professor Alex Jen, Professor Jihui Yang, and Dr. Sei-Hum Jang. This work was the basis for his master's thesis and his second co-first author publication "A Multi-functional Interface Derived from Thiol-Modified Mesoporous Carbon in Lithium-Sulfur Batteries" (*J. Mater. Chem. A,* 2019, 7, 13372-13381), written with Dr. April Li. During his time in the Jen Lab, Ian also completed the DIRECT program, an NSF funded data-science training course for physical science researchers studying various aspects of clean energy generation and storage.

Ian transitioned to the Cossairt Lab in 2018 to further explore the role of functional surface chemistry in electrochemical systems. This concept was explored in two publications – one of which was a co-authored perspective article written with Dr. David Ung titled "Designing Nanoparticle Interfaces for Inner-Sphere Catalysis" (*Dalton Trans.,* 2020, 49, 4995-5005). Ian's self-directed project on this topic was later published as "Covalent Functionalization of Nickel Phosphide Nanocrystals with Aryl-Diazonium Salts*"* (10.33774/chemrxiv-2021-3p4pp).

During his time at UW, Ian cofounded a student organization named Global Renewables Infrastructure Development (GRID). This organization aimed to give students interested in the

real-world application of renewable energy technology hands-on experience in designing and installing self-sustaining photovoltaic-battery modules. Over the course of Ian's tenure in GRID, he served as the technical and business team's lead officer. The work that GRID did in this period provided power to more than 50 households in rural Guatemala.

After completing his Ph.D. in chemistry from the University of Washington, Ian will begin work at Twelve in Berkeley, CA as a senior electrochemical engineer developing CO_2 electrolyzers.